Dawn Aerospace Mk-III

An exploration of cost driven mission scenarios of a winged Two Stage to Orbit semi-Reusable Launch Vehicle integrated in the common airspace

Thomas Haex

Delft University of Technology, Faculty of Aerospace Engineering

Dawn Aerospace Mk-III

An exploration of cost driven mission scenarios of a winged Two Stage to Orbit semi-Reusable Launch Vehicle integrated in the common airspace

by

Thomas Haex

to obtain the degree of Master of Science
at the Delft University of Technology,
to be defended publicly on July 02, 2020 at 14:00.

Student number:	4217535	
Project duration:	December 02, 2019 – July 02, 2020	
Thesis committee:	Prof. Dr. Ir. P.N.A.M. Visser	TU Delft, chairman
	Ir. M.C. Naeije,	TU Delft, supervisor
	Ir. B.T.C. Zandbergen	TU Delft
	Ir. T.R. Knop,	Dawn Aerospace, supervisor

This thesis is confidential and cannot be made public until July 02, 2022.

An electronic version of this thesis is available at http://repository.tudelft.nl/.

Cover photo adapted from an image taken by Jeffrey N. Williams, taken from Twitter.[1]

---

[1] Williams, J., 'Good morning! Northern Europe as we look over the North Sea and the Netherlands.', *International Space Station*, https://twitter.com/Astro_Jeff/status/735093350504796160, (accessed January 10, 2020).

Summary

The demand of small payload launch vehicles has been growing over the past years. Customers base their selection of launch vehicles on cost-effectiveness, flexibility, availability and reliability. A new launch vehicle, the Dawn Aerospace Mk-III, is proposed to be developed, while designed to take into account all these criteria.

For flexible and frequently available operations the launch trajectory is integrated in the common airspace. Manoeuvrability is identified as a key capability for safe operations in the common airspace. For high manoeuvrability the first stage is designed as a rocket propelled airplane, a so-called 'spaceplane'. The expendable upper stage is stored internally. After payload injection the first stage returns to the spaceport of take-off. This means the System is a Two Stage to Orbit semi-Reusable Launch Vehicle integrated in the common airspace.

Cost-effectiveness is a primary selection criterium in the decision making of customers, which is why cost is included from an early stage in the development. This study shows that for identifying the cost gradient in the design space the total dry mass of the vehicle is sufficient. In this way cost optimality is included, although the Cost per Flight cannot be determined. What is determined is the effect of different technical and operational considerations. Taking into account qualitative cost differences, a selection of cost derived mission scenarios are studied. This includes different Return to Launch Site methods, first stage engine design and lay-out, the prohibition of fairing usage and integrated landing gear for take-off and landing.

To analyse and optimize the different designs a Multidisciplinary Design Optimization tool is developed. This tool optimizes the vehicle and the ascent trajectory simultaneously to determine the lowest total dry mass solution meeting all requirements and constraints. To estimate the aerodynamic performance of the first stage the X-34 Advanced Technology Demonstrator is used as a reference vehicle. This means the geometry of the first stage is not optimized, while the size is. The upper stage is modelled as a conventional upper stage, of which the size and geometry is optimized.

The study shows that the proposed design is feasible, meeting all requirements and constraints. The result is a vehicle with a total dry mass of 6273.0 kg, Gross Take-Off Weight of 42972.8 kg and a first stage length of 19.4 m. Of the total dry mass 94.5% is reusable. The return of the first stage is driving the trajectory design, as a steep ascent trajectory is required for limiting the downrange of the first stage. This results in 30%-50% more gravity loss in the System, which demands for a high ΔV performance. Due to the size of the first stage and the propellant required for returning, the first stage ascent ΔV is limited. For that reason, the upper stage design has a Propellant Mass Fraction of 0.939, increasing the upper stage ascent ΔV performance. Achieving such a Propellant Mass Fraction is possible, but challenging. The upper stage design is identified as a key element in the System performance for successfully meeting all mission requirements.

Three different Return to Launch Site methods are compared. Two methods, in-plane pitch over and aeroturn, are active which requires return propellant. The third method, glideback, is passive. The study shows that glideback can be favourable. The total dry mass increase is 4.4% when compared to in-plane pitch over. The increase in heat load is ~16%, but the heat load in this study is limited with a total heat load of ~2.0 $\mathrm{MJ/m^2}$. However, for glideback an even higher upper stage Propellant Mass Fraction of 0.946 is required. This means that the result of the upper stage design determines if this return method is feasible.

Using a shared engine design on the first and upper stage shows promising results. Using a single first stage engine reduces the first stage dry mass by 4.0%. However, using a shared engine design is expected to decrease the development cost drastically, due to the reduced size of individual engines. The prohibition of fairing usage shows a stronger effect on the result. Allowing the use of a fairing decreases the first stage dry mass by a maximum of 9.6%. Fairing usage on the other hand harms the safe operations in the common airspace as the ejection of uncontrolled material requires large safety zones. The penalty on mass is acceptable for allowing integration in the common airspace. A landing gear sized for take-off results in a heavier vehicle. When the first stage is supported by a cart during take-off the first stage dry mass is decreased by 24.6%. When the first stage is air-launched the first stage dry mass decreases by 33.3%.

Keywords: *Spaceplane, Semi-Reusable Launch Vehicle, Return to Launch Site, Cost derived mission scenarios, Common airspace, Multidisciplinary Design Optimization*

Preface

Writing this preface is one of the final tasks I have to do in order to finish my Master at the Delft University of Technology. This means the transition has arrived between one of the most exiting periods of my life and a period with great challenges ahead, all new for me to discover. Being able to do this transition would never have been possible without people around me playing an important role in my academic, professional and personal life.

The report you hold in your hands is the result of my graduation research performed over the last ten months at Dawn Aerospace. I always said: "I have to graduate at a company for working with people and feeling inspired". I am very glad that the opportunity presented itself to graduate at Dawn. Rob Hermsen, thanks for bringing me in contact with the company. Jeroen Wink, thanks for inviting me to an interview. The way you showed your understanding for my position as a graduate student was very pleasant, just like the way you supported me in the initial phase of this research. All the other colleagues, thanks for the great time I had working at Dawn. The coffee breaks near the noisy coffee machine, the occasional drinks at the river and the Fishy Fridays. A special shout-out to Peter van den Berg and Roy Theussing, my fellow members of the first Dawn Christmas Committee, which I had the honour to chair.

No research goes without good quality control. For this I want to specifically thank my two supervisors. Tobias Knop, my daily supervisor at Dawn, thanks for always challenging me. I enjoyed our meetings which had great positive influence on the research, allowing for exchange of ideas and a critical reflection. You gave me a lot of freedom in designing the vehicle and trajectory and I think we really worked together as a team on the preliminary development of the Mk-III. Marc Naeije, my university supervisor, thanks for all the weekly meetings. There was a joke here about you occasionally not responding to emails, but in the end you even send one on Saturday evening! Thanks for being so reliable and thoughtful, showing a great amount of commitment and enthusiasm while always in for a joke. I really enjoyed working together.

Two members of the university staff I want to thank especially. Dominic Dirkx, thanks for all the support in the development process of the numerical tool. It is amazing how you find the time to respond that quick and it is even more amazing to see how deeply you understand Tudat. Not a single bug goes unnoticed. Barry Zandbergen, I want to thank you for your role in the mid-term and the research in general. The effort in commenting on a presentation in that amount is not self-evident. I think this shows your passion for education, which is praiseworthy.

My time at university also allowed for so many encounters with lovely people. I want to thank the great group of people we studied with in the Bachelors. I also want to thank the very motivated group of Master students with which we studied for all those endless projects and deadlines. Furthermore, I want to thank all the great friends I have with which I experienced and will experience so many adventures. Living together, party together, making music together, going on holiday together, always dining together. This all made my time in Delft unforgettable.

Finally, I want to thank my family. Robrecht, my brother, thanks for being one of the persons I feel most comfortable with. We had great fun, travelling East Africa, but we can also be very serious and focussed. This seriousness you showed by proofreading my thesis and giving very necessary comments. It was a lot of work, but it improved the textual quality a lot. Cecilia, my fantastic future sister in law, thanks for proofreading as well. My parents, Peter and Geertruid, thanks for always being so supportive. I am lucky to have such wonderful parents who inspire me and always motivate me for doing the best I can. Damini, my girlfriend, thanks for being there for me, getting my mind off things, helping me with tasks I am very bad at and above all giving me a great and exciting time.

And dear reader, thanks for showing your interest. If you are here for information or inspiration required for your own project or research, I hope you find it. And above all, I wish you enjoy reading this thesis as much as I enjoyed studying this topic!

Thomas Haex
June 17, 2020

Contents

Summary iii

Preface v

List of Figures xi

List of Tables xv

Nomenclature xvii

List of Abbreviations xix

1 Introduction 1
- 1.1 Dawn Aerospace and the Mk-III 1
  - 1.1.1 Dawn Aerospace Mk-III 2
- 1.2 State-of-the-art of closely related launch vehicles. 3
- 1.3 Introduction to the thesis research 5
- 1.4 Structure of the report 6

2 The implementation of a cost philosophy within the mission study 9
- 2.1 Market prediction of future demand for payload 9
- 2.2 Cost modelling of launch vehicles. 10
- 2.3 Cost approach emphasising the Mk-III feasibility and market value 10
  - 2.3.1 Implementation of the cost comparison function 11
- 2.4 Cost derived mission scenarios 13
- 2.5 Summary of the cost philosophy implemented in the mission study 15

3 Theory on numerical modelling and optimization of space vehicles and trajectories 17
- 3.1 Numerical optimization. 17
  - 3.1.1 Differential Evolution (DE1220) 18
  - 3.1.2 Multidisciplinary Design Optimization 19
  - 3.1.3 Optimal control 20
- 3.2 Motion fundamentals. 21
  - 3.2.1 Ordinary Differential Equations 21
  - 3.2.2 State variables 22
  - 3.2.3 Reference frames. 22
  - 3.2.4 Equations of Motion 23
- 3.3 Propagation and integration 24
  - 3.3.1 Propagation with Cowell's method. 24
  - 3.3.2 Integration with Runge-Kutta-Fehlberg method (RKF45) 25

4 An introduction to the mission and the implementation of the trajectory model 27
- 4.1 Mission profile 27
- 4.2 Ascent trajectory 28
  - 4.2.1 Constraints 29
  - 4.2.2 Velocity losses 30
- 4.3 Return to Launch Site 31
  - 4.3.1 Thermal loads 33

4.4 Trajectory model and implemented guidance . . . 34
4.4.1 Ascent . . . 34
4.4.2 Bearing angle . . . 35
4.4.3 In-plane pitch over guidance . . . 35
4.4.4 Aeroturn guidance . . . 36
4.4.5 Glideback guidance . . . 36
4.4.6 Take-off roll . . . 36
4.5 Environment models . . . 37
4.5.1 Atmosphere model - The United States Standard Atmosphere 1976 . . . 37
4.5.2 Gravity model - Newton's law of universal attraction . . . 38

5 Sizing of the vehicle and the estimation of corresponding performance 39
5.1 Propulsion . . . 39
5.1.1 Ideal Rocket Theory . . . 39
5.1.2 Thermo-chemistry . . . 40
5.1.3 Propulsion model design variables . . . 41
5.2 Aerodynamics . . . 41
5.2.1 Lift and drag . . . 41
5.2.2 First stage - X-34 Advanced Technology Demonstrator . . . 41
5.2.3 Upper stage . . . 42
5.3 Geometry and mass . . . 42
5.3.1 Upper stage . . . 42
5.3.2 First stage . . . 46

6 The integration and validation of the Multidisciplinary Design Optimization tool 51
6.1 Integration of the vehicle model and trajectory model into a Multidisciplinary Design Optimization tool . . . 51
6.1.1 TU Delft Astrodynamics Toolbox . . . 51
6.1.2 Structure of the Multidisciplinary Optimization Tool . . . 52
6.2 Vehicle model validation . . . 54
6.2.1 Propulsion validation . . . 54
6.2.2 Upper stage geometry and mass validation . . . 57
6.2.3 First stage geometry and mass validation . . . 59
6.3 Trajectory model validation . . . 64

7 Results and comparisons of the different cost derived mission scenarios 67
7.1 Results of the baseline scenario . . . 67
7.2 Variations in target altitude . . . 72
7.3 Variations in payload mass . . . 74
7.4 The effect of the selected return method . . . 77
7.5 Variations in design and operational scenarios . . . 79
7.5.1 Engine design . . . 79
7.5.2 Prohibition of fairing usage . . . 82
7.5.3 Alternative launch configurations . . . 84
7.6 Trajectory behaviour in the dense atmospheric layers . . . 86
7.7 Summary of the discussed results . . . 87

8 Sensitivity of the studied results 89
8.1 One-at-the-time approach . . . 89
8.1.1 Control node variation . . . 89
8.1.2 Time and vehicle design variation . . . 90
8.2 Monte-Carlo analysis . . . 92
8.3 Model based sensitivity analysis . . . 94
8.3.1 Propulsion model . . . 94
8.3.2 Aerodynamics model . . . 97
8.3.3 Geometry and mass model . . . 100
8.3.4 Runway heading . . . 104

9 Conclusions and recommendations 105
9.1 Conclusions. 105
9.2 Recommendations 112

Bibliography 113

A Baseline design input and result 117

B Glideback return loss analysis 119

C Sensitivity analysis results 121

List of Figures

1.1 Sketch of the Dawn Aerospace Mk-II (see Footnote 2) 2
1.2 Dawn Aerospace PM200 in-space propulsion unit (see Footnote 1) 2
1.3 FESTIP Sub-orbital Hopper Internal Arrangement with a 7000 kg payload (Spies and Kuczera, 1999) 3
1.4 Tsuchiya and Mori (2004) optimized horizontal take-off vehicle with an 8000 kg payload 3
1.5 Polaris Raumflugzeuge based on the Aurora space launcher concept (see Footnote 4) 4
1.6 Orbital Access 500R based on the Maddock et al. (2018) launch system concept (see Footnote 5) . . 4

2.1 Future baseline forecast on the volume of payloads per year, segmented by mass (McIntyre et al., 2016) 10
2.2 Average payload mass per year between 2017 and 2036, with perspective segmentation (McIntyre et al., 2016) 10
2.3 Total cost comparison number per flight plotted against Gross Take-Off Weight (based on 50 launches with a learning factor of 0.9 and a refurbishment factor of 0.1) 12
2.4 Total cost comparison number per flight plotted against total vehicle dry mass (based on 50 launches with a learning factor of 0.9 and a refurbishment factor of 0.1) 12
2.5 Space Shuttle Main Engine test at the NASA Stennis B-1 test stand - Mass flow approximately 500 kg/s (Sachdev et al., 2010)(see Footnote 5) 13
2.6 Rutherford engine test at Rocket Lab's test facility - Mass flow approximately 7 kg/s (see Footnote 6, 7) 13

3.1 The basic optimization process (reproduced from (Weck et al., 2007)) 18
3.2 Graphical representation of the Differential Evolution algorithm (see Footnote 2) 19
3.3 Architecture of the Multi Discipline Feasible method as implemented in this study (adapted figure from (Balesdent, 2011)) 20
3.4 Some of the classical orbital elements (Leomanni et al., 2017) 23
3.5 Earth-Centred-Earth-Fixed rotating reference frame (adapted figure from (Balesdent, 2011)) 24

4.1 Launch vehicle mission profile with three distinct flight phases 27
4.2 Sketch of a Direct Ascent and Hohmann Transfer Ascent (Wakker, 2015) 29
4.3 Return to Launch Site manoeuvre of the SpaceX Falcon 9 (see Footnote 5) 31
4.4 In-plane pitch over manoeuvre (Bradford and St. Germain, 2010) 32
4.5 Aeroturn manoeuvre (Bradford and St. Germain, 2010) 33
4.6 Example of an optimization result of the parametric control law determining the desired flight path angle profile for orbit injection 34
4.7 Runway 24 of Rotterdam The Hague Airport (see Footnote 8) 36

5.1 Test results of the X-34 Advanced Technology Demonstrator wind-tunnel test: 3D lift coefficient as a function of Angle of Attack (left) and 3D drag coefficient as a function of Angle of Attack (right) for a set of Mach numbers (Brauckmann, 1999) 42
5.2 Common bulkhead tank design on the Advanced Common Evolved Stage (adapted image from (Zegler and Kutter, 2010)) 44
5.3 Schematic of the complete lay-out of the upper stage 46
5.4 Schematic of the complete lay-out of the first stage (adapted image from (Weiland, 2014)) 47
5.5 Wing area of several fighter jets (see Footnote 6, 7, 8, 9, 10, 11) 49

6.1 Inner structure of the Multidisciplinary Design Optimization tool in which the design input is optimized by the optimization algorithm increasing the fitness of the solution 53
6.2 Aurora-R1 total mass breakdown (Kopp et al., 2018) 60

6.3 Maddock et al. (2018) total mass breakdown . . . 60

6.4 First stage dry mass breakdown of the Electron with spaceplane configuration ($\dot{m}$ = 6.936 kg/s) . . . 62

6.5 First stage total mass breakdown of the Electron with spaceplane configuration ($\dot{m}$ = 6.936 kg/s) . . 62

6.6 First stage dry mass breakdown of the Electron with spaceplane configuration ($\dot{m}$ = 13.872 kg/s) . . 62

6.7 First stage total mass breakdown of the Electron with spaceplane configuration ($\dot{m}$ = 13.872 kg/s) . 62

6.8 First stage dry mass breakdown of the Electron with spaceplane configuration ($\dot{m}$ = 20.808 kg/s) . . 62

6.9 First stage total mass breakdown of the Electron with spaceplane configuration ($\dot{m}$ = 20.808 kg/s) . 62

6.10 First stage dry mass breakdown of a hydrogen peroxide/kerosene launcher with spaceplane configuration ($\dot{m}$ = 5.0 kg/s) . . . 63

6.11 First stage total mass breakdown of a hydrogen peroxide/kerosene launcher with spaceplane configuration ($\dot{m}$ = 5.0 kg/s) . . . 63

6.12 First stage dry mass breakdown of a hydrogen peroxide/kerosene launcher with spaceplane configuration ($\dot{m}$ = 10.0 kg/s) . . . 63

6.13 First stage total mass breakdown of a hydrogen peroxide/kerosene launcher with spaceplane configuration ($\dot{m}$ = 10.0 kg/s) . . . 63

6.14 First stage dry mass breakdown of a hydrogen peroxide/kerosene launcher with spaceplane configuration ($\dot{m}$ = 20.0 kg/s) . . . 63

6.15 First stage total mass breakdown of a hydrogen peroxide/kerosene launcher with spaceplane configuration ($\dot{m}$ = 20.0 kg/s) . . . 63

6.16 Internal geometry of the Maddock et al. (2018) launch vehicle used for deriving wing area 64

6.17 Altitude comparison over time between the optimization tool optimal trajectory result (seed = 321) and the Maddock et al. (2018) optimal trajectory . . . 65

6.18 Velocity comparison over time between the optimization tool optimal trajectory result (seed = 321) and the Maddock et al. (2018) optimal trajectory . . . 65

6.19 Altitude comparison over downrange between the optimization tool optimal trajectory result (seed = 321) and the Maddock et al. (2018) optimal trajectory . . . 65

6.20 Optimized trajectory flight path angles of the best performing individual of every seed for the Maddock validation case . . . 65

7.1 Range of optimal flight path angles of 20 individual solutions with the best performing solution marked, of three different seeds . . . 68

7.2 Range of optimal times of 20 individual solutions with the best performing solution marked, of three different seeds (legend is valid for Figure 7.1 to 7.3) . . . 68

7.3 Range of optimal engine amount, mass flow, first and upper stage exit diameter and upper stage diameter of 20 individual solutions with the best performing solution marked, of three different seeds 68

7.4 Fitness value of the objective function shown for the 20 individuals of the three different seeds, accompanied by the minimum fitness value based on dry mass . . . 69

7.5 Orbital injection precision of the 20 individuals of the three different seeds showing the pericenter altitude and the eccentricity of the orbit . . . 69

7.6 ΔV distribution of the first stage during ascent, showing the increase in velocity and the occurring losses . . . 70

7.7 ΔV distribution of the upper stage during ascent, showing the increase in velocity and the occurring losses . . . 70

7.8 Accelerations in the body frame during the ascent of the first stage . . . 70

7.9 Accelerations in the body frame during the return of the first stage (legend is also valid for Figure 7.8 and 7.18) . . . 70

7.10 Altitude over time of the lightest three individuals of each seed, with the absolute lightest highlighted (legend shows the line structure used for all figures in this chapter which show the different flight phases) . . . 71

7.11 Velocity over time of the lightest three individuals of each seed, with the absolute lightest highlighted (legend is valid for Figures 7.10 to 7.17) . . . 71

7.12 Ascent Angle of Attack of the first and upper stage of the lightest three individuals of each seed, with the absolute lightest highlighted . . . 71

7.13 Ascent Flight Path Angle of the first and upper stage of the lightest three individuals of each seed, with the absolute lightest highlighted . . . 71

7.14 Dynamic pressure during first stage ascent and return of the lightest three individuals of each seed, with the absolute lightest highlighted . . . 71
7.15 Stagnation point heat flux during re-entry of the first stage of the lightest three individuals of each seed, with the absolute lightest highlighted . . . 71
7.16 qα bending load during first stage ascent of the lightest three individuals of each seed, with the absolute lightest highlighted . . . 71
7.17 Aerothermal flux of the upper stage in the begin phase of the ascent of the lightest three individuals of each seed, with the absolute lightest highlighted . . . 71
7.18 Accelerations in the body frame during the ascent of the upper stage . . . 72
7.19 Optimal mass distribution of the first stage for four different orbital altitudes . . . 73
7.20 Optimal mass distribution of the upper stage for four different orbital altitudes . . . 73
7.21 Optimal ascent and return trajectories for four different orbital altitudes (legend valid for Figure 7.21 and 7.22) . . . 74
7.22 Optimal return trajectories for four different orbital altitudes . . . 74
7.23 Velocity over time of the optimal ascent and return trajectories for four different orbital altitudes (legend valid for Figure 7.23 and 7.24) . . . 74
7.24 First stage velocity over time of the optimal ascent and return trajectories for four different orbital altitudes . . . 74
7.25 Optimal mass distribution of the first stage for four different payload masses . . . 75
7.26 Optimal mass distribution of the upper stage for four different payload masses . . . 75
7.27 Optimal ascent and return trajectories for four different payload masses (legend valid for Figure 7.27 and 7.28) . . . 76
7.28 Optimal return trajectories for four different payload masses . . . 76
7.29 Velocity over time of the optimal ascent and return trajectories for four different payload masses (legend valid for Figure 7.29 and 7.30) . . . 76
7.30 First stage velocity over time of the optimal ascent and return trajectories for four different payload masses . . . 76
7.31 Optimal mass distribution of the first stage for four different return methods . . . 78
7.32 Optimal mass distribution of the upper stage for four different return methods . . . 78
7.33 Optimal ascent and return trajectories for four different return methods (legend valid for Figure 7.33 and 7.34) . . . 78
7.34 Optimal return trajectories for four different return methods . . . 78
7.35 Velocity over time of the optimal ascent and return trajectories for four different return methods (legend valid for Figure 7.35 and 7.36) . . . 78
7.36 First stage velocity over time of the optimal ascent and return trajectories for four different return methods . . . 78
7.37 Dynamic pressure experienced by the first stage during ascent and return (legend valid for Figure 7.37 and 7.38) . . . 79
7.38 Stagnation point heat flux experienced by the first stage during ascent and return . . . 79
7.39 Optimal mass distribution of the first stage for three different engine configurations . . . 80
7.40 Optimal mass distribution of the upper stage for three different engine configurations . . . 80
7.41 Optimal ascent and return trajectories for three different engine configurations (legend valid for Figure 7.41 and 7.42) . . . 81
7.42 Optimal return trajectories for three different engine configurations . . . 81
7.43 Velocity over time of the optimal ascent and return trajectories for three different engine configurations (legend valid for Figure 7.43 and 7.44) . . . 81
7.44 First stage velocity over time of the optimal ascent and return trajectories for three different engine configurations . . . 81
7.45 Optimal mass distribution of the first stage for configurations without and with the use of a fairing at two different orbital altitudes . . . 83
7.46 Optimal mass distribution of the upper stage for configurations without and with the use of a fairing at two different orbital altitudes . . . 83
7.47 Optimal ascent and return trajectories for configurations without and with the use of a fairing at two different orbital altitudes (legend valid for Figure 7.47 and 7.48) . . . 83
7.48 Optimal return trajectories for configurations without and with the use of a fairing at two different orbital altitudes . . . 83

7.49 Velocity over time of the optimal ascent and return trajectories for configurations without and with the use of a fairing at two different orbital altitudes (legend valid for Figure 7.49 and 7.50) 84
7.50 First stage velocity over time of the optimal ascent and return trajectories for configurations without and with the use of a fairing at two different orbital altitudes 84
7.51 Optimal mass distribution of the first stage for three alternative launch configurations 85
7.52 Optimal mass distribution of the upper stage for three alternative launch configurations 85
7.53 Optimal ascent and return trajectories for three alternative launch configurations (legend valid for Figure 7.53 and 7.54) 85
7.54 Optimal return trajectories for three alternative launch configurations 85
7.55 Velocity over time of the optimal ascent and return trajectories for three alternative launch configurations (legend valid for Figure 7.55 and 7.56) 86
7.56 First stage velocity over time of the optimal ascent and return trajectories for three alternative launch configurations 86
7.57 Ground track of the launch vehicle for different turn altitudes, showing the threshold behaviour of changing the azimuth 87

8.1 Normalized change of the semi-major axis altitude and eccentricity for in- and decrements of control node 1 (legend valid for Figure 8.1 to 8.4, a cross indicates exceeding the limit) 90
8.2 Normalized change of the semi-major axis altitude and eccentricity for in- and decrements of control node 5 90
8.3 Normalized change of the semi-major axis altitude and eccentricity for in- and decrements of control node 6 90
8.4 Normalized change of the semi-major axis altitude and eccentricity for in- and decrements of control node 10 90
8.5 Sensitivity of the return for a one-at-the-time change of the individual control nodes at different levels of change (red indicates a non-return, while green indicates a successful return) 91
8.6 Normalized change of the semi-major axis altitude and eccentricity for a change of first stage burn time (legend also valid for Figure 8.8, a cross indicates exceeding the limit) 91
8.7 Normalized change of the total dry mass and ΔV for a change of first stage burn time (legend also valid for Figure 8.9) 91
8.8 Normalized change of the semi-major axis altitude and eccentricity for a change of mass flow . . . 92
8.9 Normalized change of the total dry mass and ΔV for a change of mass flow 92
8.10 Result of the Monte-Carlo analysis showing the distribution of the orbital injection for three different normal distributed ranges of change of the control nodes 93
8.11 Result of the Monte-Carlo analysis showing the distribution of the orbital injection for three different normal distributed ranges of change in time (legend also valid for Figure 8.12) 93
8.12 Result of the Monte-Carlo analysis showing the distribution of the total dry mass and ΔV for three different normal distributed ranges of change in time 93
8.13 Result of the Monte-Carlo analysis showing the distribution of the orbital injection for three different normal distributed ranges of change in vehicle design parameters (legend also valid for Figure 8.14) 94
8.14 Result of the Monte-Carlo analysis showing the distribution of the total dry mass and ΔV for three different normal distributed ranges of change in vehicle design parameters 94
8.15 Upper stage propellant mass fraction against usable propellant mass (Holt and Monk, 2009) 102
8.16 Propellant mass fraction trend over the years of spacecraft development (Holt and Monk, 2009) . . 103
8.17 Orbital injection for take-off of the baseline vehicle at different runway headings shown in degrees 104

9.1 Optimal ascent and return trajectory of the baseline scenario as an answer to the Primary Research Question (legend valid for Figure 9.1 and 9.2) 107
9.2 Optimal return trajectory of the baseline scenario as an answer to the Primary Research Question . 107
9.3 Take-off trajectory of the Mk-III at runway 06 of Rotterdam The Hague Airport 109
9.4 'Good morning! Northern Europe as we look over the North Sea and the Netherlands' inspired take-off trajectory image 109
9.5 Take-off trajectory of the Mk-III as seen from the historical centre of Delft 111
9.6 Take-off trajectory of the Mk-III as seen from the centre of London 111

List of Tables

2.1 Cost Estimating Relationships statistical parameters for components of a liquid rocket stage derived from sample data with valid mass range (Drenthe, 2016) . . . 12

3.1 Comparison of numerical integrator behaviour with a precision ϵ_{tol} of 10^{-4} for a general trajectory problem . . . 26

4.1 Reference heights, temperature gradients and pressures for the different layers of the United States Standard Atmosphere 1976 (Kesteren, 2013b) . . . 37

5.1 Upper stage geometry and mass estimation elements . . . 43
5.2 First stage geometry and mass estimation elements . . . 46

6.1 Validation data, model result and quality factors of the Merlin-1D engine (see Footnote 2) . . . 55
6.2 Validation data, model result and quality factors of the H-1 engine (see Footnote 3, 4, 5) - *(*) Derived value* . . . 55
6.3 Validation data, model result and quality factors of the Rutherford engine (see Footnote 6) - *(*) Derived value* . . . 56
6.4 Validation data of the Gamma 8 engine (see Footnote 7) - *(*) Derived value* . . . 56
6.5 Model results and quality factors of the Gamma 8 engine . . . 56
6.6 Comparison of the range of quality factors found in different studies (Huzel and Huang, 1971)(Sutton and Biblarz, 2001) . . . 57
6.7 Constant design parameters and physical properties of a carbon composite LOX/RP-1 rocket stage (Zandbergen, 2018)(see Footnote 8) . . . 57
6.8 Electron upper stage validation case (see Footnote 9) - *(*) Derived value* . . . 58
6.9 Changed constant design parameters and physical properties as compared to Table 6.7 (see Footnote 12, 13) . . . 58
6.10 Blok D validation case (see Footnote 10, 11) . . . 59
6.11 Conventional rocket elements compared to the Electron first stage (see Footnote 6, 9) - *(*) Derived value* . . . 60
6.12 A hydrogen peroxide/kerosene first stage validation case . . . 61
6.13 Model results and fractions of wing, tail and landing gear mass of the Electron with spaceplane configuration . . . 62
6.14 Model results and fractions of wing, tail and landing gear mass of a general hydrogen peroxide/kerosene launcher with spaceplane configuration . . . 63
6.15 Vehicle characteristics of the Maddock et al. (2018) launch vehicle used in the trajectory validation case - *(*) Derived value* . . . 64
6.16 Optimized trajectory coasting times of the best performing individual of every seed for the Maddock validation case . . . 64
6.17 Orbital fitness of the best performing individual of every seed for the Maddock validation case . . . 65
6.18 RKF-45 numerical integrator tolerance behaviour of the Maddock et al. (2018) validation case (best performing solution seed 123) . . . 66

7.1 Optimal baseline design of the nominal launch scenario (found in optimization of seed 321) . . . 69
7.2 Optimal design input of the launch vehicle for three different orbital altitudes . . . 72
7.3 Optimal design of the launch vehicle for three different orbital altitudes . . . 73
7.4 Optimal design input of the launch vehicle for three different payload masses . . . 75
7.5 Optimal design of the launch vehicle for three different payload masses . . . 75
7.6 Optimal design input of the launch vehicle for three different return methods . . . 77
7.7 Optimal design of the launch vehicle for three different return methods . . . 77

7.8 Optimal design input of the launch vehicle for two different first stage engine configurations 80
7.9 Optimal design of the launch vehicle for two different first stage engine configurations 80
7.10 Optimal design input of the launch vehicle when the use of a fairing is allowed for two different orbital altitudes 82
7.11 Optimal design of the launch vehicle when the use of a fairing is allowed for two different orbital altitudes 82
7.12 Optimal design input of the launch vehicle for two alternative launch configurations 84
7.13 Optimal design of the launch vehicle for two alternative launch configurations 85
7.14 Launch vehicle mass distribution for different turn altitudes (5000 m turn does not result in a polar orbit) 86

8.1 Optimal design input of the launch vehicle for two different oxidizer-over-fuel ratios 95
8.2 Optimal design of the launch vehicle for two different oxidizer-over-fuel ratios 95
8.3 Optimal vehicle design input of the launch vehicle for four different engine qualities 96
8.4 Optimal trajectory design input of the launch vehicle for four different engine qualities 96
8.5 Optimal design of the first stage for four different engine qualities 97
8.6 Optimal design of the upper stage for four different engine qualities 97
8.7 Optimal design input of the launch vehicle for two different aerodynamic coefficient sets with in-plane pitch over return 98
8.8 Optimal design of the launch vehicle for two different aerodynamic coefficient sets with in-plane pitch over return 98
8.9 Optimal design input of the launch vehicle for two different aerodynamic coefficient sets with glide-back return 99
8.10 Optimal design of the launch vehicle for two different aerodynamic coefficient sets with glideback return 99
8.11 Structure of the sensitivity analysis on the mass model 100
8.12 Optimal vehicle design input of the launch vehicle for four different mass model scenarios (Case 2 and Case 4 do not return, noticed by constraint violation) 100
8.13 Optimal trajectory design input of the launch vehicle for four different mass model scenarios (Case 2 and Case 4 do not return, noticed by constraint violation) 101
8.14 Optimal design of the first stage for four different mass model scenarios (Case 2 and Case 4 do not return, noticed by constraint violation) 101
8.15 Optimal design of the upper stage for four different mass model scenarios (Case 2 and Case 4 do not return, noticed by constraint violation) 102

9.1 Optimal design input of the baseline scenario as an answer to the Primary Research Question . . . 107
9.2 Optimal design of the baseline scenario as an answer to the Primary Research Question 107

Nomenclature

Greek symbols

α	Angle of Attack	[deg]
α_T	Thermal accommodation coefficient	[-]
β	Safety factor	[-]
Γ	Vandenkerckhove parameter	[-]
γ	Flight path angle	[deg]
	Specific heat ratio	[-]
δ	Latitude	[deg]
ϵ	Construction mass ratio	[-]
	Tolerance error	[-]
ζ	Quality factor	[-]
θ	Pitch angle	[deg]
λ	Payload fraction	[-]
μ	Absolute viscosity	[Pa s]
	Bank angle	[deg]
ρ	Density	[kg m^{-3}]
σ	Stress	[Pa]
	Ultimate load strength	[Pa]
τ	Longitude	[deg]
Φ	Increment function	[-]
χ	Heading angle	[deg]
Ω	Longitude of the ascending node	[deg]
ω	Argument of perigee	[deg]
ω_E	Earth's angular velocity	[deg s^{-1}]

Roman symbols

A	Area	[m^2]
a	Acceleration	[m s^{-2}]
	Semi-major axis	[m]
C_D	Drag coefficient	[-]
C_d	Discharge coefficient	[-]
C_F	Thrust coefficient	[-]
C_L	Lift coefficient	[-]
c^*	Characteristic velocity	[m s^{-1}]
c_p	Profit retention factor	[-]
c_ref	Refurbishment factor	[-]
D	Drag	[N]
d	Diameter	[m]
e	Eccentricity	[-]
F	Force	[N]
f	Fitness	[-]
	Fraction	[-]
G	Universal gravitational constant	[m^3 s^{-2}kg^{-1}]
g	Gravitational acceleration	[m s^{-2}]
g_0	Earth's gravitational acceleration	[m s^{-2}]

H	Geopotential altitude	[m’]
	Total enthalpy	[J]
H_{s}	Scale height	[m]
h	Altitude	[m]
	Static enthalpy	[J]
h_{opt}	Optimal step-size	[-]
I_{sp}	Specific impulse	[s]
i	Inclination	[deg]
K	Correction factor	[-]
K_{c}	Control gain	[-]
k	Boltzmann constant	[J K^{-1}]
L	Lift	[N]
L^*	Characteristic length	[m]
$L_{\mathrm{c_n}}$	Batch factor	[-]
l	Length	[m]
M	Bending moment	[Nm]
	Mach number	[-]
	Mean anomaly	[deg]
	Mean molecular weight	[kg mole^{-1}]
m	Mass	[kg]
N_{A}	Avogadro’s constant	[mole^{-1}]
O/F	Oxidizer-over-fuel ratio	[-]
Pr	Prandtl number	[-]
p	Penalty	[-]
	Pressure	[Pa]
Q	Heat load	[J m^{-2}]
q	Dynamic pressure	[Pa]
	Heat flux	[W m^{-2}]
	Mass flow rate	[kg s^{-1}]
R^*	Universal gas constant	[JK mole^{-1}]
R_{A}	Avogadro’s number	[mole^{-1}]
R_{N}	Nose radius	[m]
r	Radial distance	[m]
S	Surface area	[m^2]
T	Temperature	[K]
	Thrust	[N]
t	Thickness	[m]
	Time	[s]
U_{e}	Exhaust velocity	[m s^{-1}]
U_{eq}	Equivalent exhaust velocity	[m s^{-1}]
V	Velocity magnitude	[m s^{-1}]
	Volume	[m^3]
X	Model input vector	[-]
Z	Geometric altitude	[m]

List of Abbreviations

AoA	Angle of Attack
CEA	Chemical Equilibrium with Applications
CpF	Cost per Flight
EOMs	Equations of Motion
FPA	Flight Path Angle
GTOW	Gross Take-Off Weight
HTOHL	Horizontal Take-Off Horizontal Landing
IRT	Ideal Rocket Theory
LEO	Low Earth Orbit
LOX	Liquid oxygen
MDA	Multidisciplinary Design Analysis
MDO	Multidisciplinary Design Optimization
Mk-III	Dawn Aerospace Mk-III - *'Mark-three'*
ODE	Ordinary Differential Equation
PMF	Propellant Mass Fraction
PpF	Price per Flight
PRQ	Primary Research Question
PSQ	Primary Sub-Question
(s)RLV	(semi-)Reusable Launch Vehicle
RP-1	Rocket Propellant-1
RTLS	Return to Launch Site
TPS	Thermal Protection System
TSTO	Two Stage to Orbit
Tudat	TU Delft Astrodynamics Toolbox
UAV	Unmanned Aerial Vehicle
X-34	X-34 Advanced Technology Demonstrator

1
Introduction

A new era in space vehicle development has arrived. Since the early years of developing space technology large government funded organisations were founded and projects were conducted. This rapidly increased the possibilities of launching payload into space or even accessing space by human flight. However, over the last few years the landscape totally changed. Not only did the payload itself become smaller because of increased technological knowledge on miniaturization, also the ambition of launching payload into space became a driver for privately owned companies. Currently there is an ongoing rapid commercialization of the launch industry, developing cost effective solutions targeting the increase in demand of small payload launch.

Dawn Aerospace is one of such companies, currently involved in the development of the *Dawn Aerospace Mk-III* (Mk-III). A very ambitious mission and vehicle design is envisioned, ready for launching small satellites into orbit in 2024. The fundamental requirements for the operations were formulated, however, the behaviour of the System - both considering the vehicle design as well as the mission geometry - has not been studied yet. Moreover, especially considering the size of the vehicle, this kind of vehicle has never been studied in academic research. What makes this vehicle unique is the fact that it is rocket propelled, completely autonomous, takes off and lands horizontally, reuses the first stage and all this while integrated in the common airspace. The aim of this thesis study is twofold. Firstly, increasing the collective understanding of this kind of vehicle and mission geometry. Secondly, identifying primary drivers in the design influencing the performance and cost of the vehicle in order to support the development process of Dawn Aerospace.

In this introductory chapter first Dawn Aerospace as well as the Mk-III are introduced. Next, the state-of-the-art of closely related launch vehicles is discussed. Finally, the objective and research questions of the thesis research itself are presented and the structure of the report is explicated.

1.1. Dawn Aerospace and the Mk-III

Dawn Aerospace is a young start-up, founded in late 2018, with facilities in the Netherlands and New Zealand. The company aims for a market share in both the in-space propulsion as well as the launch industry. The available products for in-space propulsion are the PM200 for cubesats and the NP22 for small satellites.[1] The unique selling point is the fact that these modules offer high thrust for low power consumption, while only making use of green propellants. Furthermore, the ΔV offered by these modules is considerably large in a small amount of time. The modules were developed over the past two years and are now available for sale.

For conquering market share in the launch industry a revolutionary vehicle is envisioned flying a highly innovative mission design. This vehicle, the Mk-III, is introduced in the next section. Predecessors of the Mk-III were developed and tested already. In 2018 the Dawn Aerospace Mk-I showed the feasibility of using rocket propulsion on aircraft. The small *Unmanned Aerial Vehicle* (UAV) was flight tested showing the in-flight capabilities of rocket propulsion. Next is the Dawn Aerospace Mk-II, of which the development is finished and first test flights are planned for mid 2020.[2] This vehicle will show sub-orbital capabilities of a rocket propelled UAV, both in subsonic

---

[1] 'Satellite positioning so green, you can eat it', *Dawn Aerospace*, `https://www.dawnaerospace.com/position`, (accessed on May 08, 2020).

[2] 'Any runway, any orbit, any day', *Dawn Aerospace*, `https://www.dawnaerospace.com/deliver`, (accessed on May 08, 2020).

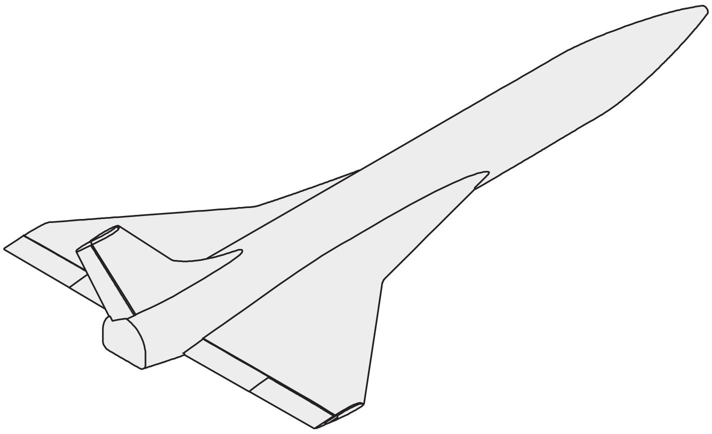

Figure 1.1: Sketch of the Dawn Aerospace Mk-II (see Footnote 2)

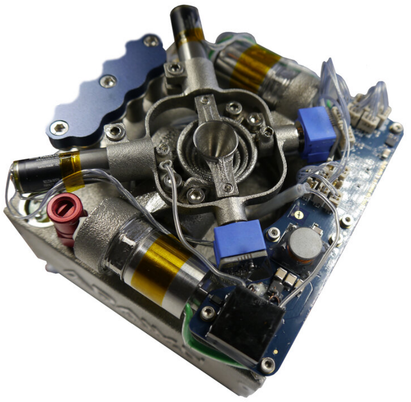

Figure 1.2: Dawn Aerospace PM200 in-space propulsion unit (see Footnote 1)

and supersonic conditions. Furthermore, it is available as a platform to do research in microgravity conditions. The propellant choice for these vehicles is in line with the in-space propulsion, being non-toxic and storable at room temperature conditions.

1.1.1. Dawn Aerospace Mk-III

The Mk-III will be the first orbital vehicle designed and operated by Dawn Aerospace. One of the unique aspects of this vehicle is the fact that it shall be integrated in the common airspace, which means that in the future it can takeoff from any runway in any location on Earth. Nowadays launch vehicles are launched from dedicated launch facilities, around which large safety zones are regulated following a major part of the ascent trajectory ground path. These safety zones account for both planned and unplanned ejection of material during launch. It is common to eject large parts of the launch vehicle back to Earth, including first stage boosters, payload fairing or even batteries. Unplanned material can be everything up to the complete vehicle, which in a worst case scenario explodes in an uncontrolled manner resulting in a rain of debris falling back to Earth. Both the launch facilities as well as the safety zones are extremely expensive to use and regulate. And due to organizational challenges the frequency in which this whole operation can be executed is rather low. The result is an expensive launch with low frequency and low flexibility.

The goal of integrating a launch vehicle into the common airspace is to tackle this problem. It is for this reason that one of the mottos frequently used by Dawn Aerospace is: '*Fly to space twice a day*'. In other words frequently available, cost efficient and location insensitive launch of small payload. However, considering the constraints of conventional launch vehicles on both the launch facility and the area beneath the ground track this means that the design of the Mk-III shall be approached from a completely different perspective.

The vision of Dawn Aerospace is clarified mainly from a top-level design and operational perspective. The main requirement for any vehicle integrated in the common airspace is manoeuvrability to deal with any unforeseen situation. This can be in case of a malfunctioning, in which the vehicle shall manoeuvre back to a landing site. But also during accidentally occurring collision courses with other vehicles, requiring for an immediate avoidance manoeuvre. To be able to do this the first stage of the launch vehicle shall be designed as the combination of an airplane and a rocket, making it a so-called 'spaceplane'. This also allows for reusing the first stage, resulting in a *semi-Reusable Launch Vehicle* (sRLV).

Furthermore, autonomous operations are identified as one of the key selling points of the vehicle. Hence it shall both takeoff and land on a runway. This means that the first stage shall be designed with a landing gear sized for take-off, enabling for *Horizontal Take-off Horizontal Landing* (HTOHL). Finally, for performance reasons, both considering the required velocity and altitude of a first stage, this vehicle shall propel itself using rocket engines.

The launch capabilities of the vehicle are determined for launching small payload into orbit. This means that the target payload mass is 150 kg, while injecting this into polar *Low Earth Orbit* (LEO) with an altitude of 600 km.

But more operational considerations are taken into account, which mainly improve the competitive position of the vehicle relative to other launch vehicles. It is required that the first stage shall return to the original spaceport of take-off. When launching twice a day, both the impact on the schedule and the impact on the operational costs are considerably large when the spaceplane lands on a separate landing site hundreds of kilometres away from the take-off site. Also the dependency on a relative geometry between two different airports makes the vehicle more sensitive to a take-off location, which is undesirable.

For maintaining safe operations at any take-off location the first stage is never allowed to eject uncontrolled material, protecting the area covered during flight. This means that the use of a fairing for payload protection is not allowed (or when allowed cannot be ejected). Furthermore, the vehicle can only consist of a *Two Stage to Orbit* (TSTO) configuration, as the re-entry of an intermediate stage is also not allowed.

Finally, simple ground operations are essential in order to quickly maintain the vehicle after flight within reasonable budget. This means that the vehicle is only fuelled by storable propellants. As the rocket engines demand a certain specific combination of oxidizer and fuel, this combination was determined to be hydrogen peroxide as the oxidizer and kerosene as the fuel. Lastly, especially for quickly executed maintenance, the use of ablative *Thermal Protection System* (TPS) shall be avoided in the design of the vehicle.

Summarizing these top-level design and operational considerations the following Stakeholder Requirements are formulated:

- The System Shall launch a payload mass of 150 kg
- The System Shall inject the payload into polar Low Earth Orbit below 1000 km in altitude
- The System Shall consist of a Two Stage to Orbit configuration
- The System Shall operate autonomously
- The System Shall not eject components in an uncontrolled manner

- The First Stage Shall be designed as a rocket propelled spaceplane
- The First Stage Shall be designed with hydrogen peroxide as oxidizer and kerosene as fuel
- The First Stage Shall takeoff and land horizontally
- The First Stage Shall return to the spaceport of take-off
- The First Stage Shall re-enter without the use of an ablative Thermal Protection System
- The First Stage Shall house the upper stage internally

- The Upper Stage Shall be designed with hydrogen peroxide as oxidizer and kerosene as fuel

1.2. State-of-the-art of closely related launch vehicles

Vehicles with similarities to the vehicle class of the Mk-III were studied in the past containing overlap in mission or vehicle design elements. However, these studies never contained the exact configuration in mission or vehicle design elements as studied in this research, as for example differences can be found in payload capability or launch configuration. The relevant studies on similar vehicles, paramount for understanding the context in which this thesis research is conducted, are discussed in this section.

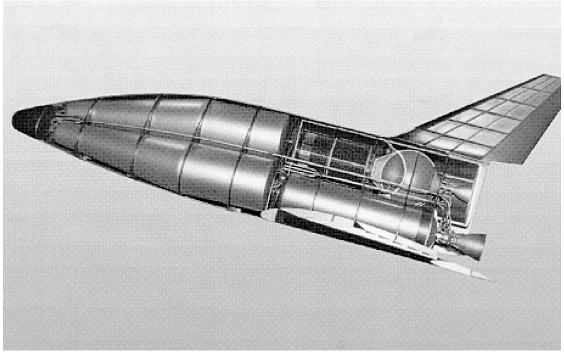

Figure 1.3: FESTIP Sub-orbital Hopper Internal Arrangement with a 7000 kg payload (Spies and Kuczera, 1999)

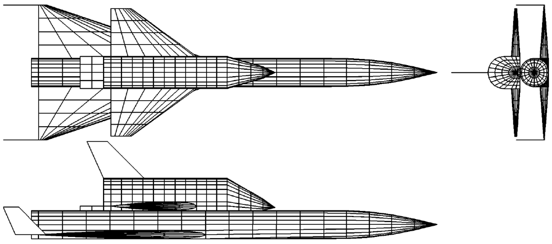

Figure 1.4: Tsuchiya and Mori (2004) optimized horizontal take-off vehicle with an 8000 kg payload

Figure 1.5: Polaris Raumflugzeuge based on the Aurora space launcher concept (see Footnote 4)

Figure 1.6: Orbital Access 500R based on the Maddock et al. (2018) launch system concept (see Footnote 5)

At the end of the twentieth century the interest of developing reusable space vehicles rose, which lead to the idea of using winged vehicles for launching payload into orbit. Most of the studies exploring launch capabilities of these vehicles focussed on the launch of large payloads (>5ton). The Hopper concept, researched in the European FESTIP study (Spies and Kuczera, 1999), was required to launch a 7000 kg payload into low-inclination LEO. Furthermore, the concept involved horizontal launch making use of a magnetic track supporting and accelerating the vehicle. The rocket propelled first stage was supposed to land on a separate landing site, while the expandable upper stage should have injected the payload into orbit. This concept showed that the goals and requirements of the mission were met and size, mass and cost of RLV could be reduced. However, after the first three test flights of the miniaturized Phoenix test vehicle (Gockel et al., 2004) the project never continued into further development.

Tsuchiya and Mori (2004) studied an autonomous RLV that was able to return the first and upper stage to the spaceport of launch. The research of this conceptual launch vehicle, designed for a payload capability of 8000 kg, primarily concluded that the vehicle was larger and heavier than both existing airplanes and comparable expendable launchers. Furthermore, horizontal and vertical launch profiles were compared. It was concluded that HTOHL vehicles were always heavier, due to take-off sized landing gear. However, taking into account cost, operability, reliability, and other factors besides weight vertical launch was not necessarily always preferred. The study showed that from a technical perspective designing a fully autonomous RLV was possible, however, weight reduction and miniaturization of components was required to increase the vehicles feasibility.

For a different payload class the *X-34 Advanced Technology Demonstrator* (X-34), part of the American X-plane program, was studied. Freeman Jr et al. (1997) described the main objective of this launch vehicle, as being the launch of 450 kg to 900 kg payload in LEO. The vehicle was air-launched and the first stage was designed for returning to a landing site after injecting an expendable upper stage into an orbital trajectory. After a preliminary study and test of the vehicle, involving tow-testing on the runway and captive flight tests, the development process was stopped due to increasing development risk and the subsequent cost.[3]

A more recent study by Kopp et al. (2018) showed that the use of novel thin-ply composite material to the Aurora space launcher concept reduced structural mass in the order of ~20%. The mission design included autonomous operations with a payload capability of 7000 kg in LEO, while minimizing expendable material. The study showed promising results minimizing airframe mass and being cost-efficient in compliance with the mission goals. Due to these promising results this vehicle is currently under development by Polaris Raumflugzeuge.[4]

The final study discussed was recently conducted by Maddock et al. (2018). This study evolved around a small payload launcher designed for a payload of 500 kg. The vehicle was air-launched and after injection of the expendable upper stage the first stage landed at a separate landing site. Furthermore, all development was done taking into account a near-term development process. Hence only using high Technology Readiness Levels technologies. The study concluded on the optimal engine configuration as well as wing area. Also this study showed such promising results that the vehicle is currently under development by Orbital Access.[5]

---

[3] Gibbs, Y., 'NASA Armstrong Fact Sheet: X-34 Advanced Technology Demonstrator', *National Aeronautics and Space Administration*, `https://www.nasa.gov/centers/armstrong/news/FactSheets/FS-060-DFRC.html`, (accessed May 11, 2020).

[4] *Polaris Raumflugzeuge*, `https://www.polaris-raumflugzeuge.de/`, (accessed May 11, 2020).

1.3. Introduction to the thesis research

The combination of academic relevance and stakeholder interests of Dawn Aerospace was used to identify and formulate the topic and content of the thesis research. The area covering technical feasibility and the optimization of market value was recognized most promising. Both having value for the development process of the Mk-III and for increasing the academic understanding of winged rocket propelled sRLV for small payload. This lead to the following Research Objective:

Research Objective: *To assess the optimal design in different cost derived mission scenarios of a rocket propelled Two Stage to Orbit Horizontal Take-off Horizontal Landing semi-Reusable Launch Vehicle for small payload integrated in the common airspace, by developing a numerical optimization model including the vehicle and trajectory design optimized for dry mass, with the aim of identifying key vehicle and trajectory design parameters influencing feasibility of the System while including the market value of the System.*

For achieving the Research Objective the following *Primary Research Question* (PRQ) was formulated:

Primary Research Question: *What is the mass optimal vehicle and corresponding trajectory for cost derived mission scenarios of a rocket propelled Two Stage to Orbit Horizontal Take-off Horizontal Landing semi-Reusable Launch Vehicle for small payload integrated in the common airspace?*

This includes both the mission design and the design of the vehicle as well as a qualification of market value based on different cost derived mission scenarios. The more detailed structure addressing the elements of the PRQ is given below, subdivided in different sets of *Primary Sub-Questions* (PSQ):

- **PSQ1:** What are the qualitative cost differences between different mission scenarios?
  - **PSQ1.1:** What are the elements determining the cost of launching payload into orbit?
  - **PSQ1.2:** Are there relations between resulting vehicle design parameters, such as dry or total mass, and the expected cost of launch?
  - **PSQ1.3:** What operational considerations influence the cost of launch and how can this be derived into mission scenarios?
- **PSQ2:** How do the primary vehicle and mission design parameters and constraints influence vehicle dry mass?
  - **PSQ2.1:** What is the ΔV distribution between the first and second stage for an optimal mission design within the mission requirements?
  - **PSQ2.2:** What is the increase in vehicle dry mass for an increase in orbit injection altitude?
  - **PSQ2.3:** What is the increase in vehicle dry mass for an increase in payload mass?
  - **PSQ2.4:** What is the influence on vehicle dry mass when using a shared engine design for first and upper stage propulsion?
  - **PSQ2.5:** What is the penalty on vehicle dry mass requiring the first stage to return to the spaceport of take-off?
  - **PSQ2.6:** How does vehicle dry mass change when an upper stage fairing is allowed?
  - **PSQ2.7:** What is the effect of take-off sized landing gear on vehicle dry mass?
- **PSQ3:** How do the active "in-plane pitch over" and "aeroturn" Return to Launch Site methods and the passive "glideback" Return to Launch Site method compare?
  - **PSQ3.1:** How do the return methods compare in vehicle dry mass?
  - **PSQ3.2:** How do the return methods compare in propellant consumption?
  - **PSQ3.3:** How do the return methods compare in heat rate and heat load on the vehicle?
  - **PSQ3.4:** Is it required to have an active return method?
- **PSQ4:** How does the airplane configuration of the first stage influence the trajectory?
  - **PSQ4.1:** What is the trajectory of the vehicle in dense layers of the atmosphere?
  - **PSQ4.2:** What is the most propellant-efficient trajectory changing the azimuth of the vehicle in the dense layers of the atmosphere?

---

[5] *Orbital Access Limited*, `https://www.orbital-access.com/`, (accessed May 11, 2020).

1.4. Structure of the report

The report is structured in the following way. First the implemented cost philosophy is addressed in Chapter 2. Understanding this is required to understand the numerical research. The numerical research is conducted around several mission scenarios which are derived based on the cost analysis discussed in this chapter. Chapter 2 examines the reasoning behind these scenarios and concludes with the implemented mission scenarios used throughout the study.

For studying the behaviour of the vehicle in the different mission scenarios several fundamental numerical theories and techniques are required. The primary goal of the research tool is to optimize both the vehicle and trajectory design minimizing dry mass of the vehicle. To do so, a *Multidisciplinary Design Optimization* (MDO) tool is developed. Chapter 3 discusses numerical optimization, MDO and optimal control, all required for optimizing the design and trajectory simultaneously. Also addressed in this chapter is how to define and model motion. The chapter is concluded by a discussion on numerical propagation and integration.

The first major segment of the numerical tool is the trajectory model. The trajectory of the vehicle in the different mission scenarios consists of three major components, being the ascent of the first stage, the ascent of the upper stage and the return of the first stage. The existence of a large dependency between these different mission phases is identified and discussed in Chapter 4. This chapter shows how these different phases are modelled, connected and constrained. Both the theory behind ascent and *Return to Launch Site* (RTLS) trajectories is discussed, also addressing the constraints and expected losses. To achieve the required mission design the vehicle shall be guided along the correct path. The guidance model for doing so, implemented in the trajectory model, is introduced. To conclude this chapter the environment models are shown, which estimate gravity and the atmosphere both having great influence on the shape of the trajectory.

The second major part of the numerical model is the model of the vehicle. Chapter 5 discusses this model, which contains models of the rudimentary subsystems of a launch vehicle. First, the propulsion model, based on *Ideal Rocket Theory* (IRT), is introduced showing how the engine design parameters result in an estimation of engine performance. Next, the aerodynamic model of the vehicle is discussed, which is an implementation of known wind tunnel test data of the X-34. As this is one of the primary assumptions in this research, the reasoning behind this implementation is explained as well. Finally, the geometry and mass model is introduced, which is mainly responsible for sizing the vehicle and determining the corresponding mass based on the vehicle design parameters.

After the introduction of the trajectory and vehicle model the combined integration into an MDO tool is discussed in Chapter 6. The structure of the tool is presented, as well as the software environment in which it is developed. To determine if the model estimates reality within defined boundaries a validation procedure is executed. Due to the highly innovative nature of the vehicle, validation of the first stage as well as of the trajectory is a challenging task. This is discussed and the method of overcoming these challenges is shown, concluding on the validity of the model.

With the validated tool the numerical study is conducted. Chapter 7 presents the results of this study. First, the baseline scenario is shown, which is used as a reference case to compare the other scenarios with. The other scenarios are, in order of appearance: variations in target altitude, variations in payload mass, the comparison of different return methods, the effect of engine design and lay-out, allowing fairing usage, alternative launch configurations and the trajectory behaviour in dense layers of the atmosphere. All is discussed and compared.

It is important to understand how uncertainties in the model change the results found by the tool. For gaining this understanding a sensitivity analysis is conducted. This is done in different levels of model understanding. First, the one-at-the-time approach is presented. In a systematic way this determines how variation of individual design parameters varies the outcome of the model showing the sensitivity of the results towards individual design parameter variation. Next, a Monte-Carlo analysis is shown. Also in a systematic way this determines how the combination of variation of the design parameters varies the outcome of the model showing the sensitivity of the results towards combined design parameter variation. Finally, model based sensitivities are discussed. This requires understanding of the uncertainties in the model. In this sensitivity analysis specific elements of the model are targeted to understand how the assumptions during design of the vehicle and trajectory impact the results. The included elements are the engine model, the aerodynamics model, the geometry and mass model and the effect of the runway heading during take-off.

Chapter 9 concludes the thesis study. Conclusions are drawn and presented, discussing the different mission scenarios and relating them back to the PRQ and PSQs. Also recommendations are given on interesting topics following from this thesis research that allow for a more detailed understanding.

2

The implementation of a cost philosophy within the mission study

The fact that the space industry is commercializing affects the way in which budgeting is included in the development process of space industry projects. More companies, both traditional and in the NewSpace industry, offer the launch of payload into orbit. This means that customers have more choice between different suppliers, driving the industry towards lower cost solutions. Launch service providers developing these launch vehicles have to include the final cost of launch from an early stage in the development process, both for selecting certain vehicle designs as well as for choosing between operational scenarios.

However, customers do not only base their selection on the cost of launch. Also operational capabilities of the launch vehicle can be a major factor in the decision-making of a customer towards a certain launch service provider. With an increased amount of payload being launched, of which the majority consists of small satellites, operating a flexible launch vehicle which is frequently available and reliable can result in a lead market position (Tugnoli et al., 2019).

Due to the importance of cost as well as the operational capabilities of the launch vehicle both are included in this thesis research. For understanding the future payload market first the prediction of future demand for launching payload into orbit is shown. Next, theory on how to model the cost of launch vehicles is discussed. It is immediately clear that the concept of the *Dawn Aerospace Mk-III* (Mk-III) does not have close resemblance to traditional launch vehicles. Also some of the benefits of this concept do arise more from the operational capabilities of the vehicle, which are not directly shown in traditional cost models. It is for this reason a renewed approach on cost is proposed, which is introduced in this chapter. Finally, with this renewed approach mission scenarios are derived based on cost, which form the key comparison aspect in this study.

2.1. Market prediction of future demand for payload

One of the major trends in future payload evolution is the reduced mass of individual satellites. McIntyre et al. (2016) studied the expected payload distribution by mass classification until 2036. The used payload classification system was introduced by the Federal Aviation Administration.[1] The shown nano class contains satellites of masses between 1.1 kg and 10 kg, while the micro class contains satellites of masses between 11 kg to 200 kg. Figure 2.1 clearly shows that the prediction of future launch volume consists mainly of satellites in the nano and micro class, which also reduces the average launch mass as shown in Figure 2.2. Furthermore, the study showed that the majority of these satellites are injected into an orbit between 450 km and 650 km in altitude, with an inclination between 60° and 90°. However, a second popular destination predicted is orbits with an altitude larger than 650 km.

Important to realise is the fact that a major contributor to the market prediction in this study is the OneWeb con-

---

[1] 'The Annual Compendium of Commercial Space Transportation: 2016', *Federal Aviation Administration*, `https://www.faa.gov/about/office_org/headquarters_offices/ast/media/2016_compendium.pdf`, (accessed on April 28, 2020).

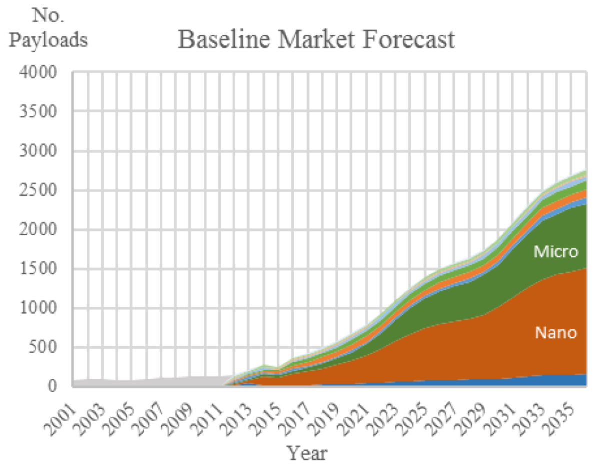

Figure 2.1: Future baseline forecast on the volume of payloads per year, segmented by mass (McIntyre et al., 2016)

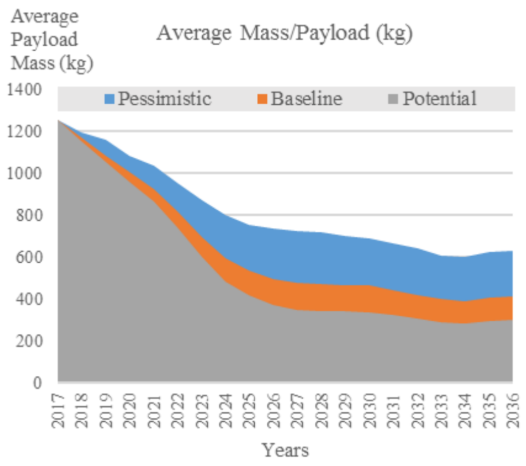

Figure 2.2: Average payload mass per year between 2017 and 2036, with perspective segmentation (McIntyre et al., 2016)

stellation, which planned on launching 900 satellites of 150 kg in a 1200 km orbit.[2,3] However, during the period of this study the company behind the OneWeb constellation filed for relief under Chapter 11 of the Bankruptcy Code in the U.S. Bankruptcy Court due to the financial impact and market turbulence related to the spread of COVID-19.[4] Especially the conclusion by McIntyre et al. (2016) on target altitude for the micro-satellite class was derived on the OneWeb constellation. Hence this is put in a different perspective by this current development.

2.2. Cost modelling of launch vehicles

For modelling the cost of a launch it is common to quantify the *Cost per Flight* (CpF) or *Price per Flight* (PpF), of which the first is the actual cost of the launch while the latter is the price the customer pays for the launch service. To quantify these costs three major elements add up to the total cost, being (Drenthe, 2016):

- **Development cost:** Estimation of the non-recurring design and development cost of the launch vehicle, including the cost of testing the subsystem and system models.
- **Manufacturing cost:** Estimation of the recurring cost of manufacturing, assembly, integration and testing of the hardware of the launch vehicle, including the management and product assurance.
- **Operating cost:** Estimation on the recurring cost of integration of the launch vehicle and testing, processing and integration of payload, launch management and control, logistics and post launch responsibilities.

For a long time the main method used to quantify these three different elements of cost was the TransCost method developed by Koelle (2013). Drenthe (2016), however, argued that for small payload launch vehicles this method results in an overestimation of the total cost. Instead of estimating the development and manufacturing cost using this method, he proposed a method using the so-called Theoretical First Unit. The cost of the Theoretical First Unit was estimated based on the conceptual design of the launch vehicle. Based on the estimated mass of the individual subsystems, combined with historically determined Cost Estimation Relationships of these subsystems, the Theoretical First Unit cost was determined. By a series of equations, combining assumptions on the business operations, contracting and learning experience, the Theoretical First Unit cost was used to determine the development and manufacturing cost. Yet, for the operating cost the TransCost model was used.

2.3. Cost approach emphasising the Mk-III feasibility and market value

The goal of this thesis study is twofold. The first is to address the feasibility of different mission designs. The second is to map where in the design of the vehicle and the trajectory margins can be accomplished to make the

---

[2] 'OneWeb Satellites constellation', *Airbus S.A.S.*, `https://www.airbus.com/space/telecommunications-satellites/oneweb-satellites-connection-for-people-all-over-the-globe.html`, (accessed on April 28, 2020).

[3] 'OneWeb lifts off: Next batch ready to launch', *Airbus S.A.S.*, `https://www.airbus.com/newsroom/press-releases/en/2020/02/oneweb-lifts-off-next-batch-ready-to-launch.html`, (accessed on April 28, 2020).

[4] 'OneWeb Files for Chapter 11 Restructuring to Execute Sale Process', *OneWeb*, `https://www.oneweb.world/media-center/oneweb-files-for-chapter-11-restructuring-to-execute-sale-process`, (accessed on April 28, 2020).

vehicle more competitive in the launch industry. Both aim for emphasizing engineering choices. In this context competitive means including all four trade-off criteria of customers introduced by Tugnoli et al. (2019) being price-effectiveness, flexibility, availability and reliability. However, the outer framework in which both the vehicle design as well as the trajectory design is defined was already determined by Dawn Aerospace (see Chapter 1). The differences studied are inside of this framework, with the goal of understanding design choices. Taking this into account resulted in the logic that a CpF or PpF comparison is not the desired answer of this study (Haex, 2019). Rather, is the identification of a cost gradient (or cost derived gradient) within the design space of the System driving towards the optimal solution in terms of feasibility and market value.

Considering the fact that only the cost gradient (or cost derived gradient) is of interest led to the conclusion that not all of the cost elements shown in Section 2.2 are relevant to include in the cost comparison (Haex, 2019). As both the development cost and manufacturing cost are dependent on the Theoretical First Unit - the model by Drenthe (2016) was determined to be the most applicable - both express in a similar manner the differences between different designs. However, the estimation of the manufacturing cost includes a learning factor - acting as a weighting on the reusable first stage versus expendable second stage comparison - important for defining the reusability of the first stage. For this reason it is decided to discard the development cost in the cost comparison of the System. Instead, only the manufacturing cost is implemented to identify the design-based cost gradient of the System.

The operating cost in the TransCost model, both direct and indirect, are primarily related to the total mass of the vehicle at lift-off. However, when comparing the operational scenario of a conventional launch vehicle with the operational scenario of the Mk-III it becomes apparent that this is very different. In the vision of Dawn Aerospace the ground, mission and flight operations show closer resemblance to today's aircraft operations than to the launch of conventional launch vehicles. This has two major consequences. First, it is doubtful if the relations proposed in the TransCost model are applicable at all. Secondly, when comparing different designs in the framework proposed by Dawn Aerospace it is questionable whether or not the operational differences can be expressed in a meaningful manner by relating this to the total vehicle mass. This resulted in the conclusion that it was only relevant to model the propellant and transport cost (emphasizing reusability of the first stage) as operating cost (Haex, 2019).

Ground and flight operations are neglected, as the cost of those do not drastically differ in the design space of the System. An example of this is the use of airport facilities. Even the largest designs in the design space are not larger than small passenger aircraft. This allows for a variety of airports suited for handling the vehicle. Smaller or larger variations of the vehicle are not expected to change these operations such that it leads to substantial cost differences.

The included elements required for identifying the cost gradient within the design space lead to the following cost comparison function, as defined by Haex (2019). For k amount of launches in which the first stage is re-used the cost comparison number $TOTC_{\mathrm{com}}(k)$, expressing a difference in cost, is determined by:

$$\begin{aligned} TOTC_{\mathrm{com}}(k) = {} & MAN_{\mathrm{b,stage1}_{n=1}} + TRANS_{\mathrm{stage1}} + MAN_{\mathrm{b,stage2}_{n=k}} + \\ & k\left(c_{\mathrm{ref}} MAN_{\mathrm{b,stage1}_{n=1}} + PROP + TRANS_{\mathrm{stage2}}\right) \end{aligned} \tag{2.1}$$

with $MAN_{\mathrm{b,stage}}$ being the batch manufacturing cost of the corresponding stage, $TRANS_{\mathrm{stage}}$ being the transport cost of the corresponding stage, $PROP$ being the total propellant consumption and c_{ref} being the refurbishment factor of refurbishing the first stage after a single flight. The relations describing the individual components of this equation were discussed by Drenthe (2016). One of the major limitations to this renewed cost formulation is that indeed the Cpf and PpF cannot be determined with this model.

2.3.1. Implementation of the cost comparison function

To determine the behaviour of the implemented cost comparison function a Monte-Carlo analysis was performed once the vehicle model was complete (see Chapter 5). The goal of this analysis was to determine how the cost comparison function behaves in a large design space. This large design space was selected such it overlapped completely with the design space of the actual thesis research with extended margins on all design variables.

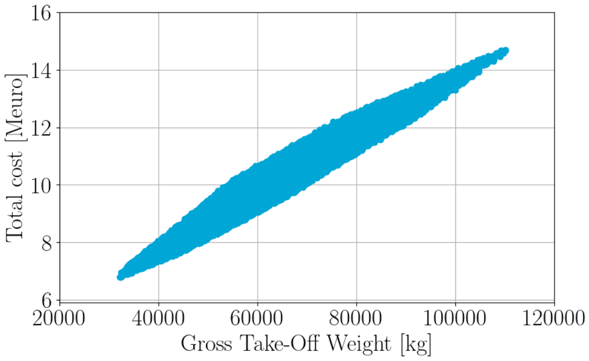

Figure 2.3: Total cost comparison number per flight plotted against Gross Take-Off Weight (based on 50 launches with a learning factor of 0.9 and a refurbishment factor of 0.1)

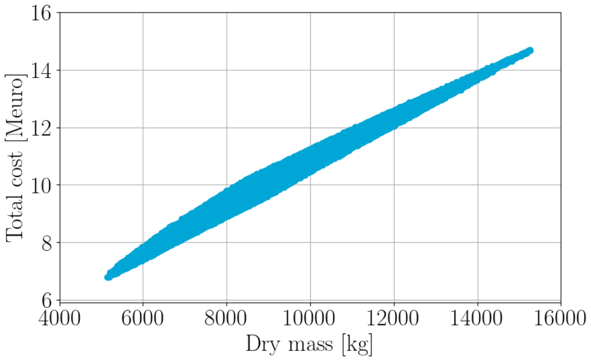

Figure 2.4: Total cost comparison number per flight plotted against total vehicle dry mass (based on 50 launches with a learning factor of 0.9 and a refurbishment factor of 0.1)

For computing the manufacturing cost the historical Cost Estimation Relationships of the several subsystems were implemented as described by Drenthe (2016) using the following relation:

$$MAN_{b_n} = c_p \cdot L_{c_n} \cdot \left(a \cdot m^b\right) \tag{2.2}$$

in which c_p is the profit retention factor (estimated as 0.970), L_{c_n} is the batch factor of n individuals including a learning factor, (a,b) are statistical parameters based on historical data of similar components and m is the mass of the subsystem. Table 2.1 shows the coefficients used in the estimation based on historical data on similar subsystems. By summing all individual subsystems the total cost of the corresponding vehicle was found. Furthermore, a learning factor of 0.9 was assumed on the batch production of the upper stage and the engines. The first stage was assumed to endure at least 50 launches, while 10% refurbishment cost was assumed after every launch. Furthermore, for the estimation of the transport cost the ESA internal cost-per-kilogram reference of 5365 €/kg was used (Drenthe, 2016). Finally, the propellant cost was estimated based on current market price of helium, kerosene and hydrogen peroxide.

		a value	**b value**	**Valid mass range [kg]**
Stage				
	Tank(s)	19.99465	0.71253	62 - 4742
	Stage structure(s)	2.79930	0.91199	22 - 1036
	Engine(s)	31.48271	0.78811	200 - 6740
	Thrust vector control	33.90978	0.60977	23 - 110
	Pressurization system	11.50618	1.06948	5 - 134
	Pipes and valves	8.95877	0.68815	6 - 400
	Stage harness	27.45211	0.44623	4 - 35
Payload				
	Payload adapter	124.86209	0.31031	30 - 123
	Payload fairing	4.09558	0.96587	26 - 3000

Table 2.1: Cost Estimating Relationships statistical parameters for components of a liquid rocket stage derived from sample data with valid mass range (Drenthe, 2016)

Table 2.1 shows that some of the subsystems have a high lower-limit in the valid mass range. Especially the engine mass is expected to be well below the valid mass range. However, it was immediately identified that building a new relationship is rather challenging, due to the unavailability of data on the cost of lightweight rocket engines. Instead, this was treated as an uncertainty, assuming that the trend shown by the equation is order of magnitude correct even for small engines. A consequence of this is a possible overestimation of the true engine cost. Furthermore, some of the subsystems of the first stage are unavailable in this data set, due to the unconventional design of this first stage. This includes fuselage, payload bay, wings, tail and landing gear. Most of these components have a high structural nature and for that reason were individually estimated as stage structure(s). This second approach can, however, result in an underestimation of the cost of the first stage, due to the negligence of the moving components in these subsystems.

Especially interesting is the behaviour of the cost comparison function when comparing this to the mass of the vehicle. Figure 2.3 and 2.4 show this behaviour. In Figure 2.3 the total cost comparison number found with the cost comparison function is plotted against the *Gross Take-Off Weight* (GTOW) of the launch vehicle. The correlation between the two is strong. Still a spread of ~20% is observed on the comparison number for solutions between 50000 kg and 80000 kg in GTOW. Figure 2.4 shows that the correlation between the total cost comparison number and dry mass of the vehicle is even stronger, showing a spread of maximum ~10% in comparison number for solutions with a dry mass between 7000 kg and 11000 kg.

The cost model is implemented with rough assumptions on some subsystems, especially during the estimation of the manufacturing cost of the first stage. However, the dry mass of this first stage is found to be approximately 90% to 95% of the total vehicle dry mass. The assumption of modelling the aircraft components as stage structures is expected to reduce the total estimated cost, which means that the correlation between dry mass and total cost is foreseen to be even stronger in a more detailed analysis. Based on this strong correlation it was decided to optimise for vehicle dry mass in this thesis research. The benefit of this is a smaller computational effort for each iteration, while the result is also relevant for identifying the cost gradient of the System.

2.4. Cost derived mission scenarios

In the cost comparison function and the derived analysis on dry mass unexposed contributors to a difference in cost do exist. Between various designs and missions conceptual differences are identified that are hard to quantify directly by an analysis on total vehicle dry mass. They do, however, have a considerable influence on the expected development process and operations of the vehicle. It is argued that it is important to address these conceptual differences and include them in the analysis, resulting in cost derived mission scenarios that form part of the backbone of this research. These scenarios are selected by taking into account expected financial consequences on both the market position, development process as well as the operations. By quantifying the required design for these different scenarios feasibility of the vehicle can be compared between the scenarios. This creates insight in the behaviour and trends within the vehicle design space while including the wider framework of market value. Mission scenarios are defined in the broadest sense of the word, meaning that also a conceptual different lay-out of the vehicle is treated as an individual mission.

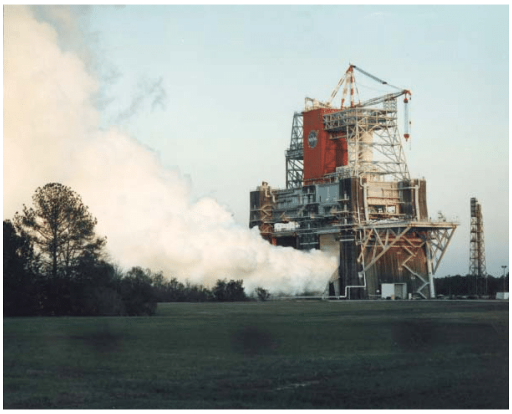

Figure 2.5: Space Shuttle Main Engine test at the NASA Stennis B-1 test stand - Mass flow approximately 500 kg/s (Sachdev et al., 2010)(see Footnote 5)

Figure 2.6: Rutherford engine test at Rocket Lab's test facility - Mass flow approximately 7 kg/s (see Footnote 6, 7)

The first mission scenario derived in this philosophy focusses on the lay-out of the engines. A method identified, primarily applicable for reducing the development cost, is by only using one engine design on both the first and upper stage. This means that for propelling the first stage a multiple of those engines shall be installed, while for the upper stage a vacuum nozzle shall be added on the fixed nozzle. Both SpaceX as well as Rocket Lab designed launch vehicles applying this philosophy, although in a very different scale of vehicle. The impact of this method on the development process is twofold.

The first improvement is the fact that the development process can be simplified. Instead of having two parallel design processes focussing on both a first and upper stage engine, one engine can be designed. In a study particularly focussed on estimating the CpF and PpF it is possible to address this, although for small launch vehicles this is hard to quantify due to a lack of historical data on small engines. In the proposed analysis on dry mass, however, it is expected that a design with a single first stage engine or one with a shared first and upper stage engine design differs only little in dry mass and probably favours towards a single first stage engine lay-out. This in contrast with the imaged development perspective, in which it is argued that a design with multiple small engines is the preferable option.

This is especially true when considering another factor expected to have great influence on the development cost, even more so for small launch vehicles. When using a shared engine design a single engine is rather small. Exponential behaviour in the size of test facilities required for testing the engine is expected, which means that when engines differ in size the test facilities do even more so. Figure 2.5 and 2.6 show the different test facilities of both the Space Shuttle Main Engine and the Rutherford engine.[5,6,7] In the NewSpace industry launch vehicles developed for launching small payload can reduce engine size so much that a completely different ball park of test facilities is required for testing these engines (shown in Figure 2.6). This is expected to decrease the cost of development drastically, especially when the engine is reduced to upper stage size.

This means the following mission scenarios are compared. One in which the first and upper stage both have an individual engine and one in which the first and upper stage share the engine design, of which a multiple is installed on the first stage.

A very interesting design feature of the Mk-III is the fact that the upper stage is stored internally in the first stage. This means that for protection of the payload in the dense layers of the atmosphere a fairing is not required, given that the upper stage is released and stays in conditions in which a fairing is indeed unnecessary. The second mission scenario derived is around the fact that prohibiting fairing usage is identified a key element in increasing the market value of the vehicle, especially considering the operations. Ejecting a fairing results in uncontrolled components re-entering the atmosphere and hitting the ground. The inventiveness of the Mk-III mission is that launch is integrated in the common airspace, without having to include great safety zones. Ejecting uncontrolled material jeopardizes this vision enormously, decreasing market value by decreasing flexible worldwide operations. It is for this reason that the second cost derived mission scenario is one in which the prohibition of fairing usage is compared with a design allowing fairing usage.

Another consideration derived from storage of the upper stage is not one during flight but, rather, during transport. As the first stage is used multiple times, possibly from the same spaceport, a new upper stage shall be transported to the spaceport for every launch. If this is possible in standardized shipping containers the cost of transport is expected to decrease substantially. It is for this reason that the upper stage is designed such that it always fits (without payload) a 20 ft dry shipping container.[8]

Along this road of innovation another set of mission scenarios is derived. Key in the decision-making of customers is both flexibility as well as availability. This means that a fully autonomous vehicle with the capability of operating in any part of the world ensures great advantage over other competitors, which do rely more on individual launch facilities. Key in operating this autonomous vehicle are two aspects.

First, for availability and high launch rates it is important that the first stage returns to the original spaceport of take-off. Not only does this decrease the turnaround time, also the vehicle can be operated more flexible as it is not dependent on the relative position of two airports. Furthermore, operations become less costly, as no transportation of the first stage is required when returning. The so-called *Return to Launch Site* (RTLS) has consequences on the design of the vehicle, especially if extra propellant is required for an active RTLS manoeuvre. Chapter 4 discusses this in detail. The mission scenarios derived around the RTLS requirement compare both a mission in which the return is not required and missions in which return is required, also comparing different methods of return.

Secondly, autonomous operations also require the vehicle to operate independent of any other vehicle or assisting tool. In rocket technology one of the major concepts in increasing performance is to store as much propellant in an as light as possible vehicle. This means that during take-off the vehicle can be up to 10 times heavier than during landing. One can imagine that designing landing gear for take-off results in very heavy landing gear,

---

[5] 'RS-25 Engine', *Aerojet Rocketdyne*, `https://www.rocket.com/space/liquid-engines/rs-25-engine`, (accessed on May 01, 2020).

[6] 'Rutherford Engine Test Fire', *Rocket Lab*, `https://www.rocketlabusa.com/news/updates/rutherford-engine-test-fire/`, (accessed on April 30, 2020).

[7] 'Electron', *Rocket Lab*, `https://www.rocketlabusa.com/electron/`, (accessed on May 01, 2020).

[8] 'Shipping container dimensions guide', *Freight Forwarder Quote Online*, `https://www.freightforwarderquoteonline.com.au/shipping-container-dimensions-australia/#!/import`, (accessed on May 14, 2020).

especially considering this mass is only used efficiently for a small portion of the total flight. However, omitting this results in the use of another system at launch or a different launch geometry. This is expensive in terms of development and operations and again disrupts the envisioned mission profile. It is for this reason that the final set of mission scenarios compared focusses on take-off of the vehicle and compares different launch configurations with and without take-off sized landing gear.

2.5. Summary of the cost philosophy implemented in the mission study

This chapter showed that it is important to include a cost strategy in the research, as the market of launching small payload is rapidly growing and commercialising resulting in more competition. This means that price-effectiveness, but also flexibility, availability and reliability play a primary role in the selection process of customers towards a specific launch vehicle.

Furthermore, it was identified that the elements of a traditional cost model are not all applicable directly in this study, due to the innovative nature of the vehicle and trajectory design. Hence estimating the CpF and PpF was omitted and, rather, a formulation was presented which emphasizes cost differences between different designs, by quantifying a cost comparison number in the cost comparison function. In this way different missions can be compared in a relevant manner and the feasibility and margins of the design can be quantified. However, the analysis of a large design space, also fully covering the design space of this thesis study, showed that there is a strong correlation between the cost comparison number and total vehicle dry mass. Hence it was concluded that instead of optimising the cost comparison number, rather, the vehicle dry mass is optimised reducing the computational effort of each iteration.

Not addressed in this analysis on dry mass are cost differences that exist, but in a more qualitative manner. On a conceptual level it was possible to argue that certain design choices do have a beneficial impact on the cost of the development process and operations and by that ensure a more competitive position of the launch vehicle in the market. Following this cost philosophy several mission scenarios were derived, which are compared in this study both showing feasibility or unfeasibility of these concepts and showing what is the design consequence on the vehicle by achieving certain market derived goals. These cost derived mission scenarios are the following:

- **Return to Launch Site:** Flexible operations all around the world is what makes the Mk-III competitive towards other launch vehicles. This is especially true for a mission which is able to act completely around a single airport, decreasing turnaround time between launches and reducing cost of transport of the first stage. The following missions are compared:
  - The first stage returns to the spaceport of take-off by passively guiding back towards the spaceport
  - The first stage returns to the spaceport of take-off by an active RTLS method
  - The first stage does not return to the spaceport of take-off
- **Engine design and lay-out:** Using a shared engine design to propel the first and upper stage is beneficial for the development process of the vehicle in two ways. The first is the fact that instead of two parallel engine design processes only one is required. The second is the fact that due to the (much) smaller size testing of the engine can be done in smaller and more accessible facilities. This results in the following missions to be compared:
  - The first stage is designed with a multiple of commonly designed engines, in which the amount is an optimization parameter
  - The first stage is designed with nine commonly designed engines, in compliance with both the Electron rocket as well as the Falcon 9
  - The first stage is designed with one individual engine and the upper stage as well
- **Fairing usage:** One of the key aspects of the envisioned mission of the Mk-III is integration in the common airspace, without requiring large safety zones. This means that ejecting material, such as a fairing, in an uncontrolled manner is disruptive for this vision. This results in the following mission scenarios to be compared:
  - The use of a fairing on the upper stage is prohibited
  - The use of a fairing on the upper stage is allowed

- **Alternative launch configurations:** One of the main challenges is that for autonomous operations the landing gear shall be designed strong enough to support the first stage during take-off, including all propellant and the upper stage. This means that the landing gear is sized for only a very small period of the total flight, while being over-dimensioned for the rest of the mission. However, from an operational point of view - affecting the business case - this is the preferred option. For this reason the following mission scenarios are compared, also including alternative launch configurations:
    - The landing gear is sized for take-off
    - A cart is used to support the first stage during take-off, however, the thrust is still applied by the rocket engines
    - The first stage is air-launched at the common altitude of 12 km

3

Theory on numerical modelling and optimization of space vehicles and trajectories

Studying the different mission scenarios requires a numerical model which tries to estimate the behaviour of the System within a certain required precision. Furthermore, this numerical model needs to optimise the design and the trajectory of the vehicle. To develop such a numerical tool several general concepts in the field of numerical modelling and optimization are of importance. This chapter introduces these different concepts. First, numerical optimization is addressed showing the general optimization problem and more specific forms relevant for this study such as optimal control. Secondly, fundamentals in the analysis of motion are discussed. Finally, it is shown how the problem is numerically propagated and integrated.

3.1. Numerical optimization

Optimization is best described as the process to find the best possible solution to a certain problem. When this is done using numerical analyses this is called numerical optimization. The solution itself is described by the design vector X and within numerical optimization the 'goodness' (called fitness) of a certain solution is defined by the objective function f. Furthermore, it is very common for this solution to be constrained within certain boundaries. This can be done by a combination of both inequality constraint functions g defining limits which are not allowed to be exceeded and equality constraint functions h forcing the solution to meet certain values. This is formulated as:[1]

$$\begin{array}{lll} \textbf{Minimize} & f(X) & \\ \textbf{Subjected to} & g_j(X) \leq 0 & \textit{for } j = 1, 2, \cdots, l \\ & h_k(X) = 0 & \textit{for } k = 1, 2, \cdots, m \end{array} \tag{3.1}$$

Figure 3.1 shows the general optimization problem. Based on the design vector X_q (iterative counter q) the objective and constraint functions are determined. By iteratively improving the design vector X_{q+1} the convergence criterium can be met. When the optimizer succeeds in meeting the convergence criterium the optimal design X^* is found. An important note is that maximizing and minimizing can be done both by the same process by only changing the sign of the objective function. It is standard convention to present the optimization process based on minimizing the objective function.

The figure also shows how dependent the optimization process is on the selection of the optimizer. There are two distinct categories of optimization algorithms, the first being gradient-based algorithms and the second being gradient-free algorithms (Balesdent, 2011). The main difference between these kinds of algorithms is the implementation of the problem. For the first large mathematical understanding of the problem is required to define

---

[1] Rocca, G. l., Lecture notes on: 'Notes on MDO', *Delft University of Technology*, (accessed on April 04, 2020).

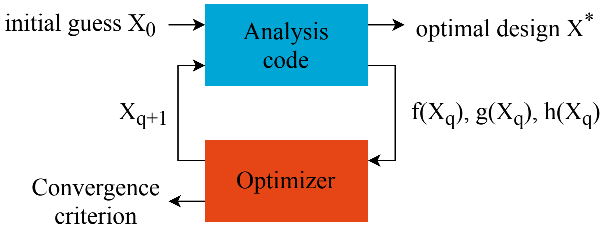

Figure 3.1: The basic optimization process (reproduced from (Weck et al., 2007))

the gradient. In the latter the problem can be implemented more straightforward by an input-output structure. This is more demanding in computational effort.

There is contradiction between different studies on which optimization algorithm is best to implement in vehicle and trajectory design research. Betts (1998) for example - often referenced in other studies - concluded that the use of gradient free algorithms in a trajectory study is a waste of computational effort, as the physical properties of trajectories can be mathematically described very well in a way to exploit the gradient information for fast convergence. On the other hand modern work by Balesdent (2011), as well as numerous thesis students - Vandamme (2012), van Kesteren (2013a) and Contant (2019) -, showed the powerful capabilities of gradient-free optimization algorithms in vehicle and trajectory design studies. Furthermore, the development environment of the tool itself (introduced in Chapter 6) has a stronger tendency towards the implementation of gradient-free algorithms due to the definition of the problem and the implementation of constraints. Combining this with the fact that good results of this implementation were shown in the past a gradient-free algorithm is selected as the optimization algorithm in this study.

3.1.1. Differential Evolution (DE1220)

Within the class of gradient-free optimization algorithms still a large variety of different algorithms is available. Pagmo is a C++ scientific library containing a large selection of bio-inspired and evolutionary algorithms capable of solving the problem within a massively parallel optimization environment.[2] Pagmo can be used to solve a variety of problems, for example linear or non-linear, unconstrained or constrained and single objective or multi-objective problems. Due to the powerful capabilities and possible integration within the development environment this library is used for optimization in this study.

The selected algorithm for the optimization tool is DE1220, an adaptation to the heuristic Differential Evolution algorithm developed by Storn and Price (1997). The Differential Evolution algorithm works by starting with a randomly created population of multiple individuals which evolves over a certain amount of iterations to increase the fitness of the individuals. Figure 3.2 graphically shows the structure. In a randomized process a selection of three individual design vectors is mutated to get a new trial design vector. This cross-over mutation is done based on the vector differences, thus Differential Evolution. If the trial design vector gives a smaller fitness value to the objective function this new design vector is selected as an individual to the population of the next generation.

The adaptation of the Differential Evolution algorithm towards DE1220 is twofold. The first change is the fact that the DE1220 algorithm is a self-adapting algorithm. Within the cross-over process in Differential Evolution two variables, F and CF, play an influential role. The Differential Evolution strategy, defined by the search operator, controls how the values of these both variables are determined. Elsayed et al. (2011) showed that by using multiple search operators and by adapting how to mix these search operators during the optimization process (called self-adapting) the algorithm became more consistent over a range of problems. The Pagmo development team added a second change of the original algorithm on top of that, which is the fact that a similar self-adapting property is also included on the individual chromosomes in the mutation process.

The Pagmo development team describes Differential Evolution as one of the best performing meta-heuristic algorithms in the Pagmo library. With both adaptations the algorithm becomes even more agile and robust and it is for this reason the DE1220 algorithm is selected for optimizing the vehicle and trajectory design problem of this study.

---

[2] 'Pagmo', *European Space Agency*, `https://esa.github.io/pagmo2/index.html#`, (accessed on April 04, 2020).

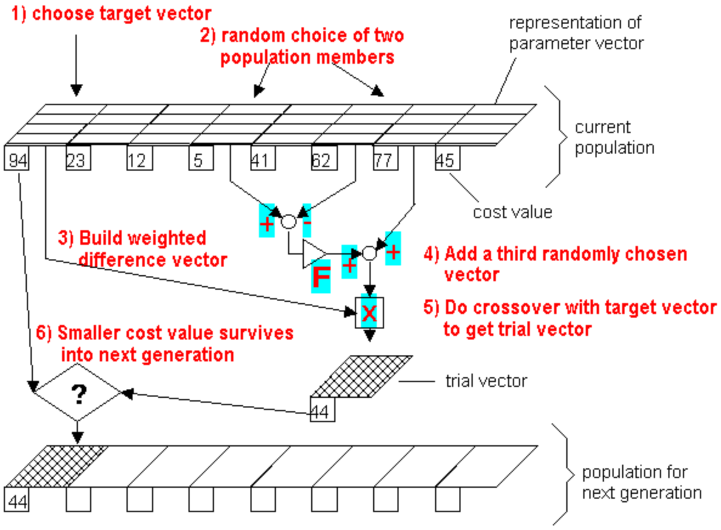
1) choose target vector
2) random choice of two population members
representation of parameter vector
current population
94
23
12
5
41
62
77
45
cost value
3) Build weighted difference vector
+
-
F
+
+
4) Add a third randomly chosen vector
X
5) Do crossover with target vector to get trial vector
6) Smaller cost value survives into next generation
?
trial vector
44
44
population for next generation

Figure 3.2: Graphical representation of the Differential Evolution algorithm (see Footnote 2)

3.1.2. Multidisciplinary Design Optimization

In the design of any vehicle, in this case the launch vehicle, multiple disciplines play individual roles in the design and interact with each other. Wings for example require a structural element, but their shape is driven by the aerodynamic requirements. In modern studies, for estimating the optimal design of a vehicle, the individual disciplines are not optimized separately. Rather, it is common to model all disciplines and their interactions and to optimize this system as a whole. This process called *Multidisciplinary Design Optimization* (MDO) enables for finding the optimal balance between the different disciplines involved in the design. The following disciplines are modelled in this study:

- Propulsion
- Aerodynamics
- Geometry
- Mass
- Trajectory

The theory behind MDO is discussed briefly, summarizing the key aspects as discussed extensively by Balesdent (2011).

Multidisciplinary Design Analysis

It is important to realize there is a difference between a *Multidisciplinary Design Analysis* (MDA) and MDO. In and between all the different disciplines feasibilities and consistencies are modelled by **state variable computation functions** $X(y,z)$ and **coupling functions** $c(x,y,z)$. The MDA has the main goal of satisfying all the individual feasibilities and coupling consistencies between these different disciplines. The MDA tries to solve the **state variables** x_i and the **coupling variables** y_i such that the state equations are satisfied and the couplings are consistent. By defining a **residual function** $R(x,y,z)$ (implicit form of the state variable computation function) to quantify the satisfaction of the state equations, the MDA is expressed as (with the **design variables** z_i):

$$\begin{cases} \forall i \in \{1,\cdots,n\}, \forall j \neq i, y_i = \{c_{ji}(x_j, y_j, z_j)\}_j \\ \forall i \in \{1,\cdots,n\}, R_i(x_i, y_i, z_i) = 0 \end{cases} \tag{3.2}$$

It is common to perform this analysis by the use of an iterative method. However, within this study the different disciplines are modelled based on internal feasibility and forward dependency. This means that an iterative loop of the MDA is not required. Rather, the analysis is performed sequentially.

Multidisciplinary Design Optimization by a Multi Discipline Feasible method

The MDO loop is defined around the MDA. The easiest but computationally most expensive method to do so is the Multi Discipline Feasible method. This method has the closest resemblance to the classical optimization problem shown in Equation 3.1, in which the analysis code is the MDA solved in every iteration loop of the optimizer. Due to the fact that in this study the MDA is defined sequentially the computational burden of this method is limited. Figure 3.3 shows the architecture of the Multi Discipline Feasible method implemented in this study. Indeed it shows the sequential behaviour of the different disciplines. The MDO is performed with an all-at-once strategy, meaning that the full design vector containing all design variables is fully initialized at the start of the process and optimized in every iteration.

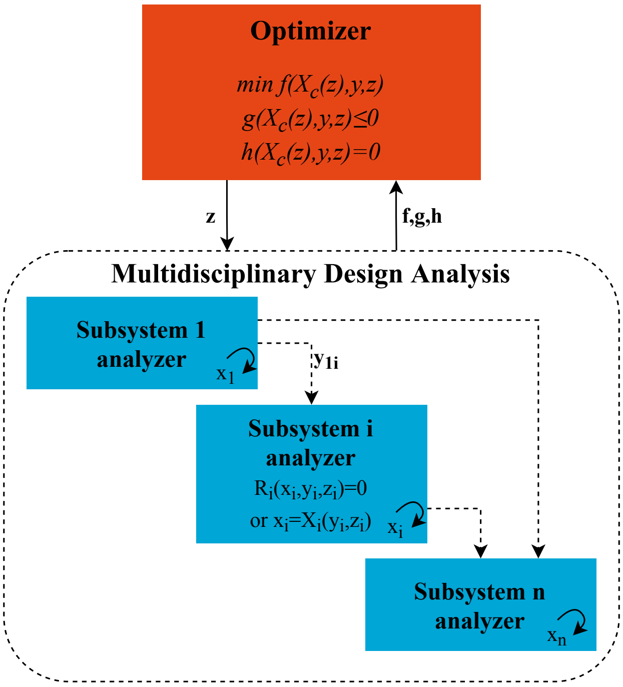

Figure 3.3: Architecture of the Multi Discipline Feasible method as implemented in this study (adapted figure from (Balesdent, 2011))

3.1.3. Optimal control

To integrate the trajectory discipline within the optimization structure a formulation is required in which the trajectory itself can be optimized as well. Within the field of optimal control good formulations of control problems exist to implement in the optimization loop. In this study a direct explicit control law is selected, which is explained in this section.

Optimal control is a branch of mathematics that concerns with finding a control law for a dynamical system in order to optimize an objective function. The control law has to satisfy the dynamics of the system as well as the defined constraints. Betts (1998) formulated the optimal control problem, in which the control law $u(t)$ has to minimize the objective function, as:

$$F = f(x(t_f), t_f) \tag{3.3}$$

in which x is the state vector and t_f is the final time which may or may not be fixed. The dynamics of the system are described by the following *Ordinary Differential Equation* (ODE):

$$\dot{x} = s(x(t), u(t)) \tag{3.4}$$

where s is the state equation. Boundary conditions can be imposed on the problem by:

$$h_f(x(t_f), u(t_f), t_f) = 0 \tag{3.5}$$

The control law itself can be formulated in different ways. Common practice in trajectory studies (Balesdent, 2011) is the use of a direct method. In a direct method the control law is defined by a finite set of parameters u_{p_i}, which the optimizer uses to meet the optimality conditions. In this study this is implemented as follows, in which piecewise interpolation is used to define the control law in every instance of time:

$$u(u_{p_i}, t) = \begin{cases} u_{p_0} + u_{p_{0,1}}\, t & \text{if } t \in [t_0, t_1] \\ u_{p_1} + u_{p_{1,i}}\, t & \text{if } t \in [t_1, t_i] \\ & \vdots \\ u_{p_i} + u_{p_{i,i+1}}\, t & \text{if } t \in [t_i, t_{i+1}] \\ & \vdots \\ u_{p_n} & \text{if } t \in [t_n] \end{cases} \tag{3.6}$$

The optimization problem is now defined as:

$$\begin{array}{ll} \textbf{Minimize} & f(x(t_f), t_f) \\ \textbf{With respect to} & u_{p_i}, i = 1, \cdots, n \\ \textbf{Subjected to} & \dot{x}(t) = s(x(t), u(u_{p_i}, t)) \\ & h_f(x(t_f), u(u_{p_i}, t_f), t_f) = 0 \end{array} \tag{3.7}$$

To implement this direct control law into the optimization structure also different methods exist. As discussed the optimization algorithm used in this study is a meta-heuristic algorithm and due to this gradient information on the trajectory is not easily available. It is for this reason the control law is implemented in an explicit way, which means that the different parameters u_{p_i} are implemented as design variables in the optimization process. This also shows why the selection is made for a direct method. By formulating the optimal control problem in a direct and explicit way it is straightforward to implement this within the heuristic optimization environment.

A final remark is on the constraint handling during trajectory optimization. As the optimization is performed with an all-at-once strategy and the control law is both direct and explicit the resulting trajectory is explicitly defined by the design variables. To find possible path constraint violations along the trajectory an iterative loop is used to find those violations. If violations do exist penalty values are applied on the optimization objective function to create convergence towards solutions that do meet the trajectory path constraints.

3.2. Motion fundamentals

Modelling the motion of a vehicle in space requires several fundamental concepts. In this section these concepts are discussed and their implementation in this study is shown.

3.2.1. Ordinary Differential Equations

One of the fundamental concepts required for describing motion is the ODE. An ODE is a type of differential equation which only contains one or more functions and derivative functions with respect to the same independent variable (Zill, 2012). The term ordinary in this case is used to describe the contrast with for example Partial Differential Equations, which do contain functions and derivative functions with respect to more than one independent variable.

ODEs are common in a variety of scientific fields due to the fact that a lot of processes do describe change with respect to a certain variable. In motion for example the position and velocity can be expressed by the combination of mass and the acting accelerations over a certain change in time, as shown by Newton's Second Law of Motion. This is an example of a simple ODE.

More advanced studies in motion make use of so-called systems of ODEs. In these more complex problems several different identities can be related to a change in time resulting in a system of multiple time dependent equations. Also control inputs can be described within these equations, although these can also be related to the attitude of the vehicle. By solving the behaviour over time the solution at a specific time is found. However, due to the high non-linearity, control input and time dependence of these kind of problems, solutions cannot be found by an analytical approach. This shows the need for a numerical integrator, which is addressed in a later section.

3.2.2. State variables

To define motion mathematically it is required to express both position and velocity. State variables are used to define the position and velocity. Three representations of the state variables are implemented in this study.

The first is by describing the position and velocity as vectors based on the Cartesian coordinate system as (Mooij, 2017):

$$\mathbf{r} = [x, y, z]^{\mathrm{T}}; \ \mathbf{v} = [\dot{x}, \dot{y}, \dot{z}]^{\mathrm{T}} \tag{3.8}$$

From a mathematical perspective this is a correct way of representing position and velocity, with the downside that it gives no insight in the motion itself. On the other hand singularities do not exist, creating a suitable set of variables for trajectory integration.

The second set of state variables gives more intuitive insight in the trajectory, by making use of the spherical properties of the trajectory. These are the so-called spherical components. Position is defined based on the radius of the trajectory r, as well as the longitude τ and latitude δ. The velocity is described by the magnitude V, as well as the flightpath angle γ and heading angle χ. The downside of this description is the fact that singularities do exist, for example a flight path angle of ±90°. However, the Guidance, Navigation and Control in this study is primarily defined in spherical components, due to the intuitive relation with the defined control parameters. In spherical components the position and velocity vector are described as (Mooij, 2017):

$$\mathbf{r} = [r, \delta, \tau]^{\mathrm{T}}; \ \mathbf{v} = [V, \gamma, \chi]^{\mathrm{T}} \tag{3.9}$$

The final set of state variables used in this study is the set of classical orbital elements (Kepler elements). Orbital elements are especially used for the description of satellite orbits and give direct insight in shape of a satellite orbit. This set of six state variables describing both position and velocity is defined as (Mooij, 2017):

$$\mathbf{x}_{\mathrm{kep}} = [a, e, i, \omega, \Omega, M]^{\mathrm{T}} \tag{3.10}$$

in which a is the semi-major axis, e is the eccentricity, i is the inclination, ω is the argument of perigee, Ω is the longitude of the ascending node and M is the mean anomaly. Figure 3.4 shows some of the classical orbital elements. Missing are the semi-major axis and the eccentricity. The combination of these two entities defines the radius of the orbit at both the perigee and apogee, determining the elliptical shape of the orbit. The inclination of the orbit determines the relative orientation of the orbital plane related to the equatorial plane of the central body. The remaining elements define the position relative to the coordinate system. The intuitive nature of classical orbital elements comes from the fact that it is now possible to define a measure of radius combined with an expression for ellipticity and orientation very easily. Furthermore, only the mean anomaly, which defines the current position within the orbit, is oscillating between 0° and 360° making it a robust formulation for long-term orbit propagation.

3.2.3. Reference frames

Vectors are important entities in expressing motion. Not only the state variables themselves can be defined by vectors, but also the occurring accelerations on the vehicle. To define a vector it is important to state the reference frame in which it is defined. Several different reference frames are used throughout this study, which can be divided into two main categories. The first are inertial frames, which are non-rotating and by that allow Newton's laws to be applied directly. The second are non-inertial frames, which do rotate and do need the introduction of apparent forces to apply Newton's laws (Mooij, 2017).

Due to this difference between inertial and non-inertial frames the main reference frame for trajectory propagation is selected an inertial Cartesian reference frame, of which the centre is defined in the barycentre of the Solar System. It is realized that defining an inertial system with the centre defined in the Earth's centre of gravity is another possibility due to the lack of simulating third body perturbations. The difference between those definitions is minor, although the latter has the slight advantage of reducing errors due to numerical precision. However, this difference due to numerical precision is noticed only when propagating small perturbed satellite orbits over long

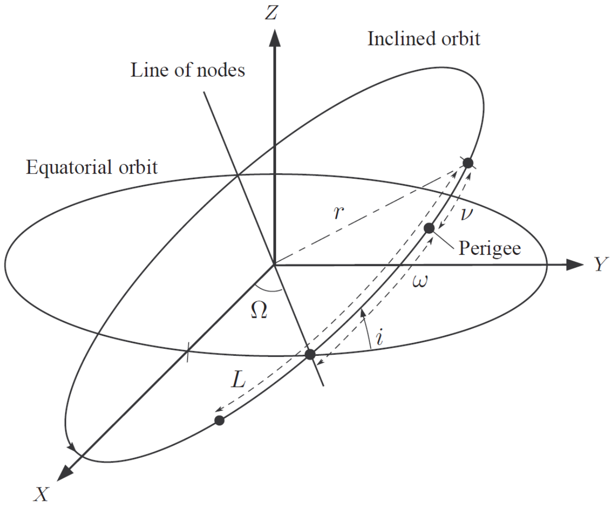

Figure 3.4: Some of the classical orbital elements (Leomanni et al., 2017)

periods of time.[3] To propagate the orbit all other definitions in different reference frames are transformed to the main inertial reference frame. The theory behind reference frame transformations is discussed by Mooij (2017).

The second reference frame used throughout the simulation is the Earth-Centred-Earth-Fixed reference frame shown in Figure 3.5. This reference frame makes use of the spherical components and defines them with respect to the rotating Earth. While being fixed to the rotating Earth, this means that at any time the position and velocity can be expressed relative to a specific location on Earth. Due to this property this reference frame is used for Guidance, Navigation and Control as well as to define the classical orbital elements.

A third reference frame used is the aerodynamic (air-path) reference frame. This reference frame is used to express the lift and drag of the vehicle. The x-axis is defined along the velocity vector. The z-axis is collinear with the aerodynamic lift force always perpendicular on the velocity, while opposite in direction of this lift force. The y-axis completes the right hand system.

Finally, a propulsion reference frame is used to express the thrust force. Due to the fact that the thrust force is defined along the longitudinal body axis of the vehicle, this reference frame coincides with the body frame itself. A consequence of this definition is the fact that the thrust force can only change direction by changing the attitude of the vehicle. The propulsion reference frame is defined by the x-axis along the plane of symmetry and positive in forward direction. The z-axis is defined on the same plane of symmetry and is positive in downward direction. The y-axis completes the right hand system.

3.2.4. Equations of Motion

The system of ODEs used in this study can be expressed in different reference frames. An intuitive expression, used for implementing the guidance model, is within the Earth-Centred-Earth-Fixed rotational reference frame. In this reference frame the *Equations of Motion* (EOMs) in spherical components are expressed as (Balesdent, 2011):

$$\dot{r} = V \sin\gamma \tag{3.11}$$

$$\dot{\delta} = \frac{V\cos\gamma\cos\chi}{r} \tag{3.12}$$

$$\dot{\tau} = \frac{V\cos\gamma\sin\chi}{r\cos\delta} \tag{3.13}$$

---

[3] '1. Unperturbed Earth-orbiting Satellite', *TU Delft Astrodynamics Toolbox*, `https://tudat.tudelft.nl/tutorials/applicationWalkthroughs/unperturbedEarthOrbitingSatellite.html`, (accessed on April 07, 2020).

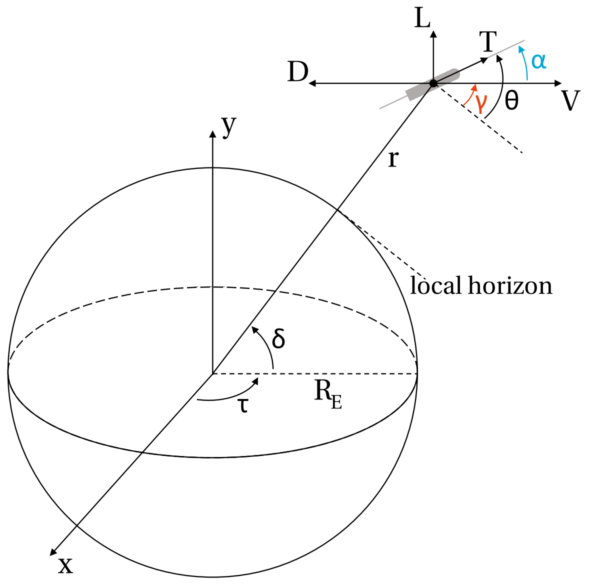

Figure 3.5: Earth-Centred-Earth-Fixed rotating reference frame (adapted figure from (Balesdent, 2011))

$$\dot{V} = \frac{T\cos(\theta-\gamma) - D}{m_{\text{veh}}} - g(r)\sin\gamma + {\omega_{\text{E}}}^2 r\cos\delta(\sin\gamma\cos\delta - \cos\gamma\sin\delta\cos\chi) \tag{3.14}$$

$$\dot{\gamma} = \frac{[L + T\sin(\theta-\gamma)]\cos\mu}{m_{\text{veh}}V} + \left(\frac{V}{r} - \frac{g(r)}{V}\right)\cos\gamma + 2\omega_{\text{E}}\sin\chi\cos\delta + \frac{{\omega_{\text{E}}}^2 r\cos\delta(\cos\gamma\cos\delta + \sin\gamma\sin\delta\cos\chi)}{V} \tag{3.15}$$

$$\dot{\chi} = \frac{[L + T\sin(\theta-\gamma)]\sin\mu}{m_{\text{veh}}V\cos\gamma} + \frac{V\cos\gamma\sin\chi\tan\delta}{r} + 2\omega_{\text{E}}(\sin\delta - \cos\chi\cos\delta\tan\gamma) + \frac{{\omega_{\text{E}}}^2 r\sin\delta\cos\delta\sin\chi}{V\cos\gamma} \tag{3.16}$$

in which T, L and D are thrust, lift and drag respectively; θ and μ are the pitch and bank angle ($\theta - \gamma = \alpha$); m_{veh} is the mass of the vehicle; $g(r)$ is the gravitational acceleration as a function of radial distance; ω_{E} is the angular velocity of the Earth. To complete the trajectory model the change in mass is modelled by:

$$\dot{m}_{\text{veh}} = -q \tag{3.17}$$

with q being the total propellant mass flow rate.

3.3. Propagation and integration

Until now several concepts to define motion were discussed and also the EOMs were shown. The discussion showed that motion can be abstracted into a system of ODEs, expressed by the selected state variables in the corresponding reference frame. To numerically compute the resulting trajectory two additional tools are required, being the propagator and the integrator. The propagator does the bookkeeping to map the state variables, while the integrator solves the system of ODEs.

3.3.1. Propagation with Cowell's method

Cowell's method is selected for propagation of the trajectory. This method defines both the state and the derivative of this state, to get the complete dynamics of the system, as:[4]

---

[4] Dirkx, D. and Geul, J., Lecture slides on: 'AE4867 Numerical Astrodynamics - Simulation Settings', *Delft University of Technology*, (accessed on April 07, 2020).

$$\mathbf{x} = \begin{pmatrix} \mathbf{r} \\ \mathbf{v} \end{pmatrix}; \, \dot{\mathbf{x}} = \begin{pmatrix} \dot{\mathbf{r}} \\ \dot{\mathbf{v}} \end{pmatrix} \tag{3.18}$$

in order to solve:

$$\dot{\mathbf{x}} = f(\mathbf{x}, t; p) \tag{3.19}$$

with p being dependent parameters in the model. As the propagation of the trajectory is done in Cartesian components this method can be directly applied.

3.3.2. Integration with Runge-Kutta-Fehlberg method (RKF45)

As discussed motion can be expressed in a system of ODEs. The motion in this study is non-linear, time dependent and attitude dependent on the control input. Due to this an analytical solution to the EOMs is unavailable. Hence a numerical method is required to integrate the EOMs. The general expression of an integrator is formulated as:[5]

$$y(t+h) \approx y(t) + h\Phi = \eta(t+h) \tag{3.20}$$

where y is the function to integrate, $(t,(t+h))$ is the begin and end time of the interval, Φ the increment function and $\eta(t+h)$ the approximate solution. It is the increment function that defines the working of the integrator, which has been studied over decades resulting in very different integration methods.

Although the different integrators can be classified along a wide variety of properties the main property important for this study is the so-called fixed versus variable step-size property. A variable step-size integrator is able to change the timestep (time is the independent integration variable) of a single integration step during the propagation of the problem based on the demand in the problem. One can imagine that when a launch vehicle is in dense layers of the atmosphere with high thrust and high oscillating control a small timestep is required to maintain a certain precision. On the other hand during a coasting phase in which only gravity acts one can imagine this timestep can be larger for the same precision. Making the timestep smaller and smaller in the whole simulation is not an option, due to the increasing computational demand and run time of the algorithm. Due to this very different demand on the integrator during the trajectory propagation a variable step-size integrator is the most effective integrator trading computational precision and runtime. Several variable step-size integrators do exist, however, early in the study the Runge-Kutta class of integrators was selected due to proven performance in earlier studies. Due to similarities between different integrators in this class the integration scheme is discussed based on one specific integrator design, the Runge-Kutta-Fehlberg method.

The Runge-Kutta-Fehlberg method was invented by Fehlberg (1969), as an adaptation of the classical Runge-Kutta integration scheme. The idea is the following: by comparing two different order solutions of the Runge-Kutta approximation (increment function) an error can be determined between these approximations. Now, with a quantification on the limit of this error, the error itself can be used to determine the required step-size for a certain precision. The order of the two Runge-Kutta approximations that are compared determines the name of the integrator. In the classical Runge-Kutta-Fehlberg method a fourth and fifth order approximation are compared, thus RKF45. But also an RKF56 or RKF78 do exist. The fourth and fifth order increment functions both have to be defined using the same six stages as:

$$\Phi_{\mathrm{RK4}} = \sum_{i=1}^{6} c_i k_i + O(h^5) \tag{3.21}$$

$$\Phi_{\mathrm{RK5}} = \sum_{i=1}^{6} \hat{c}_i k_i + O(h^6) \tag{3.22}$$

with c_i and k_i being properties of the general Runge-Kutta integration scheme (see Footnote 5). Now the error can be quantified as:

$$\epsilon = \sum_{i=1}^{6} (c_i - \hat{c}_i) k_i \tag{3.23}$$

which is used to determine the optimal step-size h_{opt} as:

---

[5] Noomen, R., Lecture slides on: 'Space Mission Design: Integrators', *Delft University of Technology*, (accessed on April 07, 2020).

$$h_{\text{opt}} = \beta h \left(\frac{\epsilon_{\text{tol}}}{\epsilon}\right)^{0.2} \tag{3.24}$$

with ϵ_{tol} being a defined required precision and β a safety factor. Although it is possible to determine a fixed step-size fourth order Runge-Kutta approximation only with four stages, the same six stages can be used by both the fourth and fifth order approximation in the RKF45 method. Hence the computational effort of this method increases by 50% in every step of the integration process compared to a classical fourth order Runge-Kutta integration. However, due to the fact that the step-size can be increased when allowed by the problem, still in most trajectory studies the total computational effort is decreased. Always the computational effort is better distributed due to the fact that it is only applied according to the demand of the problem.

It was discussed that there is a variety of variable step-size Runge-Kutta integrators, comparing different order estimates. In initialization runs of the numerical tool used in this study it was found that for the RKF45 method the precision ϵ_{tol} could be decreased the most while staying within the defined range of orbital injection precision. This is shown in Table 3.1, which shows the result of a trajectory integration with different integrators for the same precision setting. The benchmark is determined by the convergence behaviour of the problem at higher precision. Based on this result the RKF45 method was selected for use throughout this study.

Integrator	**Semi-major axis (a) [m]**	**Eccentricity (e) [-]**	**Δa [m]**	**Δe [-]**
Benchmark	7106370	$1.94 \cdot 10^{-2}$	-	-
RKF45	7119150	$2.11 \cdot 10^{-2}$	12780	$1.73 \cdot 10^{-3}$
RKF56	7453410	$6.70 \cdot 10^{-2}$	347040	$4.76 \cdot 10^{-2}$
RKF78	7132100	$2.25 \cdot 10^{-2}$	25730	$3.08 \cdot 10^{-3}$

Table 3.1: Comparison of numerical integrator behaviour with a precision ϵ_{tol} of 10^{-4} for a general trajectory problem

4

An introduction to the mission and the implementation of the trajectory model

The mission of the launch vehicle is largely influenced by the ascent and return requirements on the trajectory. This innovative trajectory design is analysed and optimized during the *Multidisciplinary Design Optimization* (MDO). This chapter first introduces the mission and shows the required theory for both the ascent and return phase of the trajectory. This is followed by a discussion on the implementation of the guidance model used to let the vehicle perform the proposed flight phases. Finally, the environment models are introduced for estimating the behaviour of the vehicle around the Earth.

4.1. Mission profile

The mission in this study consists out of three distinct flight phases as shown in Figure 4.1. The first and second phase are ascent phases and the third phase is the return phase. The (1) ascent of the first stage starts at the runway. The main engines are used for the take-off roll after which the launch vehicles rotates and pitches upward. The ascending trajectory is continued until the staging point, after which the (2) upper stage is released from the first stage and ascents further into orbit to inject the payload. Simultaneously, the (3) first stage itself re-enters the atmosphere and returns to the initial spaceport of take-off.

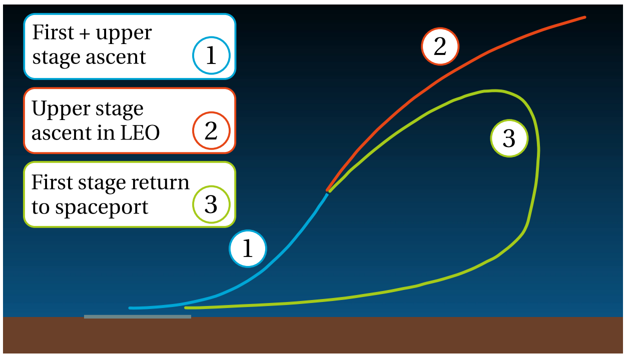
First + upper stage ascent ①
Upper stage ascent in LEO ②
First stage return to spaceport ③
②
③
①

Figure 4.1: Launch vehicle mission profile with three distinct flight phases

It is apparent that there is a large connection between the three flight phases. In phase one and three the same first stage vehicle is used and the design of this vehicle is dependent on both phases. Furthermore, the initial conditions of phase two are dependent on phase one and due to this also is the upper stage design. The first stage design is also dependent on the upper stage design, as the upper stage is stored inside the fuselage. Finally, also the staging conditions are the initial conditions of the return phase. Hence they influence the return possibility. Due to this large dependency between the different flight phases for studying the behaviour of the total launch vehicle in this trajectory design all three flight phases have to be included in the trajectory model.

4.2. Ascent trajectory

The goal of the ascent trajectory is to bring the payload into orbit within the defined injection requirement range, which is a combination of altitude, eccentricity and inclination. In essence this is nothing more than accelerating the payload towards the required orbital velocity and letting it loose at the right moment and correct orientation. The practice, however, is more complicated due to design challenges - thermal and mechanical loads acting inside on the engine and outside on the launch vehicle are enormous -, the environment during the launch and the control of the vehicle at high velocities.

Within the process of understanding rocket technology one of the first major breakthroughs was a straightforward equation derived by Tsiolkovsky (1903). This equation shows that the total amount of velocity increase ΔV of a rocket is only dependent on the performance of the engine and the amount of propellant that is expelled as:

$$\Delta \mathrm{V} = I_{\mathrm{sp}} g_0 \ln \frac{m_0}{m_{\mathrm{e}}} \tag{4.1}$$

in which I_{sp} is the specific impulse as a measure of engine performance and (m_0, m_{e}) are the initial and final mass respectively as a measure of propellant consumption. The physics that lead to this equation allow for two essential performance optimization techniques in the design of launch vehicles. These are the increase of engine performance and the decrease of empty mass as compared to propellant mass. As seen in the equation both actions do increase the total amount of velocity increase the launch vehicle can deliver.

Of course not all of the total ΔV is delivered to the payload. During the ascent several losses play a role in the decrease of injection velocity $\Delta \mathrm{V}_{\mathrm{inj}}$. Vandamme (2012) summarized this in the following equation (the pressure loss $\Delta \mathrm{V}_{\mathrm{p}}$ is added):

$$\Delta \mathrm{V} = \Delta \mathrm{V}_{\mathrm{inj}} + \Delta \mathrm{V}_{\mathrm{g}} + \Delta \mathrm{V}_{\mathrm{d}} + \Delta \mathrm{V}_{\mathrm{s}} + \Delta \mathrm{V}_{\mathrm{p}} \tag{4.2}$$

in which $(\Delta \mathrm{V}_{\mathrm{g}}, \Delta \mathrm{V}_{\mathrm{d}}, \Delta \mathrm{V}_{\mathrm{s}}, \Delta \mathrm{V}_{\mathrm{p}})$ are the gravity, drag, steering and pressure loss respectively.

Another important realization from Tsiolkovsky's equation is the fact that within the practical bounds of *Propellant Mass Fraction* (PMF) and engine performance the total velocity increase of a launch vehicle is limited and almost in any case lower than the required velocity to get into orbit. It is for this reason staging was invented. As discussed by Wittenberg et al. (2014) staging is the technique in which a launch vehicle consists of several stages, which are ignited sequentially and ejected in series. The idea behind this staging technique is that dry mass, once the objective of this mass is accomplished, is ejected creating a more efficient vehicle in terms of PMF. For a single stage rocket the payload fraction λ is defined as:

$$\lambda = \frac{m_{\mathrm{u}}}{m_0} \tag{4.3}$$

with m_{u} being the payload mass and m_0 being the total mass of the launch vehicle. Furthermore, the construction mass ratio ϵ can be defined as:

$$\epsilon = \frac{m_{\mathrm{c}}}{m_{\mathrm{c}} + m_{\mathrm{p}}} \tag{4.4}$$

in which m_{c} is the structural dry mass of the rocket stage and m_{p} is the propellant consumption of this rocket stage. Substituting both in Tsiolkovsky's equation results in the following equation determining the total velocity increase of the rocket stage (Wittenberg et al., 2014):

$$\Delta \mathrm{V} = -I_{\mathrm{sp}} g_0 \ln \{\lambda(1-\epsilon)+\epsilon\} \tag{4.5}$$

Again the limitation in total velocity increase is clearly visible, however, when taking into account an N amount of stages the total velocity increase $\Delta \mathrm{V}_N$ of these N stages is determined by (Wittenberg et al., 2014):

$$\Delta \mathrm{V}_N = -\sum_{i=1}^{N} \left(I_{\mathrm{sp}} g_0\right)_i \ln \{\lambda(1-\epsilon)+\epsilon\} \tag{4.6}$$

which shows that for a system of N stages it is much easier to accomplish orbital velocity due to the summation of individual stage velocities. It is for this reason all orbital launch vehicles use two or more stages. Hence does the launch vehicle in this study. The PMF in this study is defined as:

$$\mathrm{PMF} = \frac{m_\mathrm{p}}{m_\mathrm{p} + m_\mathrm{c}} \tag{4.7}$$

Besides the rocket performance another important factor playing a role in the ascent of the launch vehicle is the design of the ascent trajectory itself. There are two basic types of ascent trajectories, the first being a Direct Ascent and the second a Hohmann Transfer Ascent, both shown in Figure 4.2. The differences between the two ascent trajectories were described by Wakker (2015). The main difference is that in almost all cases the Hohmann Transfer Ascent is more propellant efficient, although within the context of a lot of operational constraints still the Direct Ascent can be preferable. Especially considering that Direct Ascent is easier in terms of vehicle design and control as well as the fact that it is much easier to track the upper stage from the spaceport, within this study the choice is made on a Direct Ascent trajectory.

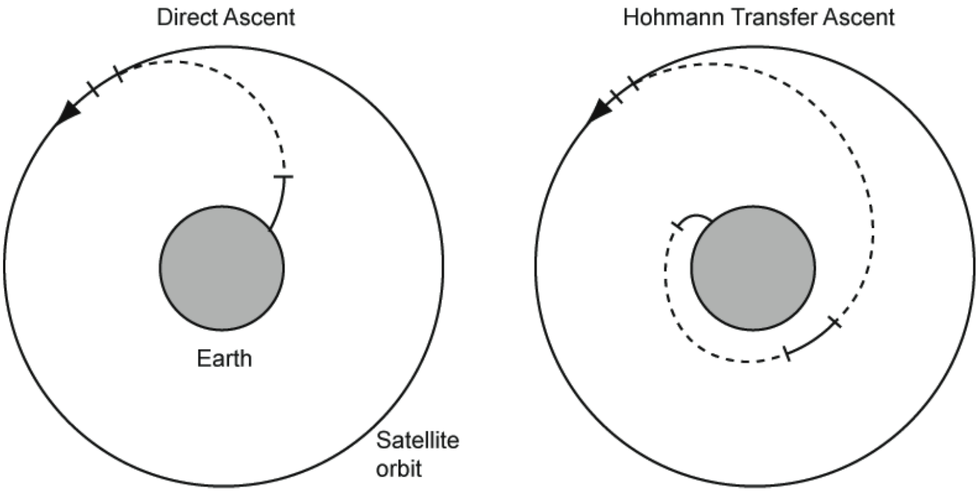

Figure 4.2: Sketch of a Direct Ascent and Hohmann Transfer Ascent (Wakker, 2015)

A final consideration in the ascent trajectory of the launch vehicle is coasting time. Coasting time is a period in which the engines are off and the vehicle only continuous along the ballistic arc. In most launches this happens for a small period of time during staging, but it can also be used in the upper stage ascent trajectory to increase the altitude of the final orbit. In this study a small coasting phase during staging is modelled, but also the model allows for a larger coasting phase during the upper stage ascent.

4.2.1. Constraints

Due to the harsh environment and high velocities launch vehicle design is a difficult tasks. It is for this reason that it is important to set boundaries in which the launch vehicle has to operate without problems. These boundaries act as inequality constraints on the ascent trajectory and are primarily driven by both requirements of the launch vehicle and the payload. Furthermore, also orbital injection goals shall be achieved, which are implemented as equality constraints. The constraints are addressed shortly.

The first constraint is the **(1) acceleration** of the vehicle. This inequality constraint is primarily payload driven, as often payload consists of very sensitive equipment which cannot be forced under too much acceleration load. Within this study the axial acceleration of the payload is constrained with 100 $\mathrm{m/s^2}$. This is similar in order of magnitude as for example during a launch of the Electron launch vehicle, especially considering throttling is not modelled in this study.[1] The lateral acceleration is constrained to 40 $\mathrm{m/s^2}$ which is higher than for conventional launch vehicles, but expected to be required for the pull-up manoeuvre of the ascending first stage.

The second payload driven constraint is the desired **(2) orbit** in which the payload is injected. In this study three of the six elements describing a Kepler orbit are used for the definition of desired injection. These are semi-major axis, eccentricity and inclination. The combination of eccentricity and semi-major axis is used to determine the pericenter altitude. Together with the eccentricity itself this is directly implemented as equality constraints. The inclination is a result of the launch azimuth defined in the model and is not directly implemented as a constraint.

---

[1] 'Electron - Payload User's Guide Version 6.4', *Rocket Lab*, `https://www.rocketlabusa.com/assets/Uploads/Rocket-Lab-Payload-Users-Guide-6.4.pdf`, (accessed on March 31, 2020).

A final payload driven constraint is the **(3) aerothermal flux** that is allowed to be experienced by the payload. The aerothermal flux is a measure of the thermo-mechanical energy of the free molecular flow in the thin layers of the atmosphere and is approximated (assuming the thermal accommodation coefficient $\alpha_T = 1$) by the flow acting on the plane surface perpendicular to the velocity direction as (Lips and Fritsche, 2005):

$$q_{\mathrm{c,fm}} \approx \frac{1}{2}\rho V^3 \tag{4.8}$$

The industry standard of the maximum aerothermal flux that a payload is allowed to experience is 1135 $\mathrm{W/m^2}$ and this is implemented as an inequality constraint active after staging.[2]

Also the launch vehicle itself constraints the trajectory. During the initial phase of study, however, it was found that some of the constraints do never come close to the constraining value. Hence they are not actively implemented (saving runtime). First of all the launch vehicle cannot be exerted under to high acceleration loads, although this is not as critical as for the payload. Hence this is not constrained directly. More critical, however, is the maximum **(4) dynamic pressure**. Van Kesteren (2013a) showed that the maximum allowable dynamic pressure found in literature is between 57.5 kPa and 90.0 kPa. He concluded that the maximum value of 90.0 kPa was appropriate to implement as the inequality constraint value. This reasoning is directly implemented in this study, although it is found that a dynamic pressure of 90.0 kPa is never approached during ascent. Hence the constraint is not active.

Another important constraint that is implemented is the behaviour of the vehicle in terms of **(5) *Angle of Attack* (AoA)**, and for the first stage especially in combination with the dynamic pressure. The AoA during ascent is limited to ±60°, which is important to avoid the numerical problem of tumbling of the upper stage during coasting. During first stage ascent bending loads due to aerodynamic loads on the vehicle need to be limited. This can be expressed via the so-called **(6) $q \cdot \alpha$-limit**, which is a measure of the bending loads based on the combination of dynamic pressure and AoA. It was derived by van Kesteren (2013a), based on the Pegasus launch vehicle, that an approximation of this bending limit for winged vehicles is ~18000 Pa·rad. Also this is implemented as an inequality constraint.

A final inequality constraint implemented drives the **(7) total ΔV** of the vehicle. During the development of the numerical tool it was found that this ΔV has to have an under-limit in order for the model to converge to solutions actually getting into orbit.

4.2.2. Velocity losses

As introduced in Equation 4.2 losses do exist in the ascent trajectory. To create a framework in which these losses can be compared van Kesteren (2013a) showed the analytical approach on how to estimate the magnitude of the different losses. Also the expected ranges of loss for conventional launch vehicles, based on a variety of launch vehicle studies, were presented. As this is a very interesting framework relevant also within this study this is shortly summarized in this section.

The gravity loss ΔV_g is estimated by the following relation:

$$\Delta V_g = \int_0^{t_f} g \cdot \sin\gamma \, dt \tag{4.9}$$

in which g is the local gravitational acceleration (dependent on altitude) and γ is the flight path angle. For trajectories ascending into parking orbit (~200 km) gravity losses were found between 1150 m/s and 1576 m/s, while for direct ascent into sun-synchronous orbit these losses increase to 2000 m/s to 2400 m/s.

Drag loss ΔV_d exist due to the acceleration by the drag force in the negative velocity direction. Integrating this acceleration over time, which can be approximated by the aerodynamic properties of the vehicle, determines the drag loss as:

---

[2] Industry standard e.g.: 'Vega User's Manual Issue 4 Revision 0', *Arianespace*, `https://www.arianespace.com/wp-content/uploads/2015/09/Vega-Users-Manual_Issue-04_April-2014.pdf`, (accessed on April 01, 2020).

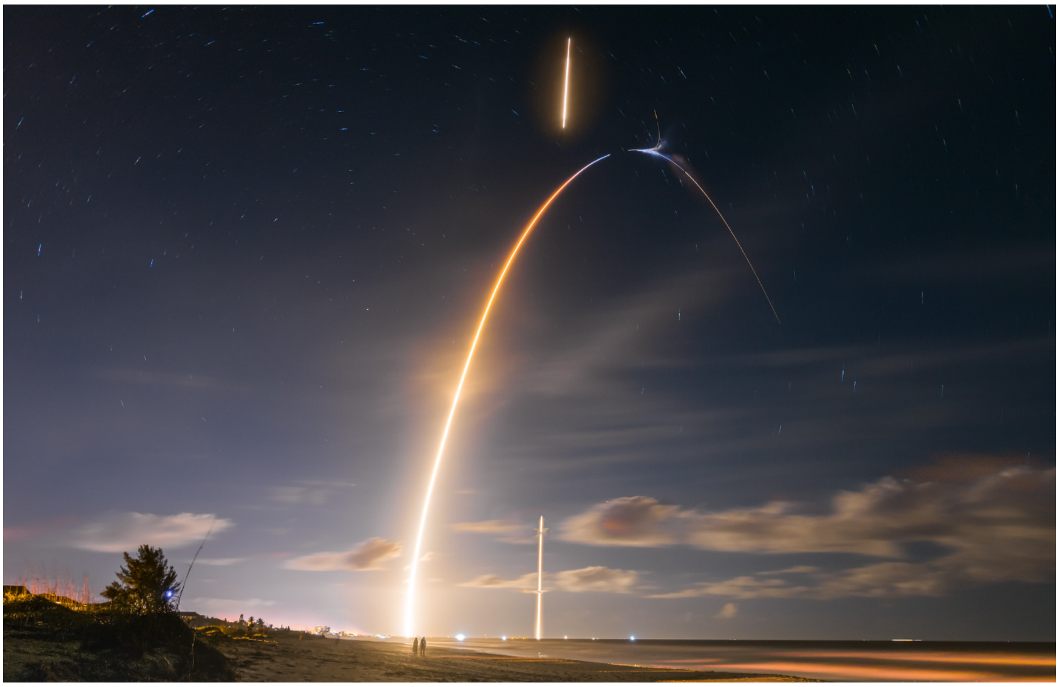

Figure 4.3: Return to Launch Site manoeuvre of the SpaceX Falcon 9 (see Footnote 5)

$$\Delta \mathrm{V_d} = \int_0^{t_f} \frac{D}{m} \mathrm{d}t = \int_0^{t_f} \frac{C_D \rho V^2 S_{\mathrm{ref}}}{2m} \mathrm{d}t \tag{4.10}$$

Typically this drag loss for conventional launch vehicles was found in the order of 40 m/s to 156 m/s.

The final loss addressed was the steering loss $\Delta \mathrm{V_s}$, which exists due to the fact that the thrust vector is not always aligned exactly along the velocity vector. In a two-dimensional scenario this is dependent on the AoA as:

$$\Delta \mathrm{V_s} = \int_0^{t_f} \frac{T}{m} (1 - \cos \alpha) \, \mathrm{d}t \tag{4.11}$$

It was found that steering losses occur in a wider range between 38 m/s and 358 m/s.

The pressure loss was not addressed in the work of van Kesteren (2013a). However, this can be determined straightforward by the difference in current thrust T and maximum vacuum thrust T_{vac} as:

$$\Delta \mathrm{V_p} = \int_0^{t_f} \frac{T_{\mathrm{vac}} - T}{m} \mathrm{d}t \tag{4.12}$$

4.3. Return to Launch Site

One of the key features of the mission design is that the first stage has to return back to the spaceport of take-off. These kind of manoeuvres are so-called *Return to Launch Site* (RTLS) manoeuvres, for example performed by the first stage boosters of the SpaceX Falcon 9 and Falcon Heavy.[3,4] Figure 4.3, a photo taken by photographer John Kraus, shows the return of the first stage booster of the Falcon 9 rocket.[5] The image beautifully shows the different actions involved in RTLS trajectories. After staging the upper stage continuous along the ascent trajectory into orbit, while the first stage booster pitches up by a first burn and continues along a totally different arc. This arc is pointed at the point of landing and the remaining two burns, both visible, are performed to reduce the vertical

---

[3] 'Falcon 9', *SpaceX*, `https://www.spacex.com/falcon9`, (accessed on April 01, 2020).

[4] 'Falcon Heavy', *SpaceX*, `https://www.spacex.com/falcon-heavy`, (accessed on April 01, 2020).

[5] Kraus, J., 'January 7th, 2018: SpaceX launches the classified Zuma payload for Northrup Grumman, and lands the first stage of the Falcon 9 rocket back at Cape Canaveral eight minutes after launch.', *John Kraus Photos*, `https://www.johnkrausphotos.com/`, (accessed on April 02, 2020).

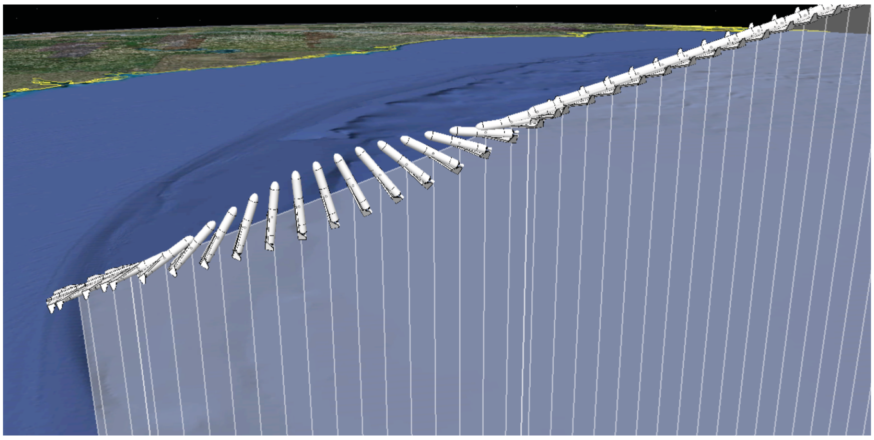

Figure 4.4: In-plane pitch over manoeuvre (Bradford and St. Germain, 2010)

velocity before re-entry and during touchdown resulting in a landing on the launch site.

Of course within this study the first stage is a winged vehicle, which increases the amount of possibilities for RTLS trajectory design. In literature three distinct RTLS techniques for winged vehicles do exist (Haex, 2019). The first being (1) glideback, a passive method in which after staging the vehicle continuous along the ballistic arc, re-enters and glides back to the spaceport. The second being (2) flyback, an active method comparable to glideback with the difference that an air-breathing engine is used to propel the vehicle inside the atmosphere for an increase in achievable downrange. The third being (3) boostback, an active method in which the rocket engines of the vehicle are used for a boost returning the vehicle to the spaceport. Based on the required vehicle design the flyback method is immediately discarded due to the dependency on air-breathing engines.

Hellman (2005) compared different glideback and boostback scenarios. One of his major conclusions was that when using the glideback method the staging velocity can never exceed the very limited magnitude of Mach 3.1, due to the limited range of gliding after re-entry. The conclusion that the gliding range of glideback is too limited for a return to the spaceport is very vehicle dependent as this is dependent on the aerodynamic capabilities of the first stage as well as the performance capabilities of the upper stage. Hence this conclusion is reviewed again in this study.

The active boostback method was studied in more detail by both Hellman (2007) and Bradford and St. Germain (2010). Two distinct return trajectories were found in both studies. The first being in-plane pitch over and the second being aeroturn. Both are shortly addressed. In this research three different methods of return are compared being (1) **in-plane pitch over**, (2) **aeroturn** and (3) **glideback**.

In-plane pitch over

Figure 4.4 shows the in-plane pitch over manoeuvre. Immediately after staging the vehicle is pitched up- or downwards and rotates almost 180°. When this rotation is completed a burn is performed which decreases the velocity of the vehicle. Hence decreasing the downrange distance. This means that it now is possible to descent and re-enter the atmosphere after which the return glide to the spaceport of launch can be accomplished.

Interesting about the in-plane pitch over manoeuvre is that Hellman (2007) showed that due to the fact that the re-entry velocity is decreased this re-entry can be performed without the use of a *Thermal Protection System* (TPS) due to the milder heating environment. Also this manoeuvre can be performed with the main engine on, omitting the necessity of a restartable engine. In this study, however, the main engine is restarted after the rotation, due to the fact that the engine has to be restartable anyway from a reusability perspective and the fact that it is expected that staging of this vehicle is difficult with the main engine on. The demand on the Attitude Control System, however, is much larger for this method, due to the control of the pitch movement outside of the atmosphere. The famous SpaceX return example uses this in-plane pitch over manoeuvre. Of course the fact that with that particular vehicle no gliding is possible makes that an even more demanding manoeuvre in terms of Guidance, Navigation and Control, aiming the dart at the inner bullseye of the dart board.

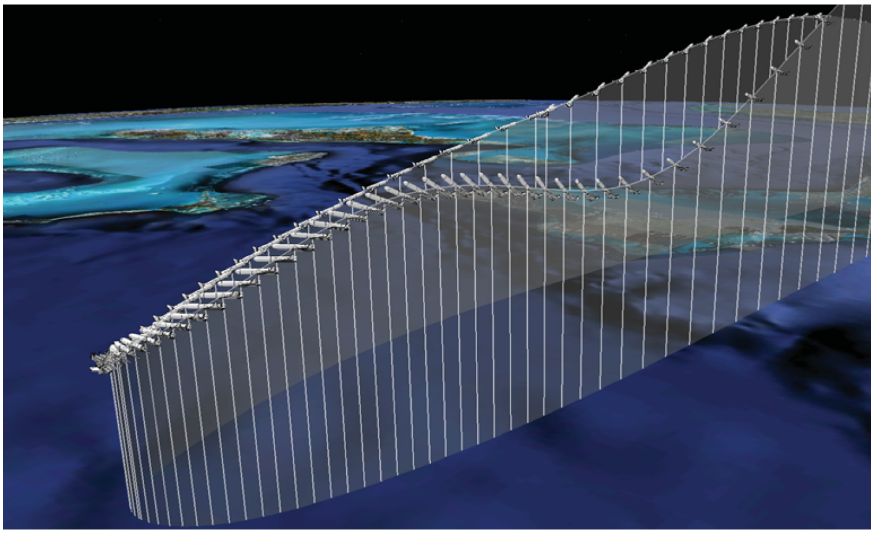

Figure 4.5: Aeroturn manoeuvre (Bradford and St. Germain, 2010)

Aeroturn

The aeroturn manoeuvre, as shown in Figure 4.5, is a very different manoeuvre and is only possible with a winged vehicle. Instead of starting the manoeuvre immediately after staging the vehicle first follows the ballistic arc following from the staging conditions. After re-entering the atmosphere the vehicle uses the aerodynamic capabilities of the wings to change the heading towards the spaceport after which the return burn is performed.

One of the major benefits is that this manoeuvre is simpler from a control perspective. No difficult rotational manoeuvre outside of the atmosphere is required reducing the demand on the Attitude Control System. However, this comes with the penalty of a more harsh re-entry environment due to the higher velocity. Also the covered area by launch is much larger. Finally, restarting the engine is required, which can add in the complexity of engine design.

4.3.1. Thermal loads

It was found in literature that there is an expected difference between the return methods in terms of heat rate and heat load on the vehicle. To quantify this difference the heat rate and heat load of each of the return trajectories is determined. This is done in the stagnation point. To do so the Fay-Riddell model (Fay and Riddell, 1958) is implemented with the assumption that the wall is in thermal equilibrium. To find the heat flux $q_{\mathrm{c,cont}}$ on the stagnation point the following relation is used (the Lewis number Le is already omitted assuming $Le = 1$):

$$q_{\mathrm{c,cont}} = \frac{0.763}{\left(Pr_{\mathrm{w,t}}\right)^{0.6}} \left(\rho_{\mathrm{t2}}\mu_{\mathrm{t2}}\right)^{0.4} \left(\rho_{\mathrm{w,t}}\mu_{\mathrm{w,t}}\right)^{0.1} \left(H_{\mathrm{t2}} - h_{\mathrm{w,t}}\right) \sqrt{\left(\frac{du_{\mathrm{e}}}{dx}\right)_{\mathrm{t2}}} \tag{4.13}$$

in which:

$$\left(\frac{du_{\mathrm{e}}}{dx}\right)_{\mathrm{t2}} = \frac{1}{R_{\mathrm{N}}} \sqrt{\frac{2\left(p_{\mathrm{t2}} - p\right)}{\rho_{\mathrm{t2ss}}}} \tag{4.14}$$

with Pr being the Prandtl number, μ being the absolute viscosity, H being the total enthalpy and h being the static enthalpy. The subscript t2 refers to conditions at the stagnation point outside of the boundary layer, while the subscript w,t refers to the wall conditions. To determine the total heat load on the stagnation point the heat flux is integrated over time as:

$$Q_{\mathrm{c,cont}} = \int_0^{t_{\mathrm{f}}} q_{\mathrm{c,cont}} \mathrm{d}t \tag{4.15}$$

Luckily not all the kinetic energy of the system is actually transferred to the vehicle, but only 1% to 5% is.[6] To create a sense on the order of magnitude of expected heating rates and loads, studies of two re-entry vehicles were consulted. Curry (1993) showed that the stagnation point heat flux of the Space Shuttle during re-entry is approximately 200 kW/m^2, a famous example of a vehicle using tiles as TPS. Furthermore, the figures by Ko et al. (1982) showed that for this same Space Shuttle the duration of severe heating rates is in the order of 600 s resulting in a heat load of >120 MJ/m^2. Roorda (2017) studied the design of a TPS for the Aurora launch vehicle. The maximum heat flux is discussed and it is shown this is in the order of 90 kW/m^2, with a duration of severe heating rates of about 500 s resulting in a heat load of >45 MJ/m^2.

---

[6] Lecture slides on: 'Stagnation Point Heating', *National Aeronautical and Space Administration*, `https://tfaws.nasa.gov/TFAWS12/Proceedings/Aerothermodynamics%20Course.pdf`, (accessed on April 24, 2020).

4.4. Trajectory model and implemented guidance

The trajectory model contains all the introduced flight phases, together with environmental effects and constraints. To let the vehicle perform the correct trajectory proper guidance is required. This section shows how the guidance is defined in the different phases of flight and how this is optimized to find the optimal trajectory. Important in the optimization hierarchy is the fact that only the ascent trajectory is optimized actively by the design variables. The return trajectory, however, is a mere result of the staging conditions and only the requirement of RTLS is implemented as an equality constraint.

4.4.1. Ascent

The design of the ascent trajectory of the launch vehicle is optimized in the MDO tool. As discussed in Chapter 3 a direct explicit optimal control method was selected for this study. The control law implemented is a parametric law. This was selected the most promising in the literature study (Haex, 2019) as Balesdent (2011) showed very promising results of this implementation. Furthermore, van Kesteren (2013a) showed that for a pull-up manoeuvre - within this study during the ascent of the first stage - a parametric control law is the most suited as with most other laws such as a polynomial function this pull-up manoeuvre cannot be implemented as easily.

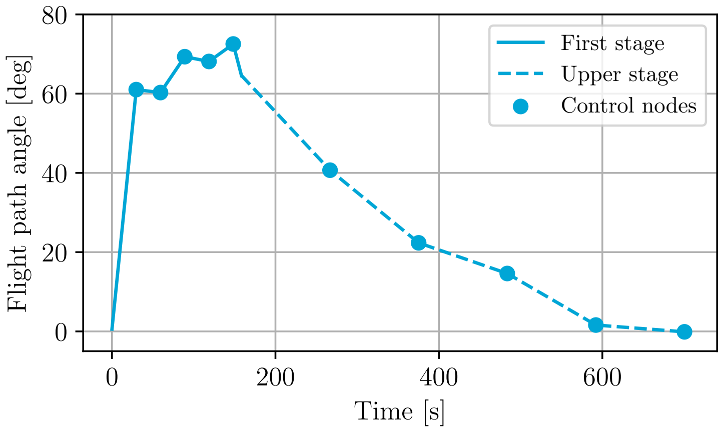

Figure 4.6: Example of an optimization result of the parametric control law determining the desired flight path angle profile for orbit injection

In Figure 4.6 an example of a result computed with this parametric control law is shown. The figure shows the control nodes, which are the optimised design variables. Both the first and upper stage ascent phase have five control nodes, which are positioned equally spaced over the burn time of each individual stage. The initial flight path angle of the first stage is part of the initial conditions, while the initial flight path angle of the upper stage is the resulting flight path angle after staging. By optimizing the value of each of these control nodes the desired flight path angle profile can be changed such that it results in the optimal trajectory. Interpolation between the flight path angles is done linearly in time.

To control the vehicle along the desired flight path angle profile the AoA is modulated. This is done by the following control law determining the AoA as:

$$\alpha = K_c(\gamma_{\text{des}} - \gamma) \tag{4.16}$$

in which (γ_{des},γ) are the desired and current flight path angle respectively and K_c is a gain factor. It was determined that the best performing control is achieved when using $K_c = 1.5$ for the first stage and $K_c = 5.0$ for the upper stage.

To examine the three dimensional trajectory of the ascent of the first stage also the bank angle is modulated. This is done with a threshold approach. The minimum altitude for this banking manoeuvre is defined and the vehicle is only allowed to bank above the threshold value in altitude. The bank manoeuvre itself is performed by a 40° bank, which is linearly levelled to 0° once the heading is changed towards the desired heading. This is summarized as (in degrees):

$$\begin{aligned} &\textbf{if } \mathbf{h} < \mathbf{h}_{\text{tres}} && \mu = 0 \\ &\textbf{if } |\Delta\chi| > \mathbf{9} \textbf{ and } \mathbf{h} > \mathbf{h}_{\text{tres}} && \mu = \pm 40 \\ &\textbf{if } |\Delta\chi| < \mathbf{9} \textbf{ and } \mathbf{h} > \mathbf{h}_{\text{tres}} && \mu = 40 \cdot \left(\chi - \chi_{\text{des}}\right)/9.0 \end{aligned} \tag{4.17}$$

in which (h,h_{tres}) is the current and threshold altitude respectively, μ is the bank angle and (χ,χ_{des}) is the current and desired heading angle respectively. This threshold altitude value is one of the parameters studied in this research.

4.4.2. Bearing angle

To return to the original spaceport the heading towards this spaceport is required. This can be determined by the so-called bearing angle. The bearing angle is the heading angle between an initial position and a final position, which can be computed based on the latitude and longitude of both positions. The bearing angle is used in both return methods to rotate back towards the spaceport. The following relations are implemented to determine the bearing angle χ_{sp} towards the spaceport:[7]

$$Y = \cos\delta_{\text{sp}} \sin(\tau_{\text{sp}} - \tau) \tag{4.18}$$

$$X = \cos\delta \sin\delta_{\text{sp}} - \sin\delta \cos\delta_{\text{sp}} \cos(\tau_{\text{sp}} - \tau) \tag{4.19}$$

$$\chi_{\text{sp}} = \text{atan2}(Y, X) \tag{4.20}$$

4.4.3. In-plane pitch over guidance

The in-plane pitch over manoeuvre can be divided into two distinct flight phases. The first being outside of the atmosphere containing the pitch and burn and the second being inside of the atmosphere containing the re-entry and glide back to the spaceport.

The pitch and burn is modelled two dimensionally, only modulating the AoA. The design of the trajectory is such that the burn is completely horizontal making the most efficient use of propellant for decreasing the horizontal component of the velocity, while using gravity to decelerate the vertical component. When the burn is long enough the horizontal component of the velocity can be reversed. The flight path angle, however, cannot increase above 90°, which means that during this reverse of velocity the heading angle flips sign. It is for this reason the AoA is defined in both these cases as (in degrees):

$$\begin{aligned} &\textbf{before heading sign flip} && \alpha = 180 - \gamma \\ &\textbf{after heading sign flip} && \alpha = -\gamma \end{aligned} \tag{4.21}$$

Initially after staging it takes time to rotate the vehicle in the right AoA orientation. This rotation time is modelled as well, assuming a rotational rate of 22.9 deg/s. The Attitude Control System itself, both in performance as well as in mass, is not modelled.

The second phase of the in-plane pitch over manoeuvre is the re-entry in the atmosphere. The AoA modulation during this re-entry is dependent on the Mach number M, similar to the Space Shuttle re-entry guidance (Harpold and Graves, 1978). This was not studied in detail and only a preliminary analysis was used to tune the AoA profile. It is tuned such that it is adequate in comparison to the Maddock et al. (2018) validation case (introduced in

---

[7] 'Formula to Find Bearing or Heading angle between two points: Latitude Longitude', *IGISMAP*, `https://www.igismap.com/formula-to-find-bearing-or-heading-angle-between-two-points-latitude-longitude/`, (accessed April 02, 2020).

Chapter 6) while being comparable to the Space Shuttle AoA law. Furthermore, gliding is done at the maximum lift-over-drag ratio. Combining this all result in the following AoA law as (in degrees):

$$\begin{aligned} &\textbf{if M > 10.0 or h > 40e3} && \alpha = 30 \\ &\textbf{if 1.0 < M < 10.0 and h < 40e3} && \alpha = 5 + 25 \cdot (M - 1.0)/9.0 \\ &\textbf{if M < 1.0 and h < 40e3} && \alpha = 8 \end{aligned} \tag{4.22}$$

To fly the three dimensional trajectory required for returning to the spaceport of launch also the bank angle is modulated. This is modelled as shown in Equation 4.17, with the only difference that in this case the threshold altitude is a maximum altitude of 40 km. If the vehicle is above this altitude, the vehicle is not allowed to bank. The desired heading is the bearing angle χ_{sp}.

4.4.4. Aeroturn guidance

The guidance of the aeroturn method has close resemblance with the guidance of the in-plane pitch over method. The AoA during re-entry is determined as shown in Equation 4.22, while the bank angle is modulated as shown in Equation 4.17 again with the bearing angle χ_{sp} as the desired heading and the same altitude threshold as in the in-plane pitch over manoeuvre.

The only difference is the return burn. This burn is performed once the first stage is rotated heading towards the spaceport and the flight path angle is positive again. If both is true the vehicle pitches up towards the burn flight path angle γ_{burn} by the same AoA law as during ascent, shown in Equation 4.16. This burn flight path angle is a design variable which is optimized in the outer optimization loop.

4.4.5. Glideback guidance

Glideback uses the same guidance as aeroturn, with the one difference that no return burn is applied once the vehicle is headed towards the spaceport of take-off.

4.4.6. Take-off roll

Very different to conventional launch vehicles is the fact that the vehicle in this study has a take-off roll on a runway.[8] It is determined that this take-off roll has a duration in the order of ~10% of the total burn time of the first stage, which cannot be neglected. To account for this take-off roll the propellant consumption to increase the velocity to the take-off velocity is determined. The initial velocity of the trajectory model is this take-off velocity and the resulting trajectory is computed taking into account this propellant loss. The following losses are included in the approximation of the propellant loss during the take-off roll:

- **Pressure loss** of the engines at sea level conditions
- **Aerodynamic loss** of the vehicle at sea level conditions and current velocity
- **Friction loss** of the vehicle for current mass

Figure 4.7: Runway 24 of Rotterdam The Hague Airport (see Footnote 8)

---

[8] Kleij, S. v.d., 'Ambitie Rotterdam The Hague Airport', *Rotterdam The Hague Airport*, `https://denhaag.raadsinformatie.nl/document/5887486/1/Presentatie_RTHA_door_S_van_der_Kleij`, (accessed April 02, 2020).

4.5. Environment models

During the ascent and return of the vehicle the environment has a great influence on the vehicle and the trajectory. The harsh environment is mainly existent due to the atmosphere, while big contributors to the losses in the trajectory are both the atmosphere and Earth's gravity field. To include these both elements in the trajectory model different environment models were studied in the literature research (Haex, 2019). The implemented models are shown.

4.5.1. Atmosphere model - The United States Standard Atmosphere 1976

In compliance with several other launch vehicle studies the implemented atmosphere model is the United States Standard Atmosphere 1976. This atmosphere model was first discussed by the COESA Working Group (1976) in 1976. The large benefit of this model is that it describes the atmosphere with good complexity, while being independent in both space and time. This latter is beneficial for comparison with other launch vehicle studies. The explanation on the model presented here is repeated from the literature study (Haex, 2019).

Two different altitudes are used in this model, being the geometric altitude Z and the geopotential altitude H. The geopotential altitude is a correction for the geometric height by using the variation of gravity with elevation. Below 86 km geometrical altitude, the lower layers of the atmosphere, eight layers are defined. The molecular temperature T_{M} of the atmosphere is given by:

$$T_{\mathrm{M}} = T_{\mathrm{M,b}} + L_{\mathrm{M,b}}(H - H_{\mathrm{b}}) \tag{4.23}$$

in which $T_{\mathrm{M,b}}$ is the molecular temperature in the lower bound of the corresponding layer b, $L_{\mathrm{M,b}}$ is the gradient in this layer b and $(H - H_{\mathrm{b}})$ is the difference between the current altitude and the altitude in the lower bound of this layer b. Both the reference heights H_{b} and temperature gradients $L_{\mathrm{M,b}}$ are shown in Table 4.1.

Layer (b)	H_{b} **[km]**	$L_{\mathrm{M,b}}$ **[K km^{-1}]**	p_{b} **[Pa]**
0	0	-6.5	101325
1	11	0	22632
2	20	1.0	5475
3	32	2.8	868
4	47	0	111
5	51	-2.8	79
6	71	-2.0	4
7	84.85	-6.5	4

Table 4.1: Reference heights, temperature gradients and pressures for the different layers of the United States Standard Atmosphere 1976 (Kesteren, 2013b)

Above 86 km geometrical altitude Equation 4.23 is no longer valid. The next layer (86 km - 91 km) defined is an isothermal layer with a temperature of 180.87 K. This is followed by a layer (91 km - 110 km) for which the temperature is described as:

$$T = T_{\mathrm{c}} - 76.32\sqrt{1 - \left(\frac{Z - Z_8}{-19.94}\right)^2} \tag{4.24}$$

where T_{c} is 263.19 K and Z_8 is 91 km. The temperature in the next layer (110 km - 120 km) is described by:

$$T = T_9 + 12(Z - Z_9) \tag{4.25}$$

with T_9 being 240 K and Z_9 being 110 km. The temperature in the final layer (120 km - 1000 km) is described by a set of equations as:

$$T = T_\infty - (T_\infty - T_{10})e^{-\lambda\xi} \tag{4.26}$$

$$\lambda = \frac{12}{T_\infty - T_{10}} \tag{4.27}$$

$$\xi = \frac{(Z - Z_{10})(r_0 + Z_{10})}{r_0 + Z} \tag{4.28}$$

where T_∞ is the exoatmospheric reference temperature (1000 K), Z_{10} is 120 km, T_{10} is 360 K and r_0 is 6356.76 km.

To compute the pressure the following relations are used. Below 86 km the pressure is calculated by:

$$p = p_\mathrm{b}\left(\frac{T_\mathrm{M,b}}{T_\mathrm{M,b} + L_\mathrm{M,b}(H - H_\mathrm{b})}\right)^{\left(\frac{g_0 M}{R^* L_\mathrm{M,b}}\right)} \tag{4.29}$$

in which R^* is the universal gas constant, M the mean molecular weight and p_b the pressure in the lower bound of the layer b (which is found in Table 4.1). The mean molecular weight M is constant up to 80 km altitude and varies for altitudes above 80 km. Values can be found in the document by the COESA Working Group (1976). The pressure for isothermal layers below 86 km is described as:

$$p = p_\mathrm{b}\left(\frac{-g_0 M(H - H_\mathrm{b})}{R_\mathrm{A} T_\mathrm{M,b}}\right) \tag{4.30}$$

Above 86 km the pressure is described based on the kinetic temperature T (as described by the geometric altitude Z) as:

$$p = \sum p_i = \sum n_i k T = \frac{\sum n_i R^* T}{N_\mathrm{A}} \tag{4.31}$$

with $\sum n_i$ being the sum of the number densities of the individual gas species comprising the atmosphere, k being the Boltzmann constant and N_A being Avogadro's constant.

The final parameter required is the air density. This is computed by using the perfect gas law as:

$$\rho = \frac{pM}{R^* T} \tag{4.32}$$

4.5.2. Gravity model - Newton's law of universal attraction

One of the most simple but powerful equations for computing the force by gravitational attraction is Newton's law of universal attraction, in three dimensions described as:

$$\vec{F}_\mathrm{B} = -G\frac{m_\mathrm{A} m_\mathrm{B}}{r_\mathrm{AB}^3}\vec{r}_\mathrm{AB} \tag{4.33}$$

with G being the universal gravitational constant, (m_A,m_B) being point masses (or homogeneous spheres) and $\vec{r}_\mathrm{AB}$ being the vector from A to B (Wakker, 2015). For a launch vehicle it is true that $m_\mathrm{veh} << m_\mathrm{E}$. Due to this the expression can be simplified in a form directly computing the gravitational acceleration as:

$$g(r) = \left|\frac{\vec{F}_\mathrm{G}}{m_\mathrm{veh}}\right| = \left|-G\frac{m_\mathrm{E}}{r^3}\vec{r}\right| \tag{4.34}$$

Due to the fact that the accelerations on the launch vehicle during ascent and return are orders of magnitude larger than the increase in precision that is achieved by implementing higher fidelity models, this is the most common implemented gravity model in launch vehicle trajectory studies. It is for this reason this is also the gravity model implemented in this study. Provoost, however, determined that for a similar study the difference in position at the end of launch between a gravity model assuming point mass and a gravity model including the J2-effect was in the order ~700 m.[9] In this study this is below the required precision of the numerical integrator. Hence this justifies that the point mass gravity field is applicable.

---

[9] Provoost, J., 'Personal discussion', *Delft University of Technology*, (discussed in April 2020).

5

Sizing of the vehicle and the estimation of corresponding performance

The vehicle model consists of a combination of the different disciplines representing all rudimentary involved subsystems in the design of a launch vehicle. To propel the vehicle an engine or set of engines is modelled by the propulsion model. For flight behaviour the aerodynamic properties are modelled by the aerodynamics model. Furthermore, the structure and the mass are scaled and sized in the geometry and mass model. Combined this results in a complete estimation of the size, mass and performance of the launch vehicle. All disciplines involved are presented in this chapter, in which it is shown how the models compute the required parameters and how this is parametrically defined to be implemented in the optimization tool.

5.1. Propulsion

The implementation of the propulsion model is primarily based on *Ideal Rocket Theory* (IRT), which consists of a set of equations used to estimate rocket engine performance based on several design parameters. This theory assumes both homogeneous and constant exhaust gases as well as the ideal gas law. The latter statement and all following equations on IRT are as found in the work of Zandbergen (2018).

5.1.1. Ideal Rocket Theory

In general the thrust of a rocket engine can be computed by using the Rocket Thrust Equation as:

$$F_\mathrm{T} = \dot{m}U_\mathrm{e} + (p_\mathrm{e} - p_\mathrm{a})A_\mathrm{e} = \dot{m}U_\mathrm{eq} = \dot{m}I_\mathrm{sp}g_0 \tag{5.1}$$

in which $\dot{m}$ is the mass flow, (U_e,U_eq) are the exhaust and equivalent exhaust velocity respectively, $(p_\mathrm{e} - p_\mathrm{a})A_\mathrm{e}$ is the pressure thrust based on the exhaust and ambient pressure difference as well as the nozzle exit area, I_sp is the specific impulse and g_0 is Earths gravitational acceleration.

With IRT this equation can be rewritten such that it forms a more direct relation to possible design parameters. The relations required for doing so are discussed. Two coefficients are defined, the first being the thrust coefficient C_F and the second the characteristic velocity c^*. Combined they are used to compute the specific impulse as:

$$I_\mathrm{sp} = \frac{C_\mathrm{F}c^*}{g_0} \tag{5.2}$$

The thrust coefficient is defined as follows, combining engine thrust F_T, chamber pressure p_c and throat area A_t:

$$C_\mathrm{F} = \frac{F_\mathrm{T}}{p_\mathrm{c}A_\mathrm{t}} \tag{5.3}$$

The Vandenkerckhove parameter Γ is defined as:

$$\Gamma = \sqrt{\gamma}\left(\frac{2}{\gamma+1}\right)^{\left(\frac{\gamma+1}{2(\gamma-1)}\right)} \tag{5.4}$$

with γ being the specific heat ratio. Combining the specific heat ratio and the Vandenkerckhove parameter, as well as the pressure term, the thrust coefficient can also be computed by:

$$C_{\mathrm{F}} = \Gamma \sqrt{\frac{2\gamma}{\gamma - 1}\left(1 - \left(\frac{p_{\mathrm{e}}}{p_{\mathrm{c}}}\right)^{\left(\frac{\gamma-1}{\gamma}\right)}\right)} + \left(\frac{p_{\mathrm{e}}}{p_{\mathrm{c}}} - \frac{p_{\mathrm{a}}}{p_{\mathrm{c}}}\right)\frac{A_e}{A_t} \tag{5.5}$$

Also for computing the characteristic velocity the Vandenkerckhove parameter is used together with properties from the thermo-chemical analysis as:

$$c^* = \frac{1}{\Gamma}\sqrt{\frac{R^*}{M}T_{\mathrm{c}}} \tag{5.6}$$

with R^* being the universal gas constant, M being the mean molar mass of the combustion products and T_{c} being the chamber temperature. By deriving the critical mass flow equation the characteristic velocity can also be computed based on the mass flow as:

$$c^* = \frac{p_{\mathrm{c}} A_{\mathrm{t}}}{\dot{m}} \tag{5.7}$$

A final equation worth mentioning is the relation between a certain pressure ratio and a certain area ratio as (e.g. throat and exit conditions):

$$\frac{A_{\mathrm{e}}}{A_{\mathrm{t}}} = \frac{\Gamma}{\sqrt{\frac{2\gamma}{\gamma-1}\left(\frac{p_{\mathrm{e}}}{p_{\mathrm{c}}}\right)^{\left(\frac{2}{\gamma}\right)}\left(1 - \left(\frac{p_{\mathrm{e}}}{p_{\mathrm{c}}}\right)^{\left(\frac{\gamma-1}{\gamma}\right)}\right)}} \tag{5.8}$$

It is important to realize that the theory shown assumes ideal conditions. To account for losses naturally occurring in any real system quality factors are used. The nozzle flow quality ζ_{n} is used on the thrust coefficient while the combustion quality ζ_{c} is used on the characteristic velocity. Multiplying both results in the propellant consumption quality ζ_{s} used on the specific impulse. Finally, due to high Reynolds numbers expected in the throat the discharge coefficient C_{d} is assumed unity. All combined results in the thrust quality factor ζ_{F} as:

$$\zeta_{\mathrm{F}} = \frac{F_{\mathrm{T,real}}}{F_{\mathrm{T,ideal}}} = \zeta_{\mathrm{s}} = \frac{I_{\mathrm{sp,real}}}{I_{\mathrm{sp,ideal}}} = \zeta_{\mathrm{n}}\zeta_{\mathrm{c}} \tag{5.9}$$

5.1.2. Thermo-chemistry

From the equations shown it is clear that for determining engine performance evaluations on the specific heat ratio γ, the mean molar mass M of the expelled gases and the chamber temperature T_{c} are required. These three parameters are a result of the chemical reactions taking place inside the engine due to the propellants getting burned.

In compliance with the work of Vandamme (2012) it is concluded that to compute these parameters for a set of propellants only the oxidizer-over-fuel ratio and the chamber pressure are required. In this study the choice of propellants is fixed, leaving the oxidizer-over-fuel ratio and the chamber pressure the only varying parameters. To include this in the analysis the program *Chemical Equilibrium with Applications* (CEA) is used.[1] This program was developed by NASA's Glenn Research Center to calculate both chemical equilibrium compositions as well as properties of complex mixtures. With the propellants specified, as well as by varying the oxidizer-over-fuel ratio and chamber pressure, all three parameters γ, M and T_{c} can be computed directly.

The implementation of this thermo-chemical analysis within the propulsion model is by the use of a two dimensional look-up-table, defined over a wide range of chamber pressures and oxidizer-over-fuel ratios. To do so a small C++ tool is used, identifying the correct values in the look-up-table and interpolating between these values. This tool was developed, validated and used in the work of Contant (2019). It was reconfirmed during this study that indeed the tool functions properly.

---

[1] 'Chemical Equilibrium with Applications', *NASA Glenn Research Center*, `https://www.grc.nasa.gov/WWW/CEAWeb/`, (accessed on October 7, 2019).

5.1.3. Propulsion model design variables

Reviewing the IRT equations in detail it is apparent that the equations can be approached from different sets of initial parameters, enabling for computing the remaining parameters. In this study the set of initial design variables was selected by the following reasoning. The first design variable is the mass flow as this roughly determines the size of the engine by the size of the throat. The second design variable used is the chamber pressure, as this dominantly influences the structural loading on the engine. Furthermore, chamber pressure is the main requirement on pump performance, where pump design is identified as one of the major challenges in the total engine design. The third design variable is the exit diameter of the nozzle, which shows the general radial dimensions of the engine and accounts for the pressure loss. Finally, this set is completed by the oxidizer-over-fuel ratio, required for the thermo-chemical analysis. The total input vector of the model is defined as follows:

$$X_{\text{eng}} = \left[\dot{m}, p_{\text{c}}, d_{\text{e}}, \frac{O}{F}\right]^{\text{T}} \tag{5.10}$$

5.2. Aerodynamics

The studied launch vehicle consists of two very different stages. The upper stage being a conventional rocket stage, while the first stage being a rocket propelled airplane. Due to this also the approach on the aerodynamic modelling is very different. First, the general equations used in the aerodynamics model are shown, after which both the implementation of the first stage as well as the implementation of the upper stage is shown.

5.2.1. Lift and drag

In general the lift and drag force can be normalized to a 3D lift and drag coefficient by:

$$C_{\text{L}} = \frac{L}{q_{\infty} S_{\text{ref}}} \tag{5.11}$$

and

$$C_{\text{D}} = \frac{D}{q_{\infty} S_{\text{ref}}} \tag{5.12}$$

in which (C_{L},C_{D}) are the 3D lift and drag coefficient respectively, q_{∞} the free-stream dynamic pressure ($\frac{1}{2}\rho_{\infty} V_{\infty}^2$) and S_{ref} the reference area of the vehicle (Weiland, 2014).

The great benefit of normalizing the lift and drag force is that for a certain geometry, independent of the size, these coefficients stay the same while the absolute lift and drag do change with size. Also smaller models, as long as the free flow conditions are simulated well, can be tested in small scale wind tunnel tests resulting in significant sets of coefficients. For this study another benefit is that by using normalized coefficients the aerodynamic behaviour can always be estimated independent of the stages becoming larger or smaller.

5.2.2. First stage - X-34 Advanced Technology Demonstrator

To simulate the aerodynamic behaviour of the first stage known wind tunnel test data is used. Figure 5.1 shows the original wind tunnel test data of the *X-34 Advanced Technology Demonstrator* (X-34) (Brauckmann, 1999). The data shows both the lift coefficient and drag coefficient at a range of *Angle of Attack* (AoA) for a set of Mach numbers. This can directly be implemented in the vehicle model. A main part of information lacking is the aerodynamic behaviour at larger AoAs. Weiland (2014) showed the lift coefficient of the vehicle at AoAs up to 40° for Mach numbers above 4.0. The drag coefficient in these conditions was, however, unknown, as well as lift coefficient for lower Mach numbers. Based on several vehicles it is concluded that for high Mach numbers the drag coefficient curve can be extrapolated linearly as a first order approximation (Weiland, 2014). The guidance model (see Chapter 4) ensures that in all occurring velocity conditions the AoA stays within a regime in which the aerodynamic data is known.

The reason of using known wind tunnel test data is the following. During the initial phase of this study the scope of the study was determined (Haex, 2019). It was estimated that the development of a parametric model computing the aerodynamic behaviour of a vehicle was outside of this scope due to the limited time budget of this study. A reference vehicle is assumed instead and the X-34 showed most applicability (Haex, 2019). The consequence of this assumption is that the geometry of the vehicle is determined and will not be optimized. The absolute size is

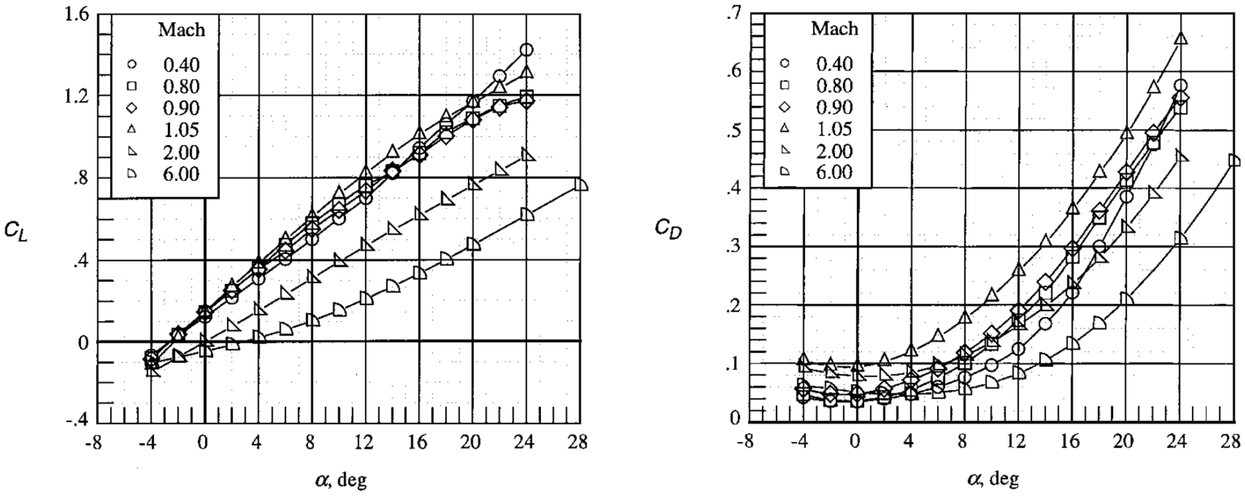

Figure 5.1: Test results of the X-34 Advanced Technology Demonstrator wind-tunnel test: 3D lift coefficient as a function of Angle of Attack (left) and 3D drag coefficient as a function of Angle of Attack (right) for a set of Mach numbers (Brauckmann, 1999)

still part of the optimization. The choice on the X-34 was made based on two criteria. The first was the fact that the X-34 shows the most resemblance with the envisioned *Dawn Aerospace Mk-III* (Mk-III). Furthermore, the fact that validated data is available was used as the second criterium.

5.2.3. Upper stage

One of the main requirements formulated by Dawn Aerospace is omitting the use of a fairing to prevent material re-entering the atmosphere in an uncontrolled manner. Due to the internal storage of the upper stage in the payload bay of the first stage this is possible, as in the dense layers of the atmosphere the upper stage is protected by the outer structure of the first stage. From a payload perspective this requirement means staging is only possible when the aerothermal flux is and stays below the industry standard of 1135 W/m^2.[2]

Within this study the same requirement is used and it is assessed what is the consequence of this requirement. Within these conditions the dynamic pressure has already reduced to a negligible amount. This means it is not required to model the aerodynamics (drag) of the upper stage. Of course when assessing the consequence of this requirement a comparison is made between a solution with and without this requirement. This means the model has to stay valid in terms of upper stage aerodynamics also in conditions with a higher dynamic pressure. In this case the upper stage is assumed a long cylinder. The lift is not modelled and the drag is modelled according to the drag coefficient of a long cylinder and the frontal area of the upper stage.[3]

5.3. Geometry and mass

Due to the strong coupling between the geometry of the vehicle and the mass estimation both are presented together in this section. Of course there is a large discrepancy between the lay-out and geometry of the upper stage when compared to the first stage. Still, some of the elements - such as the engine or the propellant tanks - show large resemblance in both stages as both contain common launch vehicle technology. It is for this reason first the upper stage is introduced with all conventional launch vehicle elements. Next, the elements for completion of the first stage model are shown. Note that, due to the assumption of the first stage aerodynamics, the first stage model is based on a reference vehicle. All parametric Mass Estimation Relationships are in SI-base units.

5.3.1. Upper stage

The upper stage model contains the elements shown in Table 5.1. The same table shows how the dry, wet and total mass are defined. To understand the upper stage model it is important to understand on which design variables it is dependent. The following input vector is used for the upper stage model:

---

[2] Industry standard e.g.: 'Vega User's Manual Issue 4 Revision 0', *Arianespace*, `https://www.arianespace.com/wp-content/uploads/2015/09/Vega-Users-Manual_Issue-04_April-2014.pdf`, (accessed on March 05, 2020).

[3] 'Drag of Cylinders and Cones', *Aerospaceweb*, `http://www.aerospaceweb.org/question/aerodynamics/q0231.shtml`, (accessed on March 05, 2020).

$$X_{\text{st,up}} = \left[X_{\text{eng,up}}, t_{\text{b}}, d_{\text{st,up}}\right]^{\text{T}} \tag{5.13}$$

in which $X_{\text{eng,up}}$ determines the upper stage engine, t_{b} is the total burn time of the upper stage and $d_{\text{st,up}}$ is the upper stage diameter. Within the engine model the mass flow is known, which combined with the total burn time results in the total propellant consumption. This can be used to determine the total propellant volume, as well as the amount of fuel and oxidizer based on the oxidizer-over-fuel ratio. Combined with information on the payload (mass and dimensions) this is enough to determine the length of the upper stage and estimate all elements shown in Table 5.1.

Upper stage	**Elements**	**Elements**	**Elements**
Dry mass	**Wet mass (+)**	**Total mass (+)**	
	Engine	Fuel	Payload
	Thrust structure	Oxidizer	
	Propellant tank(s)		
	Pressurant		
	Pressurant tank		
	Valves		
	Avionics		
	Payload adapter		

Table 5.1: Upper stage geometry and mass estimation elements

Engine and thrust structure

The mass estimation of the engine is based on the work of Zandbergen (2015). The following equation was proposed estimating the mass of the engine m_{eng} based on the thrust force as:

$$m_{\text{eng}} = 1.104 \cdot 10^{-3} F_{\text{T}} + 27.702 \tag{5.14}$$

The validity range of this equation was defined between 15 kN and 8 MN, which is expected to be just sufficient for this study as rather small engines are expected. Furthermore, the same work contained two relations estimating the length l_{eng} and diameter d_{eng} of the engine as:

$$l_{\text{eng}} = 0.1362 F_{\text{T}}^{0.2279} \tag{5.15}$$

$$d_{\text{eng}} = 0.0455 F_{\text{T}}^{0.2745} \tag{5.16}$$

both valid in the same thrust force range. The thrust structure mass m_{tstr} estimation implemented was presented by Akin:[4]

$$m_{\text{tstr}} = 2.55 \cdot 10^{-4} F_{\text{T}} \tag{5.17}$$

Propellant tank(s)

The mass estimation of the propellant tanks consists of several different steps. First the fuel mass m_{fuel} and oxidizer mass m_{oxi} are determined based on the total propellant mass m_{prop} as:

$$m_{\text{oxi}} = \frac{O/F \cdot m_{\text{prop}}}{O/F + 1} \tag{5.18}$$

$$m_{\text{fuel}} = \frac{m_{\text{prop}}}{O/F + 1} \tag{5.19}$$

Next, with the fuel and oxidizer density the fuel volume V_{fuel} and oxidizer volume V_{oxi} can be determined, which are both increased by a defined ullage fraction.

---

[4] Akin, D., Lecture slides on: 'Mass Estimating Relations', *University of Maryland*, `https://spacecraft.ssl.umd.edu/academics/791S16/791S16L08.MERsx.pdf`, (accessed on January 13, 2020).

It is known that within tank design spherical tanks are always lighter than cylindrical tanks, due to a more efficient stress distribution. Due to this reason the following step is to determine if it is possible to have two separate spherical tanks, large enough to fit the required fuel and oxidizer volume within the diameter of the upper stage. If the diameter allows for this configuration the shell mass of the tanks $m_{\mathrm{t,shell}}$ is determined by (Zandbergen, 2018):

$$m_{\mathrm{t,shell}} = 1.5\frac{\rho_{\mathrm{t}}}{\sigma_{\mathrm{t}}}V_{\mathrm{t}}p_{\mathrm{t}} \tag{5.20}$$

in which ρ_{t} is the density of the tank material, σ_{t} is the ultimate load strength of the tank material, V_{t} is the volume of the tank and p_{t} is the pressure in the tank. For feasibility, based on the minimum design thickness of the tank material, it is reviewed if the tank meets the minimal thickness requirement. If this is not the case, the mass is increased to meet the minimum thickness requirement. To find the total tank mass m_{t} a shell-to-tank correction factor K_{t} is used (1.2-2.5 (Zandbergen, 2018)) as:

$$m_{\mathrm{t}} = K_{\mathrm{t}}m_{\mathrm{t,shell}} \tag{5.21}$$

The total length l_{t} of this spherical tank system is now determined by:

$$l_{\mathrm{t}} = d_{\mathrm{t,oxi}} + d_{\mathrm{t,fuel}} \tag{5.22}$$

If the diameter of the upper stage does not allow for spherical tanks a common bulkhead design is selected. First a cylindrical oxidizer tank is designed. The thickness required for this tank is computed by the pressure in the tank and reviewed to be above the minimum design thickness as (Zandbergen, 2018):

$$t_{\mathrm{t}} = \frac{p_{\mathrm{t}}d_{\mathrm{st,up}}}{2\sigma_{\mathrm{t}}} \tag{5.23}$$

Next, the dimensions of the tank are determined. The cylindrical tank consists out of two spherical caps connected by a cylindrical middle piece with length $l_{\mathrm{mid,oxi}}$. This length is determined based on the required oxidizer volume V_{oxi}. With this length and the known geometry the mass $m_{\mathrm{t,oxi}}$ of the cylindrical oxidizer tank is determined by:

$$m_{\mathrm{t,oxi}} = \left(\pi d_{\mathrm{st,up}}^2 + \pi d_{\mathrm{st,up}}l_{\mathrm{mid,oxi}}\right)t_{\mathrm{t}}\rho_{\mathrm{t}} \tag{5.24}$$

On top of this tank the fuel tank is constructed. Due to similar pressure the thickness is the same. As the bulkhead is shared the only extra volume arises from a cylindrical middle piece with length $l_{\mathrm{mid,fuel}}$. Again based on the length and geometry the mass $m_{\mathrm{t,fuel}}$ of the fuel tank is computed by:

$$m_{\mathrm{t,fuel}} = \left(0.5\pi d_{\mathrm{st,up}}^2 + \pi d_{\mathrm{st,up}}l_{\mathrm{mid,fuel}}\right)t_{\mathrm{t}}\rho_{\mathrm{t}} \tag{5.25}$$

The total common bulkhead tank shell mass $m_{\mathrm{t,shell}}$, with length l_{t}, is the combination of both the fuel and oxidizer tank shell mass as:

$$m_{\mathrm{t,shell}} = m_{\mathrm{t,oxi}} + m_{\mathrm{t,fuel}} \tag{5.26}$$

$$l_{\mathrm{t}} = l_{\mathrm{mid,oxi}} + l_{\mathrm{mid,fuel}} + d_{\mathrm{st,up}} \tag{5.27}$$

Also for the common bulkhead tank the shell-to-tank correction factor is used to determine the total tank mass as shown in Equation 5.21.

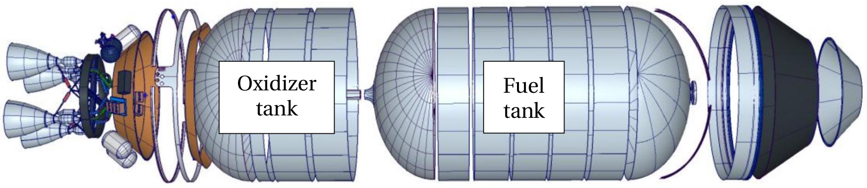

Figure 5.2: Common bulkhead tank design on the Advanced Common Evolved Stage (adapted image from (Zegler and Kutter, 2010))

Pressurant and pressurant tank

To keep the tanks under pressure during the release of propellant a pressurant gas is required. The amount of pressurant gas m_{pres} is determined based on the propellant tanks pressures, volumes and temperatures and properties of the pressurant gas as well as the initial pressurant pressure $p_{\text{pres,i}}$ as shown by Zandbergen (2018):

$$m_{\text{pres}} = \frac{p_t V_t}{(R^* / M_{\text{pres}}) T_t} \left[\frac{\gamma_{\text{pres}}}{1 - (p_t / p_{\text{pres,i}})} \right] \tag{5.28}$$

The required volume V_{pres} is computed by:

$$V_{\text{pres}} = \frac{m_{\text{pres}} (R^* / M_{\text{pres}}) T_t}{p_{\text{pres,i}}} \tag{5.29}$$

The pressurant gas is distributed between several small spherical tanks. This is done to make designing within the limited volume around the engine (common for upper stages) easier, while no mass penalty is occurring for such a measure. The mass of the tanks is estimated as shown in Equation 5.20 and 5.21, again with an ullage fraction included.

Valves, avionics and payload adapter

The mass of the valves m_{valves} is estimated by a mass estimation relationship proposed by Schlingloff (2005) as:

$$m_{\text{valves}} = 0.0268 \left(\frac{F_T p_c}{1 \cdot 10^8} \right)^{0.71} \tag{5.30}$$

The mass of the avionics is estimated by a constant mass. This approach is chosen as for these small launch systems all available mass estimation relationships overestimate the avionics mass tremendously, while not enough data points are available for an own developed mass estimation relationship. Instead known information on the avionics mass of the Rocket Lab's Electron rocket is used.[5] As the Electron rocket uses electric pump fed engines, large battery packs are available also for powering the avionics. Avionics batteries have to be included in the mass estimation. For this the mass of the batteries of the Agena upper stage is used as a reference case (LMSC Space Systems Division, 1972).

Part of the payload adapter mass m_{adap} is estimated by the following mass estimation relationship as proposed by Castellini (2012) based on the payload mass m_{pay} as:

$$m_{\text{adap}} = 0.004775 m_{\text{pay}}^{1.0132} \tag{5.31}$$

Of course this adapter needs mounting on top of the spherical end cap of the tank. This is done in a similar fashion as the Agena upper stage frame. A profile is constructed based on the diameter of the frame and the minimum design thickness. With this profile a circular frame is constructed, supported by several legs. The mass of this frame is added to the mass of the payload adapter.

Lay-out and dimensions

In Figure 5.3 the complete lay-out of the upper stage is shown. With the diameter of the upper stage known the length of the upper stage is determined as follows. As shown in Figure 5.3 the configuration of the upper stage is oriented around the propellant tanks. Directly underneath these tanks the engine is mounted, while on top the payload is attached. The pressurant tanks are mounted around the chamber and nozzle, while the avionics and batteries are mounted on top of the propellant tanks in the free space between the payload adapter and the top end cap. This means the dry length $l_{\text{up,dry}}$ and total length $l_{\text{up,total}}$ of the upper stage are determined as follows, with the total length being especially important for internal storage in the first stage (which includes the payload):

$$l_{\text{up,dry}} = l_t + l_{\text{eng}} \tag{5.32}$$

$$l_{\text{up,total}} = l_{\text{up,dry}} + l_{\text{pay}} \tag{5.33}$$

---

[5] Szondy, D., '"World's first battery-powered rocket" readied for launch', *New Atlas*, https://newatlas.com/electron-rocket-batery-satellite-launch-vehicle/37060/, (accessed on January 07, 2020).

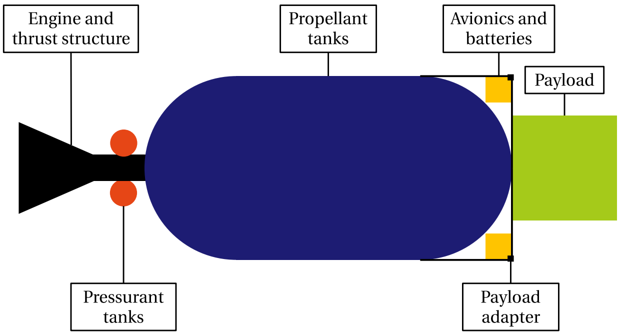

Figure 5.3: Schematic of the complete lay-out of the upper stage

5.3.2. First stage

Table 5.2 shows the elements that are included in the first stage model based on the X-34. The following input vector is used for initializing the first stage:

$$X_{\text{st,first}} = \left[X_{\text{eng,first}}, n_{\text{eng}}, t_{\text{b}}, n_{\text{eng,bb}}, t_{\text{b,bb}}, l_{\text{up,total}}, d_{\text{st,up}}, m_{\text{up,total}}\right]^{\text{T}} \tag{5.34}$$

$X_{\text{eng,first}}$ determines the first stage engine, while a certain amount n_{eng} of engines is installed on the first stage. The total propellant consumption is determined by two phases of flight. The first is the ascent phase with all engines running and burn time t_{b}. The second is the boostback phase in which a certain amount $n_{\text{eng,bb}}$ of the engines is running for the boostback burn time $t_{\text{b,bb}}$. Furthermore, the design of the first stage is also dependent on the upper stage including the payload. The result of the upper stage model in length, diameter and mass form the final input parameters in the input vector of the first stage.

First stage	**Elements**	**Elements**	**Elements**
Dry mass	**Wet mass (+)**	**Total mass (+)**	
	Engine(s)	Fuel	Upper stage
	Thrust structure	Oxidizer	
	Propellant tank(s)		
	Pressurant		
	Pressurant tank		
	Valves		
	Avionics		
	Nose		
	Fuselage		
	Payload bay		
	Wing		
	Tail		
	Landing gear		

Table 5.2: First stage geometry and mass estimation elements

Conventional elements

Most of the conventional elements already introduced in the upper stage section are also used in the design of the first stage. A short elaboration on the implementation is given.

The engine performance of the first stage is computed in a similar fashion as the performance of the upper stage, with the difference that a multiple n_{eng} of engines is installed on the first stage. This influences the total mass flow directly and by that the propellant consumption. Furthermore, the design estimates the propellant consumption of the boostback period, in which a selected amount of engines $n_{\text{eng,bb}}$ thrust with burn time $t_{\text{b,bb}}$. This is added to compute the total propellant consumption. The mass and dimensions of the engines, as well as the mass of the thrust structure, are determined in a similar manner as the upper stage engine dimensions.

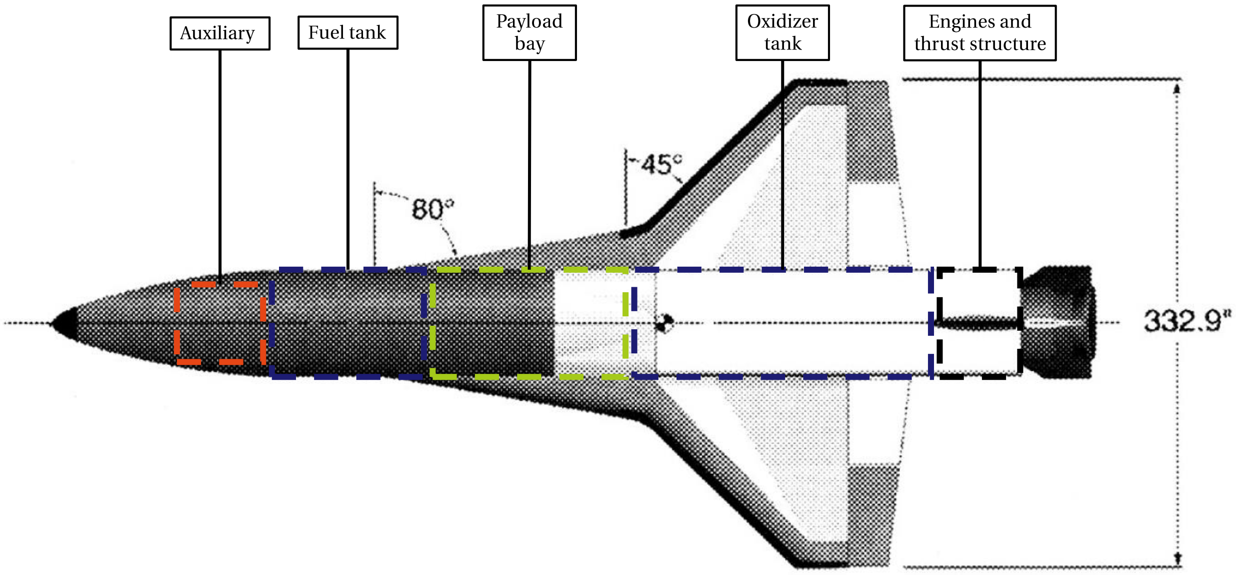

Figure 5.4: Schematic of the complete lay-out of the first stage (adapted image from (Weiland, 2014))

Two propellant tanks are installed in the first stage, one for the fuel and one for the oxidizer. Similarly as for the upper stage tanks first it is determined if it is possible to use a spherical tank. When this is the case a spherical tank is designed, taking into account a minimum design thickness and an ullage fraction. If a spherical tank is not possible, a cylindrical tank is designed again taking into account minimum design thickness and an ullage fraction.

The mass of the pressurant, pressurant tanks, valves and avionics are determined identical to the approach of the upper stage. For the avionics the battery mass is increased as the power demand is higher, for example for the actuation of control surfaces and the retraction and extension of the landing gear.

Fuselage diameter

The next step in the design of the first stage is to scale the vehicle in absolute dimensions. As the geometry is determined completely beforehand scaling one dimension is enough to scale the whole vehicle. For this the diameter of the fuselage is used. Figure 5.4 shows the geometry of the X-34. The main fuselage is used for storing several of the subsystem elements. The upper stage and payload are stored internally, the propellant tanks are stored in the fuselage, the pressurant tanks and avionics are installed in the nose and the engines are integrated in the back. As the volume and dimensions of these elements are known, this is used to scale the vehicle.

Figure 5.4 is used to determine that the straight part of the fuselage (without the tapered nose and engine) has a length-over-diameter ratio of 844/118. This straight part houses the upper stage, the main propellant tanks and the engines. To find the minimum diameter suited for housing all the elements an iterative loop is used to determine this diameter. Taking into account the fact that both propellant tanks have spherical end caps, the total available propellant volume V_{prop} can be determined based on the fuselage diameter d_{fus} as:

$$V_{\text{prop}} = \frac{\pi}{4} d_{\text{fus}}^2 \left(\left[\frac{844}{118} - 2 \right] d_{\text{fus}} - l_{\text{up,total}} - 2 l_{\text{chamb}} \right) + \frac{2\pi}{6} d_{\text{fus}}^3 \tag{5.35}$$

In the iterative loop the diameter is increased from the upper stage diameter to a diameter suited for housing the required propellant volume. Note that for the installation of the engine the chamber length l_{chamb} is used. This is determined in the propulsion model based on the throat area, characteristic length and the engine design length-over-diameter. It is assumed, based on several engines, that twice this length is enough to have proper housing while the nozzle is allowed to extent outside of the fuselage.

Nose and fuselage

Both the nose and the fuselage are modelled as a layer of composite with minimum design thickness, as due to the large radius this results in a strong and stiff structure. The area of the nose is determined, based on the geometry in Figure 5.4, by:

$$A_{\text{nose}} = \frac{2\pi}{3} d_{\text{fus}} \sqrt{\frac{125}{36} d_{\text{fus}}^2} + \frac{\pi}{18} d_{\text{fus}}^2 \tag{5.36}$$

The area of the fuselage depends on the construction of the vehicle. If the tank diameter of one of the propellant tanks is smaller than the fuselage diameter, the fuselage is constructed fully around the tank. If the tank diameter is as large as the fuselage diameter, the cylindrical outside of the tank functions as the fuselage. For the bottom this is not possible due to the square shape of the bottom fuselage. Hence a square shaped fuselage is always added. The spherical end caps of the tanks are also covered fully by the fuselage, as well as the engine chambers and corresponding thrust structure.

Payload bay

The payload bay is constructed as a middle section behind the fuel tank and before the oxidizer tank. It is expected that the centre of gravity of the full vehicle is behind this payload bay, due to the large oxidizer mass. Based on this assumption all elements in front of the payload bay are carried by the payload bay. As the upper half of this bay is swinging doors, the lower part is an open load carrying construction of which the thickness is determined based on the occurring stresses of both the normal acceleration and the bending moment during lateral acceleration. The stress due to the maximum normal acceleration is determined by:

$$\sigma_{\text{n}} = \frac{F}{A} = \frac{\sum m_{\text{elem}} a_{\text{max,norm}}}{\frac{\pi}{2} d_{\text{fus}} t_{\text{pbay,low}}} \tag{5.37}$$

$$\sum m_{\text{elem}} = m_{\text{nose}} + m_{\text{avionics}} + m_{\text{pres}} + m_{\text{t,pres}} + m_{\text{fuel}} + m_{\text{t,fuel}} + m_{\text{fus}} + m_{\text{up,total}} \tag{5.38}$$

The stress by the bending moment, based on the maximum lateral acceleration, is determined as:

$$\sigma_{\text{b}} = \frac{My}{I} = \frac{M_{\text{max}}}{\frac{\pi}{8} d_{\text{fus}}^2 t_{\text{pbay,low}}} \tag{5.39}$$

$$\begin{aligned} M_{\text{max}} = {} & a_{\text{max,lat}} \left(m_{\text{nose}} + m_{\text{avionics}} + m_{\text{pres}} + m_{\text{t,pres}} \right) \left(l_{\text{up,total}} + l_{\text{t,fuel}} + d_{\text{fus}} \right) \\ & + a_{\text{max,lat}} \left(m_{\text{fuel}} + m_{\text{t,fuel}} + m_{\text{fus}} \right) \left(l_{\text{up,total}} + 0.5 l_{\text{t,fuel}} \right) \\ & + a_{\text{max,lat}} \left(m_{\text{up,total}} \right) \left(0.5 l_{\text{up,total}} \right) \end{aligned} \tag{5.40}$$

in which it is assumed the maximum bending moment occurs at the root of the payload bay. The total stress is now determined by the following equation, which is used in an iterative loop to find the sufficient thickness of the lower payload bay keeping the stress below the maximum allowable stress:

$$\sigma_{\text{tot}} = \sigma_{\text{n}} + \sigma_{\text{b}} \tag{5.41}$$

The upper half of the payload bay is modelled by the area and the minimum design thickness of the composite material.

Wing, tail and landing gear

The mass of the wing, tail and landing gear are determined by simple parametric mass estimation relationships. The equations for the wing and tail are deliberately chosen to be based on a crude statistical approach, as proposed by Raymer (1992), for preliminary fighter jet design studies. The following equations are implemented:

$$m_{\text{wing}} = 43.9418 S_{\text{w}} \tag{5.42}$$

$$m_{\text{tail}} = 25.8769 S_{\text{vt}} \tag{5.43}$$

One of the implications of the proposed estimation is that when increasing the size of the vehicle the mass of the wings scales with the second power, while total vehicle mass scales with the third power. No validity range is given for these equations. The validity range is derived based on the assumption that it is valid in the approximate

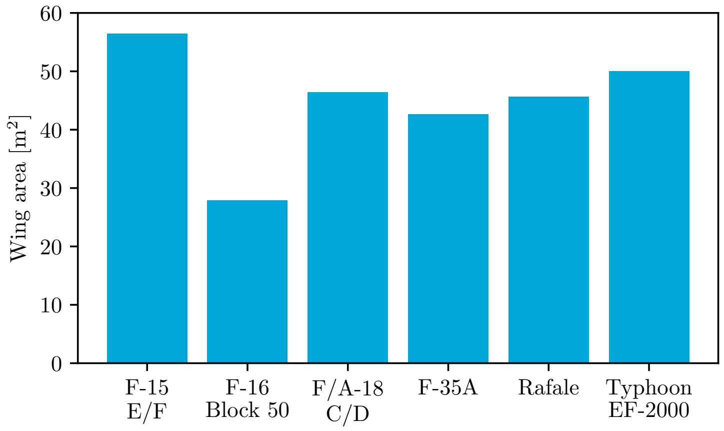

Figure 5.5: Wing area of several fighter jets (see Footnote 6, 7, 8, 9, 10, 11)

range of fighter wing areas as shown in Figure 5.5.[6,7,8,9,10,11] If the wing area of the vehicle becomes larger than the defined range the following correction factor on mass is used based on the wing area S_{wing} and the upper limit of the validity range $S_{\text{bound,up}}$:

$$K_{\text{wing}} = \sqrt{\frac{S_{\text{wing}}}{S_{\text{bound,up}}}} \tag{5.44}$$

The mass of the landing gear is estimated by an equation for spacecraft as proposed by Tsuchiya and Mori (2004) being:

$$m_{\text{gear}} = 0.0101\, m_{\text{GTOW}}^{1.124} \tag{5.45}$$

---

[6] Pike, J., 'F-15 Eagle', *Global Security*, https://www.globalsecurity.org/military/systems/aircraft/f-15-specs.htm, (accessed on February 28, 2020).

[7] Pike, J., 'F-16 Fighting Falcon', *Global Security*, https://www.globalsecurity.org/military/systems/aircraft/f-16-specs.htm, (accessed on February 28, 2020).

[8] 'F/A-18 Hornet', *FAS Military Analysis Network*, https://fas.org/man/dod-101/sys/ac/f-18.htm, (accessed on February 28, 2020).

[9] Pike, J., 'F-35 Joint Strike Fighter (JSF) Lightning II', *Global Security*, https://www.globalsecurity.org/military/systems/aircraft/f-35-specs.htm, (accessed on February 28, 2020).

[10] Palt, K., 'Dassault Rafale', *FlugzeugInfo*, http://www.flugzeuginfo.net/acdata_php/acdata_rafale_en.php, (accessed on February 28, 2020).

[11] Pike, J., 'Eurofighter Typhoon EF-2000 - Specifications', *Global Security*, https://www.globalsecurity.org/military/world/europe/eurofighter-specs.htm, (accessed on February 28, 2020).

6

The integration and validation of the Multidisciplinary Design Optimization tool

The latter two chapters discussed the trajectory and vehicle model, both primary building blocks in the total numerical model. However, to use the numerical model as a tool for answering to the *Primary Research Question* (PRQ) and *Primary Sub-Questions* (PSQs) it is important to merge the two building blocks into one optimization tool. The *Multidisciplinary Design Optimization* (MDO) tool is able of both optimizing the vehicle and trajectory design. Now that the required theory on MDO and numerical modelling is discussed (see Chapter 3) and the two major building blocks of the model are finalized (see Chapter 4 and 5) the final step is integrating this into an MDO tool used for optimising the System in the different scenarios.

This chapter shows how the MDO tool is integrated and validated. First, the software environment in which the tool is developed is discussed. This is followed by a presentation of the structure of the MDO tool, also examining the way in which the fitness and constraints are defined in the optimizer. It is important to validate that the individual elements of the numerical model as well as the integrated MDO tool estimate the behaviour of the System within a defined error margin. A validation procedure is executed to show that the results of the model indeed estimate the behaviour accurately. This chapter concludes on this validation procedure, first of the vehicle model and second of the trajectory model, and shows the validation results of individual elements of the numerical model as well as of the integrated MDO tool. This validation procedure is also used to estimate the value of several constant configurations within the model.

6.1. Integration of the vehicle model and trajectory model into a Multidisciplinary Design Optimization tool

The MDO tool used for the numerical research is developed in a C++ environment. This enables for the use of the *TU Delft Astrodynamics Toolbox* (Tudat), a powerful set of C++ libraries developed for astrodynamics and space research.[1] First Tudat is introduced, followed by a presentation of the numerical model structure and implementation of the fitness and constraints.

6.1.1. TU Delft Astrodynamics Toolbox

The main libraries used in the development of the MDO tool are found in Tudat. Tudat is a set of libraries developed for astrodynamics research. The libraries are developed to be used in a C++ environment.

Using Tudat enables for a rapid development of any space or astrodynamics related simulation, as most of the numerical aspects and environmental models of the simulation are implemented and validated. A lot of challenges arising from the numerical implementation of these kind of simulations were systematically tackled by developing powerful functions. Furthermore, the Pagmo library (see Footnote 2 in Chapter 3) is implemented in Tudat, which allows for implementing a variety of optimization algorithms directly.

---

[1] 'TU Delft Astrodynamics Toolbox', *Delft University of Technology*, `https://tudat.tudelft.nl/`, (accessed on May 13, 2020).

In the MDO tool this means that for example the computation of all accelerations, as well as propagating and integrating them, is done by Tudat libraries. With these libraries also the correct gravity and atmosphere models can be used directly. Also the transformations between reference frames and state variables and the track of dependent and independent model variables is done by Tudat libraries. All these examples show the benefit of using Tudat for creating a powerful simulator framework.

6.1.2. Structure of the Multidisciplinary Optimization Tool

The structure of the MDO tool is shown in Figure 6.1. This figure shows the inner structure, which contains the problem that in the iterative process is optimized by the optimization algorithm. The design input vector, containing all design variables, is initialized in every iteration. By using the fitness value the optimizer tries to converge to better performing solutions. Furthermore, the figure shows that for some parts of the tool to function also tabulated data is used in the model.

In a top level settings file used for initializing the optimization process the following settings can be adjusted:

- **Optimization goal:** Choose between 'trajectory only' or 'full MDO'
- **Return method:** Choose between 'glideback', 'in-plane pitch over' or 'aeroturn'
- **Target injection:** Define the desired altitude and eccentricity
- **Constraint settings:** Turn constraint settings on or off
- **Tabulated data:** Select the desired tabulated data files
- **Optimization structure:** Define the population size, output frequency and a final generation
- **Numerical integrator:** Define the integrator tolerance
- **Run specification:** Define the name of the specific optimization run for saving

With this initialization complete the tool is able to optimize the problem. First, the vehicle is constructed by the vehicle model. The correct design variables are used together with the corresponding tabulated data. To determine engine performance the engine configuration file is used, inputting the engine quality. Furthermore, the correct thermo-chemistry file, according to propellant selection, is read for use in the *Ideal Rocket Theory* (IRT) model. For estimating the geometry and mass of the upper and first stage configurations files are used, which are the main source for propellant density, tank temperature and pressure, material choice, construction thickness, pressurant selection and ullage fractions. Finally, for completion of the first stage aerodynamics model the wind tunnel test data of the *X-34 Advanced Technology Demonstrator* (X-34) is retrieved from tabulated data files.

The completed vehicle is used in the trajectory model for computing the resulting trajectory. The final design variables used are for the ascent guidance of both the first and upper stage. This is determined by the control nodes and the coasting time of the upper stage. Furthermore, the initial conditions of flight, being the take-off velocity, direction and position are imported and also is the location of the spaceport. It is important to realize that the model functions in a way in which the take-off loss required for gaining the take-off velocity is computed before the simulation. The simulation is started once this is accomplished. This results in the simulation time being the time of actual flight, not including the take-off roll. The end condition of the first stage after ascent is both the initial condition of the upper stage trajectory model as well as of the first stage return model.

Fitness definition and constraint handling

The goal of the optimizer is to minimize total vehicle dry mass, while also guaranteeing meeting all requirements and constraints. The optimization is performed by a heuristic optimization algorithm. To guarantee constraint compliance the constraints have to be defined as a part of the fitness value based on dry mass. This has the following reason. The selection was made on a single objective optimizer, minimizing only dry mass. The heuristic algorithm, which has no mathematical understanding of the model, also has no understanding of the requirements and constraints. The only decision making implemented is based on the fitness value. To create a design space forcing the solution into constraint compliance a threshold approach is used on the constraints. If a constraint is met nothing happens to the fitness value. However, if a constraint is not met, a penalty is added on top of the fitness. This means that a solution without any constraint violations has a more optimal fitness value and in that way forces the optimizer to converge into constraint compliance.

It was found that the optimizer behaves best when a constraint hierarchy is used. In the MDO tool first the resulting vehicle is computed. A vehicle violating the constraints is assigned the largest penalty. It was found especially

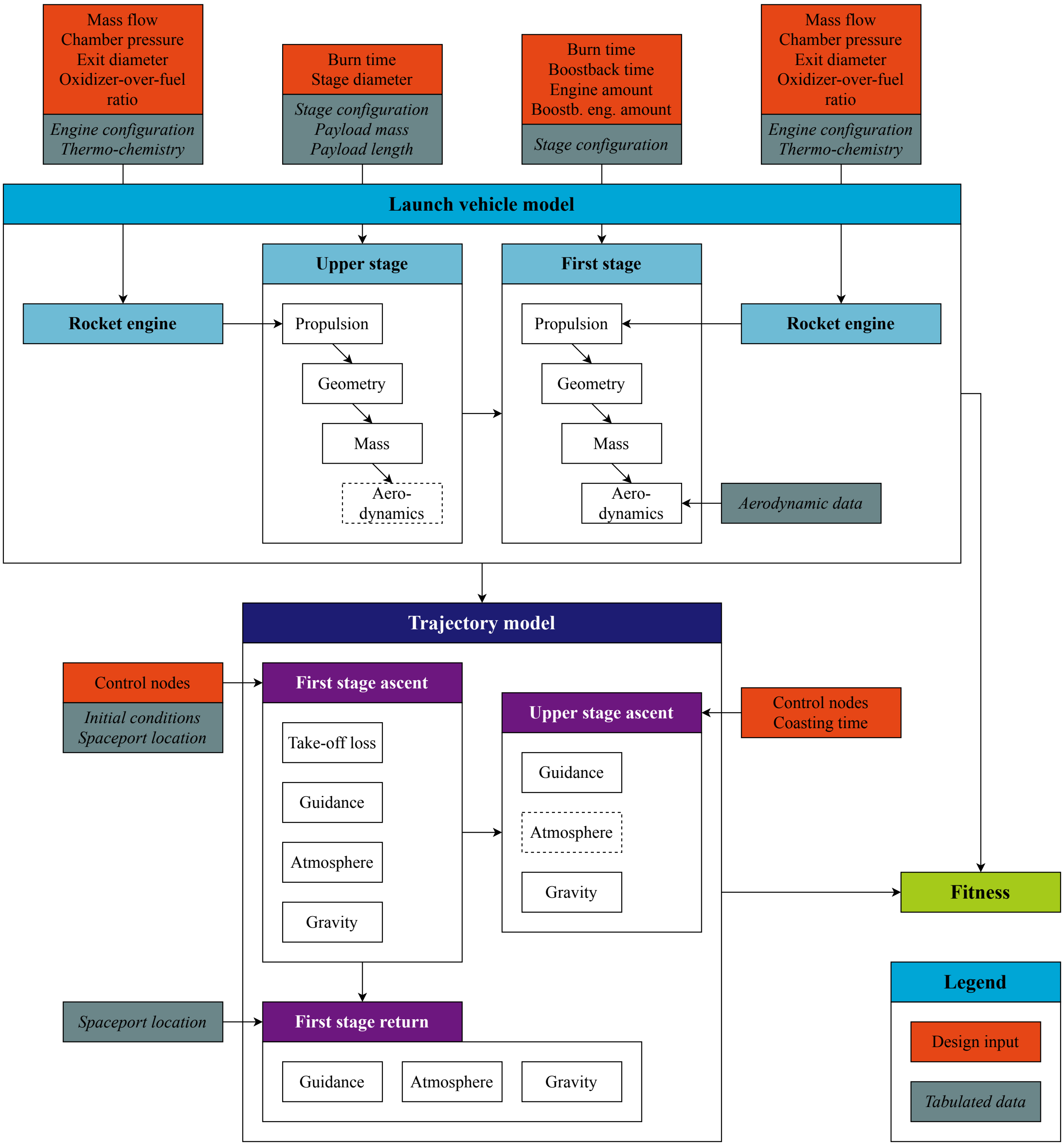
Mass flow
Chamber pressure
Exit diameter
Oxidizer-over-fuel ratio
Engine configuration
Thermo-chemistry
Burn time
Stage diameter
Stage configuration
Payload mass
Payload length
Burn time
Boostback time
Engine amount
Boostb. eng. amount
Stage configuration
Mass flow
Chamber pressure
Exit diameter
Oxidizer-over-fuel ratio
Engine configuration
Thermo-chemistry
Launch vehicle model
Upper stage
First stage
Rocket engine
Propulsion
Geometry
Mass
Aero-dynamics
Propulsion
Geometry
Mass
Aero-dynamics
Rocket engine
Aerodynamic data
Trajectory model
Control nodes
Initial conditions
Spaceport location
First stage ascent
Take-off loss
Guidance
Atmosphere
Gravity
Upper stage ascent
Guidance
Atmosphere
Gravity
Control nodes
Coasting time
Fitness
Spaceport location
First stage return
Guidance
Atmosphere
Gravity
Legend
Design input
Tabulated data

Figure 6.1: Inner structure of the Multidisciplinary Design Optimization tool in which the design input is optimized by the optimization algorithm increasing the fitness of the solution

important to constraint the minimum theoretical velocity increase of the vehicle, as the algorithm had a tendency of converging to the lightest solution not at all being able to reach orbit. Furthermore, the minimum and maximum acceleration of the vehicle are implemented as vehicle constraints, as well as the maximum size of the upper stage.

The trajectory constraints, next in the hierarchy of constraint violations, are implemented with a reduced penalty value. Injection of the payload into orbit is the most prominent requirement for the System. However, the implementation of the orbital fitness is the only constraint that is not implemented by a threshold approach and for this reason is discussed separately. The only orbital penalty implemented is for solutions which are extremely far off the target orbit. This immediately results in the largest trajectory penalty. Other constraints on the trajectory that are implemented by a smaller trajectory penalty value are the return of the first stage, the maximum bending stress on the first stage, the *Angle of Attack* (AoA) of both the first and upper stage and the aerothermal flux on the upper stage. Compliance to these constraints is determined by an iterative analysis of the solution.

For meeting the orbital injection constraint a threshold approach is not enough for forcing the solution into a compliant region. Instead a penalty gradient has to be defined which creates a path towards optimal solutions. This is still defined as a constraint. Thus the optimizer is single objective (not a trade-off between mass and orbital fitness). However, in practice this penalty is never minimized to zero, as small deviations on the required orbital injection do always occur. The resulting orbital fitness penalty $p_{\text{orb,b}}$ for solutions below the target altitude is defined based on the pericenter altitude and the eccentricity of the orbit as:

$$p_{\text{orb,b}} = 5 \cdot \left(30 \cdot |r_{\text{peri,true}} - r_{\text{peri,tar}}| + 1 \cdot 10^8 \cdot |e_{\text{true}} - e_{\text{tar}}|\right) \tag{6.1}$$

For solutions above the desired target altitude the resulting orbital fitness penalty $p_{\text{orb,a}}$ is defined as:

$$p_{\text{orb,a}} = 30 \cdot |r_{\text{peri,true}} - r_{\text{peri,tar}}| + 1 \cdot 10^8 \cdot |e_{\text{true}} - e_{\text{tar}}| \tag{6.2}$$

The described threshold on orbital fitness is used when the true injection of the orbit differs too much with the target injection. If the eccentricity difference is more than 0.10 the solution is immediately penalized. The same is true for a pericenter difference of more than 4000 km.

The fitness of the solution itself is based on the total dry mass of the vehicle, multiplied by a factor to scale the value such that it performs well in combination with the orbital penalty gradient. The following fitness $f_{\text{m,dry}}$ is implemented:

$$f_{\text{m,dry}} = 1500 m_{\text{tot,dry}} \tag{6.3}$$

6.2. Vehicle model validation

In the validation procedure of the vehicle model the different models used inside the vehicle model are validated. First, the validation of the propulsion model is shown. This model is used both in the first and upper stage model. Secondly, the geometry and mass validation of the upper stage is discussed. Thirdly, the validation of the geometry and mass model of the first stage is presented. The aerodynamics model is not validated, assuming that the referenced wind tunnel data was validated before it was published while the implementation was validated during the development of Tudat.

6.2.1. Propulsion validation

The propulsion model is validated by comparing the result of the model to known engine performance data of existing rocket engines. First the comparison with several *Liquid oxygen* (LOX)/*Rocket Propellant-1* (RP-1) engines is shown, followed by the comparison with a hydrogen peroxide/kerosene engine. As discussed in Chapter 5 the model is implemented assuming ideal conditions. The determination of a representative propellant consumption quality factor and thrust quality factor follow from the validation procedure, which is discussed.

The validation procedure is as follows. For all validation cases the four input variables of the engine model are retrieved from independent sources. With these variables the resulting performance is computed in the model, which is compared to known performance data of these engines again retrieved from independent sources. Based on this comparison the quality factors, which account for both inaccuracies in the model and natural losses occurring in any real system, are computed for both sea level and vacuum conditions.

LOX/RP-1

The performance of the following LOX/RP-1 engines is computed using a characteristic length of 1.0 m (Soller et al., 2005).

The SpaceX Merlin-1D engine is the first LOX/RP-1 engine used for validation. Table 6.1 shows the validation data of this engine, containing both the input parameters as well as the performance data.[2] Furthermore, this table shows the computed result of the model, as well as the determined quality factors. The similar thrust and propellant consumption quality factor show that indeed the discharge coefficient is unity. The total combination of inaccuracy and losses is 6.6% for vacuum conditions and 7.0% for sea level conditions.

---

[2] Brügge, N., 'Evolution of the SpaceX Merlin-1 engine (and parameter)', *Spacerockets*, `http://www.b14643.de/Spacerockets_2/United_States_1/Falcon-9/Merlin/index.htm`, (accessed on January 09, 2020).

Merlin-1D			
Validation data (input)		**Quality factors**	
$\dot{m}$ **[kg/s]**	236.6	$\zeta_{\mathrm{F,vac}}$ [-]	0.934
p_{c} **[MPa]**	9.72	$\zeta_{\mathrm{F,SL}}$ [-]	0.930
d_{e} **[m]**	1.071	$\zeta_{\mathrm{s,vac}}$ [-]	0.934
O/F [-]	2.34	$\zeta_{\mathrm{s,SL}}$ [-]	0.930
Validation data (performance)		**Model result**	
$F_{\mathrm{T,vac}}$ **[kN]**	742.41	$F_{\mathrm{T,vac}}$ **[kN]**	794.78
$F_{\mathrm{T,SL}}$ **[kN]**	654.33	$F_{\mathrm{T,SL}}$ **[kN]**	703.50
$I_{\mathrm{sp,vac}}$ **[s]**	320	$I_{\mathrm{sp,vac}}$ **[s]**	342.54
$I_{\mathrm{sp,SL}}$ **[s]**	282	$I_{\mathrm{sp,SL}}$ **[s]**	303.20

Table 6.1: Validation data, model result and quality factors of the Merlin-1D engine (see Footnote 2)

Next, the Rocketdyne H-1 engine is used as a validation case. The validation data as well as the computed result of the model and the corresponding quality factors are shown in Table 6.2.[3,4,5] The mass flow is derived from the sea level specific impulse and the sea level thrust. The difference between the model and known performance in vacuum conditions is 9.9%, while this difference is 5.7% for sea level conditions.

H-1			
Validation data (input)		**Quality factors**	
$\dot{m}$ **[kg/s]**	353.44*	$\zeta_{\mathrm{F,vac}}$ [-]	0.901
p_{c} **[MPa]**	4.826	$\zeta_{\mathrm{F,SL}}$ [-]	0.944
d_{e} **[m]**	1.494	$\zeta_{\mathrm{s,vac}}$ [-]	-
O/F [-]	2.23	$\zeta_{\mathrm{s,SL}}$ [-]	0.943
Validation data (performance)		**Model result**	
$F_{\mathrm{T,vac}}$ **[kN]**	1030.25	$F_{\mathrm{T,vac}}$ **[kN]**	1144.02
$F_{\mathrm{T,SL}}$ **[kN]**	911.88	$F_{\mathrm{T,SL}}$ **[kN]**	966.40
$I_{\mathrm{sp,vac}}$ **[s]**	-	$I_{\mathrm{sp,vac}}$ **[s]**	330.38
$I_{\mathrm{sp,SL}}$ **[s]**	263	$I_{\mathrm{sp,SL}}$ **[s]**	279.01

Table 6.2: Validation data, model result and quality factors of the H-1 engine (see Footnote 3, 4, 5) - *(*) Derived value*

Due to the small payload (and by that small engine) in this study it is interesting to also compare the model to a small rocket engine designed for this same purpose. For this reason the Rocket Lab Rutherford engine is used as a final LOX/RP-1 validation case. This engine is especially developed for the small satellite launcher Electron and operates in a totally different regime of mass flow and thrust.[6] Challenging is the fact that due to the commercial motive of the company not much detailed information on the engine design is known. This means the validation data is partly derived. The exit area is determined by the thrust difference in vacuum and sea level conditions, assuming the peak thrust mentioned is indeed the vacuum thrust. Combined with the specific impulse, assumed being the vacuum specific impulse, the mass flow is determined. The chamber pressure is unknown and set to 50 bar, a reasonable pressure assuming that electrical pumps have limited operating pressure. Also the O/F-ratio is unknown and set to an average value found for other LOX/RP-1 engines. Both the validation data as well as the

---

[3] 'H-1 engine', *National Aeronautics and Space Administration*, https://history.nasa.gov/MHR-5/Images/fig392.jpg, (accessed on January 09, 2020).

[4] 'Rocketdyne H-1', *Purdue University*, https://engineering.purdue.edu/~propulsi/propulsion/rockets/liquids/h1.html, (accessed on January 09, 2020).

[5] Braeunig, R., 'Saturn', *Rocket & Space Technology*, http://www.braeunig.us/space/specs/saturn.htm, (accessed on January 09, 2020).

[6] 'Electron', *Rocket Lab*, https://www.rocketlabusa.com/electron/, (accessed on January 09, 2020).

results of the model and the quality factors are shown in Table 6.3. The difference found in vacuum conditions is 8.2%, while in sea level conditions this is 9.5%.

Rutherford			
Validation data (input)		**Quality factors**	
$\dot{m}$ **[kg/s]**	7.176*	$\zeta_{\mathrm{F,vac}}$ [-]	0.918
p_{c} **[MPa]**	5*	$\zeta_{\mathrm{F,SL}}$ [-]	0.905
d_{e} **[m]**	0.205*	$\zeta_{\mathrm{s,vac}}$ [-]	0.918
O/F [-]	2.3*	$\zeta_{\mathrm{s,SL}}$ [-]	-
Validation data (performance)		**Model result**	
$F_{\mathrm{T,vac}}$ **[kN]**	21.33	$F_{\mathrm{T,vac}}$ **[kN]**	23.23
$F_{\mathrm{T,SL}}$ **[kN]**	18	$F_{\mathrm{T,SL}}$ **[kN]**	19.90
$I_{\mathrm{sp,vac}}$ **[s]**	303	$I_{\mathrm{sp,vac}}$ **[s]**	330.07
$I_{\mathrm{sp,SL}}$ **[s]**	-	$I_{\mathrm{sp,SL}}$ **[s]**	282.75

Table 6.3: Validation data, model result and quality factors of the Rutherford engine (see Footnote 6) - *(*) Derived value*

Hydrogen peroxide/kerosene

The data on hydrogen peroxide/kerosene engines is sparse and of mediocre quality. Due to the propellant choice within this study, however, the comparison is relevant. The Gamma 8 engine, developed by Bristol Siddeley, was developed for this propellant combination. The validation data is shown in Table 6.4, although it is unclear which purity of hydrogen peroxide was used.[7] It is for this reason the corresponding results of the model and the quality factors, shown in Table 6.5, are computed for several levels of hydrogen peroxide purity. Both the mass flow and the exit diameter are derived, based on the specific impulse and thrust of both exit conditions. The characteristic length used is 1.07 m (Jo et al., 2011). For the different purity levels of hydrogen peroxide the difference between the model and the validation data changes. Over the regime of hydrogen peroxide purity levels the difference varies between 0% and 1.6% for both exit conditions.

Gamma 8			
Validation data (input)		**Validation data (performance)**	
$\dot{m}$ **[kg/s]**	90.32*	$F_{\mathrm{T,vac}}$ **[kN]**	234.80
p_{c} **[MPa]**	4.740	$F_{\mathrm{T,SL}}$ **[kN]**	222.40
d_{e} **[m]**	0.395*	$I_{\mathrm{sp,vac}}$ **[s]**	265
O/F [-]	8.2	$I_{\mathrm{sp,SL}}$ **[s]**	251

Table 6.4: Validation data of the Gamma 8 engine (see Footnote 7) - *(*) Derived value*

Gamma 8					
Model result 90% pure		**Model result 95% pure**		**Model result 98% pure**	
$F_{\mathrm{T,vac}}$ **[kN]**	234.90	$F_{\mathrm{T,vac}}$ **[kN]**	237.19	$F_{\mathrm{T,vac}}$ **[kN]**	238.39
$F_{\mathrm{T,SL}}$ **[kN]**	222.50	$F_{\mathrm{T,SL}}$ **[kN]**	224.79	$F_{\mathrm{T,SL}}$ **[kN]**	225.99
$I_{\mathrm{sp,vac}}$ **[s]**	265.20	$I_{\mathrm{sp,vac}}$ **[s]**	267.78	$I_{\mathrm{sp,vac}}$ **[s]**	269.14
$I_{\mathrm{sp,SL}}$ **[s]**	251.20	$I_{\mathrm{sp,SL}}$ **[s]**	253.78	$I_{\mathrm{sp,SL}}$ **[s]**	255.14
Quality factors 90% pure		**Quality factors 95% pure**		**Quality factors 98% pure**	
$\zeta_{\mathrm{F,vac}}$ [-]	1.000	$\zeta_{\mathrm{F,vac}}$ [-]	0.990	$\zeta_{\mathrm{F,vac}}$ [-]	0.985
$\zeta_{\mathrm{F,SL}}$ [-]	1.000	$\zeta_{\mathrm{F,SL}}$ [-]	0.989	$\zeta_{\mathrm{F,SL}}$ [-]	0.984
$\zeta_{\mathrm{s,vac}}$ [-]	0.999	$\zeta_{\mathrm{s,vac}}$ [-]	0.990	$\zeta_{\mathrm{s,vac}}$ [-]	0.985
$I_{\mathrm{sp,SL}}$ **[s]**	0.999	$I_{\mathrm{sp,SL}}$ **[s]**	0.989	$I_{\mathrm{sp,SL}}$ **[s]**	0.984

Table 6.5: Model results and quality factors of the Gamma 8 engine

---

[7] Wade, M., 'Gamma 8', *Astronautix*, `http://www.astronautix.com/g/gamma8.html`, (accessed on January 10, 2020).

Discussion on the engine validation result and the implemented quality factors

To determine if the performance of the model is as expected and to quantify what magnitude of the quality factors can be implemented in the study it is important to position the shown validation results in the framework of loss analysis. Table 6.6 shows for the different quality factors applicable in this study what the corresponding range of magnitude is, found in the research of both Huzel and Huang (1971) and Sutton and Biblarz (2001). Based on the validation result it is apparent that the discharge coefficient indeed can be assumed unity. The result of this is that in this study the thrust quality and propellant consumption quality are the same.

Huzel and Huang			**Sutton and Biblarz**		
	Thrust quality [-]	0.92-1.00		Thrust quality [-]	0.92-1.00
	Propellant consumption quality [-]	0.85-0.98		Propellant consumption quality [-]	0.85-0.99

Table 6.6: Comparison of the range of quality factors found in different studies (Huzel and Huang, 1971)(Sutton and Biblarz, 2001)

The comparison between the results of the validation cases and the data found in literature shows that the majority of the cases is indeed within the expected range. However, not within this range is the performance estimation of the Rutherford engine, of which the thrust quality is about 0.2-1.5% below the expected range. It is assumed that this difference is mainly caused by the uncertainty on the validation input data.

When comparing the computed quality factors of the Gamma 8 engine to the expected range, it shows that the quality factors found in the model are on the high side of the spectrum or outside of the boundaries specified (depending on the reference used). It is not expected that this high performance was actually met in the design. More likely is the fact that unreliability in the data and the unknown purity of the oxidizer results in a overestimation of the engine performance.

To conclude on the engine model first of all it is shown that for most validation cases the result is within the expected range. Furthermore, when deviating outside of this range the differences do stay within 1.5%. Based on this it is concluded that the IRT model is implemented correctly. Furthermore, the actual performance of the model is primarily dependent on the selection of the quality factors, as this has a drastic impact on the final thrust and specific impulse for a certain engine. Due to the spread within the validation data it is decided to be on the conservative side of the spectrum. As both the thrust and propellant consumption quality are the same an **engine quality factor** of **0.92** is selected. This is the lower bound of the thrust quality range while being in the average domain of the propellant consumption quality range.

6.2.2. Upper stage geometry and mass validation

The upper stage geometry and mass model is validated by comparing the result of the model to upper stages with an independent set of input parameters and validation data. A selection of two upper stages is made primarily based on the propellant combination (non-solid and partly non-cryogenic) and the availability of data. The first validation case is the upper stage of the Electron rocket, very useful in comparison as both in payload range, material choice and production techniques large similarities do exist between the Electron upper stage and the proposed Mk-III upper stage. Parts of the model are dependent on several constant design parameters and physical properties shown in Table 6.7 (Zandbergen, 2018).[8]

Constants								
	ρ_{oxi} **[kg/m^3]**	1141	K_{t} **[-]**	1.85	$n_{\text{t,pres}}$ **[bar]**	4	**Ullage tank [%]**	10
	ρ_{fuel} **[kg/m^3]**	733	$\rho_{\text{cc,t}}$ **[kg/m^3]**	1600	$p_{\text{t,pres}}$ **[bar]**	200	**Ullage pres. [%]**	10
	$p_{\text{t,prop}}$ **[bar]**	3	$\sigma_{\text{cc,t}}$ **[MPa]**	850	M_{pres} **[u]**	4		
	$T_{\text{t,pres}}$ **[K]**	90.2	$t_{\text{min,t}}$ **[mm]**	3	γ_{pres} **[-]**	1.66		

Table 6.7: Constant design parameters and physical properties of a carbon composite LOX/RP-1 rocket stage (Zandbergen, 2018)(see Footnote 8)

Both the validation input parameters and the validation data are shown in Table 6.8 and the result of the model is compared to this validation data.[9] One large discrepancy is the difference in length of the upper stage. This is due to the definition within in the validation data. The validation data only contains the length of the tanks (as the engine is in the interstage construction during launch), while the computed result includes the payload adapter as well as the length of the engine itself.

---

[8] 'Mechanical Properties of Carbon Fibre Composite Materials, Fibre / Epoxy resin (120°C Cure)', *Performance Composites*, `http://www.performance-composites.com/carbonfibre/mechanicalproperties_2.asp`, (accessed on January 10, 2020).

Electron upper stage						
	Validation data (input)					
		$\dot{m}$ **[kg/s]**	6.936*	t_b **[s]**	310	
		p_c **[MPa]**	5*	$d_{st,up}$ **[m]**	1.2	
		d_e **[m]**	0.455*	m_{pay} **[kg]**	275	
		O/F **[-]**	2.3*	l_{pay} **[m]**	1	
	Validation data (performance)			**Model result**		**Difference**
		$m_{up,dry}$ **[kg]**	250	$m_{up,dry}$ **[kg]**	241.87	-3.252%
		$m_{up,wet}$ **[kg]**	2400	$m_{up,wet}$ **[kg]**	2392.03	-0.332%
		$m_{up,total}$ **[kg]**	2675	$m_{up,total}$ **[kg]**	2667.03	-0.298%
		$l_{up,dry}$ **[m]**	2.4	$l_{up,dry}$ **[m]**	3.882	61.750%
		$l_{up,total}$ **[m]**	-	$l_{up,total}$ **[m]**	4.882	-
		F_T **[kN]**	22	F_T **[kN]**	22.709	3.223%
		I_{sp} **[s]**	333	I_{sp} **[s]**	333.868	0.261%
		ΔV **[m/s]**	5319.24	ΔV **[m/s]**	5372.59	1.003%

Table 6.8: Electron upper stage validation case (see Footnote 9) - *(*) Derived value*

A second validation case is the Blok D upper stage developed by the Russians in the mid 1960's. Not all information is known in great detail, but the information available combined with derivations and assumptions results in the following validation case.[10,11] One of the large unknowns is the material selection used for constructing this upper stage. Based on the time period and the application it is assumed this is probably some kind of high performing aluminium alloy.[12,13] Table 6.9 shows the material properties used which are the only changed constants as compared to Table 6.7.

Changed constants			
	$\rho_{Al-Li,t}$ **[kg/m^3]**	$\sigma_{Al-Li,t}$ **[MPa]**	$t_{min,Al-Li}$ **[mm]**
	2850	450	5

Table 6.9: Changed constant design parameters and physical properties as compared to Table 6.7 (see Footnote 12, 13)

The results of the validation case are shown in Table 6.10. It is important to realize that the Blok D contained several subsystems, such as a stage casing and ullage motors, which are not present nor modelled in the upper stage model of this study. To ensure proper comparison between the validation data and the model the validation data is adjusted such that it shows the upper stage geometry and mass without these subsystems.

---

[9] 'Electron', *Spaceflight101*, `http://spaceflight101.com/spacerockets/electron/`, (accessed on January 10, 2020).

[10] Clark, P., 'The 'Block D' and 'Block DM' rocket stages', *Wayback Machine*, `https://web.archive.org/web/20120716190506/http://www.friends-partners.org/oldfriends/jgreen/blockd.html`, (accessed on January 13, 2020).

[11] Wade, M., 'RD-58M', *Astronautix*, `http://www.astronautix.com/r/rd-58m.html`, (accessed on January 13, 2020).

[12] 'Aluminium 2219-T81', *ASM Aerospace Specification Metals*, `http://asm.matweb.com/search/SpecificMaterial.asp?bassnum=MA2219T81`, (accessed on January 13, 2020).

[13] 'Minimum shell thickness', *ADR Book*, `https://adrbook.com/en/2017/ADR/6.8.2.1.17`, (accessed in January 13, 2020).

Blok D						
Validation data (input)						
	$\dot{m}$ **[kg/s]**	24.615		t_b **[s]**	600	
	p_c **[MPa]**	7.75		$d_{st,up}$ **[m]**	3.7	
	d_e **[m]**	1.17		m_{pay} **[kg]**	20000	
	O/F **[-]**	2.3		l_{pay} **[m]**	3	
Validation data (performance)			**Model result**			**Difference**
	$m_{up,dry}$ **[kg]**	1860		$m_{up,dry}$ **[kg]**	1703.91	-8.392%
	$m_{up,wet}$ **[kg]**	16660		$m_{up,wet}$ **[kg]**	16472.9	-1.123%
	$m_{up,total}$ **[kg]**	36660		$m_{up,total}$ **[kg]**	36472.9	-0.510%
	$l_{up,dry}$ **[m]**	5.37		$l_{up,dry}$ **[m]**	6.81	26.816%
	$l_{up,total}$ **[m]**	-		$l_{up,total}$ **[m]**	9.81	-
	F_T **[kN]**	85		F_T **[kN]**	84.105	-1.053%
	I_{sp} **[s]**	352		I_{sp} **[s]**	348.419	-1.017%
	ΔV [m/s]	1785.36		**ΔV [m/s]**	1773.60	-0.659%

Table 6.10: Blok D validation case (see Footnote 10, 11)

Discussion on the upper stage validation result

The main parameter of interest in the validation of the model is ΔV. The resulting ΔV capability of a certain upper stage primarily determines the performance of this upper stage, independent of the mass itself. This being said of course the two are strongly connected, as for a known propellant amount and engine performance the mass shall be estimated correctly in order to let the ΔV budget compare. During the development of the MDO tool it was deemed that inaccuracies in ΔV, resulting from assumptions or implementations, in the order of ~100 m/s are acceptable. The combination between mass estimation and engine performance, resulting in the estimated ΔV budget of both validation upper stages is well within this limit.

However, a trend that is observed is the underestimation of the dry mass of the upper stage. Especially for the Blok D validation case this is significant, being almost 8.5% underestimation. This is considered acceptable, as due to the engine performance being slightly underestimated the performance in ΔV is showed within the defined accuracy. For the Electron upper stage engine performance is not underestimated. Although in this case the combination of dry mass estimation and performance also results in an acceptable ΔV performance. Thus this is considered accurate enough as well.

6.2.3. First stage geometry and mass validation

Validation of the first stage model is a difficult task due to the very innovative nature of the vehicle. No comparing vehicles did ever meet an operational state nor proper flight models were developed. To show that the estimation of the model is representative as a first stage vehicle several validation steps are performed. First, it is analyzed how the conventional rocket elements of the first stage model compare to a real first stage. Next, within the framework of two large studies on winged launch vehicles the mass budget of the total vehicle model is assessed.

Conventional rocket elements

The first step in the validation procedure of the first stage model analyses the conventional rocket elements. To do so, the masses of all conventional subsystems in the first stage model are combined and this is compared to the Electron first stage. The subsystems included are the engines, thrust structure, propellant tanks, pressurant and pressurant tanks, valves, avionics, nose and the fuselage. The upper stage of this launch vehicle was already computed (Table 6.8) and this is part of the input of the first stage model. Table 6.11 shows the comparison between the model and the Electron validation data. Both the first and upper stage use the same engine, only differing in exit diameter. All constants are as shown in Table 6.7. An important result is the fact that the dry mass is overestimated with more than 10%. However, due to dependencies in the model, both on the upper stage as well as the propellant consumption of the first stage and the engine performance estimation, this overestimation of dry mass results in a slight underestimation of the total first stage ΔV budget.

Electron first stage						
	Validation data (input)					
		$n_{\text{eng,first}}$ **[-]**	9	$t_{\text{b,first}}$ **[s]**	152	
		$\dot{m}$ **[kg/s]**	6.936*	$t_{\text{b,up}}$ **[s]**	310	
		p_{c} **[MPa]**	5*	$d_{\text{st,up}}$ **[m]**	1.2	
		$d_{\text{e,first}}$ **[m]**	0.205*	m_{pay} **[kg]**	275	
		$d_{\text{e,up}}$ **[m]**	0.455*	l_{pay} **[m]**	1	
		O/F **[-]**	2.3*			
	Validation data (performance)			**Model result**		**Difference**
		$m_{\text{first,dry}}$ **[kg]**	950	$m_{\text{first,dry}}$ **[kg]**	1056.11	11.169%
		$m_{\text{first,wet}}$ **[kg]**	10200	$m_{\text{first,wet}}$ **[kg]**	10544.56	3.378%
		$m_{\text{first,total}}$ **[kg]**	12835	$m_{\text{first,total}}$ **[kg]**	13211.59	2.934%
		$F_{\text{T,vac}}$ **[kN]**	192	$F_{\text{T,vac}}$ **[kN]**	186.422	-2.905%
		$I_{\text{sp,vac}}$ **[s]**	303	$I_{\text{sp,vac}}$ **[s]**	304.525	0.503%
		$F_{\text{T,SL}}$ **[kN]**	162	$F_{\text{T,SL}}$ **[kN]**	158.73	-2.019%
		$I_{\text{sp,SL}}$ **[s]**	-	$I_{\text{sp,SL}}$ **[s]**	259.290	-
		$\Delta\mathbf{V}_{\text{vac}}$ **[m/s]**	3791.09	$\Delta\mathbf{V}_{\text{vac}}$ **[m/s]**	3783.61	-0.197%

Table 6.11: Conventional rocket elements compared to the Electron first stage (see Footnote 6, 9) - *(*) Derived value*

Spaceplane with wings, tail and landing gear

The second step in the validation procedure focusses on the total first stage. Due to a lack of comparing vehicles developed beyond a conceptual stage, rather, large studies conducted by a combination of industrial parties and universities are consulted. Both studies, the first on the Aurora launch vehicle (Kopp et al., 2018) and the second by Maddock et al. (2018) , were introduced in Chapter 1. Figure 6.2 and 6.3 show the mass breakdown of the optimized vehicles found in these studies. The fraction of dry mass compared to *Gross Take-Off Weight* (GTOW) is shown, as well as the propellant and payload fraction. The payload of the first stage is defined as the total upper stage mass, including the orbital payload and the propellant (see Table 5.1). For the Aurora study, however, being a semi-Single Stage to Orbit, the upper stage is not mentioned. Hence this is not included in this figure. It is due to this the payload fraction of the first stage in the study by Maddock et al. (2018) is much larger than the payload fraction found the Aurora launch vehicle study. Furthermore, the absolute mass of the payload is much larger in the Aurora study, resulting in a much larger GTOW. From an operational perspective though the Aurora is more comparable, both taking off and landing at sea level altitude, however, supported during launch by a magnetic track. This in contrast to the study by Maddock et al. (2018), which is an air-launched vehicle.

To compare the mass fraction result of the first stage model to these launch vehicle studies first the Electron validation case is used. With the same input parameters as in the previous section now the total first stage vehicle mass is computed. This is shown in Figure 6.4 and 6.5. Interesting also is to show how the mass fraction evolves for larger vehicles. To determine this two more cases are computed, one with the doubled amount of mass flow and the third with the tripled amount, shown in Figure 6.6 to 6.9. The total result of wing, tail and landing gear mass and fractions is summarized in Table 6.13.

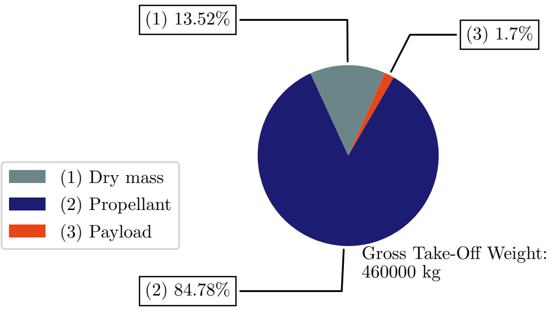

Figure 6.2: Aurora-R1 total mass breakdown (Kopp et al., 2018)

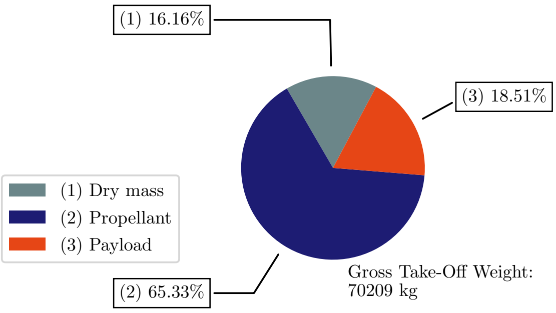

Figure 6.3: Maddock et al. (2018) total mass breakdown

In this study a hydrogen peroxide/kerosene launcher is studied with a totally different oxidizer-over-fuel ratio. Furthermore, from preliminary optimization runs done to explore the design space it was found that the expected diameter of the upper stage is larger than the one of the Electron launch vehicle. To show the validity of the model under these circumstances a general hydrogen peroxide/kerosene launcher is used as a second validation case. The input parameters are shown in Table 6.12 and were determined based on these preliminary optimization runs. Similar as to the Electron validation case also for this vehicle three different mass flows are selected to show the behaviour of the mass fractions over a range of vehicle size. The results of this validation case are shown in Figure 6.10 tot 6.15. Furthermore, the mass and corresponding fractions of wings, tail and landing gear are shown in Table 6.14.

A hydrogen peroxide/ kerosene launcher					
	Validation input data				
		$n_{\text{eng,first}}$ **[-]**	12	$t_{\text{b,first}}$ **[s]**	210
		$\dot{m}$ **[kg/s]**	$\{5.0, 10.0, 20.0\}$	$t_{\text{b,up}}$ **[s]**	400
		p_{c} **[MPa]**	10	$d_{\text{st,up}}$ **[m]**	1.5
		$d_{\text{e,first}}$ **[m]**	0.3	m_{pay} **[kg]**	250
		$d_{\text{e,up}}$ **[m]**	0.7	l_{pay} **[m]**	1
		O/F **[-]**	8.3		

Table 6.12: A hydrogen peroxide/kerosene first stage validation case

Discussion on first stage validation results

For determining if the first stage model estimates performance as desired also the ΔV difference of ~100 m/s is used as the acceptable limit. Clearly, the estimated behaviour of the Electron first stage, even with the overestimation of the first stage dry mass, is within this defined range. Combined with the validation result of the Electron upper stage this also means that the assumptions on the propellant tank factor, material thickness, pressurant configuration and ullage fraction are implemented in an adequate manner for model performance within the required range. Hence these constant model configurations are directly implemented in the numerical research as shown in Table 6.7. Different is the density of the oxidizer and the temperature of the oxidizer tank, due to the hydrogen peroxide. The density ρ_{oxi} of hydrogen peroxide is 1388 kg/m^3 (Zandbergen, 2018) stored at room temperature (293 K).

For validation of the total first stage model range based conclusions are drawn, which estimate an order of magnitude. In similar studies on winged launch vehicles the lowest dry mass fraction of the first stage found is 13.52% for the Aurora-R1. As this dry mass fraction has primary influence in the ΔV performance it is important to validate that the model does not result in much lower dry mass fractions. Both for the 'Electron with spaceplane configuration' as for the 'general hydrogen peroxide/kerosene launcher' this is never the case. For both validation cases a similar trend is apparent. For larger vehicles, with a higher mass flow, the dry mass fraction of the first stage goes down. For the 'Electron with spaceplane configuration' 17.79% is the lowest dry mass fraction found. For the 'general hydrogen peroxide/kerosene launcher' this is 13.54%. This shows that the limit case approaches the lower-limit set by the Aurora-R1. The model is determined valid, however, for the final design it is assessed if the dry mass fraction of the first stage is within an acceptable range, above to the Aurora-R1.

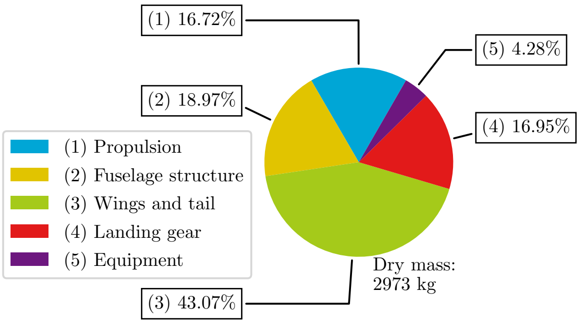

Figure 6.4: First stage dry mass breakdown of the Electron with spaceplane configuration ($\dot{m}$ = 6.936 kg/s)

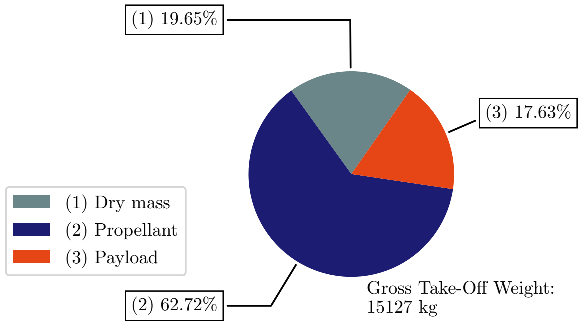

Figure 6.5: First stage total mass breakdown of the Electron with spaceplane configuration ($\dot{m}$ = 6.936 kg/s)

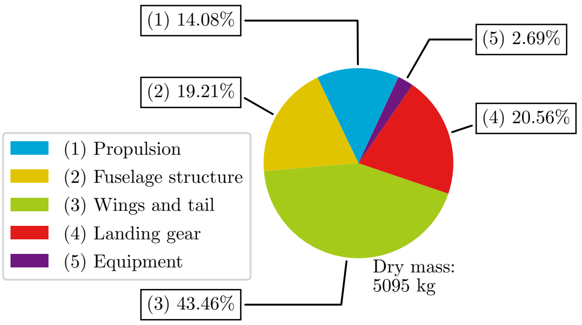

Figure 6.6: First stage dry mass breakdown of the Electron with spaceplane configuration ($\dot{m}$ = 13.872 kg/s)

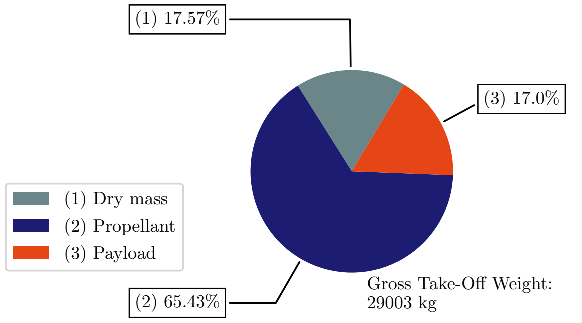

Figure 6.7: First stage total mass breakdown of the Electron with spaceplane configuration ($\dot{m}$ = 13.872 kg/s)

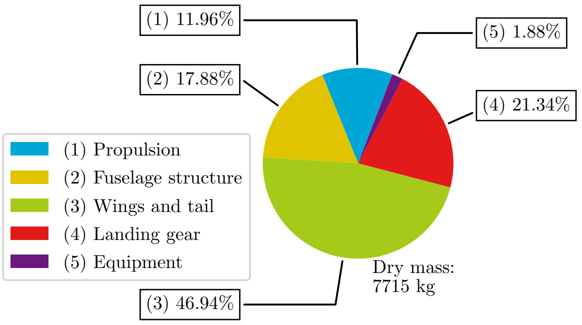

Figure 6.8: First stage dry mass breakdown of the Electron with spaceplane configuration ($\dot{m}$ = 20.808 kg/s)

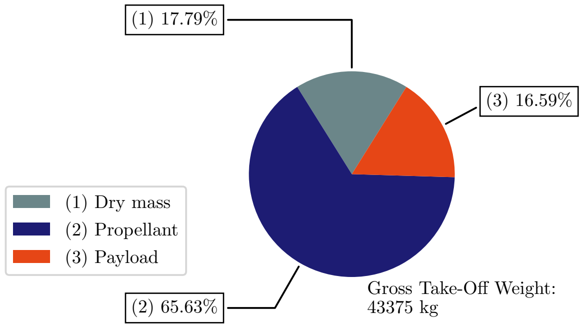

Figure 6.9: First stage total mass breakdown of the Electron with spaceplane configuration ($\dot{m}$ = 20.808 kg/s)

Validation input			**Validation input**			**Validation input**		
	$\dot{m}$ **[kg/s]**	6.936		$\dot{m}$ **[kg/s]**	13.872		$\dot{m}$ **[kg/s]**	20.808
Model result			**Model result**			**Model result**		
	m_{wing} **[kg]**	1202.74		m_{wing} **[kg]**	2080.28		m_{wing} **[kg]**	3402.04
	m_{tail} **[kg]**	77.49		m_{tail} **[kg]**	134.04		m_{tail} **[kg]**	219.20
	m_{gear} **[kg]**	503.93		m_{gear} **[kg]**	1047.40		m_{gear} **[kg]**	1646.56
	f_{wing} **[1/m_{GTOW}]**	0.0795		f_{wing} **[1/m_{GTOW}]**	0.0717		f_{wing} **[1/m_{GTOW}]**	0.0784
	f_{tail} **[1/m_{GTOW}]**	0.0051		f_{tail} **[1/m_{GTOW}]**	0.0046		f_{tail} **[1/m_{GTOW}]**	0.0051
	f_{gear} **[1/m_{GTOW}]**	0.0333		f_{gear} **[1/m_{GTOW}]**	0.0361		f_{gear} **[1/m_{GTOW}]**	0.0380
	f_{wing} **[1/$m_{\text{first,dry}}$]**	0.4046		f_{wing} **[1/$m_{\text{first,dry}}$]**	0.4083		f_{wing} **[1/$m_{\text{first,dry}}$]**	0.4410
	f_{tail} **[1/$m_{\text{first,dry}}$]**	0.0261		f_{tail} **[1/$m_{\text{first,dry}}$]**	0.0263		f_{tail} **[1/$m_{\text{first,dry}}$]**	0.0284
	f_{gear} **[1/$m_{\text{first,dry}}$]**	0.1695		f_{gear} **[1/$m_{\text{first,dry}}$]**	0.2056		f_{gear} **[1/$m_{\text{first,dry}}$]**	0.2134

Table 6.13: Model results and fractions of wing, tail and landing gear mass of the Electron with spaceplane configuration

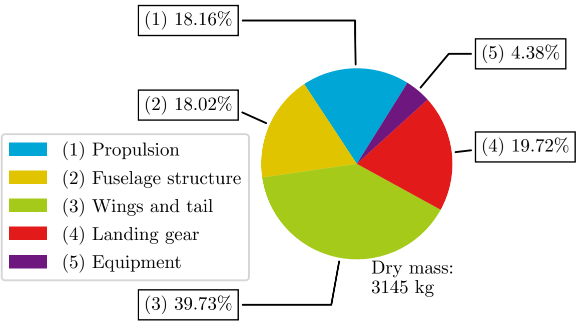

Figure 6.10: First stage dry mass breakdown of a hydrogen peroxide/kerosene launcher with spaceplane configuration ($\dot{m} = 5.0$ kg/s)

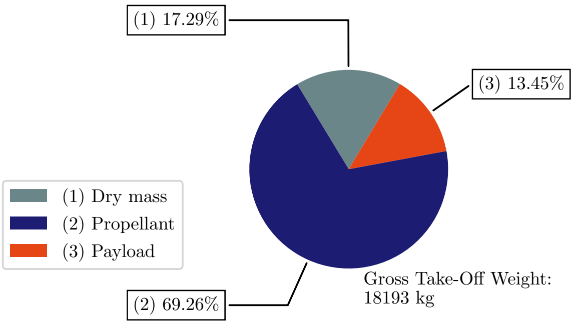

Figure 6.11: First stage total mass breakdown of a hydrogen peroxide/kerosene launcher with spaceplane configuration ($\dot{m} = 5.0$ kg/s)

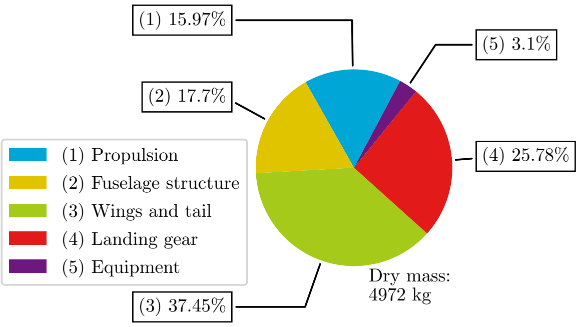

Figure 6.12: First stage dry mass breakdown of a hydrogen peroxide/kerosene launcher with spaceplane configuration ($\dot{m} = 10.0$ kg/s)

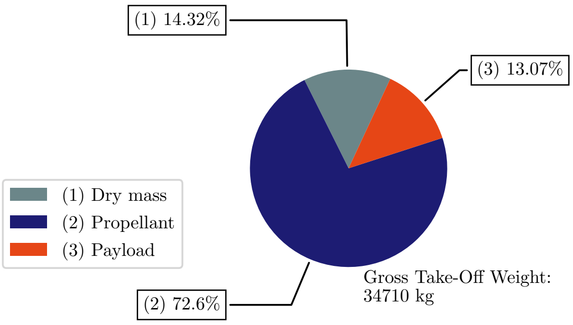

Figure 6.13: First stage total mass breakdown of a hydrogen peroxide/kerosene launcher with spaceplane configuration ($\dot{m} = 10.0$ kg/s)

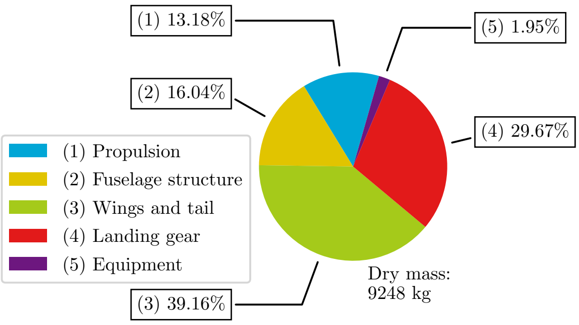

Figure 6.14: First stage dry mass breakdown of a hydrogen peroxide/kerosene launcher with spaceplane configuration ($\dot{m} = 20.0$ kg/s)

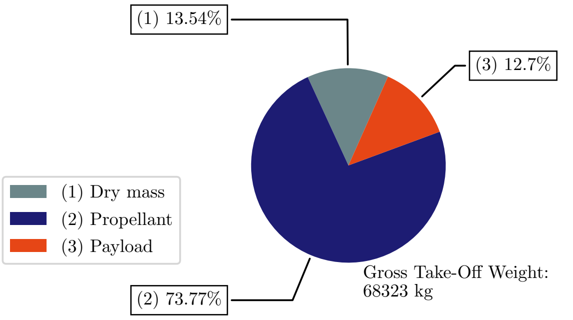

Figure 6.15: First stage total mass breakdown of a hydrogen peroxide/kerosene launcher with spaceplane configuration ($\dot{m} = 20.0$ kg/s)

Validation input			**Validation input**			**Validation input**		
	$\dot{m}$ **[kg/s]**	5.0		$\dot{m}$ **[kg/s]**	10.0		$\dot{m}$ **[kg/s]**	20.0
Model result			**Model result**			**Model result**		
	m_{wing} **[kg]**	1173.76		m_{wing} **[kg]**	1749.48		m_{wing} **[kg]**	3402.04
	m_{tail} **[kg]**	75.63		m_{tail} **[kg]**	112.72		m_{tail} **[kg]**	219.2
	m_{gear} **[kg]**	620.07		m_{gear} **[kg]**	1281.72		m_{gear} **[kg]**	2743.94
	f_{wing} **[1/m_{GTOW}]**	0.0645		f_{wing} **[1/m_{GTOW}]**	0.0504		f_{wing} **[1/m_{GTOW}]**	0.0498
	f_{tail} **[1/m_{GTOW}]**	0.0042		f_{tail} **[1/m_{GTOW}]**	0.0032		f_{tail} **[1/m_{GTOW}]**	0.0032
	f_{gear} **[1/m_{GTOW}]**	0.0341		f_{gear} **[1/m_{GTOW}]**	0.0369		f_{gear} **[1/m_{GTOW}]**	0.0402
	f_{wing} **[1/$m_{\text{first,dry}}$]**	0.3732		f_{wing} **[1/$m_{\text{first,dry}}$]**	0.3519		f_{wing} **[1/$m_{\text{first,dry}}$]**	0.3679
	f_{tail} **[1/$m_{\text{first,dry}}$]**	0.0240		f_{tail} **[1/$m_{\text{first,dry}}$]**	0.0227		f_{tail} **[1/$m_{\text{first,dry}}$]**	0.0237
	f_{gear} **[1/$m_{\text{first,dry}}$]**	0.1972		f_{gear} **[1/$m_{\text{first,dry}}$]**	0.2578		f_{gear} **[1/$m_{\text{first,dry}}$]**	0.2967

Table 6.14: Model results and fractions of wing, tail and landing gear mass of a general hydrogen peroxide/kerosene launcher with spaceplane configuration

6.3. Trajectory model validation

For validation of the trajectory model also literature is consulted. For a comparison of trajectory results especially the study by Maddock et al. (2018) is useful, as both the vehicle design and trajectory results of this study are well documented. Table 6.15 shows the design of this vehicle. The only derived value is the wing area, which is unknown. The derivation is done based on the total propellant volume, which can roughly be dimensioned inside the vehicles internal geometry as shown in Figure 6.16. Once dimensioned it is possible to estimate the wing area. Furthermore, the corresponding aerodynamic properties are unknown. It is for this reason the aerodynamic set of the X-34, as shown in Chapter 5, is also used for this validation case.

Maddock et al. validation vehicle				
	First stage		**Upper stage**	
	Dry mass [**kg**]	11343	Dry mass [**kg**]	1852.6
	Payload mass [**kg**]	12995.6	Payload mass [**kg**]	500
	Total mass [**kg**]	70872	Total mass [**kg**]	12995.6
	Thrust [**kN**]	1164.3	Thrust [**kN**]	129.61
	Specific impulse [**s**]	330.31	Specific impulse [**s**]	352
	Wing area [$\mathbf{m}^2$]	40^*		

Table 6.15: Vehicle characteristics of the Maddock et al. (2018) launch vehicle used in the trajectory validation case - *(*) Derived value*

With the vehicle design the trajectory optimization tool is run, for three different initialization seeds of the random number generator, to find the optimal desired flight path angles as well as coasting time for injecting the payload into circular 600 km polar orbit. Figure 6.20 shows the resulting set of optimized flight path angles of the three different seeds. Furthermore, the following coasting times are found corresponding to the same seeds:

Seed	**Coasting time [s]**
123	331.38
213	366.13
321	294.34

Table 6.16: Optimized trajectory coasting times of the best performing individual of every seed for the Maddock validation case

With the combination of coasting time and flight path angles the resulting trajectory is computed, which of course is also done during the fitness evaluation and evolution of the optimization algorithm. In Table 6.17 the resulting orbits of the best performing individuals of each seed as well as the computed fitness values are shown. The table shows that in terms of orbital injection the three solutions converged very closely, with a pericenter range of less than 300 m and an eccentricity range of less than $0.9 \cdot 10^{-5}$. This is especially interesting considering the larger spread in both the optimal set of flight path angles and coasting time.

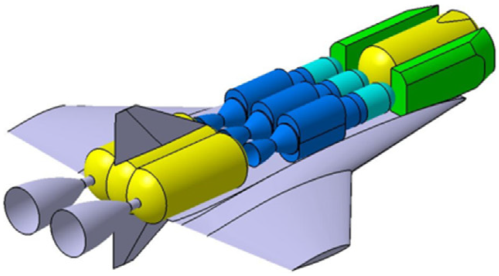

Figure 6.16: Internal geometry of the Maddock et al. (2018) launch vehicle used for deriving wing area

Seed	**Pericenter [km]**	**Eccentricity [-]**	**Fitness**
123	6971.276	$8.379\cdot10^{-5}$	16309.1
213	6970.992	$2.842\cdot10^{-5}$	16383.0
321	6971.043	$1.100\cdot10^{-4}$	12071.5

Table 6.17: Orbital fitness of the best performing individual of every seed for the Maddock validation case

Comparing the resulting orbit is done with the best performing solution, being the solution of seed 321. Figure 6.17 to 6.19 show both the optimal trajectory found by Maddock et al. (2018) and the optimal trajectory found with the optimization tool of this study. Noticeably differing the most is the upper stage trajectory and corresponding velocity profile. This is due to a fundamental difference in the model, as throttling is not modelled in the optimization tool used in this study. The tool used by Maddock et al. (2018) is capable of optimizing the throttling profile of the upper stage, which means it can find the more smooth velocity profile as shown in Figure 6.18. The trajectory of the first stage shows close resemblance to the reference trajectory. Observable is the fact that during re-entry the velocity is decreased more within this study due to the entry guidance, of which the main effect is that the vehicle stays in higher layers of the atmosphere and skips quicker, higher and with less velocity in the downrange component. The study by Maddock et al. (2018) was optimized for downrange. Hence the AoA profile was optimized such that the downrange of skipping was maximized. This in contrast with the guidance law implemented in this study, based on the current Mach number.

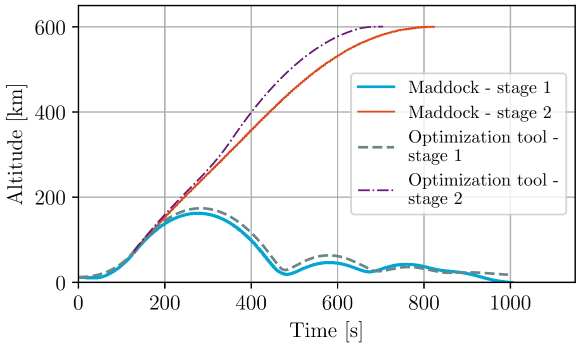

Figure 6.17: Altitude comparison over time between the optimization tool optimal trajectory result (seed = 321) and the Maddock et al. (2018) optimal trajectory

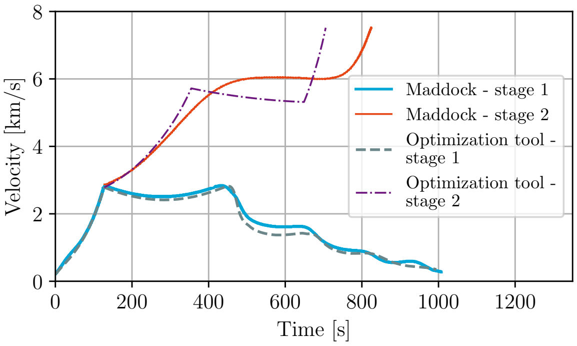

Figure 6.18: Velocity comparison over time between the optimization tool optimal trajectory result (seed = 321) and the Maddock et al. (2018) optimal trajectory

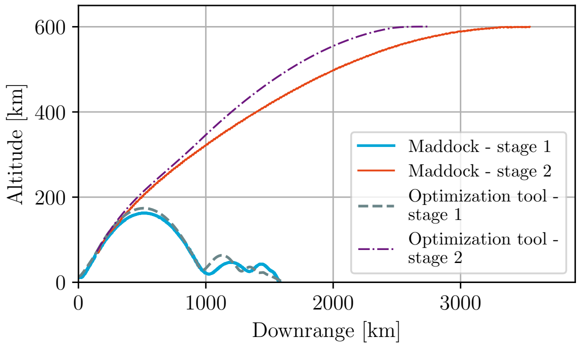

Figure 6.19: Altitude comparison over downrange between the optimization tool optimal trajectory result (seed = 321) and the Maddock et al. (2018) optimal trajectory

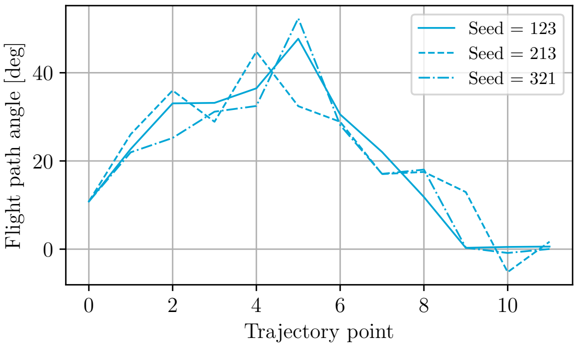

Figure 6.20: Optimized trajectory flight path angles of the best performing individual of every seed for the Maddock validation case

Integrator tolerance

One of the important settings in the optimization process is the tolerance of the variable step-size integrator. In Chapter 3 it was shown what the definition of this tolerance is. The selection of this tolerance value is dependent on the problem. To find the sufficient value for this study, again the Maddock et al. (2018) validation case is used.

The best performing solution of seed 123 is ran with different tolerance settings, as shown in Table 6.18. Based on the notice that the ΔV is allowed to differ ~100 m/s any of the shown integrator settings is sufficient. However, the time of running the code is not such a limiting factor that indeed it is required to have a tolerance of only 10^{-4}. For feeling satisfied with the results of the model the personal decision is made to implement the model with a tolerance on the numerical integrator of 10^{-5}.

Tolerance	**Semi-major axis (a) [m]**	**Eccentricity (e) [-]**	**Δa [m]**	**Δe [-]**
10^{-12}	6969460	$3.01 \cdot 10^{-4}$	-	-
10^{-10}	6969460	$3.01 \cdot 10^{-4}$	0	$4.00 \cdot 10^{-9}$
10^{-8}	6969460	$3.01 \cdot 10^{-4}$	0	$3.79 \cdot 10^{-7}$
10^{-7}	6969470	$2.98 \cdot 10^{-4}$	10	$2.77 \cdot 10^{-6}$
10^{-6}	6969560	$2.85 \cdot 10^{-4}$	100	$1.57 \cdot 10^{-5}$
10^{-5}	6971860	$8.38 \cdot 10^{-5}$	2400	$2.17 \cdot 10^{-4}$
10^{-4}	6945590	$3.11 \cdot 10^{-3}$	23870	$2.81 \cdot 10^{-3}$

Table 6.18: RKF-45 numerical integrator tolerance behaviour of the Maddock et al. (2018) validation case (best performing solution seed 123)

Discussion on the trajectory validation

When comparing the trajectory of the model with the validation trajectory both similarities and large differences are apparent. The first stage trajectory during ascent and re-entry shows a close match to the validation trajectory of the study by Maddock et al. (2018), both in altitude and velocity. Furthermore, the downrange of the model is similar to the downrange of the study by Maddock et al. (2018), which is important for validation of the gliding range. Gliding properties do differ, which is an indication that the highest lift-over-drag ratio of the vehicle in the study by Maddock et al. (2018) is lower than the highest lift-over-drag ratio of the X-34. Although, it also possible that the study by Maddock et al. (2018) deliberately selected a steep descent trajectory in the denser layers of the atmosphere. The figure shows that even for space vehicles the gliding path in the study by Maddock et al. (2018) is rather inefficient.

The upper stage shows more difference, which is judged to be mainly caused by not modelling throttling. Especially in the velocity figure this is evident, in which the study by Maddock et al. (2018) has a gentle velocity profile compared to the more discrete shaped profile in this model. What is validated is the fact that even without throttling the upper stage is able of payload injection in the desired orbit. This means that the design space of this study also contains the vehicle by Maddock et al. (2018) in terms of trajectory performance.

Based on a validated reference vehicle of a large study on winged launch vehicles, the following validation conclusion is drawn. Due to the close resemblance of the first stage trajectory as well as the ability of the upper stage to get in the desired orbit the trajectory model is deemed validated. As discussed the numerical integrator precision is selected to be 10^{-5}.

7

Results and comparisons of the different cost derived mission scenarios

A selection of different mission scenarios is derived based on qualitative cost differences between these scenarios. The results of the different mission scenarios are shown and discussed in this chapter. Two non-cost derived scenarios are added to determine the performance of the launch vehicle, the first on the available payload mass and the second on the injection altitude. To compare the differences between mission scenarios a baseline reference scenario is used as the benchmark case. All variations are defined with respect to this baseline scenario. Due to the limited size of individual tables the result of the baseline scenario is not repeated in every table. Both the input and corresponding design of the baseline scenario are repeated in Appendix A.

7.1. Results of the baseline scenario

The mission geometry of the baseline scenario was selected at the start of the study. This geometry is based on preliminary runs of the model and theoretical understanding of the System. The target payload and orbit as well as the vehicle design constraints are selected based on stakeholder interest of Dawn Aerospace.[1] The minimum heading turn altitude is decided upon based on ground clearance. Furthermore, as Hellman (2005) showed that an active return method is required for high velocity first stage vehicles, in-plane pitch over is selected showing most promising results in mass efficiency and operational implementability. The airport of take-off is Rotterdam The Hague Airport, allowing for showing the true innovative nature of the vehicle integrated in one of the most densely populated areas and crowded airspaces worldwide. This baseline scenario is summarized as:

- **Payload**: 150 kg
- **Target orbit**: 600 km polar orbit
- **First stage heading turn**: Above 150 m
- **Return method**: In-plane pitch over
- **Spaceport**: Rotterdam The Hague Airport at runway 06
- **Vehicle design**:
    - The first and upper stage share the engine design
    - Fairing usage is prohibited
    - Landing gear is sized for take-off

For better and faster convergence of the tool not all design variables are allowed to vary. It is deemed that the result is not influenced substantially by this measure. The following input variables are either constant or dependent on other input variables by the following reasoning:

- **The amount of engines used for the return burn**: Due to the fact that the first stage is much lighter during the return burn, only half of the first stage engines is used during the return burn.
- **Oxidizer-over-fuel ratio**: The oxidizer-over-fuel ratio is fixed to 8.3.[2] Although this is slightly off from the optimum found in literature (Moon et al., 2014), an oxidizer rich mixture is selected accounting for the fact

---

[1] Wink, J., 'Personal discussion', *Dawn Aerospace*, (discussed in March 2020).

[2] Knop, T., 'Personal discussion', *Dawn Aerospace*, (discussed in March 2020).

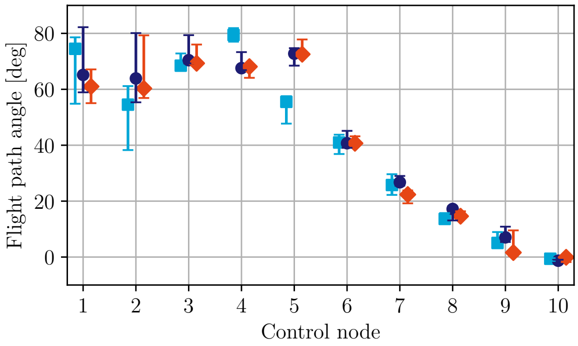

Figure 7.1: Range of optimal flight path angles of 20 individual solutions with the best performing solution marked, of three different seeds

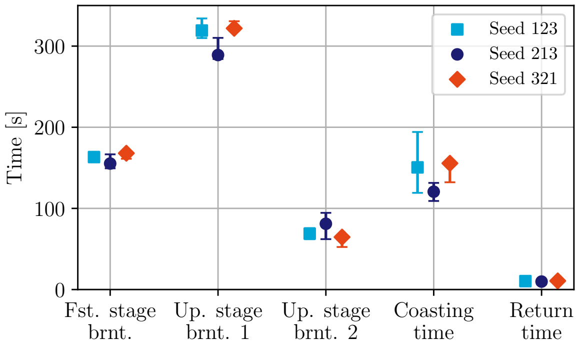

Figure 7.2: Range of optimal times of 20 individual solutions with the best performing solution marked, of three different seeds (legend is valid for Figure 7.1 to 7.3)

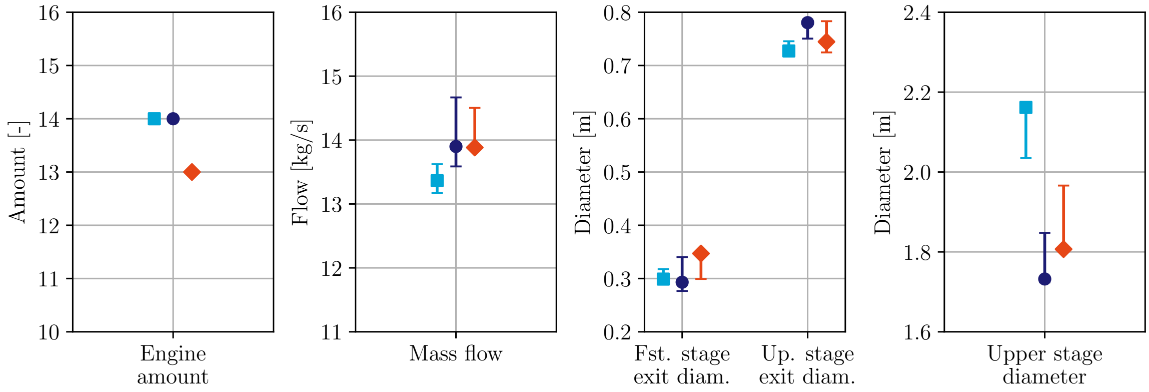

Figure 7.3: Range of optimal engine amount, mass flow, first and upper stage exit diameter and upper stage diameter of 20 individual solutions with the best performing solution marked, of three different seeds

that the turbopumps are oxidizer driven. This mixture ratio is in close resemblance with the experimental data of the Gamma 8 engine (Table 6.4).

- **Chamber pressure**: The chamber pressure of the engine is fixed to 100 bar. Engine performance increases by an increase in chamber pressure. Hence optimizing this value is not of great interest, which is why this feasibility limit is implemented. The limit is determined based on the experience of the propulsion design team of Dawn Aerospace.[3]

First, the convergence behaviour of the simulation is addressed. This is found very similar in the different scenarios. Hence the behaviour is only discussed for the baseline case. Three different runs are always initiated by three different seeds and evolved over 2000 generations. Each population exists of 80 individuals which at the end of the optimization process results in 80 different solutions to the problem. However, here only the 20 individuals with the lowest total vehicle dry mass are compared, as these are found without constraint violations. The optimized values of the design parameters are shown in Figure 7.1 to 7.3 for the three different initialization seeds of the optimizer. The figures also show the spread between the 20 different solutions. Most of the design variables show a distinct convergence towards a certain region of the design space. Some of the control nodes, the coasting time, the mass flow and the upper stage diameter show a larger spread between different solutions.

Figure 7.4 shows the computed fitness of all designs against the total vehicle dry mass. Once the optimizer converges into solutions without constraint violations the objective function consist only of a component emphasizing the dry mass of the vehicle and a component based on the orbital injection constraint. The latter is implemented as a gradient forcing the solution to meet the injection requirement. The figure shows that this implementation behaves properly. The grey line represents the fitness based only on dry mass and most solutions meet close to this line. This means that the fitness is dry mass driven, except for two outliers. Figure 7.5 supports this as most solutions have a pericenter altitude of approximately 600 km and eccentricity below 0.002. Solutions

---

[3] Huijsman, R., 'Personal discussion', *Dawn Aerospace*, (discussed in January 2020).

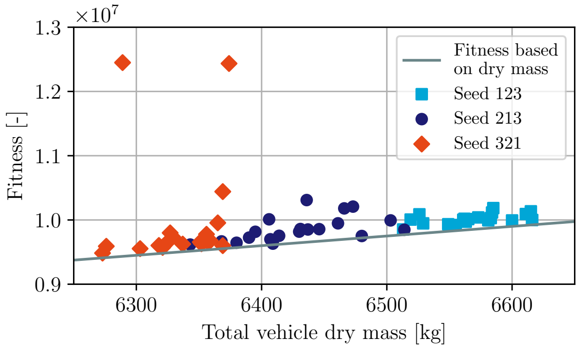

Figure 7.4: Fitness value of the objective function shown for the 20 individuals of the three different seeds, accompanied by the minimum fitness value based on dry mass

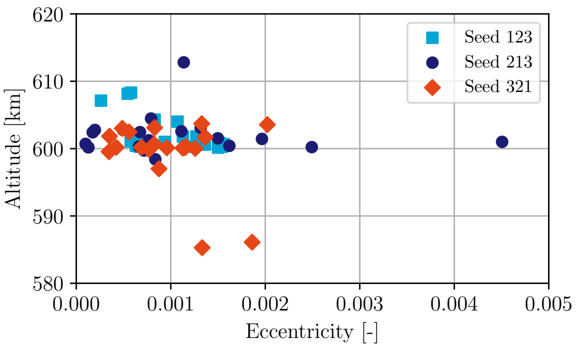

Figure 7.5: Orbital injection precision of the 20 individuals of the three different seeds showing the pericenter altitude and the eccentricity of the orbit

not meeting the orbital altitude requirement are penalized most, shown by the same two outliers.

Table 7.1 shows the design of the solution with the lowest total vehicle dry mass of 6273.04 kg (seed 321, input tabulated in Appendix A). This is ~5 times heavier than conventional launch vehicles with similar payload capacity and performance (see Footnote 9 in Chapter 6), although 94.5% of the dry mass is reusable while the defined constraints and requirements are met. The *Gross Take-Off Weight* (GTOW) is 42972.8 kg. The performance of the upper stage, designed with a common bulkhead tank, is driven by the high *Propellant Mass Fraction* (PMF) of 0.939. The dry mass fraction of the first stage is 0.138, being above the required minimum defined in Chapter 6.

The trajectory and behaviour of the vehicle is shown in Figure 7.10 to 7.17. Furthermore, the three lightest solutions of every seed are included. Combined these figures show that it is possible to get payload into orbit by the proposed design meeting all requirements and constraints.

The *Angle of Attack* (AoA) stays within the required bounds, adequate for first increasing the *Flight Path Angle* (FPA) and then decreasing it slowly towards 0°. The weaker convergence of the first stage control nodes is visible by the differences in AoA and FPA. The first stage FPA of the optimal solution is increased to approximately 60° and is kept between 60° and 70°. The upper stage slowly decreases the FPA back to 0°.

The dynamic pressure during ascent is within the allowed range. The dynamic pressure during re-entry, however, is almost twice as high as during ascent. This is accepted as during re-entry very different dynamics push the vehicle into a higher dynamic pressure. The heat flux in the stagnation point is also maximum during re-entry, being ~90 kW/m^2 for the optimal solution. The total heat load on the stagnation point is 1.8 MJ/m^2.

The bending limit, a combination of AoA and dynamic pressure, is also within the acceptable range. The aerothermal flux experienced after staging is and stays below the defined maximum of 1135 W/m^2, the consequence of prohibiting fairing usage.

Baseline design			
First stage		**Upper stage**	
Dry mass [**kg**]	5926.45	Dry mass [**kg**]	346.59
Propellant consumption [**kg**]	31204.61	Propellant consumption [**kg**]	5345.12
Total mass [**kg**]	42972.77	Total mass [**kg**]	5841.71
Vacuum thrust [**kN**]	521.294	Vacuum thrust [**kN**]	42.914
Vacuum specific impulse [**s**]	294.42	Vacuum specific impulse [**s**]	315.19
ΔV [**m/s**]	3530.51	ΔV [**m/s**]	7619.36
Return ΔV [**m/s**]	403.67	Length [**m**]	4.962
Length [**m**]	19.360		

Table 7.1: Optimal baseline design of the nominal launch scenario (found in optimization of seed 321)

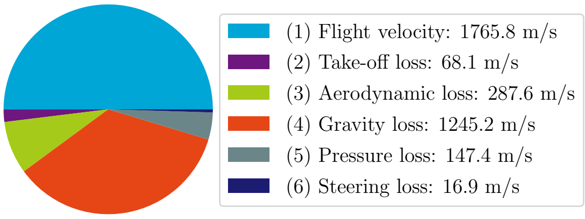

Figure 7.6: ΔV distribution of the first stage during ascent, showing the increase in velocity and the occurring losses

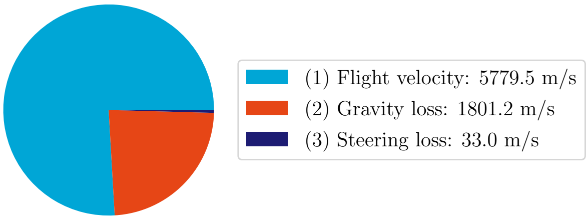

Figure 7.7: ΔV distribution of the upper stage during ascent, showing the increase in velocity and the occurring losses

One of the major consequences of the proposed design is that an above average ΔV is required to get into orbit. Figure 7.6 and 7.7 show the ΔV distribution of the first and upper stage. This ΔV distribution is determined based on an integration of the result independent of information on vehicle performance. Hence it also serves as verification of the model. When comparing these losses to the expected magnitude found in literature (see Chapter 4) the following differences are identified.

The total gravity loss of the System adds up to 3046.4 m/s. This is 650-1050 m/s higher than for conventional launch vehicles in direct ascent into polar orbit. The main reason for this difference is the return of the first stage. To limit the downrange of the first stage the ascent is done by a steep trajectory inefficient in terms of gravity loss.

The aerodynamic loss is 287.6 m/s. This is 130-250 m/s more than for conventional launchers and is caused by the aerodynamic shape of the first stage, which results in more aerodynamic drag during flight.

The steering loss is within the expected range of magnitude, even with the strong pull-up manoeuvre. This is due to the fact that by the efficient lift generation of the first stage small AoAs are enough for following the desired trajectory path. For the upper stage larger deviations in AoA are observed, mostly during coasting in which the high AoA does not result in any steering loss.

Comparing pressure loss is more difficult, due to lack on pressure loss information of other vehicles. However, during take-off at sea level conditions pressure loss is the primary loss contributor in the take-off loss. Furthermore, the time in the dense layers of the atmosphere is above average, due to the pull-up manoeuvre of the first stage. Considering both it is assumed that the pressure loss is substantial.

Finally, the loads on the vehicle during ascent and return are examined. To be able to show readable figures this is only shown for the optimal design. Figure 7.8 and 7.9 show the accelerations in the body frame during first stage ascent and return respectively. Figure 7.18 shows the accelerations during upper stage ascent. In both the first and upper stage ascent trajectory the vehicle stays within the defined limits. During re-entry of the first stage a large acceleration peak is observed outside of the defined limits. To prevent this large acceleration from happening a local optimization shall be applied on the re-entry phase. This shall determine a more suited control profile for this phase. During re-entry the vehicle is no more than 14% of the initial mass at take-off. This means that in terms of total wing loading the re-entry phase does not differ substantially from the take-off wing loading. It is for this reason that this behaviour is accepted in this study, being identified as a recommendation for further study.

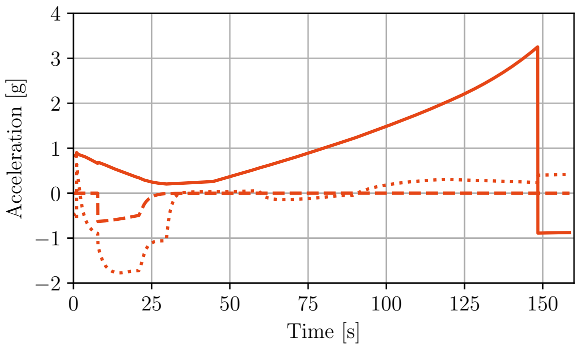

Figure 7.8: Accelerations in the body frame during the ascent of the first stage

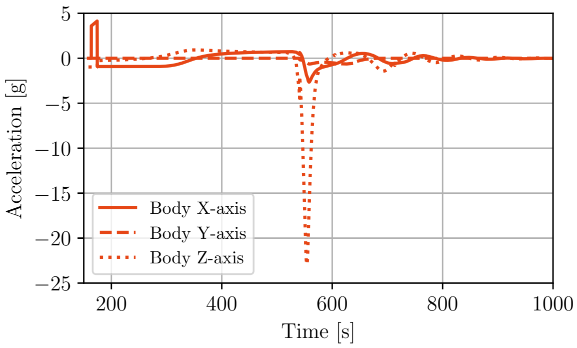

Figure 7.9: Accelerations in the body frame during the return of the first stage (legend is also valid for Figure 7.8 and 7.18)

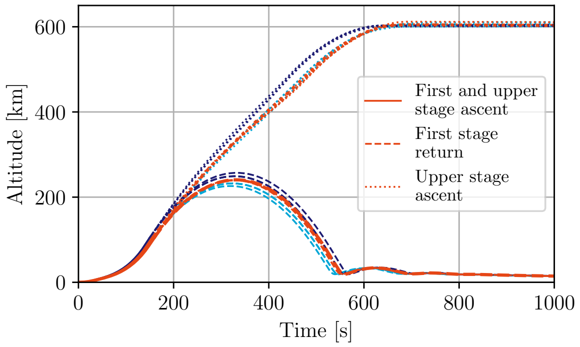

Figure 7.10: Altitude over time of the lightest three individuals of each seed, with the absolute lightest highlighted (legend shows the line structure used for all figures in this chapter which show the different flight phases)

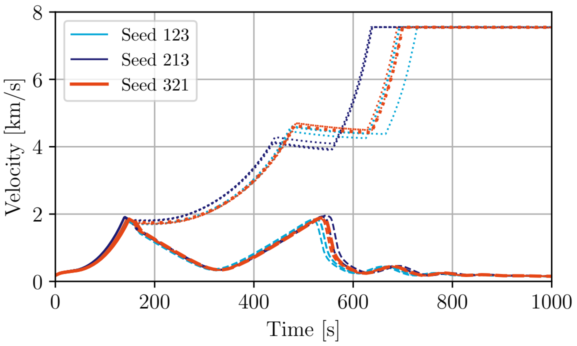

Figure 7.11: Velocity over time of the lightest three individuals of each seed, with the absolute lightest highlighted (legend is valid for Figures 7.10 to 7.17)

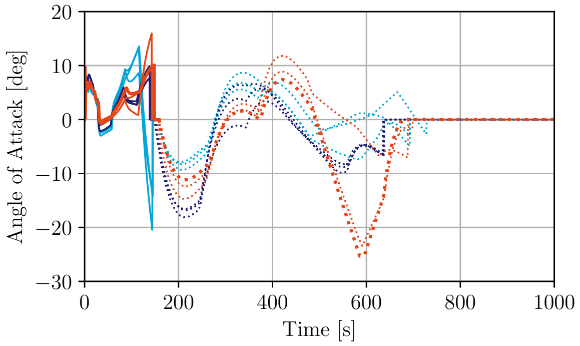

Figure 7.12: Ascent Angle of Attack of the first and upper stage of the lightest three individuals of each seed, with the absolute lightest highlighted

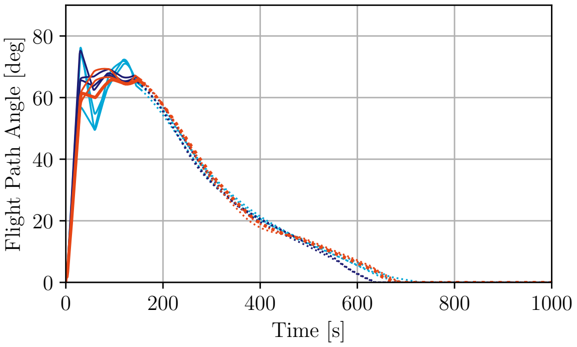

Figure 7.13: Ascent Flight Path Angle of the first and upper stage of the lightest three individuals of each seed, with the absolute lightest highlighted

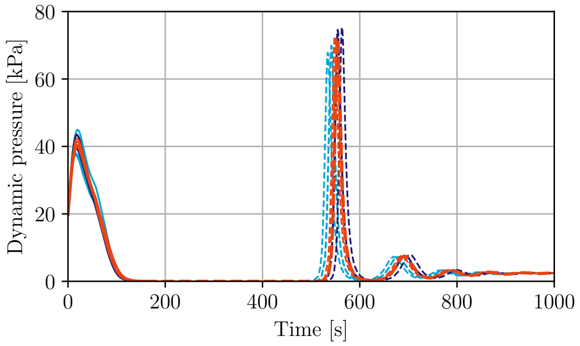

Figure 7.14: Dynamic pressure during first stage ascent and return of the lightest three individuals of each seed, with the absolute lightest highlighted

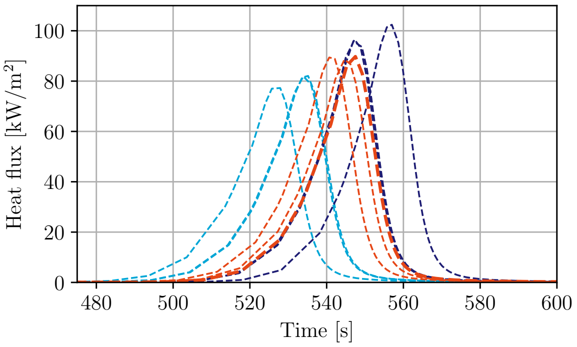

Figure 7.15: Stagnation point heat flux during re-entry of the first stage of the lightest three individuals of each seed, with the absolute lightest highlighted

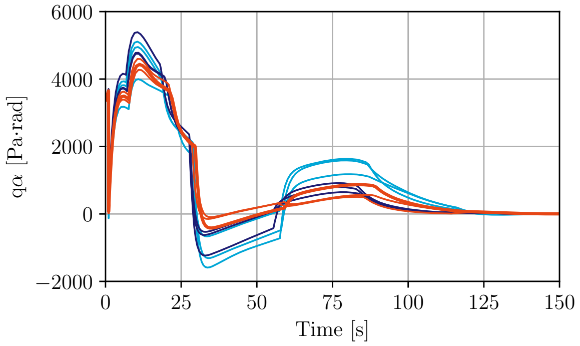

Figure 7.16: qα bending load during first stage ascent of the lightest three individuals of each seed, with the absolute lightest highlighted

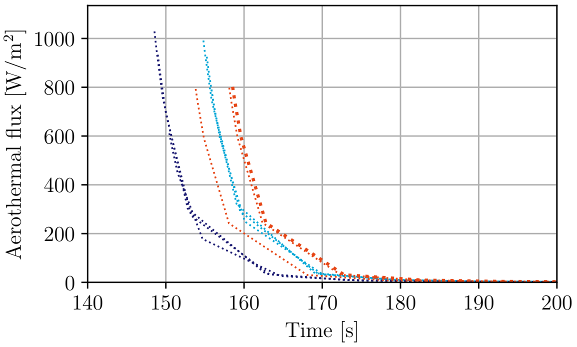

Figure 7.17: Aerothermal flux of the upper stage in the begin phase of the ascent of the lightest three individuals of each seed, with the absolute lightest highlighted

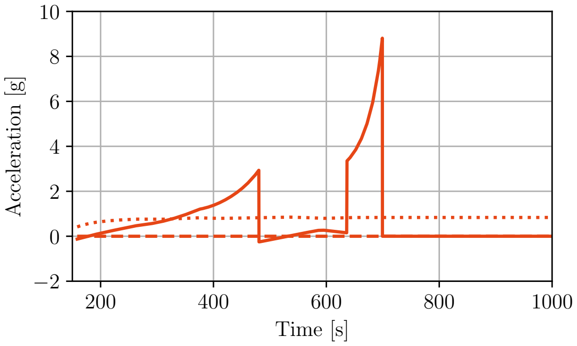

Figure 7.18: Accelerations in the body frame during the ascent of the upper stage

7.2. Variations in target altitude

The first change to the baseline scenario is a change in orbital injection altitude. Table 7.2 shows the optimized design input vector for 200 km, 400 km and 800 km orbital altitude. This table shows that for an increase in orbital altitude the burn time of the first stage is decreased. On the other hand the mass flow of the engines and the amount of first stage engines increases with the increase in orbital altitude.

For an orbital altitude of 400 km and above the total burn time of the upper stage does not differ more than 3.7%. The coasting time does increase. For 400 km the coasting time is negligible, while for 600 km this is 156 s and for 800 km this is 234 s.

The solutions for 200 km and 400 km altitude show smaller exit diameters of the first stage as compared to the solutions for 600 km and 800 km. Two effects play a role. First, the mass flow of these solutions is lower. This allows for smaller exit diameters with similar performance. Secondly, the pressure loss is more dominant due to longer flight in the dense layers of the atmosphere.

The control nodes show similar behaviour in all four solutions. One difference is found in node 5, the final node of the first stage. For the 200 km solution this node has a lower magnitude. This is required for not overshooting the upper stage above the desired orbital altitude. This also means more horizontal velocity of the first stage, counteracted by the longer return burn.

Vehicle design				**Trajectory design**			
	200 km orbit	**400 km orbit**	**800 km orbit**		**200 km orbit**	**400 km orbit**	**800 km orbit**
Fst. stage brnt. [**s**]	194.64	178.72	145.59	Node 1 [**deg**]	52.09	57.30	65.12
Up. stage brnt. 1 [**s**]	256.70	181.90	342.44	Node 2 [**deg**]	84.30	49.29	72.59
Up. stage brnt. 2 [**s**]	98.09	218.75	57.22	Node 3 [**deg**]	68.03	74.90	70.37
Coasting time [**s**]	31.13	7.68	234.44	Node 4 [**deg**]	75.59	74.47	77.42
Return time [**s**]	12.90	7.14	5.52	Node 5 [**deg**]	45.77	68.23	69.48
Engine amount [-]	10	11	15	Node 6 [**deg**]	19.04	46.55	48.82
Mass flow [**kg/s**]	11.91	13.75	15.18	Node 7 [**deg**]	14.68	32.93	27.81
Fst. stage exit diam. [**m**]	0.279	0.314	0.337	Node 8 [**deg**]	0.49	13.05	12.36
Up. stage exit diam. [**m**]	0.799	0.694	0.786	Node 9 [**deg**]	-0.60	2.86	4.66
Up. stage diameter [**m**]	1.716	1.829	2.138	Node 10 [**deg**]	1.42	-0.27	-0.52

Table 7.2: Optimal design input of the launch vehicle for three different orbital altitudes

Table 7.3 shows the resulting design of these input vectors. A summary on the mass behaviour of the vehicle is graphically shown in Figure 7.19 and 7.20. The change of dry and total mass of the upper stage does not show a clear trend. The change of dry and total mass of the first stage does show a trend.

The upper stage dry masses of the 400 km, 600 km and 800 km solutions differ less than 0.9%. Surprising is the fact that the 800 km solution with most upper stage propellant does not have the highest dry mass. This is explained by the fact that the upper stage diameter allows for spherical tanks. The other solutions use a common bulkhead tank configuration. The total stage length (including payload) shows this as well. This is largest for the 800 km solution as two spherical tanks increase the stage length.

The dry mass and GTOW of the first stage rise for higher orbital altitudes. The increase in first stage dry mass is not constant between different altitudes. The dry mass increases most between 600 km and 800 km with 13.5%.

First stage				**Upper stage**		
	200 km orbit	**400 km orbit**	**800 km orbit**	**200 km orbit**	**400 km orbit**	**800 km orbit**
Dry mass [**kg**]	4691.89	5427.30	6725.00	310.50	349.46	347.68
Propellant consumption [**kg**]	23951.06	27620.37	33827.85	4216.38	5486.14	6058.06
Total mass [**kg**]	33319.84	39033.27	47108.60	4676.89	5985.60	6555.75
Vacuum thrust [**kN**]	338.645	432.375	652.479	37.204	42.293	46.962
Vacuum specific impulse [**s**]	289.83	291.41	292.04	318.51	313.66	315.40
ΔV [**m/s**]	3383.24	3371.39	3486.31	7240.61	7639.38	7974.32
Return ΔV [**m/s**]	431.24	294.64	272.24	-	-	-
Length [**m**]	17.801	18.737	20.377	4.654	4.967	5.827

Table 7.3: Optimal design of the launch vehicle for three different orbital altitudes

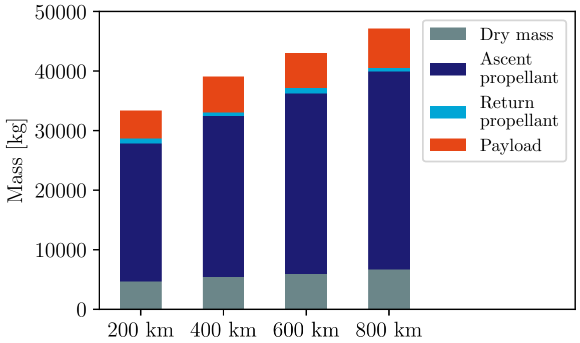

Figure 7.19: Optimal mass distribution of the first stage for four different orbital altitudes

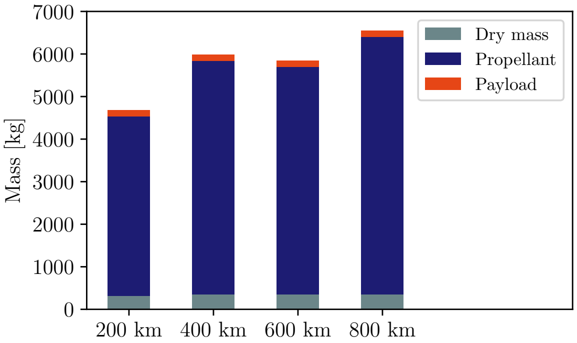

Figure 7.20: Optimal mass distribution of the upper stage for four different orbital altitudes

Between 600 km and 400 km dry mass is reduced by 8.4%, while between 600 km and 200 km this reduction is 20.8%. The difference in dry mass is caused by a combination of engine mass, total upper stage mass and total propellant consumption. The GTOW is increased by 9.6% between 600 km and 800 km. Between 600 km and 400 km the GTOW is reduced with 9.2% and between 600 km and 200 km the GTOW is decreased by 22.5%.

Table 7.3 shows a difference in engine performance and propellant consumption. The ΔV budget is not strongly affected by this difference. The ascent ΔV of first stage differs with maximum 4.5%, while the ascent ΔV of the upper stage differs with maximum 5.0%. The initial thrust-over-weight ratio is affected. For the 200 km solution this is 1.04, while this increases to 1.13 for the 400 km solution, to 1.24 for the 600 km solution and to 1.41 for the 800 km solution. Figure 7.21 to 7.24 show the altitude and velocity profile during ascent and return of the vehicle. The different thrust-over-weight ratios are visible in the velocity profile by the wave pattern going left and up. The higher acceleration results in a quicker gain of velocity. The difference in staging velocity is 22.5%, which is more than the difference in first stage ascent ΔV.

In the altitude profile the staging altitudes of the solutions are found very similar. This is due to the aerothermal flux constraint. To keep the aerothermal flux below the defined maximum the altitude of staging is always risen above 100 km. The same profile shows the difference in staging velocity, as the first stage of the 800 km solution ascents furthest after staging.

The dependency on gliding range is also shown by the altitude profile. All solutions, independent of maximum altitude, re-enter the atmosphere in approximately the same region. This region allows for gliding back to the spaceport.

Finally, the effect of the high staging altitude with steep ascent angle shows in the upper stage trajectory of the 200 km solution. The upper stage first overshoots the orbital target altitude and descends along the trajectory to meet the orbital requirement. This behaviour is found in the control nodes and shows the importance of the final first stage control node for flattening the trajectory. A nice detail in the final upper stage velocities is that the orbital altitude is visible. The lower the altitude the higher the final velocity.

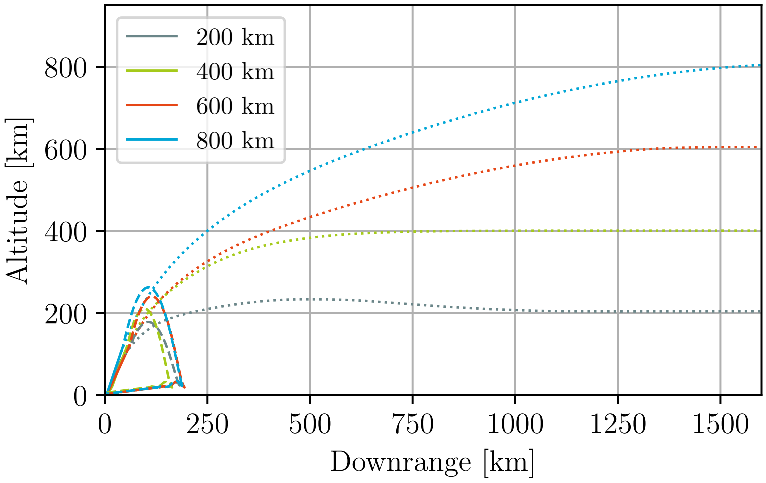

Figure 7.21: Optimal ascent and return trajectories for four different orbital altitudes (legend valid for Figure 7.21 and 7.22)

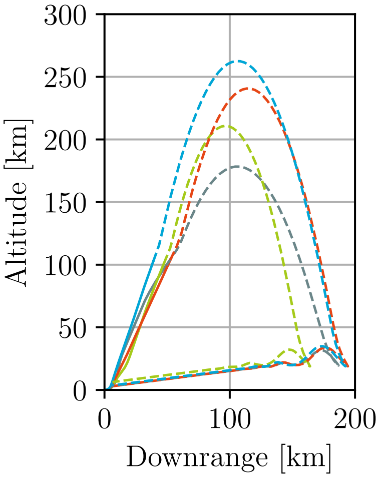

Figure 7.22: Optimal return trajectories for four different orbital altitudes

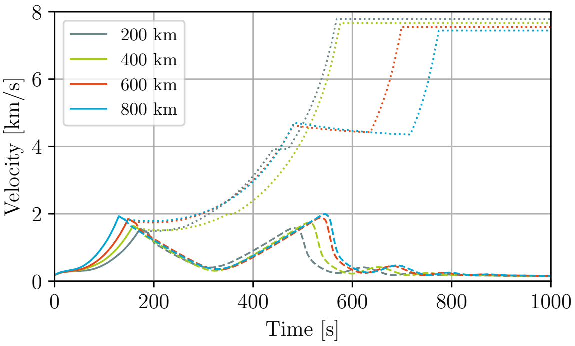

Figure 7.23: Velocity over time of the optimal ascent and return trajectories for four different orbital altitudes (legend valid for Figure 7.23 and 7.24)

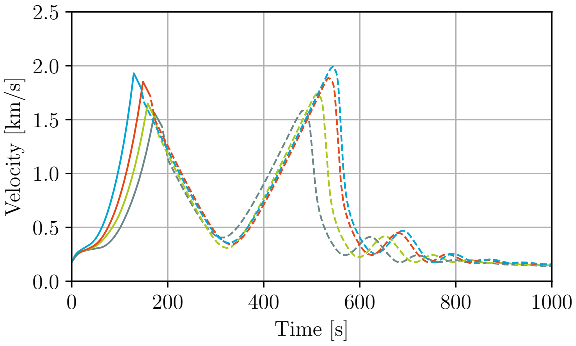

Figure 7.24: First stage velocity over time of the optimal ascent and return trajectories for four different orbital altitudes

7.3. Variations in payload mass

The second change of the baseline scenario examines the payload performance of the vehicle. First the payload mass is increased and decreased by 100 kg. This is followed by an increase to 500 kg, the upper mass limit of small satellites.[4]

Table 7.4 shows the optimal design vector for the three different payload masses. The table shows that the first stage burn time is decreased for an increase in payload mass. The mass flow and engine amount are increased by an increase in payload mass. The trend of higher mass flow for larger vehicles is similar as found in the result when varying target altitude, although between different payload masses this effect is much stronger.

The burn time of the upper stage does not change more than 4.1%, however, with a larger mass flow. This larger mass flow is possible due to the larger payload mass, which reduces the final acceleration of the stage for similar thrust. The upper stage diameter (and size) is driven by the higher mass flow. The maximum difference in coasting time is 16.3%.

The desired FPA profile, shown by the control nodes, shows a very similar trend.

---

[4] Kulu, E., 'What is a CubeSat & other picosatellites', *Nanosats Database*, `https://www.nanosats.eu/cubesat`, (accessed May 15, 2020).

Vehicle design				**Trajectory design**			
	50 kg payload	**250 kg payload**	**500 kg payload**		**50 kg payload**	**250 kg payload**	**500 kg payload**
Fst. stage brnt. [**s**]	198.63	146.49	141.07	Node 1 [**deg**]	59.78	59.56	61.08
Up. stage brnt. 1 [**s**]	343.89	307.45	346.31	Node 2 [**deg**]	60.42	74.38	73.07
Up. stage brnt. 2 [**s**]	58.53	89.88	52.27	Node 3 [**deg**]	59.84	68.45	73.55
Coasting time [**s**]	130.24	140.73	172.69	Node 4 [**deg**]	77.61	70.42	69.42
Return time [**s**]	5.34	7.87	7.66	Node 5 [**deg**]	76.55	72.22	74.77
Engine amount [**-**]	13	15	15	Node 6 [**deg**]	49.72	42.06	38.59
Mass flow [**kg/s**]	8.66	18.25	30.05	Node 7 [**deg**]	26.10	25.28	21.94
Fst. stage exit diam. [**m**]	0.346	0.297	0.343	Node 8 [**deg**]	14.16	17.00	10.92
Up. stage exit diam. [**m**]	0.785	0.793	0.792	Node 9 [**deg**]	7.28	1.08	2.04
Up. stage diameter [**m**]	1.687	1.959	2.249	Node 10 [**deg**]	-1.15	0.26	-0.01

Table 7.4: Optimal design input of the launch vehicle for three different payload masses

The different designs that result from the optimal input vectors are shown in Table 7.5. The mass budget is graphically shown in Figure 7.25 and 7.26. Both the first and upper stage show a high correlation between mass and payload mass. An increase of payload drives the vehicle heavier. The increase in GTOW of the vehicle is found almost linear with payload mass. Between a payload mass of 50 kg and 150 kg the GTOW increases 118.1 kg for every kilogram of payload. Between 150 kg and 250 kg of payload mass this increase is 138.0 kg per kilogram of payload. Between 250 kg and 500 kg this increase per kilogram of payload is 133.0 kg. On average the increase is 130.8 kg for every kilogram of payload.

For the total mass of the upper stage similar behaviour is found. For every kilogram of extra payload between 50 kg and 150 kg the total upper stage mass is increased with 20.7 kg. Between a payload mass of 150 kg and 250 kg this increase is 20.4 kg. And for payloads between 250 kg and 500 kg this increase is 20.5 kg for every kilogram of payload. On average the total upper stage mass increases 20.5 kg for every kilogram of payload.

First stage				**Upper stage**		
	50 kg payload	**250 kg payload**	**500 kg payload**	**50 kg payload**	**250 kg payload**	**500 kg payload**
Dry mass [**kg**]	4716.07	7654.25	11804.45	255.07	410.16	558.43
Propellant consumption [**kg**]	22673.97	41238.21	65207.27	3470.93	7225.04	11961.58
Total mass [**kg**]	31166.03	56777.66	90031.74	3776.00	7885.20	13020.02
Vacuum thrust [**kN**]	332.715	764.004	1241.542	27.295	56.086	90.536
Vacuum specific impulse [**s**]	301.41	284.57	280.73	321.56	313.46	307.18
ΔV [**m/s**]	3733.96	3418.21	3374.79	7933.57	7624.37	7560.28
Return ΔV [**m/s**]	196.12	390.34	352.57	-	-	-
Length [**m**]	17.809	21.207	24.682	5.093	5.382	6.202

Table 7.5: Optimal design of the launch vehicle for three different payload masses

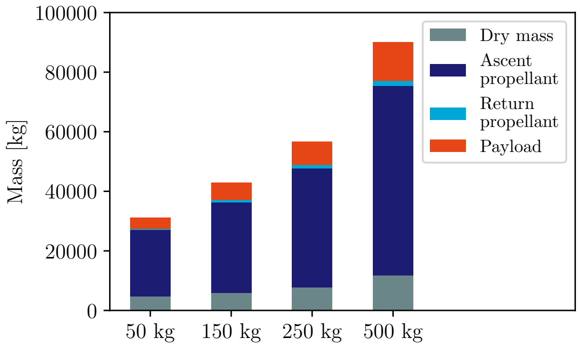

Figure 7.25: Optimal mass distribution of the first stage for four different payload masses

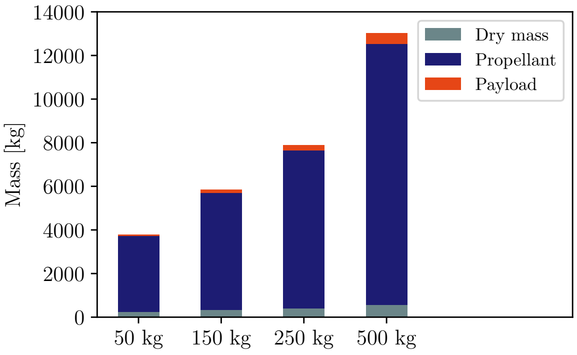

Figure 7.26: Optimal mass distribution of the upper stage for four different payload masses

For the dry mass of the first and upper stage the trend is less distinct. Between 50 kg of payload and 150 kg of payload the dry mass of the first stage only increases by 12.1 kg for every kilogram of payload. This increases to 17.3 kg for every kilogram of payload between a payload mass of 150 kg to 250 kg, while being 16.6 kg for every kilogram of payload between a payload mass of 250 kg to 500 kg. For the upper stage in the same payload ranges this is 0.92 kg per kilogram, 0.64 kg per kilogram and 0.59 kg per kilogram respectively.

The performance of the optimal designs in Table 7.5 show similar behaviour as found when varying orbital altitude. Larger and heavier vehicles converge to a solution with a higher thrust-over-weight ratio. The altitude and velocity profiles in Figure 7.27 to 7.30 show this behaviour. In the velocity profile the waved shape is visible, showing that the vehicle with more payload increases velocity more and at a higher rate. Different is the fact that the first stage ascent ΔV performance reduces consistent with payload mass. The ascent ΔV of heavier first stages is lower. The velocity profile, however, shows a larger velocity increase of heavier stages.

The shape of the trajectory shows close resemblance between the different solutions. Both the first and upper stages follow a similar flight path. The difference in staging velocity can be observed by the higher maximum altitude of the heavier stages.

The specific impulse shows that for an increase in payload the engine performance drops. This may sound counter-intuitive, but is explained by the following reason. Before the simulation was run it was determined that the exit diameter of the first stage engine is not allowed above 35 cm. The exit diameter of the upper stage engine is not allowed above 80 cm. The fact that the engines have to be mounted within the available diameter of the first and upper stage determined these dimensions. Beforehand the increase in size of the stage was not known. Hence for comparison reasons the maximum diameter was kept the same. As for heavier solutions the mass flow increases, so does the throat diameter. Combining a similar exit diameter with a larger throat results in a smaller expansion ratio. This results the engine performance decreasing.

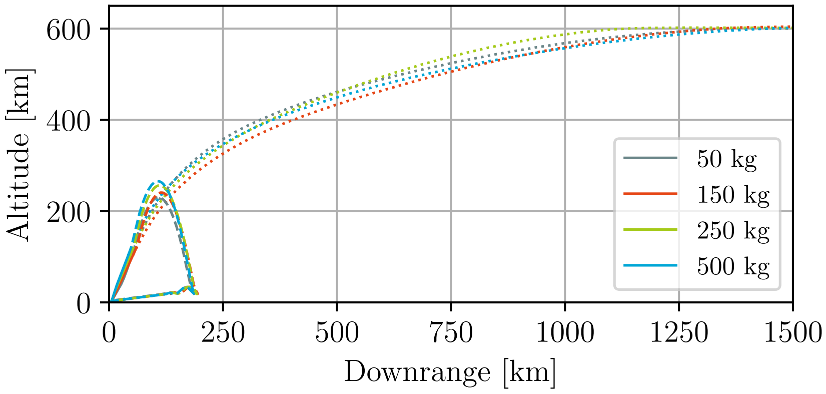

Figure 7.27: Optimal ascent and return trajectories for four different payload masses (legend valid for Figure 7.27 and 7.28)

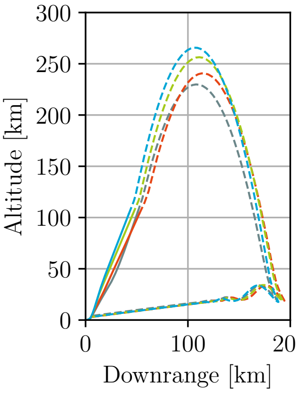

Figure 7.28: Optimal return trajectories for four different payload masses

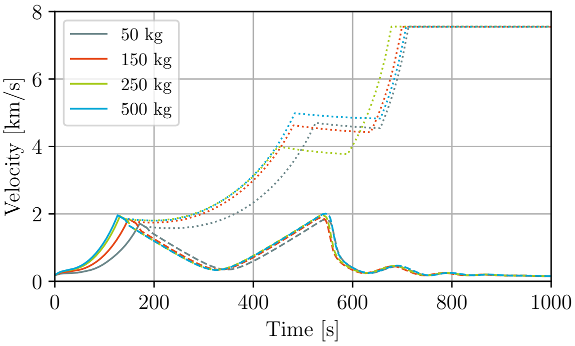

Figure 7.29: Velocity over time of the optimal ascent and return trajectories for four different payload masses (legend valid for Figure 7.29 and 7.30)

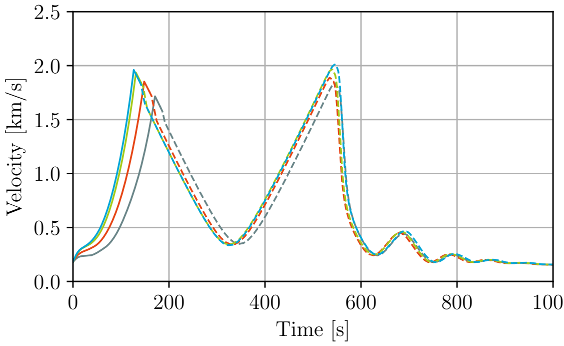

Figure 7.30: First stage velocity over time of the optimal ascent and return trajectories for four different payload masses

7.4. The effect of the selected return method

One of the main requirements of the first stage is to return to the spaceport of take-off. Two active methods were deemed most promising in the literature study (Haex, 2019), being aeroturn and in-plane pitch over. Furthermore, it is interesting to see if an active method is required for return. With glideback this results in three scenarios. Added to this is a scenario without return, to benchmark the impact of returning the vehicle.

Table 7.6 shows the optimal design vector for the different scenarios introduced. The corresponding designs are shown in Table 7.7. The mass budget of these designs is graphically shown in Figure 7.31 and 7.32. Not returning the first stage results in the lightest vehicle, with a first stage dry mass decrease of 13.7% and a GTOW decrease of 18.2%. For aeroturn the first stage dry mass increases by 7.6% with a GTOW increase of 4.7%. For glideback the increase in first stage dry mass is 4.6% with a 0.5% increase in GTOW. Both have a similar total upper stage mass, with an increase of 11.8% and 13.3% respectively. The first stage initial thrust-over-weight is higher for aeroturn and glideback. For aeroturn this increases to 1.29, while for glideback this increases to 1.35.

The difference in performance and mission geometry between different return methods is best shown by the total upper stage mass. The reason for this difference is shown in Figure 7.33 and 7.34. Not returning the first stage to the spaceport of launch makes the ascent trajectory more gradual. The reason for this is that by ascending more gradual the gravity loss is reduced. The gravity loss of this System is larger as compared to conventional launch vehicles, which is driven by the first stage return. On the one hand a gradual ascent is beneficial for gravity loss. On the other hand the first stage has more horizontal velocity when ascending more gradual. This results in more downrange, which at some point is violating the return constraint.

In-plane pitch over is able of steepening the first stage trajectory after staging by reducing the horizontal velocity component. The point of first stage re-entry is driven by the gliding range of the vehicle. Hence the burn of in-plane pitch over is such that it reduces the horizontal velocity enough for meeting the gliding range. This means that the upper stage is released at conditions beneficial for gravity loss, while the first stage is still able to return. The propellant of this burn limits the ascent performance of the first stage. More return propellant penalizes the ascent ΔV. The trade-off between ascent and return propellant shifts the first stage trajectory away from the unconstrained optimum, resulting in a steeper ascent. This shows also in the upper stage mass, which is

Vehicle design				**Trajectory design**			
	No return method	**Aeroturn**	**Glideback**		**No return method**	**Aeroturn**	**Glideback**
Fst. stage brnt. [**s**]	171.07	154.25	150.77	Node 1 [**deg**]	65.49	57.90	56.11
Up. stage brnt. 1 [**s**]	258.50	332.94	287.19	Node 2 [**deg**]	72.42	72.03	78.21
Up. stage brnt. 2 [**s**]	83.51	54.60	108.85	Node 3 [**deg**]	56.97	81.40	80.04
Coasting time [**s**]	127.77	150.50	101.68	Node 4 [**deg**]	55.93	77.17	79.51
Return time [**s**]	0	6.91	0	Node 5 [**deg**]	64.02	79.22	79.01
Engine amount [**-**]	14	13	13	Node 6 [**deg**]	38.86	48.12	54.31
Mass flow [**kg/s**]	10.82	15.63	15.49	Node 7 [**deg**]	22.29	23.82	31.76
Fst. stage exit diam. [**m**]	0.304	0.292	0.315	Node 8 [**deg**]	16.48	13.77	18.32
Up. stage exit diam. [**m**]	0.791	0.777	0.795	Node 9 [**deg**]	4.75	6.40	10.20
Up. stage diameter [**m**]	1.659	2.162	2.141	Node 10 [**deg**]	-0.99	-0.77	-1.64

Table 7.6: Optimal design input of the launch vehicle for three different return methods

First stage				**Upper stage**		
	No return method	**Aeroturn**	**Glideback**	**No return method**	**Aeroturn**	**Glideback**
Dry mass [**kg**]	5116.15	6376.79	6200.56	291.46	349.53	350.43
Propellant consumption [**kg**]	25923.44	32100.73	30368.05	3690.93	6033.80	6119.96
Total mass [**kg**]	35171.97	45010.84	43188.99	4132.39	6533.33	6620.39
Vacuum thrust [**kN**]	437.358	571.612	571.989	33.897	48.259	47.928
Vacuum specific impulse [**s**]	294.09	286.74	289.48	319.34	314.82	315.44
ΔV [**m/s**]	3855.35	3352.96	3448.99	7004.12	7937.42	7988.60
Return ΔV [**m/s**]	0	315.09	0	-	-	-
Length [**m**]	18.098	20.137	19.852	4.504	5.833	5.846

Table 7.7: Optimal design of the launch vehicle for three different return methods

heavier than when no return method is applied.

Aeroturn and glideback show a very similar upper stage. These two are highest in mass, as the trajectories are most inefficient in terms of gravity loss (for glideback see Appendix B). The trajectory profile shows a steep ascent for aeroturn and the steepest ascent for glideback. Considering gravity loss it may sound contradictory that both have a similar upper stage ΔV budget. This is explained by the fact that the first stage of glideback gains more velocity due to a lack of return propellant. This shows in Figure 7.35 and 7.36. Due to the higher injection velocity of the upper stage ascent with a similar ΔV budget is possible along a more inefficient trajectory in terms of gravity loss.

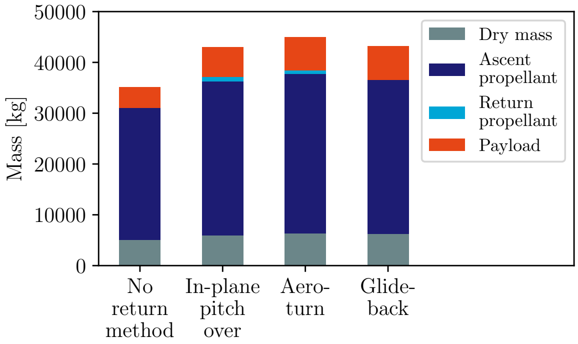

Figure 7.31: Optimal mass distribution of the first stage for four different return methods

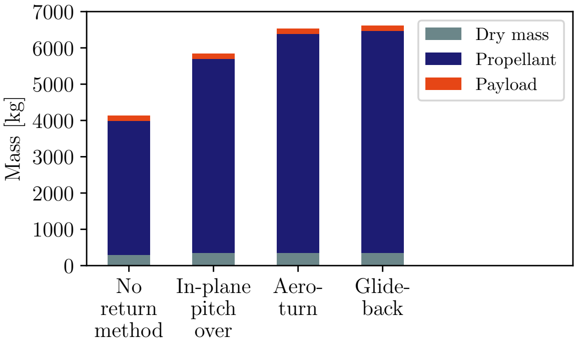

Figure 7.32: Optimal mass distribution of the upper stage for four different return methods

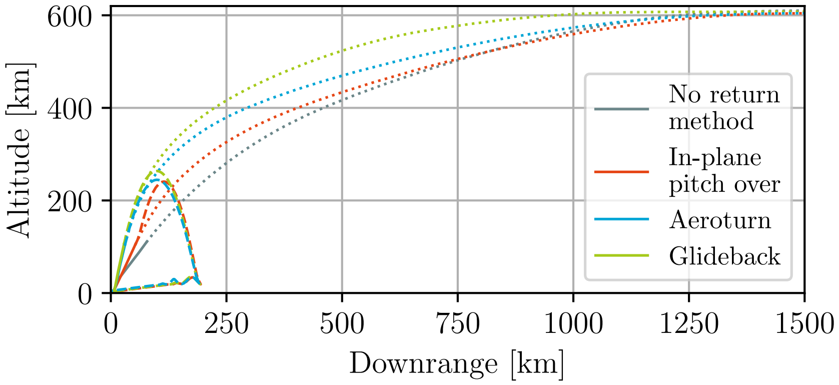

Figure 7.33: Optimal ascent and return trajectories for four different return methods (legend valid for Figure 7.33 and 7.34)

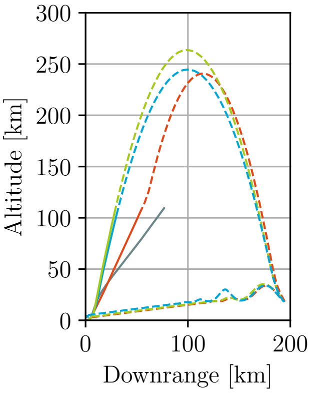

Figure 7.34: Optimal return trajectories for four different return methods

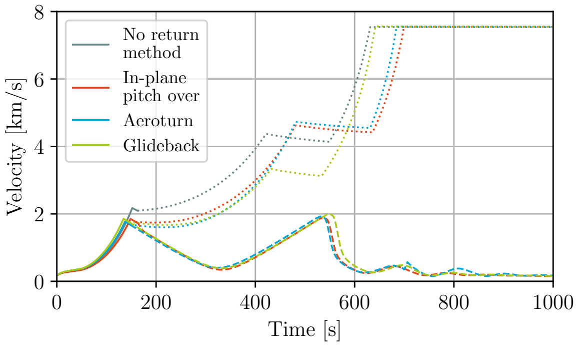

Figure 7.35: Velocity over time of the optimal ascent and return trajectories for four different return methods (legend valid for Figure 7.35 and 7.36)

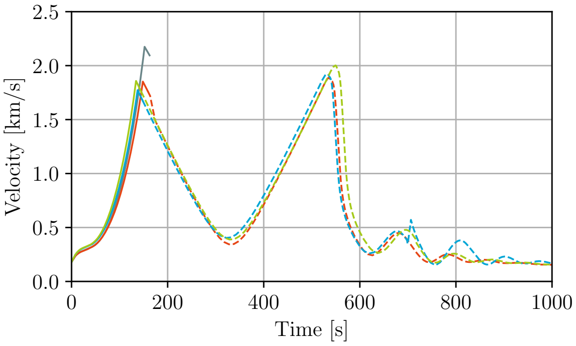

Figure 7.36: First stage velocity over time of the optimal ascent and return trajectories for four different return methods

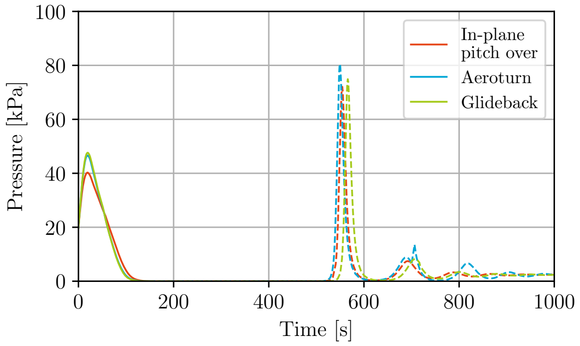

Figure 7.37: Dynamic pressure experienced by the first stage during ascent and return (legend valid for Figure 7.37 and 7.38)

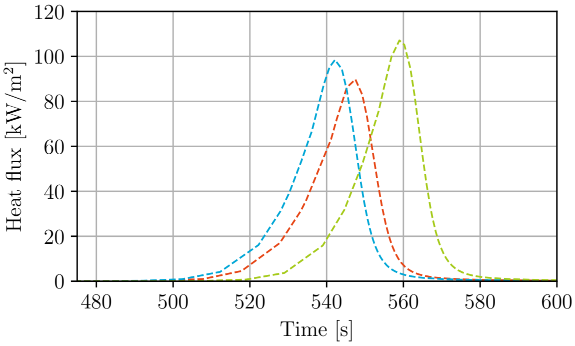

Figure 7.38: Stagnation point heat flux experienced by the first stage during ascent and return

In the comparison between aeroturn and glideback something very interesting is visible. Both vehicles show great similarity both in the design and in the trajectory. The only difference is the return burn of aeroturn after staging. However, this return burn is not required for gliding towards the spaceport. Apparently the optimum is such that rather a steep ascent is selected, instead of using a large return burn. In the aeroturn method still some return propellant is carried, making the configuration inefficient and heavy. The result shows that when comparing aeroturn and glideback the latter is preferred.

The comparison of main interest is found to be between in-plane pitch over and glideback. For glideback to be possible high upper stage performance is strictly necessary. This can only be achieved by having a very high PMF (= 0.946). When this is achieved glideback has great potential possibly favouring for in-plane pitch over. There is a small difference in total vehicle dry mass mass of 4.4%. However, the subsystems for attitude control are not modelled in the in-plane pitch over model, which in reality will make the difference even smaller. In-plane pitch over does require a complex manoeuvre to be done right after staging. Omitting this manoeuvre makes the System less complex and more robust. It is expected that when the upper stage allows for glideback, this is the favoured option.

The heat load on the vehicle does differ between the different return methods. Hellman (2007) discussed that the in-plane pitch over return method reduces the heat load on the vehicle by reducing the vehicles velocity outside of the atmosphere. Figure 7.38 shows that indeed in-plane pitch over shows the lowest heat flux (~90 kW/m^2) in the stagnation point due to the lower entry velocity. The entry velocity of aeroturn is higher resulting in a heat flux of almost 100 kW/m^2. For glideback this is highest resulting in a heat flux of more than 105 kW/m^2. The difference is as expected. Important is the fact that the difference is ~16%, which makes the three methods similarly feasible.

Next the total heat load on the stagnation point is compared. This is 1.8 MJ/m^2 for in-plane pitch over. For aeroturn this increases to 2.0 MJ/m^2. Glideback results in a total heat load of 2.1 MJ/m^2 in the stagnation point. Also this difference is ~16% which supports the statement that the three methods are similarly feasible. This means that in the selection of the preferred return method the heat analysis is discarded from the trade-off.

For completion Figure 7.37 shows the dynamic pressure of the different return methods. Also this figure supports the idea that the differences in terms of pressure and heat between the different solutions are negligible.

7.5. Variations in design and operational scenarios

This section shows smaller variations in the design and operational scenarios of the vehicle. First the engine layout and design is addressed, next the fairing prohibition is examined and finally alternative launch configurations are compared.

7.5.1. Engine design

The development process benefits from using a shared engine design to propel the first and upper stage. To identify if this is a feasible idea and to find the design consequence of this idea different engine configurations are compared. In the first configuration the first and upper stage engines are individually designed. Electron and SpaceX use nine commonly designed engines to propel the first stage. To see if this optimum is also valid for this vehicle the second first stage design holds nine engines.

Table 7.8 shows the optimal design vectors for the different engine configurations. First the configuration with a single first stage engine is compared. The total first stage mass flow of this configuration is 2.5% smaller, while the upper stage mass flow is 3.0% smaller. The first stage burn time is 5.0% larger, while the upper stage burn time is 11.0% smaller.

The configuration with nine first stage engines shows larger differences. The total first stage mass flow is 13.0% lower, while the upper stage mass flow is 25.7% larger. The increase in first stage burn time due to the lower mass flow is 23.2%. The upper stage burn time is similar with a 2.9% reduction.

In the corresponding design these differences are visible. When comparing the single first stage engine config-

Vehicle design			**Trajectory design**		
	One first stage engine	**Nine first stage engines**		**One first stage engine**	**Nine first stage engines**
Fst. stage brnt. [**s**]	176.30	206.92	Node 1 [**deg**]	48.88	61.13
Up. stage brnt. 1 [**s**]	278.18	323.14	Node 2 [**deg**]	68.47	64.69
Up. stage brnt. 2 [**s**]	65.95	52.05	Node 3 [**deg**]	72.78	73.00
Coasting time [**s**]	189.62	190.92	Node 4 [**deg**]	63.47	73.58
Return time [**s**]	7.44	6.80	Node 5 [**deg**]	62.74	66.96
Fst. stage mass flow [**kg/s**]	175.87	17.45	Node 6 [**deg**]	34.39	38.52
Up. stage mass flow [**kg/s**]	13.46	17.45	Node 7 [**deg**]	21.03	21.71
Fst. stage exit diam. [**m**]	1.448	0.346	Node 8 [**deg**]	13.30	14.09
Up. stage exit diam. [**m**]	0.781	0.798	Node 9 [**deg**]	5.19	11.21
Up. stage diameter [**m**]	1.780	2.004	Node 10 [**deg**]	-0.61	-1.38

Table 7.8: Optimal design input of the launch vehicle for two different first stage engine configurations

First stage			**Upper stage**		
	One first stage engine	**Nine first stage engines**		**One first stage engine**	**Nine first stage engines**
Dry mass [**kg**]	5686.69	5985.11		328.87	396.00
Propellant consumption [**kg**]	32314.08	33092.25		4615.79	6544.12
Total mass [**kg**]	43095.43	46167.49		5094.66	7090.13
Vacuum thrust [**kN**]	516.322	447.714		41.789	53.761
Vacuum specific impulse [**s**]	299.27	290.60		316.66	314.14
ΔV [**m/s**]	3731.69	3469.69		7342.62	7898.29
Return ΔV [**m/s**]	607.762	269.45		-	-
Length [**m**]	19.661	19.794		4.744	5.100

Table 7.9: Optimal design of the launch vehicle for two different first stage engine configurations

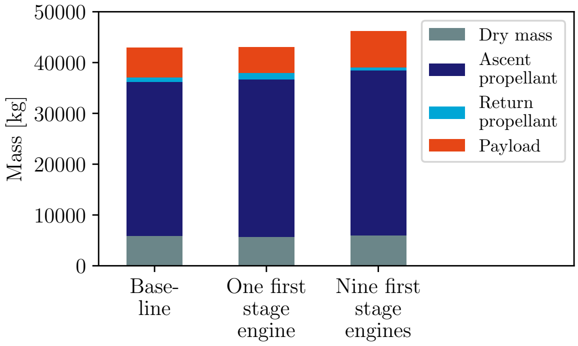

Figure 7.39: Optimal mass distribution of the first stage for three different engine configurations

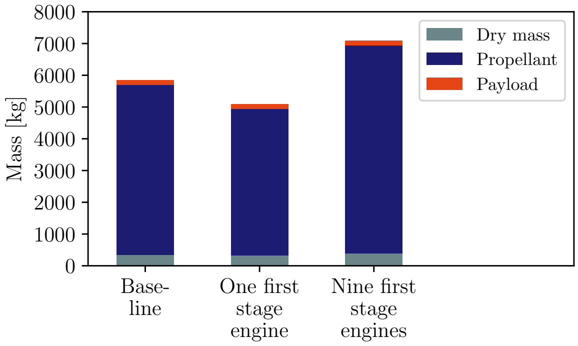

Figure 7.40: Optimal mass distribution of the upper stage for three different engine configurations

uration with the baseline the thrust is found 1.0% lower. The upper stage thrust is 2.6% lower. The dry mass of the vehicle is different. The first stage dry mass is 4.0% lower, which shows that a single engine configuration is more mass efficient. The upper stage dry mass is 5.1% lower. The specific impulse of the first stage engine is 1.6% higher. This is due to the expansion ratio being larger, which is allowed within the geometry of the first stage. Due to a larger propellant consumption the GTOW of the vehicle is increased by 0.3%.

The configuration with nine first stage engines shows a reduction in thrust of 14.1% for the first stage. The upper stage thrust is increased by 25.3%. This shows that the design is shifted from the optimum, primarily for not violating the acceleration constraint on the upper stage. The dry mass of the first stage is increased by 1.0%, while the dry mass of the upper stage is increased by 14.3%. This means that especially the upper stage becomes larger, which also shows in the 21.4% increase of total upper stage mass. The GTOW increases with 7.4%.

The trajectory and velocity profile are shown in Figure 7.41 to 7.44. The similarity between the baseline scenario and the scenario with a single first stage engine is clear. There is a large overlap in both the trajectory and velocity profile. The first stage with a single engine shows a slightly higher staging velocity. The corresponding upper stage shows a more gradual ascent. Combined this explains the lower upper stage mass.

The under performance of the nine engine lay-out is evident, with a thrust-over-weight ratio of 0.989. The first stage with nine engines is underpowered and even with the increased burn time is not able to inject the upper stage at the required velocity. This drives the size of the corresponding upper stage. The fact that this is different to the Electron or Falcon 9 is a result of the unconventional shape of the first stage. In this study the first stage is relatively heavy compared to the upper stage. This means that the first stage demands more thrust, while the upper stage does not. The result is a different multiple of commonly designed engines in the optimal design.

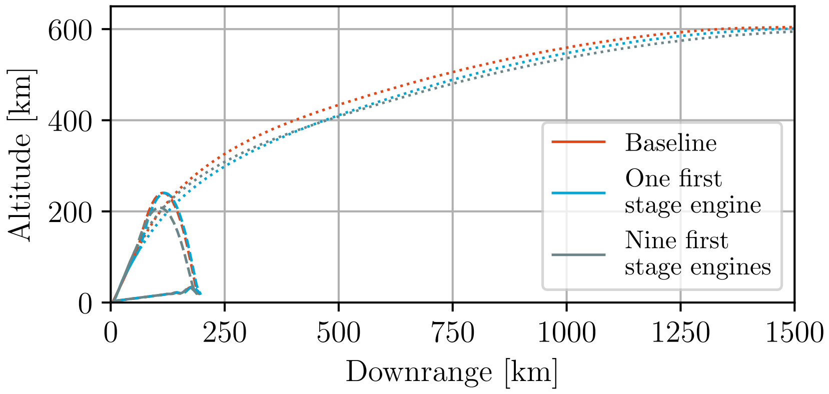

Figure 7.41: Optimal ascent and return trajectories for three different engine configurations (legend valid for Figure 7.41 and 7.42)

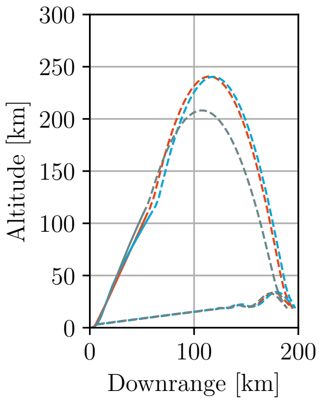

Figure 7.42: Optimal return trajectories for three different engine configurations

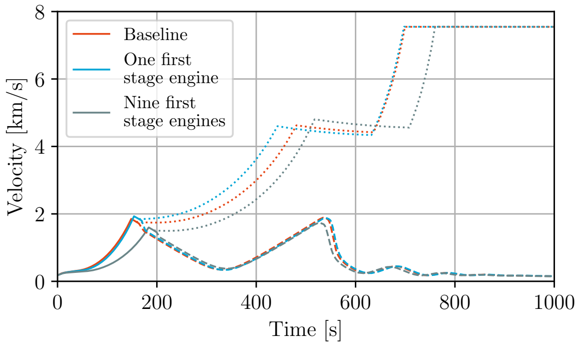

Figure 7.43: Velocity over time of the optimal ascent and return trajectories for three different engine configurations (legend valid for Figure 7.43 and 7.44)

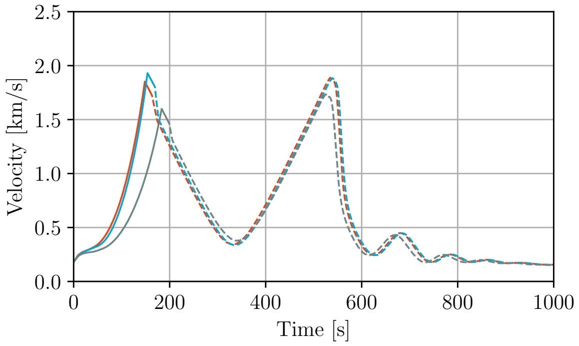

Figure 7.44: First stage velocity over time of the optimal ascent and return trajectories for three different engine configurations

7.5.2. Prohibition of fairing usage

Prohibiting fairing usage is identified crucial for the envisioned operations of the vehicle. It is expected that this drives the design, as it has a major influence on the moment of staging. If a fairing is used on the upper stage it can be injected in the optimal point from a trajectory perspective. However, if fairing usage is prohibited the upper stage can only be injected in a position meeting the aerothermal flux constraint.

The comparison between a scenario in which a fairing is allowed and in which it is prohibited is done for two different orbital injection altitudes. It is expected that the aerothermal flux constraint drives a low altitude solution more away from the optimum than a higher altitude solution. The scenarios in which a fairing is prohibited are the ones discussed in Section 7.2. The optimal design vectors as well as corresponding designs of the two scenarios in which a fairing is allowed are shown in Table 7.10 and 7.11. The mass budgets of these solutions are also shown in Figure 7.45 and 7.46.

At both injection altitudes the difference in design between solutions prohibiting and allowing a fairing shows a similar trend. At both altitudes allowing fairing usage results in a lighter vehicle. The trend is stronger for the 200 km solution, in which the first stage dry mass decreases with 9.6%. For 600 km the first stage dry mass decreases 1.0%. It is interesting to see that this difference is not driven by the design of the upper stage but, rather, by the total propellant mass of the first stage. The decrease in GTOW for the 200 km solution is 14.6%, while for the 600 km solution is 7.4%.

The increase in total upper stage mass when a fairing is allowed is 1.8% for the 600 km case. For the 200 km case this is much higher, being 26.3%. The reason for this is that when a fairing is allowed the staging point can be lowered. From an unconstrained perspective the optimal vehicle leans on a large upper stage. When the staging

Vehicle design			**Trajectory design**		
	600 km orbit with fairing	**200 km orbit with fairing**		**600 km orbit with fairing**	**200 km orbit with fairing**
Fst. stage brnt. [**s**]	142.02	138.13	Node 1 [**deg**]	52.25	54.02
Up. stage brnt. 1 [**s**]	349.19	280.72	Node 2 [**deg**]	56.82	33.03
Up. stage brnt. 2 [**s**]	55.81	96.89	Node 3 [**deg**]	66.45	57.26
Coasting time [**s**]	206.73	12.35	Node 4 [**deg**]	70.75	68.98
Return time [**s**]	11.11	5.89	Node 5 [**deg**]	57.68	64.78
Engine amount [-]	14	9	Node 6 [**deg**]	35.85	26.85
Mass flow [**kg/s**]	13.54	14.38	Node 7 [**deg**]	22.59	19.04
Fst. stage exit diam. [**m**]	0.307	0.277	Node 8 [**deg**]	13.64	5.83
Up. stage exit diam. [**m**]	0.792	0.713	Node 9 [**deg**]	-2.40	-0.21
Up. stage diameter [**m**]	2.014	1.808	Node 10 [**deg**]	0.65	0.98

Table 7.10: Optimal design input of the launch vehicle when the use of a fairing is allowed for two different orbital altitudes

First stage			**Upper stage**	
	600 km orbit with fairing	**200 km orbit with fairing**	**600 km orbit with fairing**	**200 km orbit with fairing**
Dry mass [**kg**]	5866.64	4241.82	326.51	349.85
Propellant consumption [**kg**]	27965.82	18295.91	5468.69	5405.50
Total mass [**kg**]	39777.67	28443.08	5945.20	5905.35
Vacuum thrust [**kN**]	540.783	363.415	42.065	44.236
Vacuum specific impulse [**s**]	290.89	286.31	316.88	313.76
ΔV [**m/s**]	3221.33	2780.19	7843.03	7597.99
Return ΔV [**m/s**]	470.76	267.21	-	-
Length [**m**]	19.335	16.810	5.679	4.991

Table 7.11: Optimal design of the launch vehicle when the use of a fairing is allowed for two different orbital altitudes

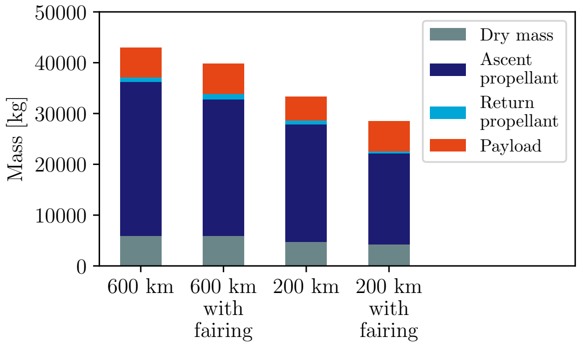

Figure 7.45: Optimal mass distribution of the first stage for configurations without and with the use of a fairing at two different orbital altitudes

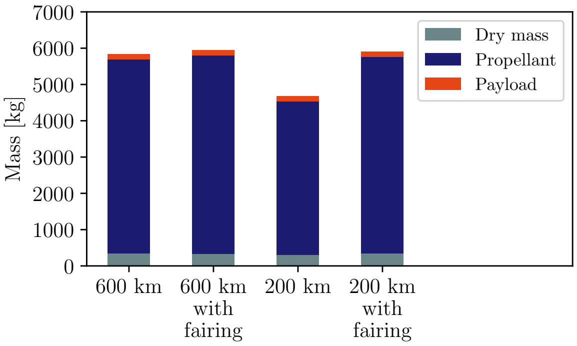

Figure 7.46: Optimal mass distribution of the upper stage for configurations without and with the use of a fairing at two different orbital altitudes

point is constrained by the aerothermal flux the first stage increases in size, while the upper stage decreases in size. For a low altitude scenario the difference between the staging altitudes is larger. Hence is the difference in first and upper stage dry mass, upper stage total mass and GTOW.

The trajectory and velocity profiles shown in Figure 7.47 to 7.50 support this observation. For both scenarios in which the use of a fairing is prohibited the staging altitude is risen above 100 km. When a fairing is allowed this altitude drops to 90 km for the 600 km solution. For the 200 km solution this altitude drops below 75 km. Both drops result in less propellant use of the first stage, however, for the latter this is more dominant. For the 200 km solution the drop allows for increasing the upper stage size (read ΔV contribution), converging closer to the optimal ratio. The trajectory profile shows that the 200 km upper stage allowing fairing usage does not overshoot the target altitude as much as the one prohibiting fairing usage.

The velocity figures show that not only the staging altitude, but also the staging velocity drops when the use of a fairing is allowed. Again this is similar for both orbital altitudes, however, stronger for the 200 km altitude solution.

The compared scenarios show that prohibiting the use of a fairing drives the vehicle away from the optimal ΔV distribution between the first and upper stage. This is a result of the staging conditions being constrained. When a fairing is not allowed the vehicle stages above 100 km in altitude. Both this altitude and the corresponding velocity lower when a fairing is allowed.

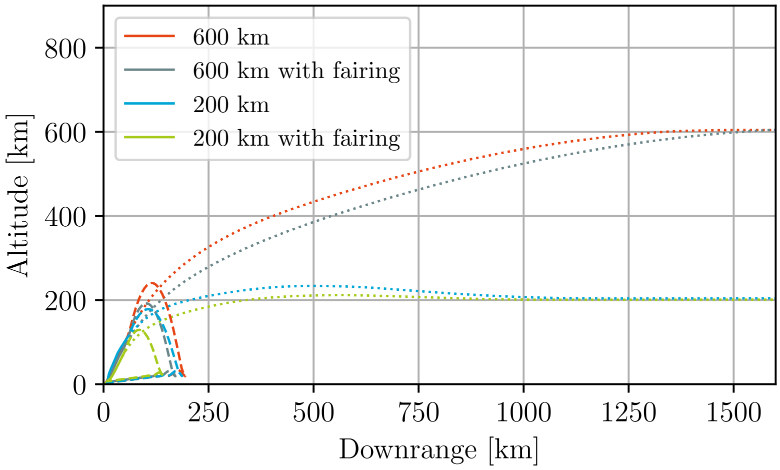

Figure 7.47: Optimal ascent and return trajectories for configurations without and with the use of a fairing at two different orbital altitudes (legend valid for Figure 7.47 and 7.48)

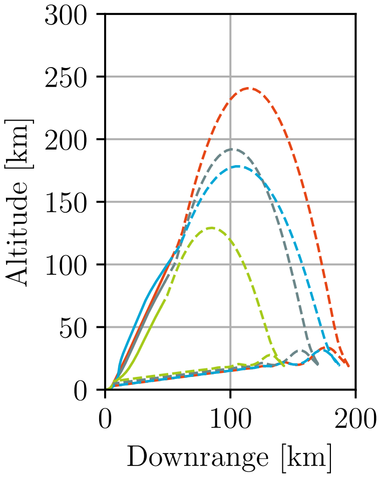

Figure 7.48: Optimal return trajectories for configurations without and with the use of a fairing at two different orbital altitudes

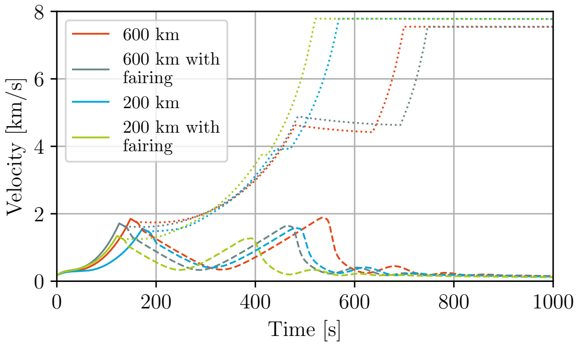

Figure 7.49: Velocity over time of the optimal ascent and return trajectories for configurations without and with the use of a fairing at two different orbital altitudes (legend valid for Figure 7.49 and 7.50)

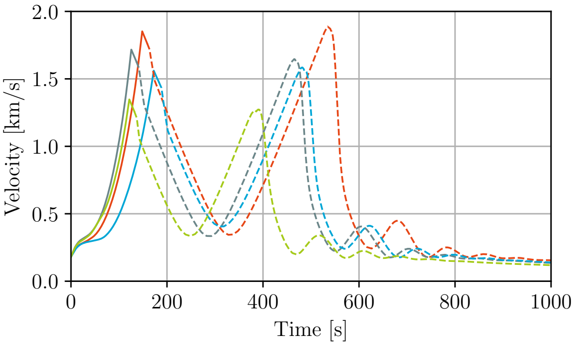

Figure 7.50: First stage velocity over time of the optimal ascent and return trajectories for configurations without and with the use of a fairing at two different orbital altitudes

It is shown that this effect is stronger for a solution going into a lower altitude orbit. This is due to the fact that the difference in staging conditions for these solutions is larger. Hence the result on the design is also larger.

7.5.3. Alternative launch configurations

Different launch configurations are compared. The idea of a different configurations is that by using some form of assistance during take-off the mass of the landing gear is reduced. This is possible due to the fact that the landing gear is now sized for landing loads. For a launch vehicle the mass difference between take-off and landing is enormous. Only using the landing gear during landing creates a lighter vehicle, but also introduces a dependency on another system.

The first scenario uses a cart on the runway to support the first stage. The cart does not actively propel the vehicle. This is still done by the main engines. The second scenario is more common and uses air-launch to launch the vehicle. Air-launch is a technique in which the launch vehicle is mounted underneath a carrier aircraft. This carrier aircraft takes off and gains altitude and velocity until the required separation conditions are met. Once met the vehicle is released, which is the start of the independent flight. In this study the first stage is released at 40000 ft altitude with a velocity of 220 m/s and at a flight path angle of 10.8° with a heading of 0° (similar to the injection conditions of the vehicle by Maddock et al. (2018)).

The optimal design vectors of the alternative launch configurations are shown in Table 7.12. The corresponding designs are shown in Table 7.13. The mass budget is graphically shown in Figure 7.51 and 7.52. The reduction in first stage dry mass is obvious. Assisting the vehicle during take-off reduces the first stage dry mass with 24.6%, while the GTOW is only reduced by 7.7%. The corresponding upper stage total mass is reduced by 16.0%, which reduces the dry mass by 8.5%. Due to the lower dry mass the ascent ΔV budget of the first stage is increased by

Vehicle design			**Trajectory design**		
	Take-off assist	**Air launch**		**Take-off assist**	**Air launch**
Fst. stage brnt. [**s**]	171.12	119.20	Node 1 [**deg**]	60.22	35.23
Up. stage brnt. 1 [**s**]	278.14	253.17	Node 2 [**deg**]	53.35	82.86
Up. stage brnt. 2 [**s**]	90.07	105.45	Node 3 [**deg**]	65.56	55.70
Coasting time [**s**]	108.58	132.03	Node 4 [**deg**]	68.56	65.65
Return time [**s**]	16.62	17.69	Node 5 [**deg**]	58.56	59.90
Engine amount [-]	14	12	Node 6 [**deg**]	43.46	32.73
Mass flow [**kg/s**]	12.06	13.91	Node 7 [**deg**]	22.52	29.50
Fst. stage exit diam. [**m**]	0.301	0.318	Node 8 [**deg**]	17.60	18.73
Up. stage exit diam. [**m**]	0.740	0.599	Node 9 [**deg**]	9.58	7.12
Up. stage diameter [**m**]	1.752	1.779	Node 10 [**deg**]	-2.28	-1.29

Table 7.12: Optimal design input of the launch vehicle for two alternative launch configurations

First stage			**Upper stage**	
	Take-off assist	**Air launch**	**Take-off assist**	**Air launch**
Dry mass [**kg**]	4467.13	3955.61	317.22	336.99
Propellant consumption [**kg**]	30303.79	21374.93	4438.53	4980.06
Total mass [**kg**]	39676.67	30797.58	4905.75	5467.05
Vacuum thrust [**kN**]	483.849	477.416	37.454	42.277
Vacuum specific impulse [**s**]	292.09	291.54	316.65	309.91
ΔV [**m/s**]	3734.97	2970.83	7301.71	7349.44
Return ΔV [**m/s**]	782.62	907.13	-	-
Length [**m**]	19.039	17.460	4.685	4.877

Table 7.13: Optimal design of the launch vehicle for two alternative launch configurations

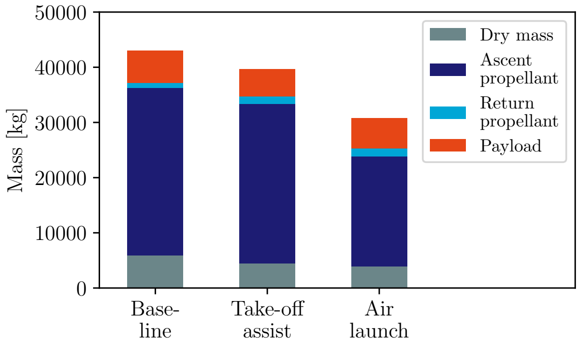

Figure 7.51: Optimal mass distribution of the first stage for three alternative launch configurations

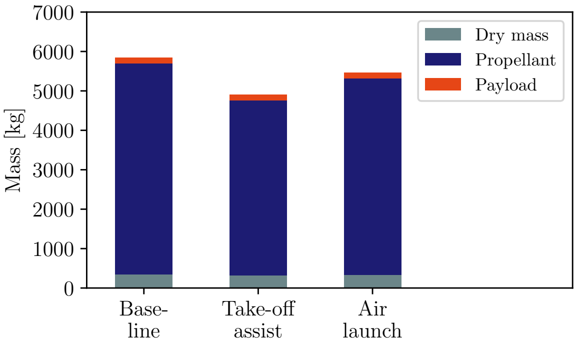

Figure 7.52: Optimal mass distribution of the upper stage for three alternative launch configurations

5.8%. The return ΔV is increased even more by 93.9%. Due to the higher first stage ascent ΔV the upper stage ΔV is reduced by 4.2%. The first stage thrust-over-weight ratio is only 0.6% higher.

For the air-launched vehicle the difference is even larger. In this case the carrier aircraft takes care of the first part of velocity and altitude gain. Also the pressure loss is smaller. The first stage dry mass is reduced by 33.3%, with a GTOW reduction of 28.3%. The main reason for this reduction is the fact that the ascent ΔV of the first stage is reduced by 15.9%. The return ΔV, however, is increased by 124.7%. The reduction of dry upper stage mass is 2.8%, with a total mass reduction of 6.4%. The ascent ΔV of the upper stage is reduced by 3.5%. The first stage

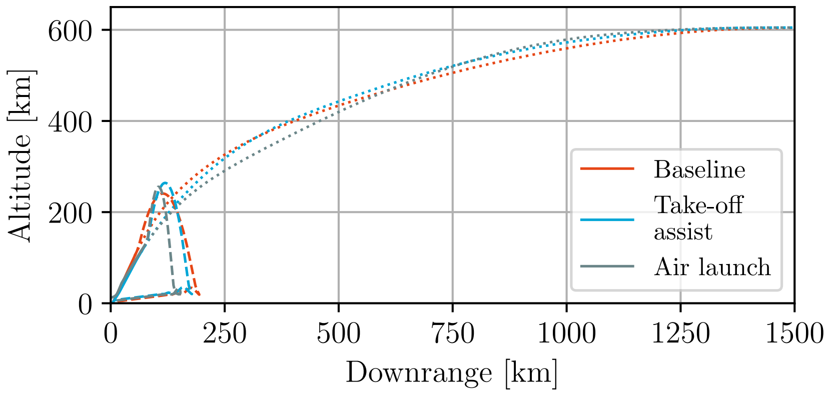

Figure 7.53: Optimal ascent and return trajectories for three alternative launch configurations (legend valid for Figure 7.53 and 7.54)

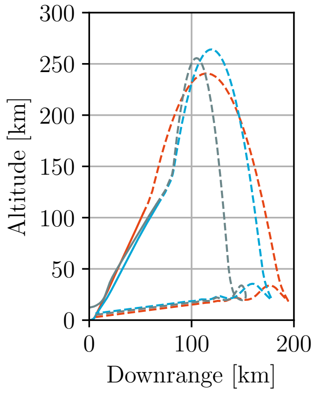

Figure 7.54: Optimal return trajectories for three alternative launch configurations

thrust-over-weight ratio is 27.8% higher.

Especially the return performance of the two different launch configurations is interesting. Figure 7.53 and 7.54 show this. Due to the lower first stage dry mass the vehicle has a tendency to lean more on the return method. The larger change in the first stage flight path angle after staging shows that the return burn is more energetic. The reason for this is the following. Due to the lighter first stage the total ΔV budget of this first stage is not as tightly constrained. This means that more return propellant can be added without the stage being unfeasible in terms of ascent ΔV performance. The ascent ΔV remains sufficient for injection of the upper stage even with a larger return ΔV. The resulting ascent trajectory can be more gradual for better performance in terms of gravity loss. And still the first stage is able of returning to the spaceport of take-off.

Figure 7.55 and 7.56 support this by showing that indeed the injection velocity of the upper stage is sufficient. It is more than 10% higher than the injection velocity of the baseline case. Also the return burn is visible. Just after staging the alternative launch configurations show a larger reduction of velocity. The fact this reduction in velocity does not come close to the return ΔV is due to the horizontal burn. The return burn is primarily used for limiting downrange by reducing the horizontal velocity. The rest is done by gravity. This means that the burn is not optimal for reducing velocity but, rather, for changing direction. Most of the remaining velocity is transformed into potential energy, which is released during the descent back to Earth.

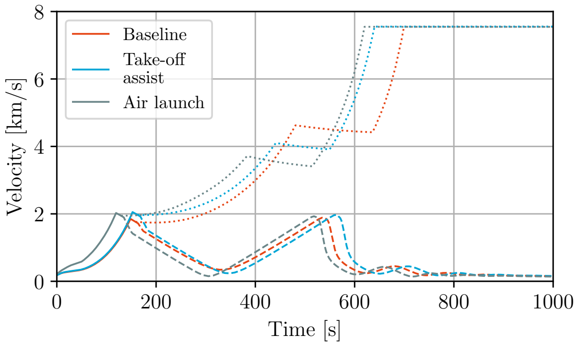

Figure 7.55: Velocity over time of the optimal ascent and return trajectories for three alternative launch configurations (legend valid for Figure 7.55 and 7.56)

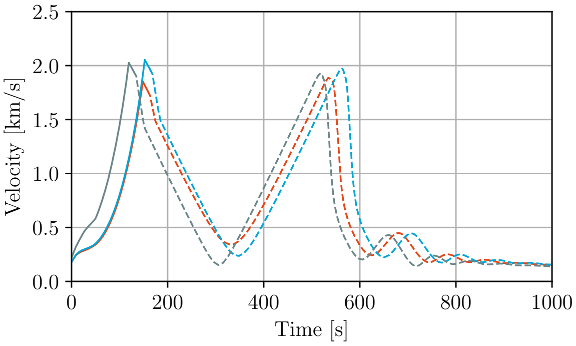

Figure 7.56: First stage velocity over time of the optimal ascent and return trajectories for three alternative launch configurations

7.6. Trajectory behaviour in the dense atmospheric layers

Launch vehicle					
	150 m turn	**1500 m turn**	**3000 m turn**	**4000 m turn**	**5000 m turn**
First stage dry mass [**kg**]	5926.45	6023.19	5840.96	6103.95	5809.45
First stage propellant consumption [**kg**]	31204.61	31514.81	29725.80	32706.38	29943.23
First stage total mass [**kg**]	42972.77	43667.42	41234.63	44503.15	40327.89
Upper stage dry mass [**kg**]	346.59	359.15	328.91	343.14	290.17
Upper stage propellant consumption [**kg**]	5345.18	5620.28	5188.97	5199.68	4135.04
Upper stage total mass [**kg**]	5841.71	6129.42	5667.87	5692.83	4575.21

Table 7.14: Launch vehicle mass distribution for different turn altitudes (5000 m turn does not result in a polar orbit)

The airplane design of the first stage allows for aerodynamic manoeuvring in the dense layers of the atmosphere. On the other hand this same design increases the aerodynamic drag of the launch vehicle. Most airports do not have runways exactly in the desired heading of launch. The aerodynamic manoeuvring allows the launch vehicle to change the heading into the correct orientation for the desired orbit inclination. This section aims to identify the optimal trajectory of the launch vehicle in the dense layers of the atmosphere. This trajectory shall allow for an efficient change of heading, minimizing aerodynamic and gravity loss.

The following strategy is implemented. The altitude at which the heading turn is performed is gradually increased. The optimal design to get into orbit is determined for the different turn altitudes. Table 7.14 shows the result of this. Surprising is the fact that it does not matter at what altitude the turn is performed. There is no clear trend in the solutions, only differences do exist to the global optimizer.

What differs by increasing the altitude of turning is the ability of a successful heading change. Figure 7.57 shows the ground track of the different solutions all with a different altitude of turn. The figure shows that the solutions up to 4000 m are able of successfully changing the heading. The solution turning above 5000 m is not successful in doing so. The upper stage is injected eastward along a trajectory course matching with the latitude of launch. The figure shows that below a certain threshold the turn altitude does not matter. Above the threshold the vehicle cannot successfully turn, due to a fast reduction of the air density in the trajectory.

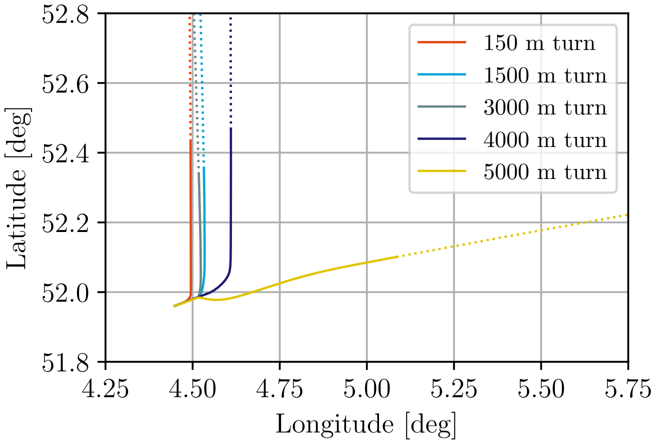

Figure 7.57: Ground track of the launch vehicle for different turn altitudes, showing the threshold behaviour of changing the azimuth

The shown behaviour is explained as follows. The velocity profile of the baseline case in Figure 7.11 shows that in the beginning of flight the velocity levels. This is due to the fact that in the beginning of flight an equilibrium is found between thrust, gravity and aerodynamic drag. The result is no acceleration of the vehicle. It is in this same period that the turn takes place. The only effect that the turn has on the trajectory is a slight reduction in ascent rate due to the bank angle. However, the beginning of the trajectory is not very sensitive to differences in the ascent rate.

The reason for an insufficient turn at higher altitudes is the air density. A minimum air density is required for aerodynamic manoeuvring. When the turn is initialized too late the ascent rate is already so large that the turn cannot be completed before leaving the dense atmosphere. The result is an Eastward heading around the centre of gravity of the Earth in correspondence with the latitude of take-off.

7.7. Summary of the discussed results

The results discussed in this chapter show the designs and corresponding trajectories of the launch vehicle, optimized for various scenarios. All variations are compared to the baseline scenario, in which the launch vehicle takes off at Rotterdam The Hague Airport. A 150 kg payload is injected into a 600 km polar orbit. The first stage returns to the spaceport by using the in-plane pitch over return method. Furthermore, this first stage is designed with 13 engines with a shared first and upper stage design, fairing usage is prohibited and the landing gear is sized for take-off.

The result is a vehicle with a total dry mass of 6273.04 kg of which 94.5% is reusable. The GTOW is 42972.8 kg. All design and operational requirements are met. For injection of the payload the upper stage is designed with a high PMF of 0.939, which is driven by the steep ascent trajectory of the first stage. This ascent trajectory is required for returning the first stage. The consequence of this is 30%-50% more gravity loss in the System when compared to traditional launch vehicles. On top of that, the first stage has more pressure and aerodynamic loss due to the different aerodynamic shape of the vehicle and the corresponding ascent with a longer duration in the dense layers of the atmosphere.

The change of the design as a result of a different orbital injection altitude is determined. For an increase in altitude the dry mass of the vehicle increases. This is mainly caused by an increase in first stage dry mass. The largest increase of 13.5% is found when the injection altitude is increased by 200 km. The largest decrease of 20.8% is found when the injection altitude is decreased by 400 km. In the first case the GTOW is increased by 9.6%, while in the latter case the GTOW is decreased by 22.5%.

The result also shows that for an increase in vehicle mass the thrust-over-weight ratio is increased. The smallest vehicle is designed with a thrust-over-weight ratio of 1.04, while the largest vehicle is designed with a thrust-over-weight ratio of 1.41.

An increase in payload mass increases the dry and total mass of the vehicle. The total mass increase is found to behave almost linearly with an increase in payload mass. The first stage GTOW is on average increased by 130.8 kg per kilogram payload, while the upper stage total mass is on average increased by 20.5 kg per kilogram payload. For the dry mass no linear trend is found, although it is clear that an increase in payload mass increases both the dry mass of the first and upper stage.

Of the three return methods included in the research only two are found interesting to compare. This is due to the fact that aeroturn and glideback show so much similarity in vehicle and trajectory design that immediately glideback is favoured, due to the reduced complexity of this method. When comparing in-plane pitch over with glideback, the latter is determined to be 4.4% heavier in total vehicle dry mass.

The heat rate and heat load in the return trajectories is found very similar. When using in-plane pitch over the heat rate in the stagnation point is ~90 kW/m^2 with a total heat load of 1.8 MJ/m^2. For glideback the heat rate and total heat load increase by ~16%.

The decision on which return method to use depends mainly on the upper stage design. For glideback an even steeper ascent trajectory is required, as the first stage needs to return to the airport passively. The result is an upper stage design with a PMF of 0.946. If this is possible glideback is favoured, due to the least complexity in first stage design.

The different design and operational scenarios are shortly summarized. It is found feasible to use a shared engine design as first and upper stage propulsion, with a first stage dry mass difference of 4.0%. The optimal distribution between first and second stage thrust levels is achieved by using 13 engines as first stage propulsion.

The prohibition of fairing usage increases the dry and total mass of the vehicle, caused by the increase in staging altitude. This effect is stronger for lower orbital injection altitudes. For 600 km altitude the first stage dry mass decreases 1.0% when the use of a fairing is allowed, while the GTOW reduces by 7.4%. For 200 km altitude the first stage dry mass is reduced by 9.6%, with a GTOW reduction of 14.6%. Interesting is that in this case the total dry mass of the upper stage increases by 26.3%.

Alternative launch configurations do decrease the dry and total mass of the vehicle. This was expected, as in this case the landing gear design is not driven by the GTOW. When a cart is used for support during take-off the first stage dry mass is reduced by 24.6%, while the GTOW is reduced by 7.7%. When air-launched is performed the first stage dry mass decreases by 33.3%, while the GTOW is lowered by 28.3%. This shows how strong the design is driven by the landing gear. The results also show that due to a relaxation of the tight velocity budget the solutions do lean more on the return method. When using a cart the return ΔV is increased by 93.9%, while when using air-launch the return ΔV is increased by 124.7%.

The effect of changing the heading of the first stage in the dense layers of the atmosphere is found small. There is no distinct optimal path, as long as the heading turn is performed before leaving the dense layers of the atmosphere. It is found that in this study this means that the heading turn must be performed at an altitude up to and including 4000 m.

8

Sensitivity of the studied results

To study the behaviour of the *Multidisciplinary Design Optimization* (MDO) tool in more detail the sensitivity of the tool is determined. The sensitivity analysis shows the numerical behaviour of the tool around the optimum. It is also important for determining the impact that uncertainties in the model have on the results. Several different techniques are applied to determine the sensitivity. First a one-at-the-time approach is used, showing the sensitivity on individual design parameters. This is followed by a Monte-Carlo analysis showing the sensitivity of the combined design parameters. Finally, a model based sensitivity analysis is performed. In this analysis the uncertainties of the model are used to quantify the impact these uncertainties have.

8.1. One-at-the-time approach

All the input parameters of the model are varied individually in the one-at-the-time approach. The corresponding result to this variation shows how sensitive the vehicle and trajectory is to the specific input parameter. The input parameters are varied in a systematic way, independent of expected model performance. This is done to have the most objective approach on sensitivity, without including predetermined ideas on the specific variables. First the control nodes are varied, which is followed by a variation of input times and vehicle design parameters.

The sensitivity is studied by determining the injection accuracy of the payload for a varied input. Also the change in vehicle mass and ΔV performance is compared, when this is dependent on the input variable. The change of the semi-major axis altitude and the eccentricity is determined as a measure of injection performance.

A change in semi-major axis altitude has the most impact on the payload. A manoeuvre raising or decreasing the orbital altitude is highly ΔV consuming. In this study a difference of ±55 km in semi-major axis is allowed, as this corresponds with approximately 30 m/s of ΔV. For the studied payload this means a propellant consumption of about 1.5 kg, which is 1% of the total payload mass. The semi-major axis altitude is not allowed to become smaller than 0.91 or larger than 1.09 times the original semi-major axis altitude.

Circularizing the orbit is not very ΔV demanding. To set a limit on the allowable eccentricity the orbit is not allowed to vary more than 150 km in altitude (±75 km). This corresponds with an eccentricity of approximately 0.01, which is ~15 times the original eccentricity.

8.1.1. Control node variation

The control nodes are varied by systematically adding and subtracting changes on the input angle. The fact that a fixed change is used without including the magnitude of the node is due to the following reasoning. In specific regions of the trajectory it is expected that a deviation from the optimal course affects the result. The magnitude of this deviation is driving the error independent of the magnitude of the node. A course change of 1° is expected to have similar impact on a node of 30° as on a node of 60°. The following vector of node change Δ_{cn} shows how much each node is varied in degrees:

$$\Delta_{\mathrm{cn}} = \pm\{0.0,\ 0.1,\ 0.2,\ 0.4,\ 0.8,\ 1.6,\ 3.2,\ 6.4,\ 12.8\} \tag{8.1}$$

Appendix C shows the sensitivity of all ten control nodes. Figure 8.1 to 8.4 show only the first and last node of both the first and upper stage. The result of the final first stage control nodes is more sensitive to variation than

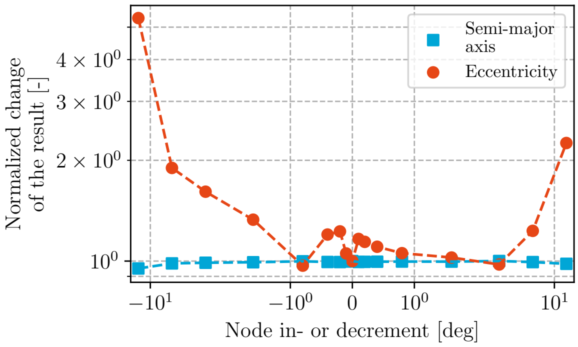

Figure 8.1: Normalized change of the semi-major axis altitude and eccentricity for in- and decrements of control node 1 (legend valid for Figure 8.1 to 8.4, a cross indicates exceeding the limit)

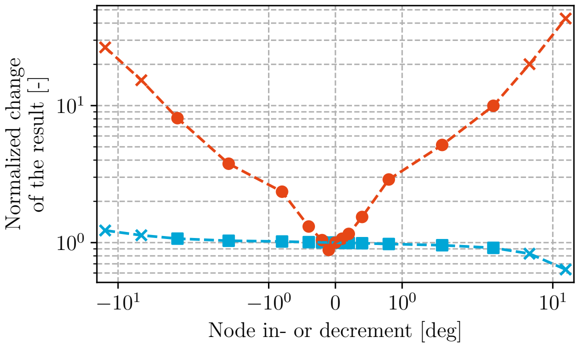

Figure 8.2: Normalized change of the semi-major axis altitude and eccentricity for in- and decrements of control node 5

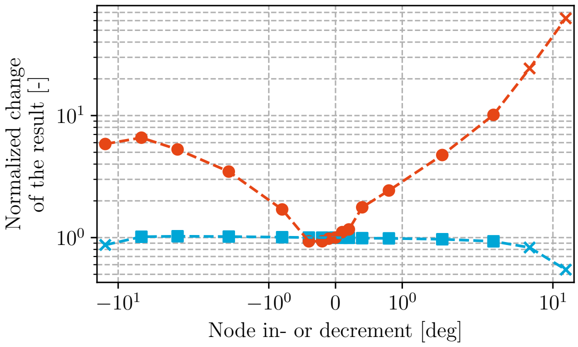

Figure 8.3: Normalized change of the semi-major axis altitude and eccentricity for in- and decrements of control node 6

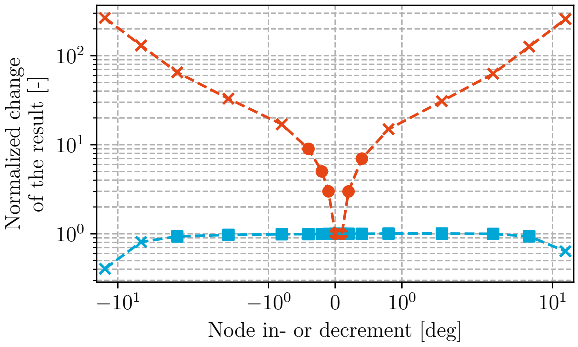

Figure 8.4: Normalized change of the semi-major axis altitude and eccentricity for in- and decrements of control node 10

the result of the beginning nodes. Varying the 2nd node shows the least sensitive behaviour, while varying the 4th node shows most sensitive behaviour. This means that the 4th node is driving the control requirement. The control requirement on the individual first stage nodes for meeting the injection criterium is less than +1.6° and -3.2° deviation of the desired flight path angle.

The upper stage control nodes show a similar sensitivity behaviour. The result becomes more sensitive to variations in consecutive nodes. Prominent is the fact that variations in the upper stage control nodes have more effect on the result than variations of the first stage control nodes have. This also showed in the convergence behaviour studied. The altitude of the semi-major axis is more sensitive to an increase than a decrease of the control nodes. For all but the last upper stage nodes the control requirement on the desired upper stage flight path angle is an accuracy of less than +0.8° and -1.6°. The final node requires a higher desired flight path angle accuracy being ±0.4°.

The control nodes of the first stage also affect the return behaviour. This is studied as well and the results are shown in Figure 8.5. The figure shows that the return result is most sensitive for the final first stage control nodes. Especially when they are lowered in magnitude the vehicle does not return. This shows that during control of the first stage it is important to assure no more than -0.2° deviation from the desired flight path angle.

8.1.2. Time and vehicle design variation

The sensitivity of individual time and vehicle design parameters is determined by increasing or decreasing the magnitude. This is done in a systematic way, however, now a multiplication structure is used. The time and vehicle design parameters do have a relation between the magnitude and the allowable change. One can imagine that for example a 1 cm error has more effect on an exit diameter of 30 cm than on an exit diameter of 80 cm. The multiplication structure used is shown by the following fraction vector f_{var}, which shows the percentage increase and decrease of each design variable:

$$f_{\text{var}} = \pm\{0.0,\ 0.1,\ 0.2,\ 0.4,\ 0.8,\ 1.6,\ 3.2,\ 6.4,\ 12.8,\ 24.6\} \tag{8.2}$$

Appendix C shows the sensitivities of all studied time and design parameters. The varied parameters have an effect on the vehicle design itself, which is why the change in total dry mass and ΔV is shown. This change also affects the orbital injection performance, which is shown by the change in semi-major axis altitude and eccentricity. Of all studied time parameters the result is found most sensitive to a variation in first stage burn time. Figure 8.6 and 8.7 show this sensitivity. The first stage burn time cannot change more than +3.2% and -1.6% before the solution violates the injection requirement. The corresponding burn time margin is +5.4 s and -2.7 s.

Assessing the sensitivity on time parameters shows how sensitive the model is for a certain propellant consumption. The sensitivities on burn and coasting time show a stepwise behaviour. In the first stage burn time figure this is hard to distinguish, however, in the first stage return time figure this is more clear. Also the variations in upper stage burn time show this effect. The reason of this behaviour is that stepwise functions are implemented in the vehicle model. The structure, internal geometry and tank configurations of both stages contain discrete differences in lay-out. The diameter of the first stage is determined based on the upper stage volume and the first stage propellant volume. When the return time is increased (this is also true for the first stage burn time, however, hard to see on that scale) more than 1.6% the vehicle steps into a wider configuration. This mainly impacts the wing mass scaling, which makes the wing 18.7 kg heavier. This increase acts as a snowball which increases the total mass by 28.2 kg.

The step increase of total vehicle mass is stronger for an increase in upper stage burn time. This is due to the fact that another effect plays a role, on top of the increase in wing mass. The increase in upper stage propellant creates a more voluminous upper stage. Close to the optimum this increase in upper stage volume affects the internal geometry of the first stage. However, the propellant consumption of the first stage is not changed. Due to this the first stage fuel tank is sized differently, with the fuselage around a spherical tank. Although a tank with a

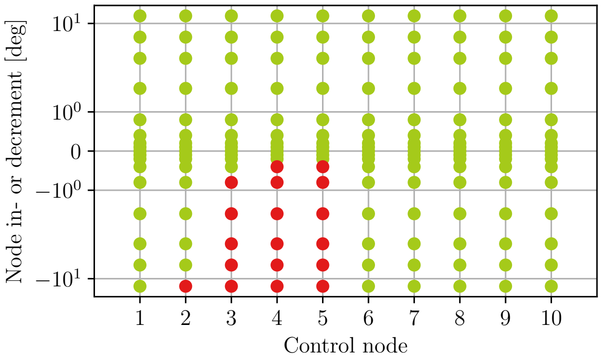

Figure 8.5: Sensitivity of the return for a one-at-the-time change of the individual control nodes at different levels of change (red indicates a non-return, while green indicates a successful return)

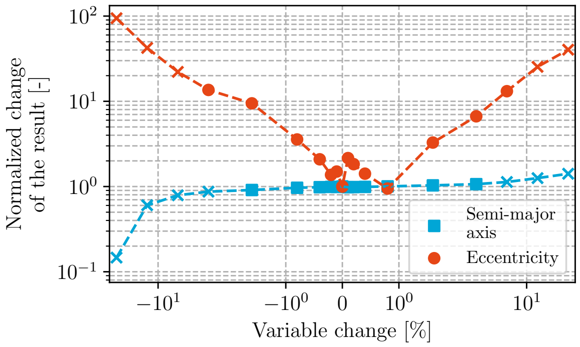

Figure 8.6: Normalized change of the semi-major axis altitude and eccentricity for a change of first stage burn time (legend also valid for Figure 8.8, a cross indicates exceeding the limit)

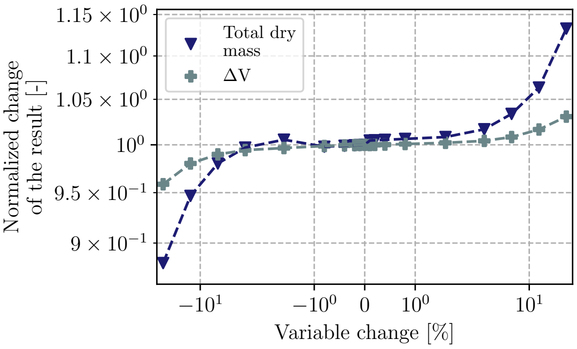

Figure 8.7: Normalized change of the total dry mass and ΔV for a change of first stage burn time (legend also valid for Figure 8.9)

spherical shape is lighter, this is not the case when the required thickness is below the minimum design thickness. Integration of a cylindrical fuel tank in the fuselage is more mass efficient. For the increased diameter this is not possible. If the upper stage burn time is increased with more than 1.0 s, the result is an increase of 58.0 kg of the integrated tank system in the first stage. This adds on top of the increase in wing mass.

Also interesting is the fact that for a large decrease of upper stage burn time the total vehicle also becomes heavier. This is explained by the fact that the reduced propellant consumption of the upper stage allows for a spherical tank configuration. The result is a 11.1% reduction of upper stage dry mass, however, with a 13.7% increase in length. This impacts the dry mass of the first stage negatively, by increasing this dry mass with 170.4 kg (2.9%).

Of all the vehicle design parameters the mass flow of the engines affects the result the most (an increase in oxidizer-over-fuel ratio is discarded, as well as an increase in engine amount). Figure 8.8 and 8.9 show this. It is important to realize that this change in mass flow is a consistent change throughout the burn of the engine also accounted for by the propellant consumption. This means that the sensitivity is not related to control issues around bias and oscillations during engine operations. Rather, it shows the design sensitivity of this parameter. The mass flow of the design cannot change more than +1.6% and -0.8% for sufficient payload injection.

Also the sensitivities of the vehicle design parameters show the stepwise behaviour. This is explained by similar reasoning. An example is the payload length. If this is increased the result is a lengthier and more voluminous upper stage. This results in a heavier first stage. The stepwise behaviour in the sensitivity to engine amount is due to the fact that the decimal number is rounded to a integer. This results in stepwise increase in the amount of engines.

The most inconsistent behaviour is found in the sensitivity to upper stage diameter. The figure shows that the total vehicle dry mass can increase, while also the ΔV budget increases. The explanation for this is the fact that this shows the trade-off between dry mass and stage performance. An increase in diameter allows for a spherical configuration of the upper stage, which makes the stage lighter. This also increases the upper stage ΔV. The increase in first stage mass, however, is larger than the decrease in upper stage mass. This means the total vehicle dry mass is higher. On the other hand the increase in upper stage ΔV is larger than the decrease in first stage ΔV, which is explaining the increase in total ΔV.

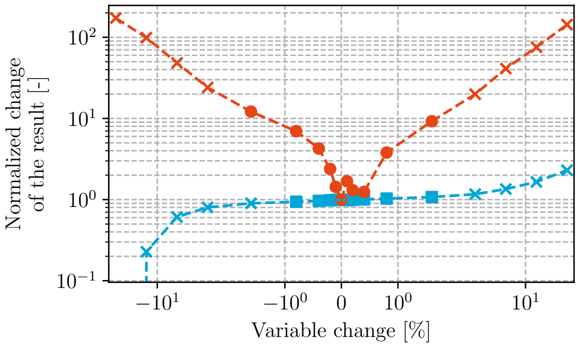

Figure 8.8: Normalized change of the semi-major axis altitude and eccentricity for a change of mass flow

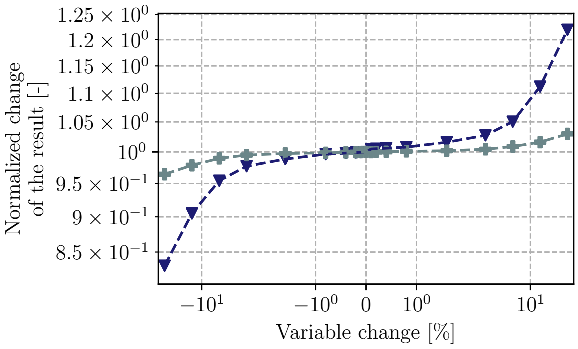

Figure 8.9: Normalized change of the total dry mass and ΔV for a change of mass flow

8.2. Monte-Carlo analysis

Uncertainties and errors never happen to only one specific variable. Instead all variables are simultaneously changed around the optimal design value. A Monte-Carlo approach is used to determine how the interaction of simultaneously varying parameters impacts the result. For all variables a normal distribution is assumed.

Figure 8.10 shows all different injection results based on a variation of control input. The standard deviation shown accounts for the increase or decrease of the control nodes. The solution is found similar sensitive when the control nodes are varied together. It was determined that all but the last control nodes are allowed to vary 0.8° individually, while the last is allowed to vary 0.4°. When the combined variation is taken into account the required accuracy for meeting the injection requirement has a standard deviation of ±0.25°, of which the 3σ value is ±0.75°.

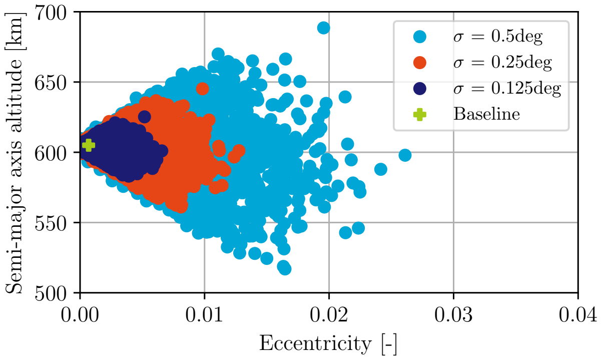

Figure 8.10: Result of the Monte-Carlo analysis showing the distribution of the orbital injection for three different normal distributed ranges of change of the control nodes

The next Monte-Carlo analysis performed quantifies the sensitivity to the different optimal time parameters. In the previous section this was done by multiplying the individual time by a factor to show the individual sensitivity behaviour. In the Monte-Carlo analysis this is done differently. Instead of multiplying the time parameters a normal distributed variation is added. This has the following reason. It is expected that designing for a certain magnitude in time is not so difficult. More difficult is to produce and operate the vehicle such that it exactly meets this designed magnitude of time. Similar as to the control nodes a normal distributed variation is used to account for this effect.

Figure 8.11 shows how the injection of the payload changes for variations in the different time parameters. The combination of the parameters results in a higher sensitivity. To meet the orbital injection requirement timing needs te be controlled with a standard deviation of 0.25 s, which means a 3σ of 0.75 s. This is less than the individual requirement of 2.7 s found on the first stage burn time. The required accuracy translates to 135.3 kg of propellant for the first stage. For the upper stage, considering both burns, the required accuracy translates to 20.82 kg of propellant.

In Figure 8.12 the stepwise behaviour of the model is also visible. The figure shows the varying total dry mass of the vehicle against the total ΔV budget. The stepwise behaviour results in islands of solutions. The most left island shows that solutions exist with a lower dry mass and similar ΔV performance. Reviewing these solutions shows that in this island solutions exist that do meet the orbital injection requirement. This means that it is worth to do a local optimization on the found solutions of the different scenarios. The Monte-Carlo analysis shows that the global optimizer approaches the optimum, but around the optimum a more optimal solution exists. The difference between these solutions, however, is 1.0% in total dry mass. Considering the margins in which the first stage model is validated, this is well within that limit.

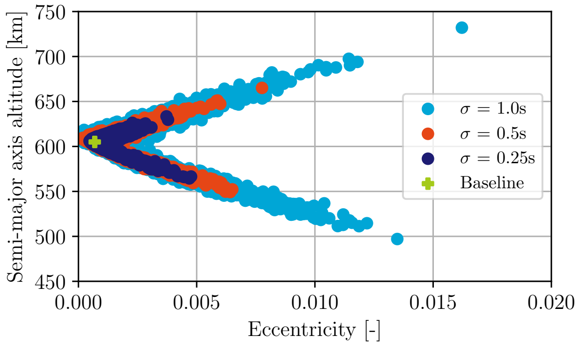

Figure 8.11: Result of the Monte-Carlo analysis showing the distribution of the orbital injection for three different normal distributed ranges of change in time (legend also valid for Figure 8.12)

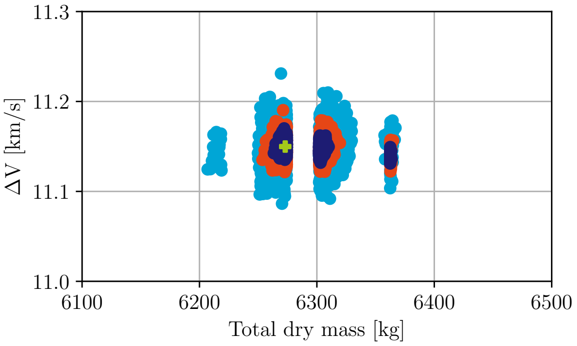

Figure 8.12: Result of the Monte-Carlo analysis showing the distribution of the total dry mass and ΔV for three different normal distributed ranges of change in time

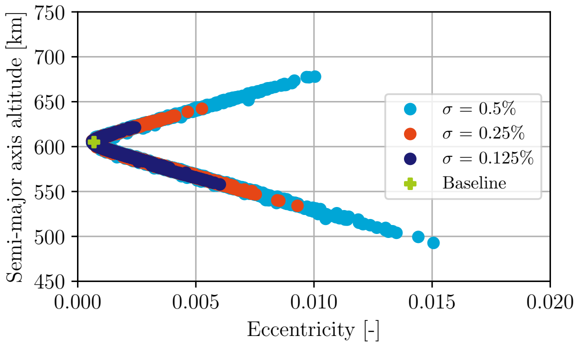

Figure 8.13: Result of the Monte-Carlo analysis showing the distribution of the orbital injection for three different normal distributed ranges of change in vehicle design parameters (legend also valid for Figure 8.14)

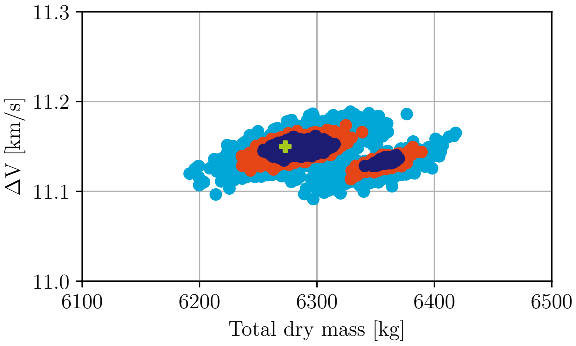

Figure 8.14: Result of the Monte-Carlo analysis showing the distribution of the total dry mass and ΔV for three different normal distributed ranges of change in vehicle design parameters

The final Monte-Carlo analysis that is performed quantifies the sensitivity of the solution for a variation of the vehicle design parameters, shown in Figure 8.13 and 8.14. In this case the change is related to the magnitude of a specific variable. Hence the standard deviation shows the percentage change of the parameters.

The solution is found sensitive to a combined variation of the vehicle design parameters. The individual parameter that effected the result the most was the mass flow which required 0.8% accuracy. For meeting the injection criterium with the combined variations an accuracy with a standard deviation of 0.125% is required, corresponding to a 3σ of 0.375%. For the mass flow this means that during the ascent the mass flow on average cannot vary more than ±52 g/s away from the optimum. For the first stage engine the exit diameter needs to be manufactured with an accuracy below 1.3 mm. The upper stage engine can be manufactured with an accuracy below 2.8 mm. Variations in engine chamber pressure are allowed not more than 0.375 bar. The upper stage diameter needs to be manufactured with an accuracy of 6.8 mm. For the payload the requirement results in an allowable difference in mass of 562.5 g, with a difference in length of 3.75 mm. When reviewing these accuracies none are found extremely hard to meet.

The stepwise behaviour shows also in the vehicle design parameter variation. However, for a variation with a standard deviation of 0.5% the solution space is found continuous again. The optimum found by the algorithm is in the island with a lower total dry mass for similar ΔV. However, the figure also shows that with a local optimizer the dry mass of the solution can be decreased approximately 1%.

8.3. Model based sensitivity analysis

In the development of the model several assumptions were made on the design of the vehicle and the trajectory. Also uncertainties exist, for example on the mass budget of the vehicle. This section aims on identifying the sensitivity of the results under influence of these assumptions and uncertainties. A model based procedure is followed, in which the assumptions and uncertainties are targeted individually. By understanding of the model changes are made to the implemented values. The optimization process is repeated, with these variations. The goal is to identify how the optimal design changes when optimized for a different value of assumptions.

The different models of the MDO tool are addressed. First the sensitivity to the propulsion model is determined. Next the aerodynamics model is addressed. This is followed by the sensitivity dependent on the geometry and mass model. Finally, the sensitivity on runway heading is computed.

8.3.1. Propulsion model

In the result of the baseline scenario two major assumptions were introduced regarding the propulsion model. It was shown that the oxidizer-over-fuel ratio is selected oxidizer rich, above the optimum found in literature. Furthermore, the engine quality is selected conservative, at the lower bound of the thrust quality range and the average domain of the propellant consumption quality.

The sensitivity dependent on these assumptions is determined. The oxidizer-over-fuel ratio is varied in regions more compliant with literature. The engine quality is systematically varied around the magnitude used in optimizing the baseline scenario.

Oxidizer-over-fuel ratio

Depending on the purity of the hydrogen peroxide the optimal oxidizer-over-fuel ratio for hydrogen peroxide/kerosene engines is approximately 7.3 (Moon et al., 2014).[1] To find how sensitive the result is to the oxidizer-over-fuel ratio two new designs are determined. The first design is optimized with an oxidizer-over-fuel ratio of 7.3. The second design is optimized with an oxidizer-over-fuel ratio of 7.8, which is in-between. Both optimal design input vectors are shown in Table 8.1. The corresponding optimal designs are shown in Table 8.2.

Vehicle design			**Trajectory design**		
	O/F - 7.8	**O/F - 7.3**		**O/F - 7.8**	**O/F - 7.3**
Fst. stage brnt. [**s**]	167.43	169.08	Node 1 [**deg**]	57.61	53.13
Up. stage brnt. 1 [**s**]	276.65	282.36	Node 2 [**deg**]	76.10	56.78
Up. stage brnt. 2 [**s**]	54.13	81.67	Node 3 [**deg**]	78.17	73.30
Coasting time [**s**]	207.00	149.04	Node 4 [**deg**]	62.12	67.92
Return time [**s**]	12.50	8.61	Node 5 [**deg**]	72.16	75.22
Engine amount [-]	11	12	Node 6 [**deg**]	39.82	42.55
Mass flow [**kg/s**]	16.47	14.37	Node 7 [**deg**]	21.28	27.01
Fst. stage exit diam. [**m**]	0.331	0.299	Node 8 [**deg**]	7.32	16.14
Up. stage exit diam. [**m**]	0.698	0.788	Node 9 [**deg**]	9.02	2.70
Up. stage diameter [**m**]	1.769	2.014	Node 10 [**deg**]	-0.98	-0.13

Table 8.1: Optimal design input of the launch vehicle for two different oxidizer-over-fuel ratios

First stage			**Upper stage**	
	O/F - 7.8	**O/F - 7.3**	**O/F - 7.8**	**O/F - 7.3**
Dry mass [**kg**]	5939.78	5883.04	359.17	327.57
Propellant consumption [**kg**]	31364.22	29892.43	5435.26	5215.34
Total mass [**kg**]	43248.43	41468.39	5944.44	5692.91
Vacuum thrust [**kN**]	519.377	492.145	50.706	44.772
Vacuum specific impulse [**s**]	292.23	290.93	313.93	317.77
ΔV [**m/s**]	3464.92	3465.03	7565.42	7722.92
Return ΔV [**m/s**]	458.19	339.11	-	-
Length [**m**]	19.561	19.698	5.129	5.688

Table 8.2: Optimal design of the launch vehicle for two different oxidizer-over-fuel ratios

First, the design with an oxidizer-over-fuel ratio of 7.3 is discussed. The total vehicle dry mass of this design is reduced by 1.0%, with a first stage dry mass reduction of 0.7% and an upper stage dry mass reduction of 5.5%. The *Gross Take-Off Weight* (GTOW) is reduced by 3.5%. Due to the reduction in mass the first stage thrust is reduced by 5.6%, while the upper stage thrust is increased by 4.3%. The total ascent ΔV performance of the vehicle is increased by 0.3%.

The solution with an oxidizer-over-fuel ratio of 7.8 is closer to the baseline scenario. The total vehicle dry mass is increased by 0.4%, with a first stage dry mass increase of 0.2% and an upper stage dry mass increase of 3.6%. The GTOW is increased by 0.6%. The reduction of first stage thrust is 0.4%, although the increase of upper stage thrust is 18.2%. This latter is explained by the fact that the solution converged to a first stage configuration with two engines less. This means a higher thrust level for the individual engines. The total ascent ΔV performance is decreased by 1.1%.

---

[1] Wade, M., 'H2O2/Kerosene', *Astronautix*, `http://www.astronautix.com/h/h2o2kerosene.html`, (accessed May 22, 2020).

Both solutions approach the baseline solution closely. Considering the fact that the margin on total dry mass due to global optimization was found in the order of 1%, the sensitivity found to the oxidizer-over-fuel ratio is deemed insignificant.

Engine quality

The engine quality assumption has great impact on the performance of the vehicle. Both the specific impulse and the thrust level get lowered by this assumption to account for losses in the engine. The result of a lower engine quality is a less efficient System with more propellant consumption. Especially the first stage dry mass is driven by the propellant consumption, which results in a snowball effect. It is expected that a variation of engine quality has a major impact on the total design.

To find the sensitivity of the result towards engine quality the assumption on the quality factor is systematically lowered and increased. Table 8.3 shows the optimal vehicle design vector for four different engine qualities, while Table 8.4 shows the corresponding optimal trajectory design vector. The corresponding first stage design is shown in Table 8.5 and the corresponding upper stage design is shown in Table 8.6.

Vehicle design				
	ζ_F - **0.88**	ζ_F - **0.90**	ζ_F - **0.94**	ζ_F - **0.96**
Fst. stage brnt. [**s**]	154.50	147.96	158.11	191.87
Up. stage brnt. 1 [**s**]	333.50	304.96	312.74	317.03
Up. stage brnt. 2 [**s**]	52.80	59.11	57.37	74.71
Coasting time [**s**]	129.74	163.33	171.69	106.33
Return time [**s**]	6.54	6.42	9.46	6.87
Engine amount [**-**]	14	14	13	11
Mass flow [**kg/s**]	18.79	16.61	13.16	12.17
Fst. stage exit diam. [**m**]	0.340	0.297	0.305	0.302
Up. stage exit diam. [**m**]	0.787	0.763	0.739	0.799
Up. stage diameter [**m**]	1.954	1.867	1.786	1.805

Table 8.3: Optimal vehicle design input of the launch vehicle for four different engine qualities

Trajectory design				
	ζ_F - **0.88**	ζ_F **-0.90**	ζ_F - **0.94**	ζ_F - **0.96**
Node 1 [**deg**]	65.65	75.85	62.50	72.67
Node 2 [**deg**]	79.10	70.21	55.84	71.20
Node 3 [**deg**]	75.45	75.74	73.46	69.18
Node 4 [**deg**]	71.99	70.31	71.95	83.30
Node 5 [**deg**]	68.30	72.90	68.05	63.25
Node 6 [**deg**]	44.78	40.02	43.49	46.14
Node 7 [**deg**]	28.14	22.01	19.77	26.12
Node 8 [**deg**]	14.39	13.76	13.53	15.59
Node 9 [**deg**]	-2.51	12.14	3.12	11.72
Node 10 [**deg**]	0.44	-1.82	-0.36	-2.44

Table 8.4: Optimal trajectory design input of the launch vehicle for four different engine qualities

Indeed the result is found sensitive to engine quality. When the engine quality is lowered to 0.88 the total dry mass of the vehicle increases by 27.4%, with an increase of first stage dry mass of 28.0% and an increase of upper stage dry mass of 17.8%. The GTOW is increased 32.4%, which shows the increased amount of propellant consumption. The total ascent ΔV performance is only decreased 0.1%, but with an increase in propellant consumption of 33.4%. The increased mass acts on the thrust level, which is increased 36.8% for the first stage and 28.5% for the upper stage.

The engine quality of 0.90 increases total vehicle dry mass by 11.5%, with a first stage dry mass increase of 11.7% and upper stage dry mass increase of 7.8%. The GTOW is increased by 12.5%. The total ascent ΔV of the vehicle

First stage				
	ζ_F - **0.88**	ζ_F - **0.90**	ζ_F - **0.94**	ζ_F - **0.96**
Dry mass [**kg**]	7583.03	6620.88	5511.40	5100.47
Propellant consumption [**kg**]	41509.91	35152.96	27921.48	26181.59
Total mass [**kg**]	56886.60	48326.89	38772.87	36519.12
Vacuum thrust [**kN**]	713.087	638.694	499.166	400.105
Vacuum specific impulse [**s**]	276.32	279.98	297.42	304.66
ΔV [**m/s**]	3398.07	3418.57	3489.99	3631.16
Return ΔV [**m/s**]	291.19	293.21	428.42	280.50
Length [**m**]	21.258	20.181	18.717	18.333

Table 8.5: Optimal design of the first stage for four different engine qualities

Upper stage				
	ζ_F - **0.88**	ζ_F - **0.90**	ζ_F - **0.94**	ζ_F - **0.96**
Dry mass [**kg**]	408.23	373.55	333.83	329.68
Propellant consumption [**kg**]	7235.43	6029.51	4856.17	4757.38
Total mass [**kg**]	7793.66	6553.06	5339.99	5237.06
Vacuum thrust [**kN**]	55.163	49.982	41.622	39.629
Vacuum specific impulse [**s**]	299.31	306.84	322.50	332.13
ΔV [**m/s**]	7738.19	7604.12	7594.42	7785.59
Length [**m**]	5.387	5.140	4.816	4.738

Table 8.6: Optimal design of the upper stage for four different engine qualities

is lowered by 1.1%, although the propellant consumption is increased by 12.7%. Due to the increase in mass the first stage thrust is increased by 22.5%, while the upper stage thrust is increased by 16.5%.

When the engine quality is increased above the baseline magnitude the vehicle becomes lighter. For an engine quality of 0.94 the total dry mass of the vehicle is decreased by 6.8%, with a first stage dry mass decrease of 7.0% and upper stage dry mass decrease of 3.7%. The GTOW decreases 9.8% due to a propellant consumption decrease of 10.5%, while the ascent ΔV performance decreases with 0.6%. First stage thrust lowers by 4.2%, while upper stage thrust lowers with 3.0%.

The highest engine quality used is 0.96. This results in a total vehicle dry mass reduction of 13.4%, with a first stage dry mass reduction of 13.9% and an upper stage dry mass reduction of 4.9%. Due to a propellant consumption reduction of 16.1% the GTOW is reduced by 15.0%. The ascent ΔV performance is increased, however, by 2.4%. The reduction in first stage thrust is 23.2%, while the reduction of upper stage thrust is 7.7%.

The sensitivity analysis to engine quality shows that indeed the result is very sensitive to engine quality, with a maximum decrease of total vehicle dry mass of 13.4% and a maximum increase in total vehicle dry mass of 27.4%. This also shows that the result is more sensitive to a decrease in engine performance than an increase. The engine quality was selected a bit conservative. For this reason it is expected that this will not decrease more than 0.1, while not increasing more than 0.2-0.3. The sensitivity analysis shows that within these margins the expected difference in total dry mass is approximately 10%.

8.3.2. Aerodynamics model

In the aerodynamics model reference data of the *X-34 Advanced Technology Demonstrator* (X-34) is used for computing the lift and drag on the vehicle. This is a major assumption, as it is unclear in this stage of the development if this aerodynamic performance can actually be met. To determine how sensitive the design is to a difference in aerodynamic performance two new aerodynamic data sets are created. In the first data set the lift is decreased by 7%, while the drag is increased by 7%. These values are determined based on the fact that this reduces the maximum lift-over-drag ratio by a whole point to ~6.5. The next aerodynamic set decreases the lift by 15%, while increasing the drag by 15%. This reduces the maximum lift-over-drag ratio by 2 points to ~5.5.

One of the interesting results of the study is the fact that glideback return is possible. It is expected that this return is more sensitive to a change in aerodynamic performance, due to the fact that the gliding range is driving the ascent angle which increases gravity loss. To quantify this expectation the sensitivity analysis is performed for the baseline scenario as well as the glideback scenario.

In-plane pitch over return

Table 8.7 shows the optimal design vectors of the solutions optimized for the new sets of aerodynamic coefficients. The corresponding designs are shown in Table 8.8.

Vehicle design			**Trajectory design**		
	(L-7%)/ (D+7%)	**(L-15%)/ (D+15%)**		**(L-7%)/ (D+7%)**	**(L-15%)/ (D+15%)**
Fst. stage brnt. [**s**]	169.15	165.61	Node 1 [**deg**]	65.56	73.56
Up. stage brnt. 1 [**s**]	347.47	309.17	Node 2 [**deg**]	75.78	77.98
Up. stage brnt. 2 [**s**]	56.64	62.36	Node 3 [**deg**]	75.76	74.24
Coasting time [**s**]	129.63	144.40	Node 4 [**deg**]	68.18	74.33
Return time [**s**]	10.89	11.32	Node 5 [**deg**]	74.48	68.26
Engine amount [**-**]	14	13	Node 6 [**deg**]	45.13	45.44
Mass flow [**kg/s**]	13.25	15.07	Node 7 [**deg**]	25.13	27.80
Fst. stage exit diam. [**m**]	0.326	0.319	Node 8 [**deg**]	14.90	13.39
Up. stage exit diam. [**m**]	0.756	0.761	Node 9 [**deg**]	3.08	5.49
Up. stage diameter [**m**]	1.998	2.007	Node 10 [**deg**]	-0.50	-0.80

Table 8.7: Optimal design input of the launch vehicle for two different aerodynamic coefficient sets with in-plane pitch over return

First stage			**Upper stage**	
	(L-7%)/ (D+7%)	**(L-15%)/ (D+15%)**	**(L-7%)/ (D+7%)**	**(L-15%)/ (D+15%)**
Dry mass [**kg**]	6293.05	6462.17	322.13	335.73
Propellant consumption [**kg**]	32391.94	33641.64	5340.68	5591.34
Total mass [**kg**]	44497.80	46180.88	5812.82	6077.07
Vacuum thrust [**kN**]	533.690	558.151	41.077	46.520
Vacuum specific impulse [**s**]	293.28	290.42	316.07	314.76
ΔV [**m/s**]	3514.02	3454.81	7781.81	7798.97
Return ΔV [**m/s**]	428.17	483.18	-	-
Length [**m**]	20.010	20.275	5.646	5.738

Table 8.8: Optimal design of the launch vehicle for two different aerodynamic coefficient sets with in-plane pitch over return

When the set of aerodynamic coefficients is altered by 7% the total dry mass of the vehicle increases by 5.5%. This increase in dry mass is driven by the 6.2% increase in first stage dry mass. The upper stage dry mass decreases by 7.1%. The main reason for this difference is the difference in propellant consumption between the first and upper stage. The first stage propellant consumption increases by 3.8%, while the upper stage propellant consumption decreases by 0.1%. The larger first stage propellant consumption increases the size of the first stage, which allows for integration of the larger spherical tank configured upper stage. The GTOW increases by 3.5%. The total ascent ΔV increases by 1.3%, which is caused by an increase in upper stage performance due to the lower dry mass. Due to the larger GTOW the first stage thrust increases by 2.4%, while the upper stage thrust decreased by 4.3%. The return ΔV budget increases by 6.1%. This is done by increasing the return propellant, although only 10.2% of the added first stage propellant is to increase the return ΔV.

When the aerodynamic coefficients are altered more the effect on the design is larger. The next set of coefficients is altered by 15%. Now the increase in total vehicle dry mass is 8.4%, which is driven by the 9.0% increase in first stage dry mass. Again due to a spherical tank configuration of the upper stage the upper stage dry mass decreases by 3.1%. The upper stage propellant consumption, however, increases by 4.6%, while the first stage propellant consumption increases by 7.8%. The increase in ascent ΔV by this is 0.9%. The thrust of the first stage is increased by 7.1%, while the upper stage thrust is increased by 8.4%. The return ΔV budget increases by 19.7%. 12.5% of the increase in first stage propellant is for increasing the return ΔV.

Even for a large variation of the aerodynamic coefficients the total dry mass of the vehicle is not impacted more than 8.4%. This means the solution is mildly sensitive to the aerodynamic performance of the first stage. When reviewing Figure 7.6 the aerodynamic loss is found 8.1% of the first stage ascent ΔV budget, which shows why the sensitivity is mild. Furthermore, the gliding range dominantly affects the point of return. This shows in the return ΔV budget. The lower performing vehicles in terms of aerodynamics show more return ΔV. The propellant consumption for doing so is relatively small. Of all the added propellant not more than 12.5% is for increasing the return ΔV. The rest is for the increased aerodynamic loss and for carrying the extra return propellant during ascent.

Glideback return

Table 8.9 shows the optimal design input for glideback with the two altered sets of aerodynamic coefficients. The corresponding optimal designs are found in Table 8.10.

Vehicle design			**Trajectory design**		
	(L-7%)/ (D+7%)	**(L-15%)/ (D+15%)**		**(L-7%)/ (D+7%)**	**(L-15%)/ (D+15%)**
Fst. stage brnt. [**s**]	150.48	162.17	Node 1 [**deg**]	68.22	45.99
Up. stage brnt. 1 [**s**]	329.88	369.93	Node 2 [**deg**]	76.76	83.34
Up. stage brnt. 2 [**s**]	71.63	64.02	Node 3 [**deg**]	74.41	83.16
Coasting time [**s**]	117.59	84.70	Node 4 [**deg**]	84.35	82.37
Return time [**s**]	-	-	Node 5 [**deg**]	85.03	87.21
Engine amount [-]	13	13	Node 6 [deg]	50.47	60.80
Mass flow [**kg/s**]	17.17	17.72	Node 7 [**deg**]	28.17	35.52
Fst. stage exit diam. [**m**]	0.341	0.345	Node 8 [**deg**]	16.57	16.89
Up. stage exit diam. [**m**]	0.768	0.762	Node 9 [**deg**]	4.10	6.03
Up. stage diameter [**m**]	2.026	2.043	Node 10 [**deg**]	-0.40	-0.80

Table 8.9: Optimal design input of the launch vehicle for two different aerodynamic coefficient sets with glideback return

First stage			**Upper stage**		
	(L-7%)/ (D+7%)	**(L-15%)/ (D+15%)**		**(L-7%)/ (D+7%)**	**(L-15%)/ (D+15%)**
Dry mass [**kg**]	6456.89	6971.85		401.54	419.31
Propellant consumption [**kg**]	33583.96	37359.42		6866.85	7672.92
Total mass [**kg**]	47459.24	52573.51		7418.39	8242.23
Vacuum thrust [**kN**]	635.754	656.051		52.763	54.367
Vacuum specific impulse [**s**]	290.34	290.31		313.41	312.85
ΔV [**m/s**]	3503.24	3531.34		7988.07	8199.66
Length [**m**]	19.900	20.608		5.149	5.348

Table 8.10: Optimal design of the launch vehicle for two different aerodynamic coefficient sets with glideback return

Also for this scenario the dry and total mass increase for the increase in drag and decrease in lift. As no return propellant is carried, only the ascent propellant amount is influenced by a change in trajectory. This change in trajectory is required, steepening the return arc to account for the decreased gliding range.

When the set of aerodynamic coefficients is altered by 7% the total dry mass of the vehicle increases by 4.7%. The first stage dry mass increases by 4.1%, due to a propellant increase of 10.6%. The upper stage dry mass increases by 14.6%, due to a propellant increase of 12.2%. The GTOW increases by 9.9%. The total ascent ΔV performance is increased by 0.5%. As both the first and upper stage are heavier the thrust increases accordingly. First stage thrust is increased by 11.1%, while upper stage thrust is increased by 10.1%.

Next, the aerodynamic coefficients are altered 15%. This increases the total dry mass of the vehicle by 12.8%. The first stage dry mass increase is 12.4%, with a propellant increase of 23.0%. The upper stage dry mass increases by 19.7%, with a propellant increase of 25.4%. The GTOW is increases by 21.7%, while the ascent ΔV performance increases 2.7%. To propel the vehicle the first stage thrust is increased by 14.7%, while the upper stage thrust is increased 13.4%.

Indeed the glideback method shows more sensitive to the change of aerodynamic coefficients. This was predicted due to the fact that without an active return method the System is more affected by the limitation in gliding range. For the largest change in aerodynamics the vehicle dry mass increases 12.4%, while the GTOW increases 21.7%. This is more than the 8.4% of increase in dry mass found in the in-plane pitch over aerodynamic sensitivity analysis. The first stage aerodynamics are driving the design of the glideback configuration more. Hence when designing the System with glideback return the aerodynamics of the first stage are identified a key driver in System performance.

8.3.3. Geometry and mass model

For any launch vehicle the ratio between dry and total mass is one of the primary features determining vehicle performance. This is due to the direct relation in the Tsiolkovsky (1903) equation. When reviewing the result in

Mass sensitivity scenarios			**Material density [kg/m^3]**	**Tank factor [-]**	**Minimum thickness [mm]**
	Case 1				
		First stage	1600	1.85	3.0
		Upper stage	2000	2.50	3.0
	Case 2				
		First stage	1600	1.85	3.0
		Upper stage	2000	2.50	4.5
	Case 3				
		First stage	2000	2.50	4.5
		Upper stage	1600	1.85	3.0
	Case 4				
		First stage	2000	2.50	4.5
		Upper stage	2000	2.50	4.5

Table 8.11: Structure of the sensitivity analysis on the mass model

Vehicle design				
	Case 1	**Case 2**	**Case 3**	**Case 4**
Fst. stage brnt. [**s**]	163.73	195.75	162.84	187.27
Up. stage brnt. 1 [**s**]	292.71	245.58	316.07	241.53
Up. stage brnt. 2 [**s**]	55.48	53.50	76.19	65.94
Coasting time [**s**]	189.68	236.72	134.11	225.36
Return time [**s**]	12.53	5.03	9.64	5.25
Engine amount [-]	13	15	14	15
Mass flow [**kg/s**]	20.39	15.99	14.73	19.86
Fst. stage exit diam. [**m**]	0.339	0.334	0.343	0.344
Up. stage exit diam. [**m**]	0.793	0.756	0.781	0.793
Up. stage diameter [**m**]	2.139	2.167	1.820	2.045

Table 8.12: Optimal vehicle design input of the launch vehicle for four different mass model scenarios (Case 2 and Case 4 do not return, noticed by constraint violation)

Trajectory design				
	Case 1	**Case 2**	**Case 3**	**Case 4**
Node 1 [**deg**]	75.72	56.33	60.13	59.38
Node 2 [**deg**]	79.37	50.98	66.46	63.42
Node 3 [**deg**]	61.43	45.59	70.27	49.05
Node 4 [**deg**]	74.23	44.52	77.92	48.33
Node 5 [**deg**]	64.44	39.41	59.77	42.03
Node 6 [**deg**]	35.70	24.72	42.91	28.19
Node 7 [**deg**]	20.19	15.27	27.24	17.42
Node 8 [**deg**]	13.17	14.55	16.11	23.33
Node 9 [**deg**]	6.02	0.86	7.06	5.47
Node 10 [**deg**]	-0.74	-0.25	-1.05	-0.92

Table 8.13: Optimal trajectory design input of the launch vehicle for four different mass model scenarios (Case 2 and Case 4 do not return, noticed by constraint violation)

closer detail one of the behaviours found in the tool is a tendency to converge to upper stage solutions with a high *Propellant Mass Fraction* (PMF). This is desirable, as this increases the ΔV performance of the upper stage. To see what is the impact on the design, a sensitivity analysis is performed on the mass and geometry model. The sensitivity of the upper stage is of primary interest, although also the mass sensitivity of the first stage is determined.

The sensitivity to a change in mass budget is determined by a model based approach. In the model several assumptions were made on the applied material and the design. The assumptions are changed to increase the dry mass compared to the propellant and payload mass. Table 8.11 shows which assumptions are targeted and how they are changed. Four scenarios are used in the analysis. In Case 1 the mass model of the upper stage is mildly changed, by increasing the tank factor and material density of the upper stage. In Case 2 the upper stage is heavily changed, by also increasing the minimum material thickness. Case 3 determines the effect of a heavily changed first stage, by increasing the tank factor, material density and material thickness. Finally, in Case 4 both the first and upper stage are heavily changed. Table 8.12 and 8.13 show the optimal vehicle and trajectory design input vectors. Table 8.14 and 8.15 show the corresponding optimal first and second stage design. For interpretation of these sensitivity results it is important to know that the first stage of Case 2 and Case 4 does not return to the spaceport of launch. This is shown in the fitness value by a penalty corresponding with a non-return of the first stage.

The upper stage PMF of the baseline case is 0.939. In Case 1 this is lowered to 0.931. The optimizer shows a strong tendency into converging to high PMFs. With the assumptions in Case 1 a stronger relation between increasing propellant consumption and increasing dry mass is expected. This indeed is the case, although for large propellant consumptions this still results in a high PMF. The dry mass of the upper stage is increased by 52.4%, while the propellant consumption increased by 32.4%.

First stage				
	Case 1	**Case 2**	**Case 3**	**Case 4**
Dry mass [**kg**]	8330.96	8248.20	7363.94	11025.55
Propellant consumption [**kg**]	44930.03	47597.41	34574.12	56619.40
Total mass [**kg**]	61014.13	61327.96	48222.04	74520.43
Vacuum thrust [**kN**]	746.908	684.460	592.985	842.236
Vacuum specific impulse [**s**]	287.24	290.90	293.12	288.20
ΔV [**m/s**]	3500.59	4139.84	3427.46	3903.60
Return ΔV [**m/s**]	475.86	214.45	363.93	206.29
Length [**m**]	22.216	22.200	20.031	23.555

Table 8.14: Optimal design of the first stage for four different mass model scenarios (Case 2 and Case 4 do not return, noticed by constraint violation)

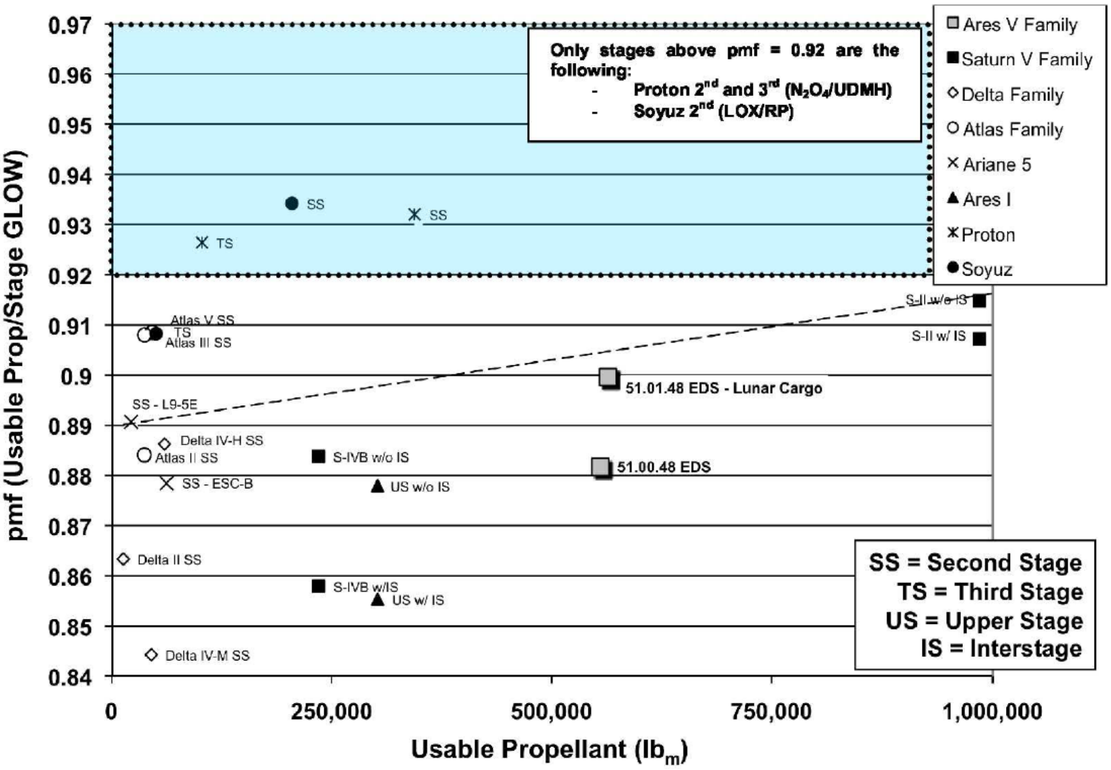

Figure 8.15: Upper stage propellant mass fraction against usable propellant mass (Holt and Monk, 2009)

Upper stage				
	Case 1	**Case 2**	**Case 3**	**Case 4**
Dry mass [**kg**]	528.17	567.00	359.79	648.57
Propellant consumption [**kg**]	7074.96	4765.35	5774.19	6076.90
Total mass [**kg**]	7753.13	5482.35	6283.98	6875.47
Vacuum thrust [**kN**]	62.406	49.224	45.590	60.850
Vacuum specific impulse [**s**]	312.11	313.89	315.60	312.45
ΔV [**m/s**]	7457.39	6261.73	7773.92	6596.63
Length [**m**]	6.105	5.595	5.105	5.927

Table 8.15: Optimal design of the upper stage for four different mass model scenarios (Case 2 and Case 4 do not return, noticed by constraint violation)

The corresponding first stage is affected by this. The dry mass of this stage increases by 40.6%, with an increase of propellant consumption of 44.0%. The GTOW increases by 42.0%. The main reason for the large increase of the first stage is the larger upper stage. While being 32.7% heavier this upper stage shows 2.1% decrease in ascent ΔV performance. This means that the first stage is carrying more payload, while similar performance is required.

For the first stage the ratio between dry mass and GTOW was used as a validation criterium. In the baseline scenario this is 0.138. In Case 3 this ratio is increased to 0.153. The increase in first stage dry mass is 24.3%, which is accompanied by an increase in propellant consumption of 10.8%. The result is a 2.9% decrease in ascent ΔV and a 9.8% decrease of return ΔV. The upper stage accounts for the loss in ascent ΔV, as the upper stage ascent ΔV is increased by 2.0%. The corresponding increase in upper stage dry mass is 3.8%, with a 8.0% increase of propellant consumption.

It is not a fair comparison to compare Case 2 and Case 4 directly to the baseline scenario. Reason for this is the fact that the first stage does not return to the spaceport of launch. The first stage does not return to the spaceport

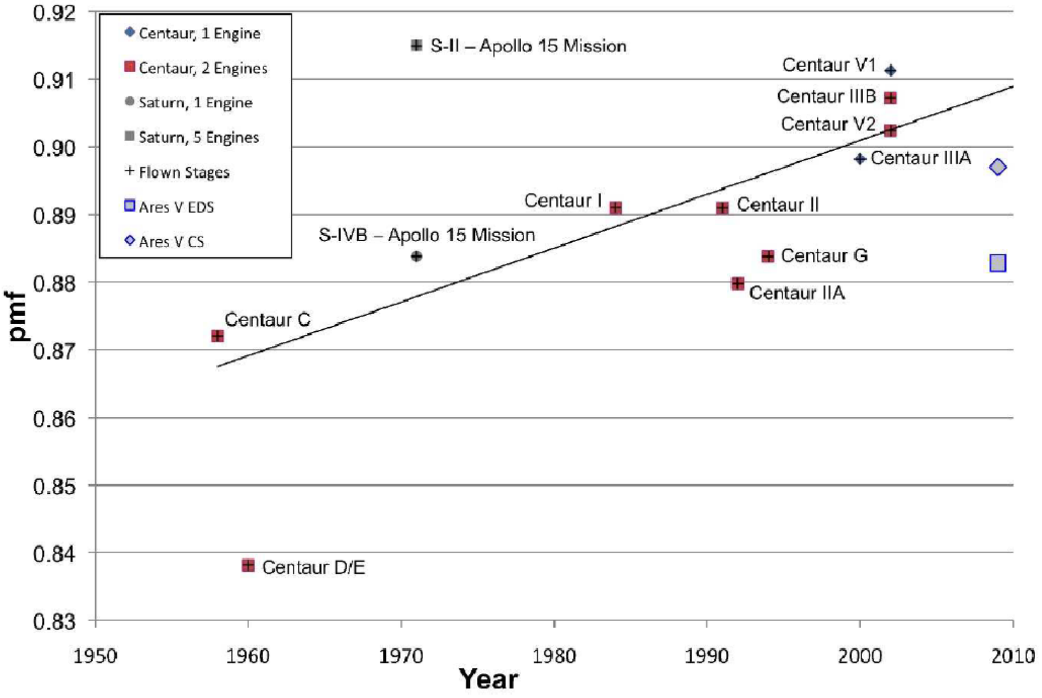

Figure 8.16: Propellant mass fraction trend over the years of spacecraft development (Holt and Monk, 2009)

of launch due to the decreased ascent performance of the upper stage. To reach orbit the ascent trajectory needs to be so gradual, that return of the first stage is not possible. In Case 4 the upper stage ΔV is decreased by 13.4% as a result of the PMF reduction to 0.904. The first stage ascent ΔV is increased by 10.6%, although this is not enough to counteract for the reduction of upper stage ΔV. The total ascent ΔV budget is decreased by 5.8%, which requires a more gradual ascent for getting into orbit. The return ΔV cannot be increased, as this is penalizes the ascent performance even more. As a result the System is unable of returning the first stage. The similar effect is true for Case 2, in which the difference is even larger.

The sensitivity analysis on mass shows how sensitive the solution is on the dry mass of the vehicle. With a mild change in the upper stage mass model the total dry mass becomes 41.2% more. When the upper stage model is changed heavily no solutions exists which satisfy all constraints. A heavily changed first stage mass model results in a 23.1% increase of total vehicle dry mass. The combination of a changed first and upper stage model does not result in solutions without constraint violation.

Holt and Monk (2009) studied the PMFs of different launch vehicles. Figure 8.15 shows the PMF of several upper stages of different launch vehicles. The figure shows that the PMFs found in this study are very ambitious, but not directly unfeasible. The second stage in this study is designed with a PMF of 0.939, which is higher than the stages shown in the figure. The difference, however, is the fact that the upper stage of this study is integrated in the first stage during ascent in the dense layers of the atmosphere. This reduces the amount of structure required for payload protection and for protection of the stage itself. Furthermore, the integration in the first stage also allows for an upper stage design without taking into account aerodynamic restrictions which allows for easier subsystem instalment. Also this is expected to increase the PMF. On top of that, the figure shows for a higher propellant consumption that the PMF is higher. In this study propellant consumption is small, approximately 11784 lbs. However, this propellant consumption is large when compared to engine size. In the framework of small payload upper stages the upper stage is large. It is expected that this increases the PMF as well. Furthermore, the use of room temperature storable propellants is expected to reduce stage complexity allowing for an increase in PMF. Finally, Figure 8.16 shows that due to the implementation of novel materials and new production techniques the PMF did increase over the years. The upper stage of this study is designed taking into account the newest materials and the possibility of 3D printed subsystems.

Concluding on the sensitivity analysis on mass it is identified that the solution is highly sensitive to the mass model and assumptions. Especially the ability of returning the first stage to the spaceport of take-off is unfeasible when the upper stage is not designed with a sufficient PMF of approximately 0.93. It is shown that this is an ambitious goal, although it is also discussed that this is not unfeasible considering the upper stage design. From an early stage in the development process the upper stage design shall be optimized for highest PMF, driving the feasibility of the System.

8.3.4. Runway heading

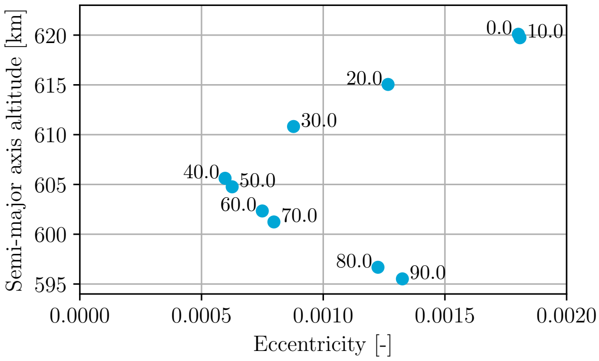

Figure 8.17: Orbital injection for take-off of the baseline vehicle at different runway headings shown in degrees

The final sensitivity analysis performed studies how sensitive the solution is for a change of runway heading. It was found that the ability of successful changing heading was independent of altitude until a certain threshold. It is, however, not determined what the impact on the solution is when the heading of the runway itself is changed.

Figure 8.17 determines this latter sensitivity. The figure shows what the injection parameters are when the runway heading is changed to the value shown (baseline scenario on runway 06 with heading of ~60°). The result is found almost insensitive to runway heading, of which both the change to 0° and the change to 90° result in an injection well within the discussed limits (less than ±55 km semi-major axis and 0.01 eccentricity change). This is another confirmation on the fact that the first stage ascent trajectory in the dense layers of the atmosphere has no great effect on the orbital injection of the payload.

9

Conclusions and recommendations

Dawn Aerospace is involved in the design of a highly innovative vehicle, the *Dawn Aerospace Mk-III* (Mk-III). This vehicle is designed with a first stage being the combination of an airplane and a rocket, a so-called 'spaceplane'. The shape of the first stage allows for *Horizontal Take-Off Horizontal Landing* (HTOHL), which also means that the first stage can be re-used after flight resulting in a *semi-Reusable Launch Vehicle* (sRLV). For performance reasons, both being the velocity and altitude, the first stage is rocket propelled. An expendable second stage brings the payload into orbit, making it a *Two Stage to Orbit* (TSTO) System.

The idea behind this vehicle is to create a more competitive way of launching small payload into orbit. The market and market share of small payload is increasing (McIntyre et al., 2016), which creates the opportunity for profitable launch service provision. Important is that the launch service is cost-effective, flexible, frequently available and reliable (Tugnoli et al., 2019). With a winged vehicle this is possible. Due to the manoeuvrability of the vehicle large regulated safety zones can be omitted. Also due to the airplane character of the first stage the vehicle is not reliant on dedicated launch facilities but, rather, an airport anywhere in the world. This allows for integrating the vehicle in the common airspace.

The vehicle class that the Mk-III is representing has never been studied before in academic research. The study presented in this report aims at increasing the collective understanding of this kind of vehicle and mission geometry. Furthermore, the results found by this study can be integrated in the development process of the Mk-III enabling an efficient design process.

This chapter concludes the study. First, the conclusions are presented. This is done following the structure of the study introduced in Chapter 1. Secondly, recommendations are given on interesting topics which are derived from this study and allow for a more detailed research. Also this chapter shows images of the determined ascent and return trajectory of the baseline scenario. This has no direct in-text relation to the conclusions or recommendations, although the images have the purpose of intuitively visualizing the size of the proposed mission taking off at Rotterdam The Hague Airport. All images are rendered in Google Earth Pro.[1]

9.1. Conclusions

The conclusions shown in this section answer to the different research questions introduced. It is important to realize that all the variations are compared to the baseline scenario. This means that if a certain change is quantified, this is a change of the baseline scenario. The top-level summary of the baseline scenario is a 150 kg payload injection into polar 600 km orbit. The spaceport is Rotterdam The Hague Airport and return to the spaceport is done by in-plane pitch over. The vehicle is designed with integrated landing gear, 13 commonly designed engines on the first stage and the use of a fairing is prohibited.

Primary Research Question: *What is the mass optimal vehicle and corresponding trajectory for cost derived mission scenarios of a rocket propelled Two Stage to Orbit Horizontal Take-off Horizontal Landing semi-Reusable Launch Vehicle for small payload integrated in the common airspace?*

---

[1] 'Google Earth', *Google*, `https://www.google.com/earth/`, (accessed on May 25, 2020).

The primary conclusions of this research is the proven feasibility of the proposed concept. From a technical perspective the vehicle shows a promising design (see Table 9.1 and 9.2 and Figure 9.1 and 9.2). The baseline scenario, which is meeting all operational and technical requirements, consists of a vehicle with a total dry mass of 6273.0 kg. This means that the vehicle is ~5 times heavier than conventional launch vehicles with similar payload capacity and performance, although 94.5% of this dry mass is reusable. The *Gross Take-Off Weight* (GTOW) of the vehicle is 42972.8 kg. This design allows for all the benefits of a vehicle integrated in the common airspace, while being compliant to all cost derived design and operational aspects.

Two concepts are identified main drivers in the operations and feasibility of this vehicle. The first is the return of the vehicle to the original spaceport of take-off. Returning the first stage steepens the ascent trajectory, which increases gravity loss by 30%-50%. This increases the dry mass of the vehicle. A second driver is the *Propellant Mass Fraction* (PMF) of the upper stage. The solution shows a high PMF of 0.939. The high PMF is required for gaining enough velocity increase with the upper stage. It is determined that this cannot decrease much further, before the requirement of returning the first stage is violated.

The shape of the trajectory depends on the chosen return method. The study shows that the in-plane pitch over return and the glideback return show close resemblance in total vehicle dry mass, with a difference of 4.4%. However, subsystems for manoeuvring the spaceplane outside of the atmosphere are not modelled. Hence the total dry mass is expected to be even closer. For glideback the vehicle is more dependent on a high upper stage PMF, as the result found has a PMF of 0.946. This high PMF is required as the ascent trajectory of glideback is steeper than the ascent trajectory of in-plane pitch over increasing gravity loss. When the upper stage design allows for this high PMF glideback is the preferred return method. This method does not require a complex manoeuvre outside of the atmosphere resulting in a less complex and more robust System. The gliding range of the first stage is dependent on the aerodynamic performance of the first stage. The sensitivity analysis shows that for glideback it is most important to optimize the lift-over-drag ratio, as increasing the gliding range decreases the total vehicle dry mass.

Primary Sub-Question 1: *What are the qualitative cost differences between different mission scenarios?*

Three major components determine the *Cost per Flight* (CpF) of a launch vehicle, being the development cost, manufacturing cost and operating cost. In this study it is argued that quantifying the CpF is not the main interest but, rather, is including cost optimality in the design space. Some of the elements in the development and operating costs can be discarded, while still remaining with a cost gradient towards the lowest cost solution. A new cost comparison function is proposed, of which it is shown that there is a strong correlation between the result of the cost comparison function and the total vehicle dry mass. It is concluded that using the total vehicle dry mass as a measure of quantifying the cost gradient is sufficient for determining results in this feasibility study. In this way cost optimality is included, although the CpF cannot be determined.

The study argues that not all contributors to a difference in CpF are modelled by the cost gradient approach. Also some of them do not show in traditional cost models. To include these effects different mission scenarios are derived, based on differences in the vehicle design or operations. The goal is to find how the design changes when these considerations are implemented. The study concludes on the following cost derived mission scenarios.

The first is the *Return to Launch Site* (RTLS) capability. For flexible operations all around the world it is important to ensure that the whole mission can be flown from a single airport. The expected improvement on cost comes from a decrease in turnaround time between launches and a reduction of required transport of the first stage. The mission scenario compares a mission with and without return of the first stage, while comparing different return methods for the return.

A contributor in the development cost is the engine design and lay-out. When a shared engine design is used to propel the first and upper stage, this reduces the cost of the launch vehicle development. This reduction is twofold. First, instead of having two parallel design processes of different engines this is reduced to only one design process. Secondly, due to a reduction of the engine size a different ball park of test facilities can be used when testing the engine. Especially for small payload launchers the engines can be so small that the operating cost of these test facilities reduces drastically. The mission scenario compares a design in which the first and upper stage both have an individual engine against a design in which the first and upper stage share the engine design.

For integration in the common airspace without safety zones uncontrolled material cannot be ejected during launch or re-entry of the vehicle. This means that the use of a fairing for payload protection is not allowed. The mission scenario compares a mission in which a fairing is prohibited against a mission in which a fairing is

Optimal design					
Vehicle design			**Trajectory design**		
	Fst. stage brnt. [**s**]	167.97		Node 1 [**deg**]	61.01
	Up. stage brnt. 1 [**s**]	321.90		Node 2 [**deg**]	60.30
	Up. stage brnt. 2 [**s**]	64.63		Node 3 [**deg**]	69.30
	Coasting time [**s**]	155.59		Node 4 [**deg**]	68.11
	Return time [**s**]	10.67		Node 5 [**deg**]	72.54
	Engine amount [-]	13		Node 6 [**deg**]	40.69
	Mass flow [**kg/s**]	13.88		Node 7 [**deg**]	22.36
	Fst. stage exit diam. [**m**]	0.347		Node 8 [**deg**]	14.61
	Up. stage exit diam. [**m**]	0.745		Node 9 [**deg**]	1.61
	Up. stage diameter [**m**]	1.807		Node 10 [**deg**]	-0.09

Table 9.1: Optimal design input of the baseline scenario as an answer to the Primary Research Question

Optimal design					
First stage			**Upper stage**		
	Dry mass [**kg**]	5926.45		Dry mass [**kg**]	346.59
	Propellant consumption [**kg**]	31204.61		Propellant consumption [**kg**]	5345.12
	Total mass [**kg**]	42972.77		Total mass [**kg**]	5841.71
	Vacuum thrust [**kN**]	521.294		Vacuum thrust [**kN**]	42.914
	Vacuum specific impulse [**s**]	294.42		Vacuum specific impulse [**s**]	315.19
	ΔV [**m/s**]	3530.51		ΔV [**m/s**]	7619.36
	Return ΔV [**m/s**]	403.67		Length [**m**]	4.962
	Length [**m**]	19.360			

Table 9.2: Optimal design of the baseline scenario as an answer to the Primary Research Question

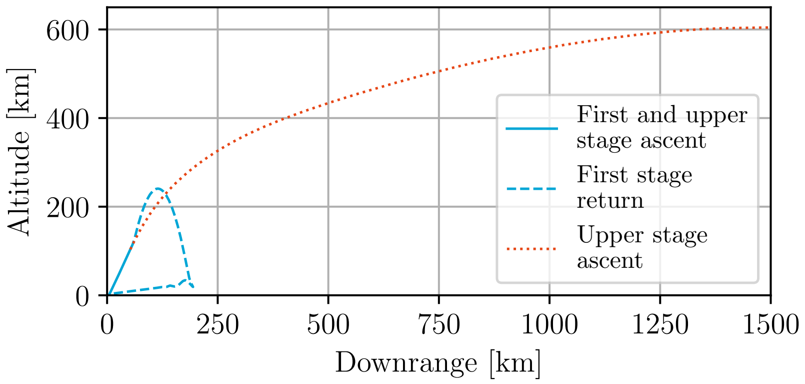

Figure 9.1: Optimal ascent and return trajectory of the baseline scenario as an answer to the Primary Research Question (legend valid for Figure 9.1 and 9.2)

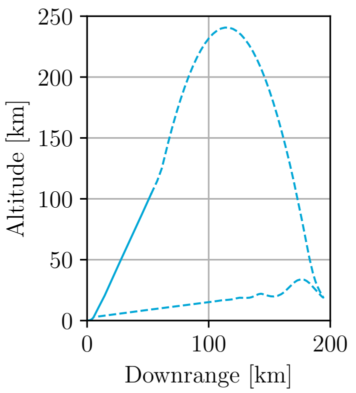

Figure 9.2: Optimal return trajectory of the baseline scenario as an answer to the Primary Research Question

allowed.

The optimal mission is completely autonomous. This means that the vehicle takes off and lands on integrated landing gear. For launch vehicles the difference in dry mass and GTOW is very large, due to the great propellant consumption. To determine the effect of a take-off sized landing gear that mission is compared to a mission in which a cart is used for supporting the first stage during take-off. Furthermore, an air-launched mission is added in this comparison.

Finally, for every launch a new upper stage is transported to the spaceport of take-off. To keep this transport cost as low as possible the upper stage is always designed to fit a 20 ft dry shipping container.

Primary Sub-Question 2: *How do the primary vehicle and mission design parameters and constraints influence vehicle dry mass?*

In the different scenarios throughout the study a similar ΔV distribution is found between the first and upper stage. The first stage has a total ascent ΔV of approximately 3500 m/s, of which ~$1/2\Delta V$ is the actual velocity increase of the vehicle and the other ~$1/2\Delta V$ is lost in several losses. The primary loss in the first stage velocity budget is gravity loss (~$1/3\Delta V$), followed by the aerodynamic loss (~$1/12\Delta V$) and the pressure loss (~$1/23\Delta V$). The total upper stage ascent ΔV is approximately 7500 m/s, of which the primary loss is gravity loss (~$1/4\Delta V$). This means the distribution of first:upper stage velocity is approximately 1:2.1.

The ΔV distribution is found tightly restrained, more than expected. It was expected that the first and upper stage were free to decrease and increase in size, resulting in different solutions with a variation in distribution. It is found, however, that the first stage restricts the distribution. In the vehicle model an increase in size does not increase the performance, due to the a drastic mass increase of the airplane components. Furthermore, the return of the vehicle creates an even tighter ΔV budget as a higher ascent velocity requires more return velocity. The propellant required for the return velocity decreases the ascent performance on the other hand. This balances to approximately 3500 m/s of first stage ascent ΔV. The rest is done by the upper stage, which is injected at a steep ascent profile for returning the first stage. The only way for the upper stage to get into orbit is by a high PMF. The PMF found is an ambitious goal, but it is shown to be feasible. The result of the sensitivity analysis shows that when this PMF is lowered below ~0.93 the first stage cannot return to the spaceport of take-off.

The dry mass of the vehicle increases when the orbital altitude is increased. This is more distinct in the first stage dry mass than the upper stage dry mass. In the baseline scenario the injection altitude is 600 km. When this is increased or decreased by 200 km the change in upper stage dry mass is not more than 0.9%. When this is decreased 400 km the upper stage dry mass is decreased by 10.4%.

The first stage dry mass shows a stronger trend with the orbital altitude. If the injection altitude is decreased by 400 km the first stage dry mass decreases with 20.8%. For a decrease of 200 km the first stage dry mass decreases with 8.4%. For an increase in orbital altitude of 200 km the first stage dry mass increases by 13.5%. This shows that the increase in orbital altitude shows a stronger effect on the result than a decrease.

The GTOW shows a more constant variation over altitude. A decrease of 400 km results in a 22.5% reduction of the GTOW. A decrease of 200 km results in a 9.2% reduction of the GTOW, while an increase of 200 km results in an increase of the GTOW of 9.6%.

When the payload is varied a distinct relation between payload and the total mass of both stages is found. The GTOW on average increases by 130.8 kg per kilogram payload, with less than 9.7% variation between different payload classes. On average the total upper stage mass increases with 20.5 kg per kilogram payload, with less than 1.0% of variation between different payload classes.

The dry masses of both stages does not show such a clear trend with the increase in payload mass. The lowest increase in first stage dry mass is found between a payload of 50 kg and 150 kg, in which the first stage dry mass only increases by 12.1 kg for every kilogram of payload. The highest increase is found between 150 kg and 250 kg of payload, in which the first stage dry mass increases by 17.3 kg for every kilogram. The upper stage dry mass increases the most between 50 kg and 150 kg of payload, with 0.92 kg for every kilogram. This increases the least between 250 kg and 500 kg, with only 0.59 kg per kilogram payload.

Using a shared engine design for propelling the first and upper stage is cost efficient for the development process. This study shows that a configuration with commonly designed engines is possible, without a great penalty on the dry mass of the vehicle. Propelling the first stage requires 13 engines. The thrust difference between this con-

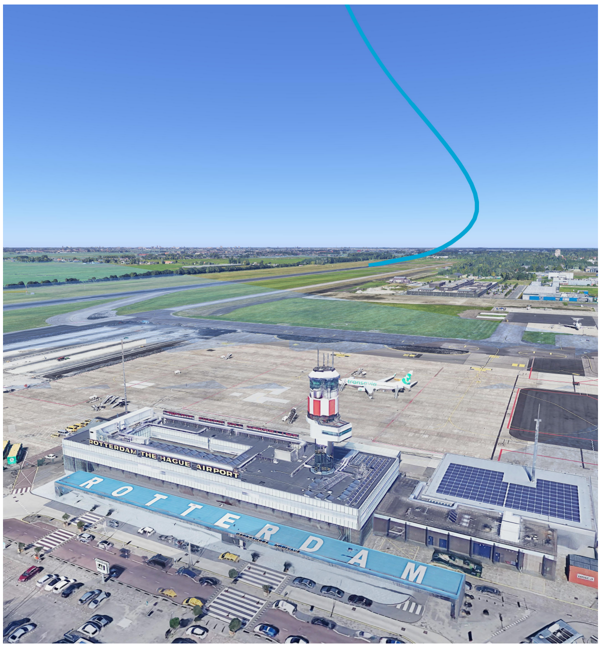

Figure 9.3: Take-off trajectory of the Mk-III at runway 06 of Rotterdam The Hague Airport

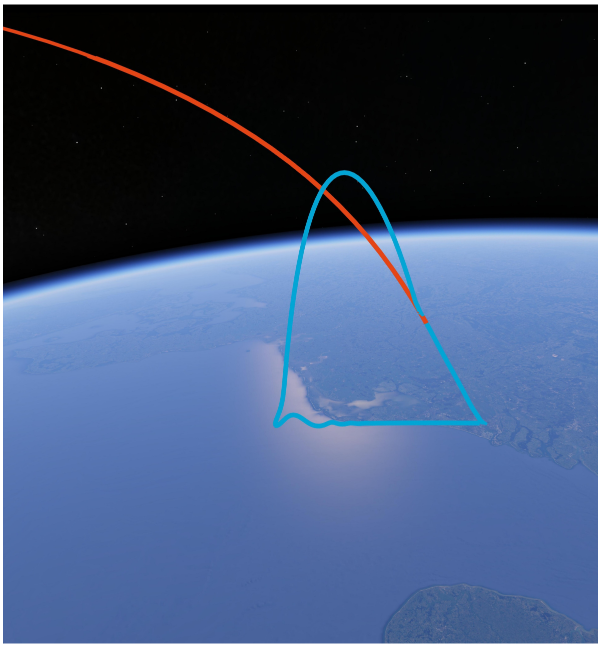

Figure 9.4: 'Good morning! Northern Europe as we look over the North Sea and the Netherlands' inspired take-off trajectory image

figuration and a single first stage engine is found 1.0%. The upper stage thrust differs 2.6%. This shows that when using 13 engines, the thrust profile is not moved far from the optimum.

The impact on the dry mass of the vehicle is reasonable small. The first stage dry mass decreases by 4.0% when a single first stage engine is used. The corresponding upper stage dry mass decreases by 5.1%. It is not expected that this difference in mass is enough for favouring a single first stage engine, especially considering the benefits of a shared design in the development process.

This study also shows that the configuration of nine first stage engines, found in several launch vehicles, is not optimal in this design. This is due to the unconventional shape of the first stage. A large difference in thrust magnitude is required between the first and upper stage in this study. This is not possible by nine first stage engines, which are restricted in thrust by the upper stage acceleration constraint.

Returning the first stage to the spaceport of take-off is one of the key elements in the operations of the vehicle. This requirement is found to be one of the primary drivers in the design.

The effect on the design is large. Not returning the first stage decreases the first stage dry mass with 13.7%, while the propellant consumption is reduced by 16.9%. The upper stage dry mass is reduced by 15.9%, with a propellant consumption reduction of 30.9%. This means the GTOW is reduced by 18.2%.

Also the velocity distribution between the first and upper stage is changed. As the first stage is not returned, this also removes the relation between the ascent and return trajectory. Due to this the ascent is more gradual, which reduces the amount of gravity loss. The total ascent ΔV performance is reduced by 2.6%. However, the first stage ascent ΔV is increased by 9.2% while the upper stage ΔV is reduced by 8.1%. This alters the ΔV distribution from 1:2.1 to 1:1.8.

Ejection of uncontrolled material is undesirable for the operations of the vehicle, as this jeopardizes safe integration in the common airspace. For this reason the use of a fairing as payload protection is prohibited. This requires the upper stage to be injected in conditions in which the aerothermal flux is and stays below 1135 W/m^2.

This requirement on the trajectory influences the design of the vehicle. When a fairing is prohibited staging occurs always at an altitude above 100 km. The effect is most prominent when an injection altitude of 200 km is achieved. If a fairing is allowed the staging altitude decreases with more than 25 km. The result on the first stage dry mass is a decrease of 9.6%, with a GTOW reduction of 14.6%. On the other hand the total upper stage mass increases with 26.3%, to create a more efficient ΔV distribution between the first and upper stage.

The same effect is true when the use of a fairing is allowed for an injection altitude of 600 km. However, due to a smaller reduction of staging altitude the effect is less strong. The staging altitude drops with approximately

10 km. This decreases the first stage dry mass with 1.0%, while the GTOW is reduced with 7.4%. The upper stage total mass is increased by 1.8%.

The envisioned mission is completely autonomous. This means that both take-off and landing are done on integrated landing gear. Due to the high PMF of launch vehicles, the difference between take-off mass and landing mass is very high. This means that the integrated landing gear sized for take-off is over-dimensioned for most of the flight. The effect of this requirement is quantified.

In the first comparison a cart is used to support the first stage during take-off. This reduces the dry mass of the first stage by 24.6% of which a large portion is the reduced landing gear mass. The total GTOW is reduced by 7.7%. Due to the smaller dry mass of the first stage the tight velocity budget is loosens a bit. The result of this is that the solution converges to a first stage ΔV budget with a large increase in return propellant. The return ΔV is increased by 93.9%. This allows for a more gradual ascent, while the first stage still returns to the spaceport of take-off.

When air-launch is used the carrier aircraft takes care of the first part of velocity and altitude increase. The result is a 33.3% reduction of first stage dry mass and a 28.3% reduction of the GTOW, also a result of the 15.9% reduction of the ascent ΔV. Due to the smaller dry mass, however, the return ΔV is increased by 124.7%.

Primary Sub-Question 3: *How do the active "in-plane pitch over" and "aeroturn" Return to Launch Site methods and the passive "glideback" Return to Launch Site method compare?*

One of the interesting questions in this study is if and what return method is required. The study compares three different methods of return, two active (in-plane pitch over and aeroturn) and one passive (glideback). The dry mass of the upper stage does not differ significantly between the different return methods, however, the dry mass of the first stage does. In-plane pitch over (baseline scenario) shows the lowest first stage dry mass of 5926.5 kg. For glideback this dry mass is increased by 4.6%, while for aeroturn return this dry mass is increased by 7.6%.

The propellant consumption is found close to each other. For in-plane pitch over the first stage propellant consumption is 31204.6 kg, while the upper stage propellant consumption is 5345.1 kg. With the aeroturn method the first stage propellant consumption increases by 2.9%, while the upper stage propellant consumption increases with 12.9%. For glideback the first stage propellant consumption decreases with 2.7%, while the upper stage propellant consumption increases with 14.5%.

The increased propellant consumption of the upper stage for both aeroturn and glideback is due to the fact that the ascent trajectory of the first stage is steeper. This is for allowing the first stage to return by gliding back to the spaceport of launch. The injection of the upper stage is also steeper, which increases the demand on ascent ΔV due to higher gravity loss. For glideback the resulting PMF is 0.946.

The trajectory difference between aeroturn and glideback is very small. In both methods the first stage ascents steep enough such that when re-entered the gliding range allows for returning to the spaceport of take-off. This means that the extra burn in aeroturn is unnecessary. This discards aeroturn as one of the favourable return methods.

In terms of heat rate and heat load during re-entry the vehicles show close resemblance. This is caused by the return velocities which are very similar. In literature in-plane pitch over is found to be the least heavy on the vehicle in terms of heat loading. In this study, however, guidance of in-plane pitch over is implemented such that the horizontal component of the velocity is removed for a maximum decrease of downrange. As this is not opposite of the velocity vector most of the velocity magnitude remains, with a change in direction.

Both the heat rate and the heat load are determined in the stagnation point of the vehicle. They are found small when compared to orbital vehicles. In-plane pitch over shows a heat rate of ~90 kW/m^2 with a total heat load of 1.8 MJ/m^2. When using the aeroturn return method the heat rate increases to almost 100 kW/m^2 with a total heat load of 2.0 MJ/m^2. During glideback the heat rate experienced is 105 kW/m^2 with a total heat load of 2.1 MJ/m^2. The difference is ~16%, which is not expected to be of major influence in the design trade-off.

This means that the question remains if an active return method is required. Of both active return methods in-plane pitch over is preferred. The mass perspective shows, however, that an active return method is not required. In-plane pitch over return and glideback return show very similar first stage dry mass. Moreover, the subsystems for doing the complex in-plane pitch over manoeuvre are not modelled. This makes the difference in first stage dry mass even smaller. Also the heat rate and heat load do not present a definite favour for one or the other. From

Figure 9.5: Take-off trajectory of the Mk-III as seen from the historical centre of Delft

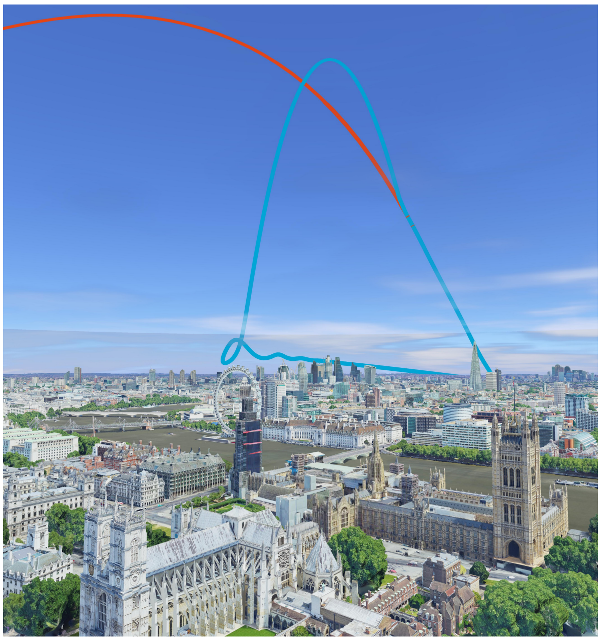

Figure 9.6: Take-off trajectory of the Mk-III as seen from the centre of London

the perspective of system complexity glideback is definitely preferred, due to simpler operations.

However, the PMF of the upper stage limits the feasibility of glideback. For glideback to be possible an even higher ΔV performance is demanded of the upper stage. To deliver this performance the upper stage converged to a PMF of 0.946. When the design of the upper stage does not allow for such a high PMF the glideback method becomes difficult to design with a *Two Stage to Orbit* (TSTO) configuration.

When designing the glideback System, the sensitivity analysis on the aerodynamic performance of the first stage showed a higher demand on the maximum lift-over-drag ratio of the first stage. The maximum lift-over-drag ratio directly determines the gliding range. For a more gradual ascent, reducing the gravity loss, the gliding range needs to be maximized.

Primary Sub-Question 4: *How does the airplane configuration of the first stage influence the trajectory?*

A very surprising result is the fact that this study shows that the trajectory of the first stage in the dense layers of the atmosphere is not very influential on the orbital injection of the payload. The sensitivity analysis shows almost no sensitivity between runway heading and orbital injection, showing that a smaller or larger heading turn does not directly influence orbital performance. Also it is found that until a threshold in altitude, it does not matter at which altitude the heading turn is performed. Furthermore, the result of the sensitivity analysis also shows the least sensitive behaviour for a change of the first stage control nodes, supporting the statement that the first stage trajectory is not of major influence on the result.

The shape of the trajectory in the dense layers of the atmosphere is dominantly influenced by the return of the first stage. For this reason the ascent trajectory is very steep, with desired *Flight Path Angles* (FPAs) between 60° and 80°. The sensitivity analysis on the control nodes of the first stage shows that the solution in terms of orbital injection is mildly sensitive to the variation of nodes. However, the return of the first stage is sensitive to variations lowering the FPA. This is due to the fact that when the FPA is lowered the horizontal velocity increases, which results in overshooting the point of entry for gliding back to the spaceport.

Also the aerodynamic and pressure loss are found larger in the first stage trajectory. This difference comes from the unconventional shape of the first stage and the corresponding trajectory. The first stage has a longer exposure time to the dense layers of the atmosphere, which increases the pressure loss. Also the airplane shape of the first stage increases the drag coefficient, which results in more aerodynamic loss during the ascent of the vehicle. In the ascent velocity profile a period is observed in which the velocity is constant, as an equilibrium between aerodynamic drag, gravity and thrust is formed.

The most propellant-efficient trajectory for changing the heading after take-off is not determined. Instead, the result of the study shows that there is not a more propellant-efficient trajectory for changing heading. After take-off a turn is performed to change the azimuth (heading) of the first stage into the desired azimuth for orbit injection. It is found that the altitude at which this turn is started does not affect the design of the vehicle. Although, the study also shows that when the altitude is increased above a threshold value the vehicle is not able to complete the turn before leaving the dense layers of the atmosphere. For the baseline scenario it is determined that up to and including 4000 m the heading turn can be performed. If the turn is started above 4000 m in altitude the vehicle is not able of completing the turn, which results in an Eastward injection of the payload at an inclination corresponding with the latitude of take-off.

9.2. Recommendations

The conclusions shown answer to the different research questions. During the development of the numerical tool as well as during answering to the research questions very interesting new topics are identified. The following recommendations are given, on topics which allow for a more detailed understanding.

First stage geometry optimization: The geometry of the first stage is not optimized due to the assumption of using the *X-34 Advanced Technology Demonstrator* (X-34) wind tunnel test data. Developing a vehicle model in which the structural and aerodynamic performance of the vehicle is related to the design will allow for a more advanced *Multidisciplinary Design Optimization* (MDO). It is interesting to research what are the options on shape and size, optimizing the aerodynamic performance while minimizing mass. This can also include a study on novel materials that are both price-efficient and well performing within the different environments experienced by the vehicle.

First stage guidance in the dense layers of the atmosphere: The trajectory found in this study is optimized by a set of 10 control nodes. Especially the trajectory of the first stage allows for a more detailed analysis. This can include an analysis on the control of the vehicle and corresponding flight mechanics. Also the re-entry phase of the trajectory needs a more detailed analysis. A local optimization is required to create a smoother re-entry trajectory, without the large peak acceleration while remaining with a similar gliding range. As the design of the trajectory is dominantly determined by the gliding range, this analysis needs to be done in correspondence with the actual vehicle design. The dependency of the two will result in an interesting trade-off, determining the mission geometry in more detail.

Upper stage preliminary design and analysis: It is found that the upper stage design is driving the performance of the System. Especially a high PMF is required to create enough ΔV performance, such that the first stage can meet all the operational requirements. It is of utmost importance to have a better understanding of the performance of the upper stage early in the development process. It is for this reason that the recommendation is to do a preliminary design and analysis on the upper stage, for estimating the performance with a higher fidelity. Also interesting is finding a lightweight fairing solution, adequate for payload protection in thin layers of the atmosphere, without the necessity of ejection during flight.

Detailing of the Multidisciplinary Design Optimization Tool: The MDO tool used in this study allows for detailing. One of the recommendations is to develop a throttling model for both the first and upper stage. It is interesting to research if the performance increases by using throttling. Another improvement that can be done is to create a local optimizer for refining the solution. The sensitivity analysis showed a spread in total dry mass of approximately 1%. With a local optimization method this can be reduced, creating closer convergence to the optimum. Finally, it is also interesting to do a multi-objective optimization around a certain design. In that case for example payload mass and orbital altitude can be optimized, creating a Pareto front of available payload performance at different altitudes.

Cost model development: To quantify the CpF a detailed cost model is required. This is a difficult task. However, for developing and selling the System it is required to have an estimate of the cost of a launch per kilogram payload. Therefore, it is recommended to create a detailed cost model.

Bibliography

Balesdent, M. (2011). *Optimisation Multidisciplinaire de Lanceurs (Multidisciplinary Design Optimization of Launch Vehicles)*. PhD thesis, Ecole centrale de Nantes.

Betts, J. (1998). Survey of numerical methods for trajectory optimization. *Journal of guidance, control, and dynamics*, 21(2):193–207. doi: 10.2514/2.4231.

Bradford, J. and St. Germain, B. (2010). Rocket back trajectory sensitivity analyses for a reusable booster system. In *AIAA SPACE 2010 Conference & Exposition*, page 8672. doi: 10.2514/6.2010-8672.

Brauckmann, G. (1999). X-34 vehicle aerodynamic characteristics. *Journal of Spacecraft and Rockets*, 36(2):229–239. doi: 10.2514/2.3453.

Castellini, F. (2012). *Multidisciplinary Design Optimization for Expendable Launch Vehicles*. PhD thesis, Politecnico di Milano.

COESA Working Group (1976). *US standard atmosphere, 1976*. National Oceanic and Atmospheric Administration and National Aeronautics and Space Administration and United States Air Force. NASA TM-X-74335.

Contant, S. (2019). *Design and Optimization of a Small Reusable Launch Vehicle Using Vertical Landing Techniques*. Delft University of Technology.

Curry, D. (1993). *Space Shuttle Orbiter thermal protection system design and flight experience*. National Aeronautical and Space Administration. NASA-TM-104773.

Drenthe, N. (2016). *Small Orbital Launch Systems, a Tentative Initial Cost Estimate*. Delft University of Technology.

Elsayed, S., Sarker, R., and Essam, D. (2011). Differential evolution with multiple strategies for solving CEC2011 real-world numerical optimization problems. In *2011 IEEE Congress of Evolutionary Computation (CEC)*, pages 1041–1048. doi: 10.1109/CEC.2011.5949732.

Fay, J. and Riddell, F. (1958). Theory of stagnation point heat transfer in dissociated air. *Journal of the Aeronautical Sciences*, 25(2):73–85. doi: 10.2514/8.7517.

Fehlberg, E. (1969). *Low-order classical Runge-Kutta formulas with stepsize control and their application to some heat transfer problems*. National Aeronautical and Space Administration. NASA-TR-R-315.

Freeman Jr, D., Talay, T., and Austin, R. (1997). Reusable launch vehicle technology program. *Acta Astronautica*, 41(11):777–790. doi: 10.1016/S0094-5765(97)00197-5.

Gockel, W., Kyr, P., Janovsky, R., and Roenneke, A. (2004). Reusable RLV Demonstrator Vehicles - Phoenix flight test results and perspectives. In *55th International Astronautical Congress of the International Astronautical Federation, the International Academy of Astronautics, and the International Institute of Space Law*. doi: 10.2514/6.IAC-04-V.6.04.

Haex, T. (2019). *Dawn Aerospace Mk-III Literature Study - The optimal first and second stage design of a winged Two Stage to Orbit semi-Reusable Launch Vehicle*. Delft University of Technology.

Harpold, J. and Graves, C. (1978). *Shuttle Entry Guidance*. National Aeronautical and Space Administration. AAS-PAPER-78-147.

Hellman, B. (2005). *Comparison of return to launch site options for a reusable booster stage*. Georgia Institute of Technology.

Hellman, B. (2007). Return to launch site trajectory aeroheating for a resuable booster. In *AIAA SPACE 2007 Conference & Exposition*, page 6151. doi: 10.2514/6.2007-6151.

Holt, J. and Monk, T. (2009). Propellant mass fraction calculation methodology for launch vehicles and application to ares vehicles. In *AIAA SPACE 2009 Conference & Exposition*, page 6655. doi: 10.2514/6.2009-6655.

Huzel, D. and Huang, D. (1971). *Design of Liquid Propellant Rocket Engines Second Edition*. Office of Technology Utilization National Aeronautical and Space Administration. NASA-SP-125.

Jo, S., An, S., Kim, J., Yoon, H., and Kwon, S. (2011). Performance characteristics of hydrogen peroxide/kerosene staged-bipropellant engine with axial fuel injector. *Journal of Propulsion and Power*, 27(3):684–691. doi: 10.2514/1.B34083.

Kesteren, M. v. (2013a). *Air Launch versus Ground Launch: a Multidisciplinary Design Optimization Study of Expendable Launch Vehicles on Cost and Performance*. Delft University of Technology.

Kesteren, M. v. (2013b). *Air Launch versus Ground Launch: Literature study V1.0*. Delft University of Technology.

Ko, W., Quinn, R., and Gong, L. (1982). *Reentry heat transfer analysis of the space shuttle orbiter*. National Aeronautical and Space Administration. NASA-82N23491.

Koelle, D. (2013). *Handbook of cost engineering for space transportation systems with TransCost 8.2 : statistical-analytical model for cost estimation and economical optimization of launch vehicles*. TCS - TransCostSystems.

Kopp, A., Stappert, S., Mattsson, D., Olofsson, K., Marklund, E., Kurth, G., Mooij, E., and Roorda, E. (2018). The Aurora space launcher concept. *CEAS Space Journal*, 10(2):167–187. doi: 10.1007/s12567-017-0184-2.

Leomanni, M., Bianchini, G., Garulli, A., and Giannitrapani, A. (2017). A class of globally stabilizing feedback controllers for the orbital rendezvous problem. *International Journal of Robust and Nonlinear Control*, 27(18):4607–4621. doi: 10.1002/rnc.3817.

Lips, T. and Fritsche, B. (2005). A comparison of commonly used re-entry analysis tools. *Acta Astronautica*, 57(2-8):312–323. doi: 10.1016/j.actaastro.2005.03.010.

LMSC Space Systems Division (1972). *Shuttle/Agena Study. Volume 1: Executive summary*. National Aeronautical and Space Administration and Lockheed Missiles and Space Company. NASA-CR-115491.

Maddock, C., Ricciardi, L., West, M., West, J., Kontis, K., Rengarajan, S., Evans, D., Milne, A., and McIntyre, S. (2018). Conceptual design analysis for a two-stage-to-orbit semi-reusable launch system for small satellites. *Acta Astronautica*, 152:782–792. doi: 10.1016/j.actaastro.2018.08.021.

McIntyre, S., Fawcett, T., Dickinson, T., Maddock, C., Mogavero, A., Ricciardi, L., Toso, F., West, M., Kontis, K., Lo, K., et al. (2016). How to launch small payloads? Evaluation of current and future small payload launch systems. In *14th Reinventing Space Conference*.

Mooij, E. (2017). *Re-entry Systems Lecture Notes*. Delft University of Technology.

Moon, Y., Park, C., Jo, S., and Kwon, S. (2014). Design specifications of H2O2/kerosene bipropellant rocket system for space missions. *Aerospace Science and Technology*, 33(1):118–121. doi: 10.1016/j.ast.2014.01.006.

Raymer, D. (1992). *Aircraft Design: A Conceptual Approach*. American Institute of Aeronautics and Astronautics. doi: 10.2514/4.104909.

Roorda, E. (2017). *Thermal Protection System Analysis and Sizing for Spaceplane Configurations*. Delft University of Technology.

Sachdev, J., Ahuja, V., Hosangadi, A., and Allgood, D. (2010). Analysis of flame deflector spray nozzles in rocket engine test stands. In *46th AIAA/ASME/SAE/ASEE Joint Propulsion Conference & Exhibit*, page 6972.

Schlingloff, H. (2005). *Astronautical engineering: an introduction to the technology of spaceflight*. Ingenieurburo Dr. Schlingloff Publications.

Soller, S., Wagner, R., Kau, H.-P., Martin, P., and Maeding, C. (2005). Characterisation of main chamber injectors for GOX/Kerosene in a single element rocket combustor. In *41st AIAA/ASME/SAE/ASEE Joint Propulsion Conference & Exhibit*, page 3750. doi: 10.2514/6.2005-3750.

Spies, J. and Kuczera, H. (1999). The sub-orbital hopper - one of FESTIP's preferred concepts. In *9th International Space Planes and Hypersonic Systems and Technologies Conference*, page 4945. doi: 10.2514/6.1999-4945.

Storn, R. and Price, K. (1997). Differential evolution - a simple and efficient heuristic for global optimization over continuous spaces. *Journal of global optimization*, 11(4):341–359. doi: 10.1023/A:1008202821328.

Sutton, G. and Biblarz, O. (2001). *Rocket Propulsion Elements - 7th ed.* John Wiley & Sons.

Tsiolkovsky, K. (1903). The exploration of cosmic space by means of reaction motors. *The Science Review*, 5.

Tsuchiya, T. and Mori, T. (2004). Optimal conceptual design of two-stage reusable rocket vehicles including trajectory optimization. *Journal of Spacecraft and Rockets*, 41(5):770–778. doi: 10.2514/1.1082.

Tugnoli, M., Sarret, M., and Aliberti, M. (2019). *European Access to Space: Business and Policy Perspectives on Micro Launchers.* Springer.

Vandamme, J. (2012). *Assisted-Launch Performance Analysis: Using Trajectory and Vehicle Optimization.* Delft University of Technology.

Wakker, K. (2015). *Fundamentals of Astrodynamics.* Delft University of Technology.

Weck, O. d., Agte, J., Sobieszczanski-Sobieski, J., Arendsen, P., Morris, A., and Spieck, M. (2007). State-of-the-art and future trends in multidisciplinary design optimization. In *48th Aiaa/Asme/Asce/Ahs/Asc Structures, Structural Dynamics, and Materials Conference*, page 1905. doi: 10.2514/6.2007-190.

Weiland, C. (2014). *Aerodynamic data of space vehicles.* Springer Science & Business Media.

Wittenberg, H., Ambrosius, B., Naeije, M., and Mooij, E. (2014). *Rocket Motion Lecture Notes.* Delft University of Technology.

Zandbergen, B. (2015). Simple mass and size estimation relationships of pump fed rocket engines for launch vehicle conceptual design. In *6th European Conference for Aeronautics and Space Sciences (EUCASS).*

Zandbergen, B. (2018). *Thermal Rocket Propulsion.* Delft University of Technology.

Zegler, F. and Kutter, B. (2010). Evolving to a depot-based space transportation architecture. In *AIAA Space 2010 Conference & Exposition*, page 8638. doi: 10.2514/6.2010-8638.

Zill, D. (2012). *A first course in differential equations with modeling applications.* Cengage Learning.

A

Baseline design input and result

Baseline design			
Vehicle design		**Trajectory design**	
Fst. stage brnt. [**s**]	167.97	Node 1 [**deg**]	61.01
Up. stage brnt. 1 [**s**]	321.90	Node 2 [**deg**]	60.30
Up. stage brnt. 2 [**s**]	64.63	Node 3 [**deg**]	69.30
Coasting time [**s**]	155.59	Node 4 [**deg**]	68.11
Return time [**s**]	10.67	Node 5 [**deg**]	72.54
Engine amount [-]	13	Node 6 [**deg**]	40.69
Mass flow [**kg/s**]	13.88	Node 7 [**deg**]	22.36
Fst. stage exit diam. [**m**]	0.347	Node 8 [**deg**]	14.61
Up. stage exit diam. [**m**]	0.745	Node 9 [**deg**]	1.61
Up. stage diameter [**m**]	1.807	Node 10 [**deg**]	-0.09

Design input of the launch vehicle for the baseline scenario

Baseline design			
First stage		**Upper stage**	
Dry mass [**kg**]	5926.45	Dry mass [**kg**]	346.59
Propellant consumption [**kg**]	31204.61	Propellant consumption [**kg**]	5345.12
Total mass [**kg**]	42972.77	Total mass [**kg**]	5841.71
Vacuum thrust [**kN**]	521.294	Vacuum thrust [**kN**]	42.914
Vacuum specific impulse [**s**]	294.42	Vacuum specific impulse [**s**]	315.19
ΔV [**m/s**]	3530.51	ΔV [**m/s**]	7619.36
Return ΔV [**m/s**]	403.67	Length [**m**]	4.962
Length [**m**]	19.360		

Design of the launch vehicle for the baseline scenario

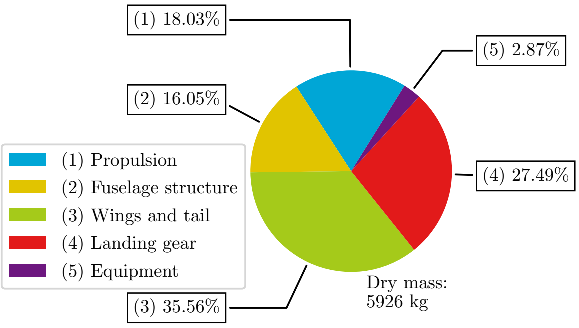

First stage dry mass breakdown of the baseline design

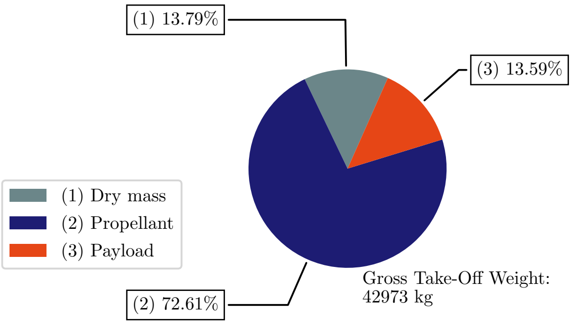

First stage total mass breakdown of the baseline design

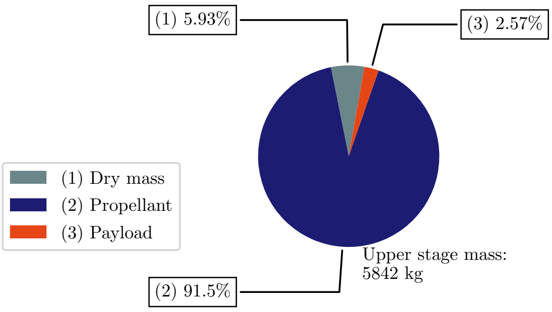

Upper stage total mass breakdown of the baseline design

B

Glideback return loss analysis

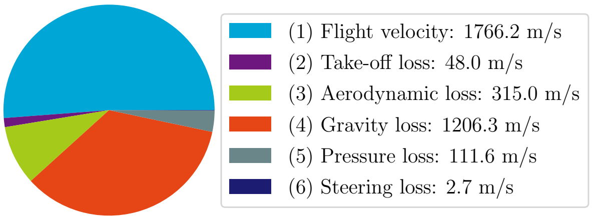

ΔV distribution of the first stage during ascent in the glideback scenario, showing the increase in velocity and the occurring losses

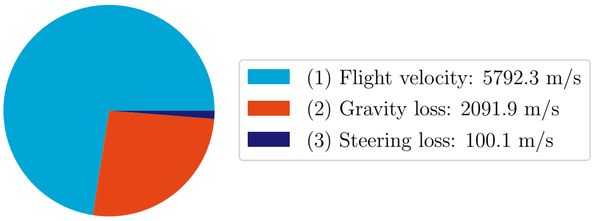

ΔV distribution of the upper stage during ascent in the glideback scenario, showing the increase in velocity and the occurring losses

C

Sensitivity analysis results

One-at-the-time approach

Control nodes (important note: different y-scale per figure for readability)

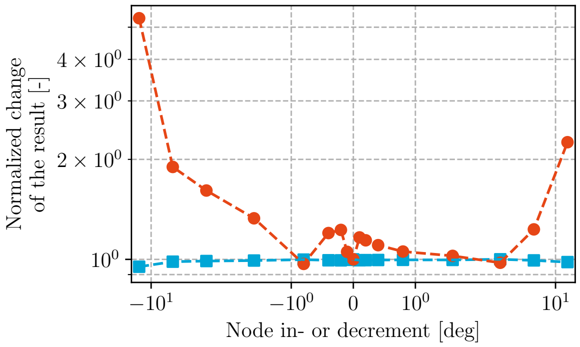

Normalized change of the semi-major axis altitude and eccentricity for in- and decrements of control node 1

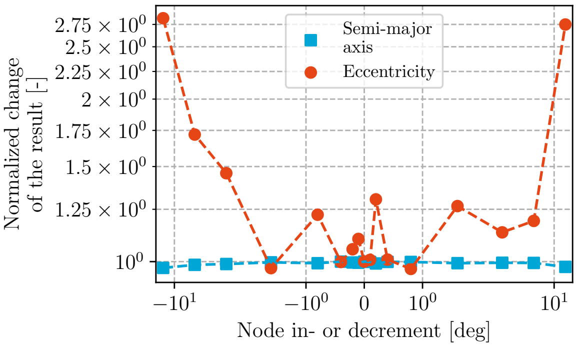

Normalized change of the semi-major axis altitude and eccentricity for in- and decrements of control node 2 (legend valid for all control node figures, a cross indicates exceeding the limit)

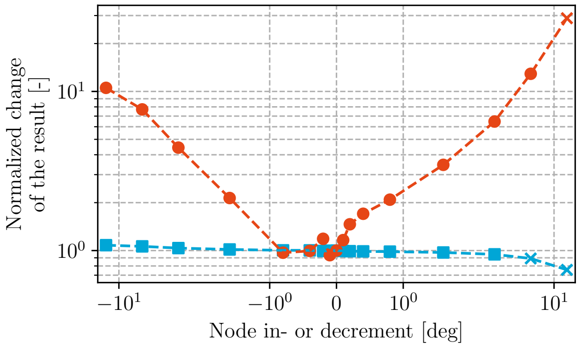

Normalized change of the semi-major axis altitude and eccentricity for in- and decrements of control node 3

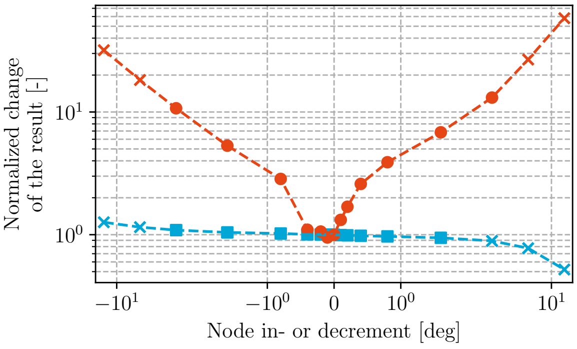

Normalized change of the semi-major axis altitude and eccentricity for in- and decrements of control node 4

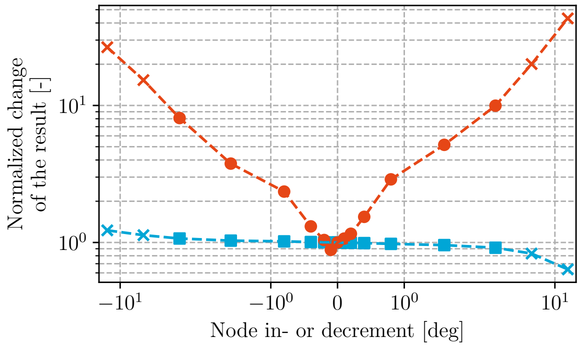

Normalized change of the semi-major axis altitude and eccentricity for in- and decrements of control node 5

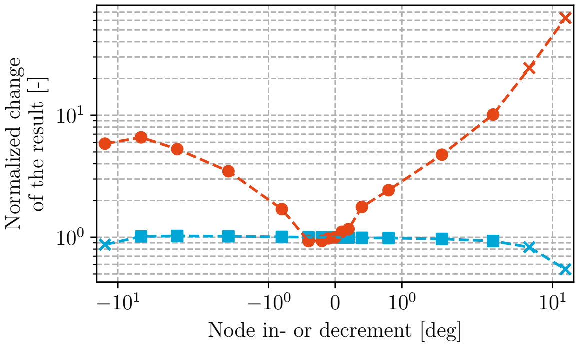

Normalized change of the semi-major axis altitude and eccentricity for in- and decrements of control node 6

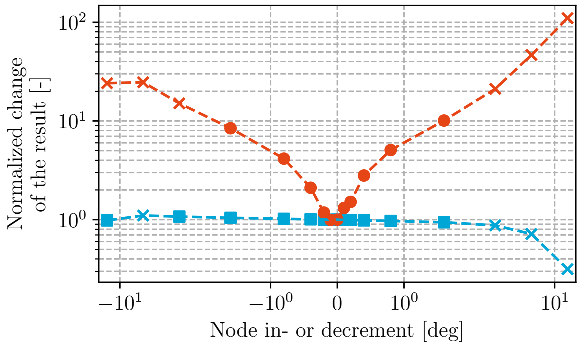

Normalized change of the semi-major axis altitude and eccentricity for in- and decrements of control node 7

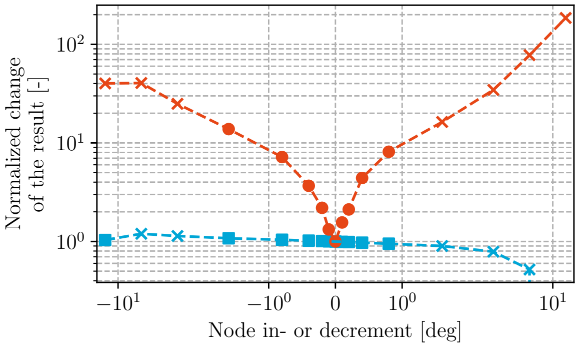

Normalized change of the semi-major axis altitude and eccentricity for in- and decrements of control node 8

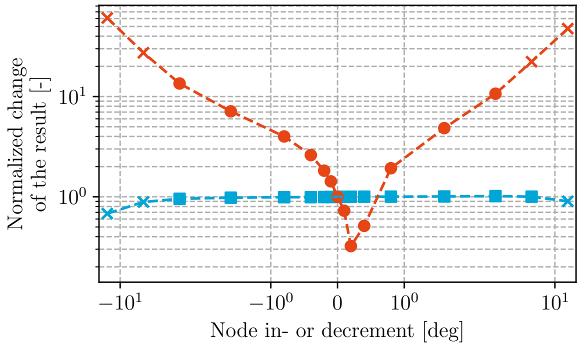

Normalized change of the semi-major axis altitude and eccentricity for in- and decrements of control node 9

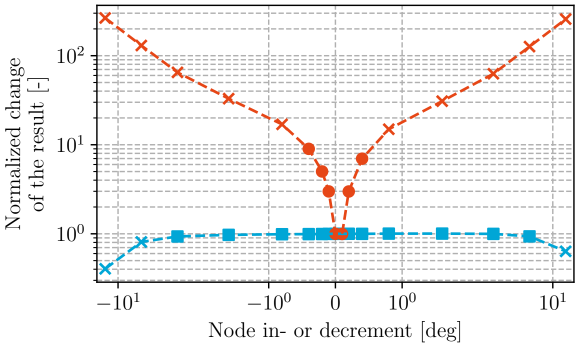

Normalized change of the semi-major axis altitude and eccentricity for in- and decrements of control node 10

Time (important note: different y-scale per figure for readability)

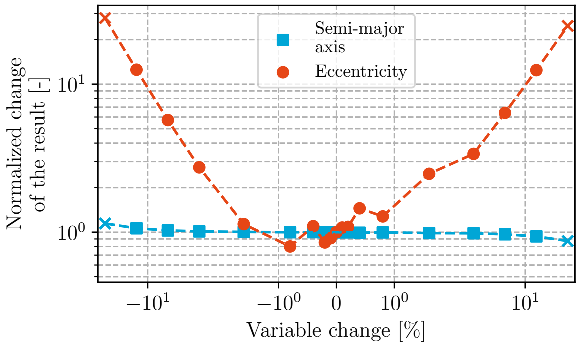

Normalized change of the semi-major axis altitude and eccentricity for a change of upper stage coasting time (legend valid for all time and vehicle design figures, a cross indicates exceeding the limit)

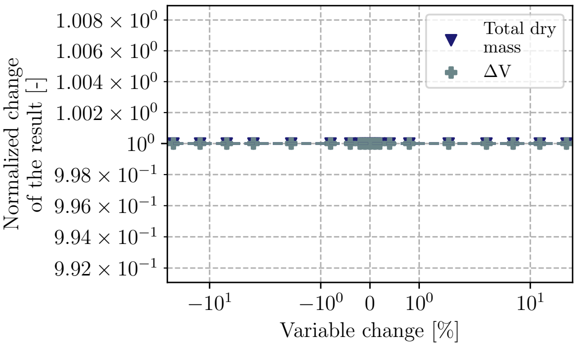

Normalized change of the total dry mass and ΔV for a change of upper stage coasting time (legend valid for all time and vehicle design figures)

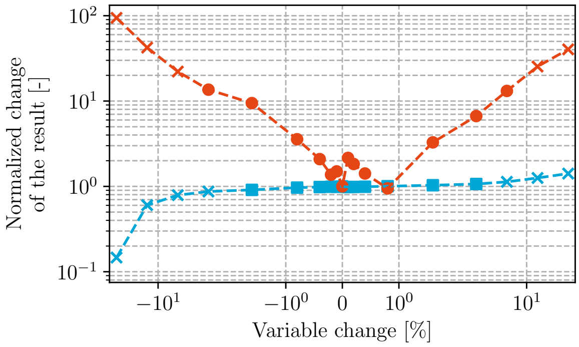

Normalized change of the semi-major axis altitude and eccentricity for a change of first stage burn time

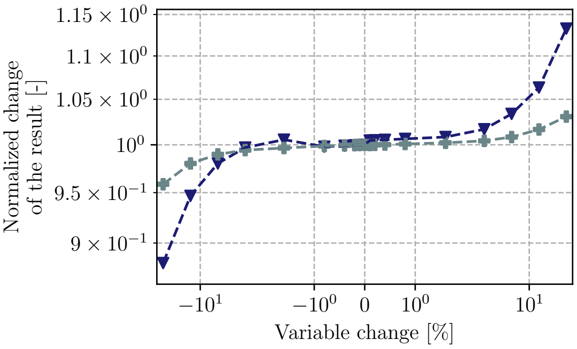

Normalized change of the total dry mass and ΔV for a change of first stage burn time

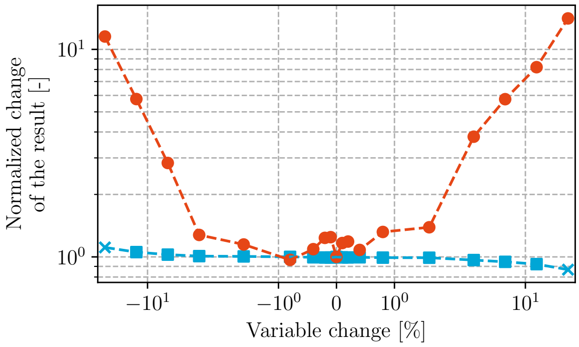

Normalized change of the semi-major axis altitude and eccentricity for a change of first stage boostback time

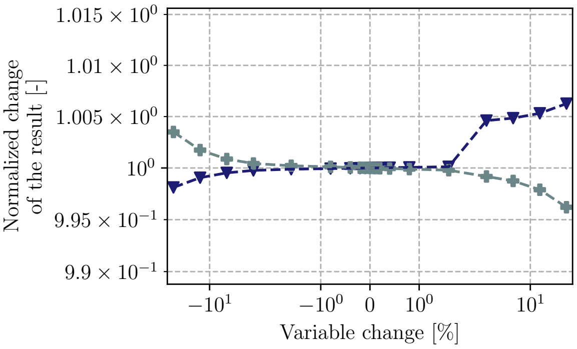

Normalized change of the total dry mass and ΔV for a change of first stage boostback time

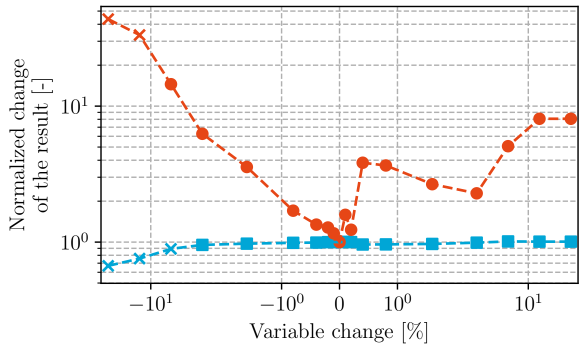

Normalized change of the semi-major axis altitude and eccentricity for a change of upper stage first burn time

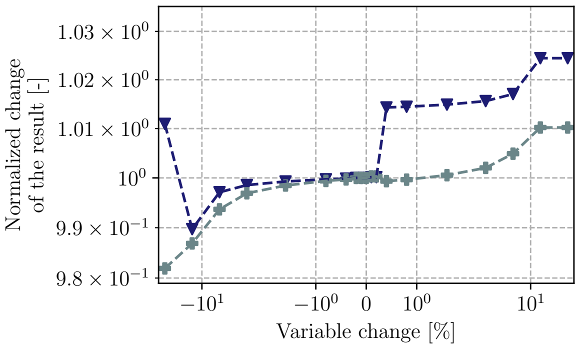

Normalized change of the total dry mass and ΔV for a change of upper stage first burn time

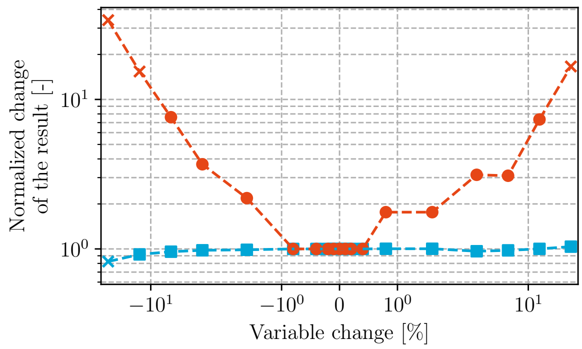

Normalized change of the semi-major axis altitude and eccentricity for a change of upper stage second burn time

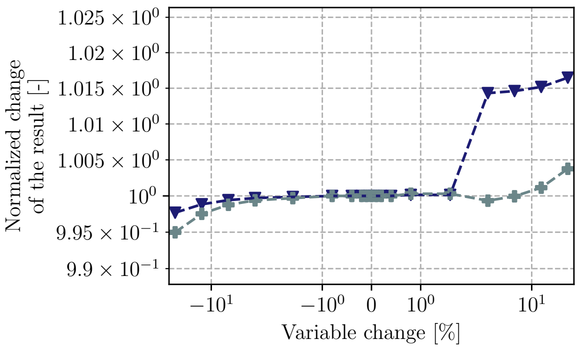

Normalized change of the total dry mass and ΔV for a change of upper stage second burn time

Vehicle design (important note: different y-scale per figure for readability)

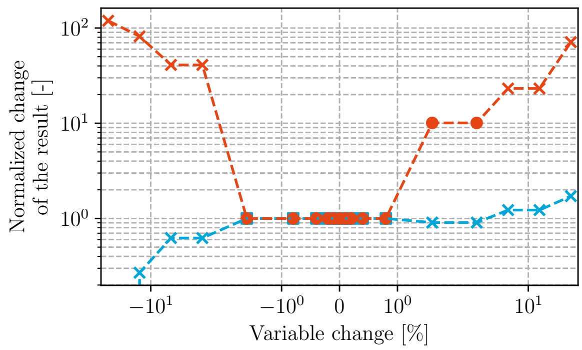

Normalized change of the semi-major axis altitude and eccentricity for a change of engine amount (scalar value is rounded to nearest integer)

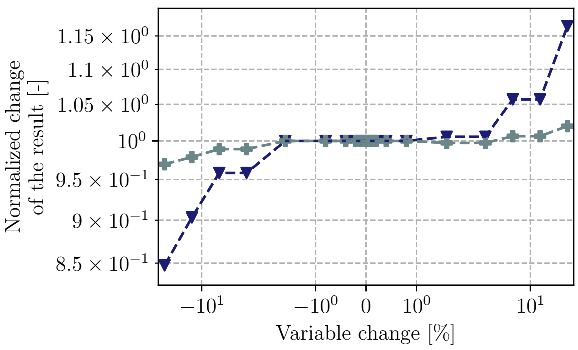

Normalized change of the total dry mass and ΔV for a change of engine amount (scalar value is rounded to nearest integer)

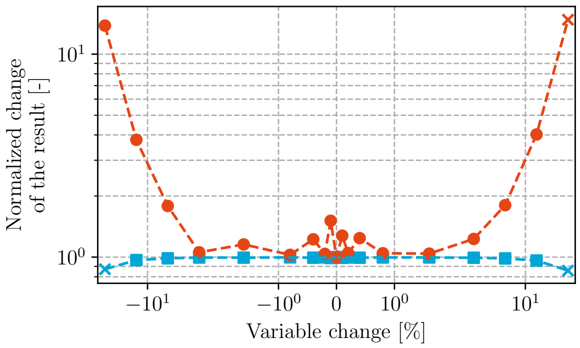

Normalized change of the semi-major axis altitude and eccentricity for a change of first stage engine exit diameter

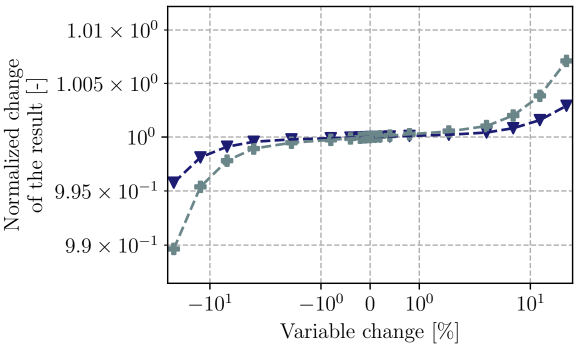

Normalized change of the total dry mass and ΔV for a change of first stage engine exit diameter

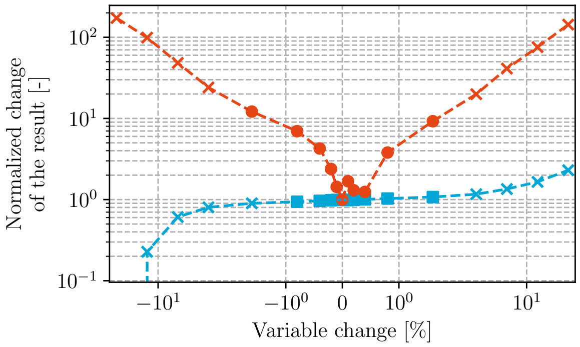

Normalized change of the semi-major axis altitude and eccentricity for a change of mass flow

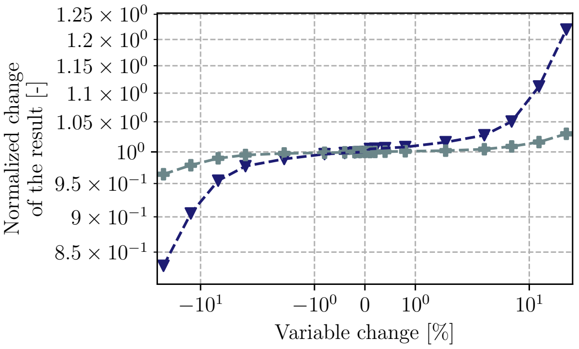

Normalized change of the total dry mass and ΔV for a change of mass flow

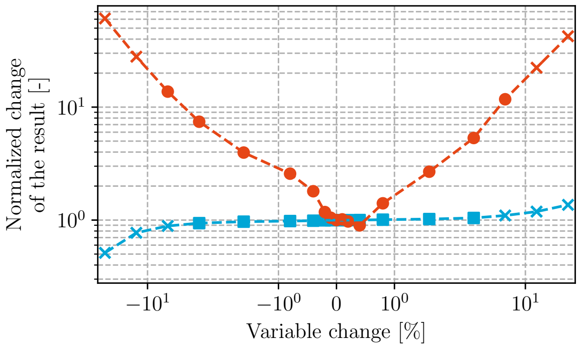

Normalized change of the semi-major axis altitude and eccentricity for a change of upper stage engine exit diameter

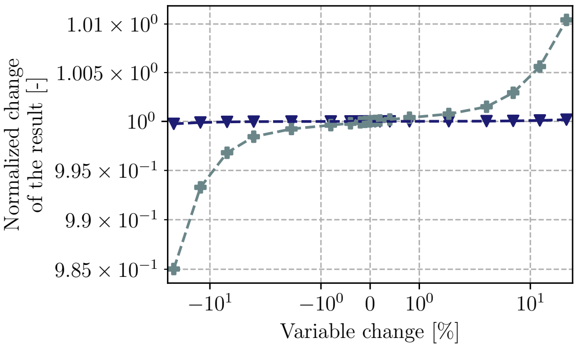

Normalized change of the total dry mass and ΔV for a change of upper stage engine exit diameter

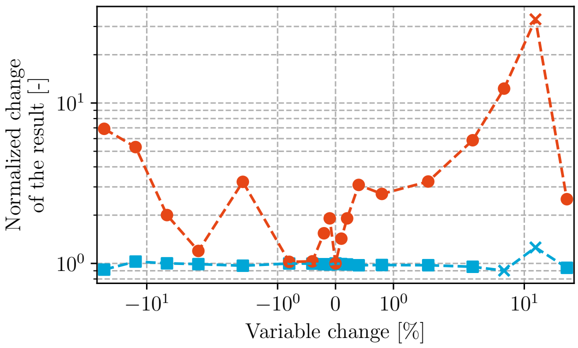

Normalized change of the semi-major axis altitude and eccentricity for a change of upper stage diameter

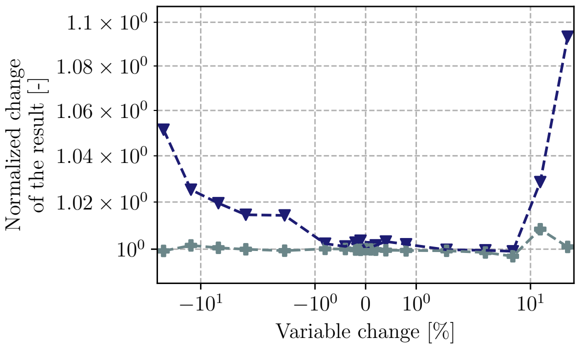

Normalized change of the total dry mass and ΔV for a change of upper stage diameter

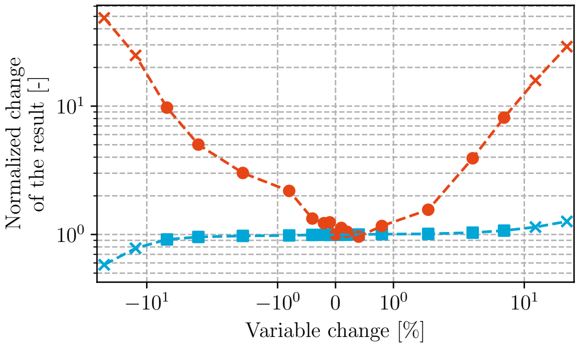

Normalized change of the semi-major axis altitude and eccentricity for a change of chamber pressure

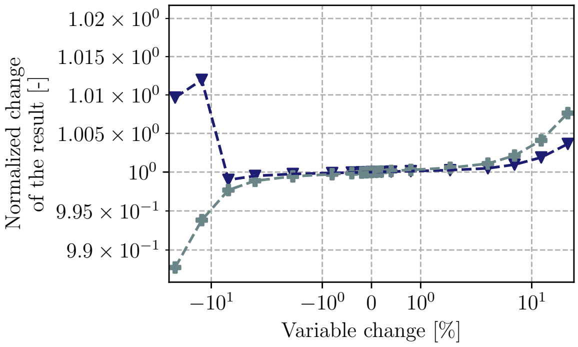

Normalized change of the total dry mass and ΔV for a change of chamber pressure

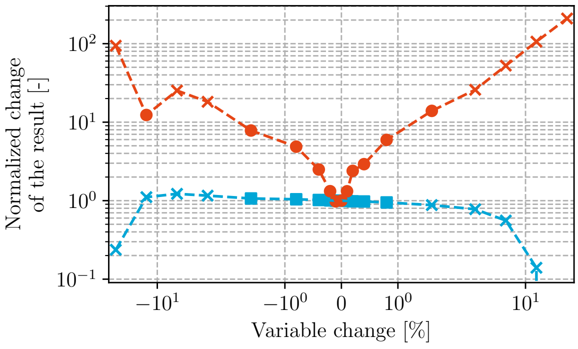

Normalized change of the semi-major axis altitude and eccentricity for a change of oxidizer-over-fuel ratio

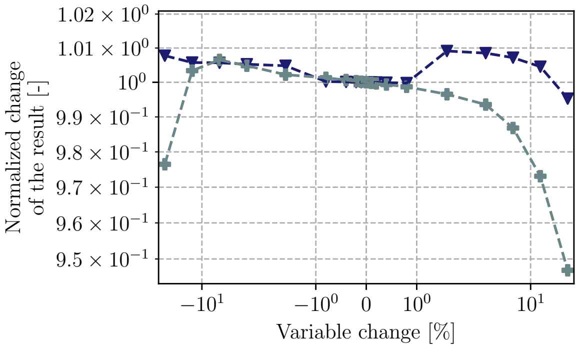

Normalized change of the total dry mass and ΔV for a change of oxidizer-over-fuel ratio

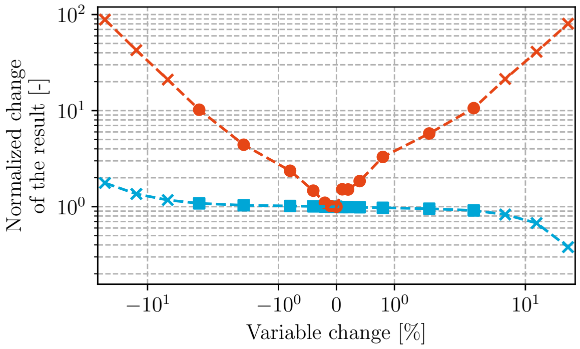

Normalized change of the semi-major axis altitude and eccentricity for a change of payload mass

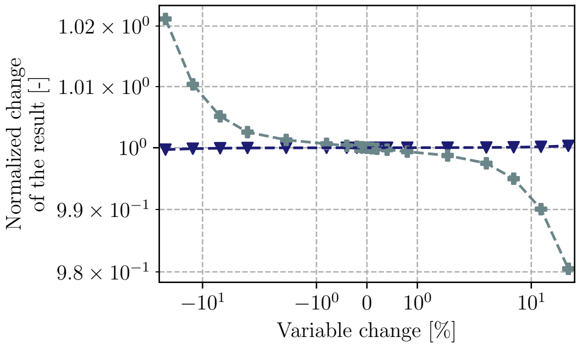

Normalized change of the total dry mass and ΔV for a change of payload mass

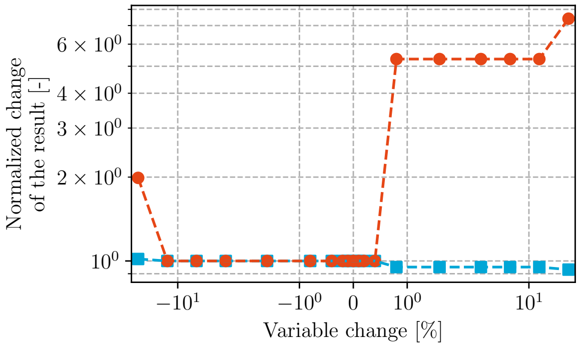

Normalized change of the semi-major axis altitude and eccentricity for a change of payload length

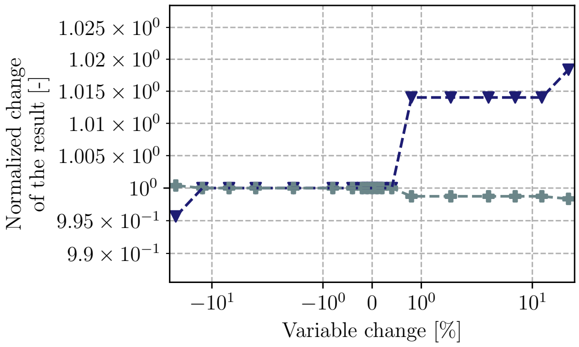

Normalized change of the total dry mass and ΔV for a change of payload length